

Helmholtz-Zentrum Berlin für Materialien und Energie und Institut für Physik,
Universität Potsdam

**A photoemission study of quasiparticle excitations,
electron-correlation effects and magnetization
dynamics in thin magnetic systems**

Dissertation

zur Erlangung des akademischen Grades
Doctor rerum naturalium (Dr.rer.nat.)
in der Wissenschaftsdisziplin Experimentalphysik

eingereicht an der
Mathematisch-Naturwissenschaftlichen Fakultät
der Universität Potsdam

von

Jaime Sánchez-Barriga

Berlin 2010

Published online at the
Institutional Repository of the University of Potsdam:
URL <http://opus.kobv.de/ubp/volltexte/2010/4849/>
URN <urn:nbn:de:kobv:517-opus-48499>
<http://nbn-resolving.org/urn:nbn:de:kobv:517-opus-48499>

Contents

1	Introduction	1
2	Methodical background	6
2.1	Technique of spin- and angle-resolved photoemission (SARPES)	6
2.1.1	Basic principles	6
2.1.2	Spin polarization	9
2.1.3	The photoemission process	12
2.1.4	Final state broadening	17
2.1.5	Symmetry of initial states and selection rules	18
2.1.6	Beyond the single particle picture	19
2.2	X-ray magnetic circular dichroism (XMCD)	20
2.2.1	XMCD in photoelectron emission microscopy (PEEM)	21
3	Experimental aspects	23
3.1	Synchrotron radiation	23
3.1.1	Bending magnet radiation and insertion devices (IDs)	24
3.1.2	Beamlines and monochromators	26
3.1.3	Time structure of synchrotron radiation	26
3.2	SARPES experiment	27
3.2.1	The hemispherical analyzer and the Mott spin detector	28
3.3	Time-resolved XMCD-PEEM experiments	32
3.3.1	Magnetron sputtering system	33
3.3.2	The PEEM microscope	33
3.3.3	Contrast mechanisms in PEEM	35
3.3.4	Time resolution in XMCD-PEEM	37
3.3.5	The laser system and the synchronization scheme	39
4	Strength of correlation effects in the electronic structure of 3d ferro-	42
	magnets	
4.1	Introduction	42
4.2	Theoretical background	44
4.2.1	Density functional theory in the local density approximation (DFT-LDA)	45
4.2.2	Dynamical mean-field theory (DMFT) and three-body scattering approximation (3BS)	47
4.3	Experimental details	49

4.3.1	The geometry of the experiment and low-energy electron diffraction (LEED)	50
4.3.2	Easy axis of magnetization	51
4.3.3	Growth mechanisms revisited	51
4.3.4	The clean W(110) substrate in normal photoemission	52
4.4	Spin-dependent electronic correlations: a comparison theory-experiment	54
4.4.1	bcc Fe(110)	54
4.4.2	hcp Co(0001)	68
4.5	Summary of conclusions	83
5	Spin-dependent properties of graphene on 3d ferromagnets	85
5.1	Introduction	85
5.2	The Rashba effect	87
5.3	Experimental details	89
5.4	Dirac-cone formation in quasi-freestanding graphene after intercalation of Au	91
5.5	Spin-dependent properties and Rashba splitting in graphene on Ni and Co	97
5.6	Summary of conclusions	103
6	Imaging of ps-resolved magnetization dynamics in magnetic microstructures	104
6.1	Introduction	104
6.2	Fundamentals of magnetization dynamics	106
6.2.1	The micromagnetic approximation	106
6.2.2	Contributions to the total micromagnetic energy	107
6.2.3	The Landau–Lifshitz–Gilbert equation	108
6.3	Experimental details	110
6.3.1	Sample holder for time-resolved investigations in the Focus IS-PEEM	111
6.3.2	Determination of the time zero and pulse shape of the experiment	115
6.4	Results and discussion: dynamics of cross-tie domain walls	118
6.5	Summary of conclusions and outlook	127
	Summary	130
	Zusammenfassung	132
	Acknowledgements	134
	Bibliography	136
	Publication List	147
	Curriculum Vitae	148

Chapter 1

Introduction

This thesis is devoted to the study of the fundamental electronic, magnetic and dynamical properties of magnetic systems with reduced dimensions. The main motivation of this work has been to explore the spin-dependent properties of these systems in the time and energy domains by means of photoemission-related techniques in combination with synchrotron radiation.

Since more than half a century a lot of research activity has been devoted to ferromagnetic materials. Since the discovery of interlayer exchange coupling (IEC) [1] and giant magnetoresistance (GMR) [2, 3] a tremendous technological advance of storage media, read-out sensors and magnetic random access memories (MRAMs) has been achieved. The finding of GMR initiated important research activities on the magnetotransport properties of different magnetic multilayer systems. The IEC, which typically occurs between two ferromagnetic layers separated by a nonferromagnetic layer, a so-called spin-valve system, is characterized by the fact that both the sign and the coupling strength change in a damped oscillatory behaviour as a function of the interlayer thickness. This property is widely employed nowadays to define a stable magnetization configuration in magnetic devices with potential applications in magnetic recording technology. On the other hand, the GMR effect, firstly discovered in Fe/Cr multilayers [2] and in Fe/Cr/Fe trilayers [3] in 1988, is characterized by a large change in resistivity when switching the magnetization of the layer stack from the antiparallel configuration at zero magnetic field to the parallel configuration in an applied saturation magnetic field. Both IEC and GMR are important examples of the benefit of industrial applications from fundamental research. Accompanied by the successful fabrication of ultrasmall magnetic multilayer structures, it allowed an enhanced performance of modern magnetic recording devices together with an important interest for fundamental understanding of low dimensional magnetism. The strong impact of the discovery of GMR in science and technology considerably changed our understanding of spin-dependent transport processes in real materials, leading to a new field of research, *spinelectronics* or *spintronics*, where the transport properties are not achieved via transmission of charge but spin.

One of the central questions in spintronics is what the spin-scattering length is, i.e. the distance that a spin-polarized electron can travel before its spin direction changes due to scattering processes. Furthermore, the spin polarization of charge

carriers in the vicinity of the Fermi level often decides about the efficiency of spin transport and spin transfer effects in multilayer nanostructures. Important effects which are directly related to these concepts are the tunneling magnetoresistance (TMR) [4, 5], Spin Hall Effect (SHE) [6] and Quantum Spin Hall Effect (QSHE) [7]. These properties stimulated the research for new materials suitable for spintronic applications. Among them, half-metallic ferromagnets such as Heusler alloys [8], dilute magnetic semiconductors [9], multiferroics [10] and carbon-based materials [11] are still at the focus of intensive research.

In recent years, with the aim of controlling and exhaustively tailoring properties such as perpendicular magnetic anisotropy (PMA) [12], a large variety of geometries for small-sized magnetic elements is being produced by different techniques. Magnetic nanoparticles [13], nanotubes [14], micron-sized platelets and dots [15], nanowires [16] or ultrathin films are typically fabricated by using various combinations of state-of-the-art experimental tools. Techniques such as molecular beam epitaxy (MBE) or magnetron sputtering, electron beam lithography or imprint lithography [17] are combined to produce high-quality magnetic structures of ultrasmall sizes [18]. Among them, lithography represents a top-down fabrication technique where a bulk material is reduced in size to a nanoscale pattern. Combined with MBE deposition it allows the fabrication of nanoelements with thicknesses which are accurately controlled on an atomic length scale. In this way, layers of different compositions and as thin as only a few atomic layers (monolayers, ML) can be prepared under ultra-high vacuum conditions. On the other hand, ultrathin films which are perfectly flat on an atomic scale can only be grown on appropriate single-crystal surfaces. This represents an important advantage because it allows the preparation of ultrathin epitaxial films in which there is no intermixing between the film and its substrate, leading to a perfect monocrystalline order inside the film which is in registry with the lattice of the substrate. Therefore, epitaxial growth becomes particularly important when the properties of the films are compared to theoretical predictions since these are typically based on ideal systems.

The possibility of manipulating the magnetic properties of low-dimensional structures is still a very important issue due to the continuous demand for devices with higher bit densities and faster performance. The confinement of individual layer thicknesses in the nanometer regime leads to novel quantum effects which directly influence the magnetic properties in the time and energy domains. For antiferromagnetic materials the finite-size effects lead to a scaling of the intrinsic magnetic properties like the ordering temperature and anisotropy as-well as to an enhanced contribution of the magnetically disordered surface to the macroscopic magnetization [19]. For ferromagnetic materials with reduced dimensions, the presence of a finite magnetization leads to an increased magnetic anisotropy which depends strongly on the geometry of the objects [18]. This manifests stronger when the lateral dimensions are touching to the nanoscale regime. Specially, the manipulation of the dynamical magnetic properties of such structures in ultrashort time scales [20] needs to be complementary to an appropriate characterization and control of their magnetic and geometrical properties. Therefore, the exhaustive manipulation of these properties as a function of the nanoscale dimensions is directly connected to the fundamental processes that govern magnetization dynamics in fast (picosecond) and ultrafast (femtosecond) time scales.

A deep understanding of such processes, which are still only partially understood, is crucial to improve the efficiency and reliability of current and near-future information storage media.

In a closer view, the microscopic origin of these magnetic properties, provided by the exchange and spin-orbit coupling, rests on quantum mechanical principles and it can be understood as a particular consequence of spin-dependent interactions between Fermions in a many-electron system. Particularly, important contributions to the magnetic properties come from electrons located in the vicinity of the Fermi level, basically the same electrons which lead to the fundamental optical and electrical properties in real materials. In the language of many-body quantum mechanics, these interactions lead to the formation of *quasiparticles* and *collective excitations*. On the one hand, a quasiparticle can be understood in simple terms as a low-lying excited state of the system possessing an energy very close to the ground state energy, basically a single elementary particle whose motion is modified by interactions with the other particles in the system. On the other hand, collective excitations or collective modes, correspond to a motion of the electronic system as a whole. Because of the strong Coulomb repulsion, electron and holes in a real solid can be interpreted as quasiparticles of opposite charge and same spin whose so called effective masses can differ substantially from the mass of elementary electrons. In this case we shall speak, then, of a strongly correlated system. In a similar way, magnons and spin waves can be interpreted as collective excitations associated to the electron spin structure, and phonons and plasmons can be directly linked to atom vibrations and high-energy oscillations of the electron density in the crystal lattice, respectively. In this context, a magnon is a spin wave with zero phase, and it can be understood as a quantum of a spin wave in a similar way as a phonon can be interpreted as a quantum of a sound wave. Both quasiparticles and collective excitations are of great importance in the understanding of the electronic origin of magnetic phenomena and therefore, the study of their properties is a key prerequisite regarding the applications in charge-based electronics and spintronics.

Disentangling the complicated picture of correlated electron systems and thus the interplay of electronic interactions in real solids depends very much not only on the progress in surface preparation techniques but also on the development of new characterization methods. The availability of synchrotron radiation has opened many opportunities to study magnetism with excitation energies which are beyond the visible range, ranging from infrared to hard x-rays. One of the most important breakthroughs in this respect was achieved by the theoretical prediction and experimental discovery of magnetic linear (XMLD) and circular (XMCD) dichroism in x-ray absorption [21, 22]. This discovery was soon followed by important achievements in the investigation of magnetic materials using a new variety of experimental tools, such as x-ray magnetic circular dichroism in photoelectron emission microscopy (XMCD-PEEM) [23], nuclear resonant magnetic scattering (NRMS) [24], magnetic dichroism in the angular distribution of photoelectrons (MDAD) [25], x-ray holography [26] or x-ray resonant magnetic scattering (XRMS) [27]. In particular, the combination of synchrotron radiation and electron spectroscopy methods is suitable for the study of ultrathin magnetic films and surfaces, since the probing depth of these methods is determined by the inelastic electron mean free path, which for kinetic energies of about 10-100 eV is limited to a few

atomic layers.

Among the different techniques with remarkable fundamental interest, spin and angle-resolved photoemission spectroscopy (SARPES) is a powerful method to determine the complicated electronic structure of ferromagnets, in particular for systems with strong overlap between majority and minority spin bands [28]. SARPES investigations allow to determine the full occupied electronic bandstructure $E(\mathbf{k})$ of ultrathin films and related properties such as group velocities and lifetime of quasiparticles, many-body effects or spin-polarization of electronic states. Involving sophisticated electron spin detection schemes, SARPES experiments are performed in the momentum and energy domains, thus ultrafast dynamics and lifetimes of quasiparticle excitations can be indirectly deduced from the Heisenberg principle. The average energy of the outgoing photoelectron has a peak at the energy of the state, but its distribution has a finite width called the natural linewidth. In this sense fast-decaying states have a broad natural linewidth, while slowly-decaying states have a narrow natural linewidth. In early studies of spin and momentum-resolved photoemission carried out on Ni [29, 30], the measured spin-polarization of photoelectrons from the valence band revealed clear information about the majority and minority spin states and the magnitude of their exchange splitting. Nowadays such investigations represent a complementary tool to transport or magnetotransport measurements and still remain at the focus of experimental and theoretical research. For that reason, the use of spin resolution requires particular attention because it may lead to important implications towards the fabrication of new-generation spintronic devices where exchange and/or spin-orbit interactions control the electron spin in a sophisticated way. Among the different manifestations of the spin-orbit interaction, the Bychkov-Rashba spin-orbit coupling, generated by an electric field in a system with broken inversion symmetry, has received considerable interest [31]. The Bychkov-Rashba effect [32] causes a spin-splitting of a spin-degenerate electron gas and is accessible in SARPES investigations. The use of the Bychkov-Rashba effect for spin manipulation in novel devices may lead to new functionalities in spintronics, where spin injection and thus the manipulation of charge carriers and spin are combined. The independent charge and spin control in a single spintronic device is the challenge in a wide range of possible applications and underlying new spin-dependent phenomena which can be directly linked to SARPES experiments.

As noted before, another major issue in magnetism is the time scale, which covers an extremely large range, from astronomic to ultrashort time scales in the range of picoseconds and femtoseconds. In such small time scales, magnetic phenomena ranging from domain wall motion and domain nucleation to spin waves and spin precession are particularly interesting. Therefore, improvements in the time-resolved characterization techniques require special attention as well. Techniques such as stroboscopic Kerr microscopy [33], time-resolved magneto-optical Kerr effect [34] or time and spin-resolved two-photon photoemission [35], which often use only laser illumination, are typically important to monitor magnetic processes with femtosecond resolution. In the nano- and picosecond regime, on the other hand, the availability of synchrotron radiation becomes exceptionally advantageous because of its intrinsic well-defined time structure. It provides picosecond light pulses with repetition rates up to several hundreds of MHz,

and when combined with synchrotron-related techniques and synchronized laser illumination, it supplies both the temporal resolution and the element selectivity. These properties have been remarkably exploited in time-resolved imaging experiments, such as time-resolved XMCD-PEEM [36], in which the magnetization reversal and the large precession of the magnetization is followed by changing the incident x-rays helicity and the time delay between the magnetic pump and the photon probe pulses. Alternatively, the temporal response of the magnetization can also be driven by current-induced mechanisms. These issues are closely related to spin transfer effects in magnetic devices, since the magnetic state and the configuration of the sample have important influence on the direction and magnitude of the spin current, which at the same time has a retroactive influence on the magnetization. Due to spin-dependent scattering events, the transfer of angular momentum or spin lead to an excitation of the magnetization, which is then dissipated via spin waves. Spin transfer acts as a torque driving the magnetization into a large precessional motion and in some instances, into a complete reversal. In these cases, the microscopic picture of the magnetization dynamics is often successfully described by the Landau-Lifshitz-Gilbert (LLG) equation. The study of both current and magnetic field-induced magnetization dynamics are crucial issues in the realization of MRAMs and of novel magnetic logic and memory devices with even faster performance.

In this thesis, some of the aforementioned aspects of modern research in the field of magnetism are studied by means of SARPES and time-resolved XMCD-PEEM investigations. This work combines topics which are interconnected in various ways from the basics of fundamental magnetism to their applications in spintronics, namely correlation effects in bulk itinerant-electron ferromagnets, fundamental properties of quasiparticle excitations in two-dimensional systems and dynamics of collective excitations in ultrathin magnetic structures.

The results of the work will be presented as follows. Being this chapter a brief introduction to most of the important aspects of modern research in the field of magnetism at the nanoscale, chapter 2 is devoted to a description of the phenomenological basis of the experimental methods used in this thesis. Chapter 3 focuses on the details of the experimental systems in which the experiments have been performed. In chapter 4, spin and angle-resolved photoemission experimental data of three-dimensional bcc Fe(110) and hcp Co(0001) ferromagnetic systems are compared in detail to many-body theoretical calculations within the three-body scattering and dynamical mean-field theories, both combined with the one step-model of photoemission. Chapter 5 deals with the spin-dependent properties occurring in the electronic structure of a two-dimensional graphene layer grown on fcc Ni(111) and hcp Co(0001) ferromagnetic substrates. SARPES experiments are performed in these systems before and after intercalation of a Au monolayer between graphene and its ferromagnetic substrate. Finally, in chapter 6 we focus on the dynamical evolution of the magnetization occurring in permalloy ($\text{Fe}_{19}\text{Ni}_{81}$) microstructures by means of time-resolved x-ray magnetic circular dichroic-photoelectron emission microscopy experiments. The experimental results are compared in detail to micromagnetic theoretical calculations on the basis of the Landau-Lifshitz-Gilbert equation.

Chapter 2

Methodical background

This chapter is devoted to description of the experimental methods which, in combination with synchrotron radiation, have been used in this thesis. Firstly, we will examine the methodology of the spin- and angle-resolved photoemission spectroscopy (SARPES) technique, a versatile tool for the study of surface and thin film magnetism. By measuring the angular distribution, kinetic energy and spin of the electrons photoemitted from a sample illuminated with sufficiently high-energy radiation, important information on the momentum, energy and spin of the electrons propagating inside a material can be obtained. Such information is of major importance when investigating the electronic and magnetic properties of solids, in particular for systems in which many-body correlations are strongly affecting the one-electron excitation spectrum and the macroscopic physical properties of the system. Secondly, we will focus on the basic principle of x-ray magnetic circular dichroism (XMCD), a synchrotron-based technique which later on we will use as a contrast mechanism for magnetic imaging.

2.1 Technique of spin- and angle-resolved photoemission: Beyond the single particle picture

2.1.1 Basic principles

Angle-resolved photoemission spectroscopy (ARPES) is one of the most important methods to study the electronic structure of molecules, solids and surfaces [37, 38]. Moreover, ARPES has been established as a tool with practical implications in various fields like surface chemistry and materials science, and it has significantly contributed to the understanding of fundamental properties of solids, gases and liquids. The basic principle behind it is the photoelectric effect, originally observed by Herz [39] in 1887 and later explained as a manifestation of the quantum nature of light by Einstein [40, 41], who received the Nobel prize in 1921 especially for his discovery of the law of the photoelectric effect. In 1905, Einstein introduced the concept of the *photon* as quantum of light and deduced the relation between the maximum kinetic energy E_{kin}^{max} of the emitted electrons and the photon energy $h\nu$, which is given by the Einstein's

fundamental photoelectric equation:

$$E_{kin}^{max} = h\nu - \Phi_0 \quad (2.1)$$

where Φ_0 is the so-called *work function*, a characteristic constant of the sample surface which represents the energy necessary to release the electron from a solid. The work function can be interpreted as a measure of the potential barrier at the surface that prevents the valence electrons from escaping into the vacuum, being typically 4-5 eV in metals. Starting in 1957, the use of photoelectron emission to study the electronic structure of solids was developed by Kai Siegbahn [42], who used it to study the energy levels of atomic core electrons. Siegbahn, who received the Nobel prize in 1981 for this work, referred to the technique as Electron Spectroscopy for Chemical Analysis (ESCA), because the core levels have typically small energy shifts depending on the chemical environment of the atom which is ionized, thus allowing the determination of the chemical structure. In this context, the extended equation of the photoelectric effect providing the kinetic energy of the photoelectron

$$E_{kin} = h\nu - \Phi_0 - |E_B| \quad (2.2)$$

can be used to determine its binding energy (E_B) in the solid. The fundamental principle of the photoemission process is sketched in Fig. 2.1. In a simplified *single-particle picture*, i.e. a non-interacting electron system, it is shown how the properties of the emitted photoelectrons basically reflect the electronic eigenstates of the system under investigation. Photoexcitations of electrons from the valence band and core-levels are produced with a beam of monochromatized radiation aligned on the sample surface, typically supplied either by a gas-discharge lamp or by a synchrotron beamline. Electrons with binding energy E_B can be excited into free-electron states above the vacuum level E_{vac} by photons with energy $h\nu > E_B + \Phi_0$. The measured photoelectron distribution $I(E_{kin})$ corresponds to the occupied density of electronic states $N(E_B)$ in the solid, being $E_B = 0$ at the *Fermi energy* (E_F). Electrons deriving from the valence band can be found at binding energies of several eV, while those from core-levels contribute from several ten eV to several ten thousand eV. Basically, one distinguishes between angle-resolved ultraviolet photoemission (ARUPS) mainly for the investigation of valence-band states at low binding energies, and x-ray photoemission (XPS) providing the investigation of core-level states at higher binding energies. If these methods are combined with the use of spin resolution, one may differentiate between spin- and angle-resolved photoemission or ultraviolet photoemission (SARPES or SARUPS) depending on the energy of the incoming photons, and spin-resolved x-ray photoemission (SRXPS).

Fig. 2.2(a) shows a sketch of a spin-integrated photoelectron spectrum in the case of a metallic sample and Fig. 2.2(b) the experimental geometry of a conventional SARPES experiment. In Fig. 2.2(a) and at low binding energies, valence-band electronic states dominate the intensity distribution in the vicinity of E_F , corresponding to electrons in the occupied part of the density of states, which are the most weakly bound. At higher binding energy, sharp peaks from core-level states corresponding to strongly bound electrons are observed. Besides other features like Auger peaks, satel-

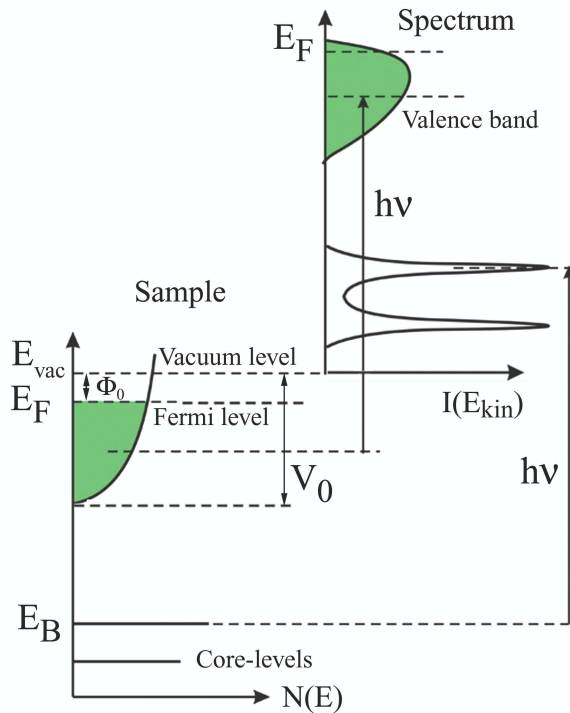


Figure 2.1: *Schematic view of the photoemission process in the single-particle picture. A photoelectron distribution $I(E_{kin})$ is produced by the incoming photons, and electrons with binding energy E_B can be excited into free-electron states above the vacuum level E_{vac} . $I(E_{kin})$ can be measured by the analyzer and in a first order corresponds to the occupied density of states $N(E_B)$ of the sample.*

lites and surface states or resonances which are typically found in real experiments, a tailed background of secondary electrons due to inelastic scattering processes which increases in intensity with increasing E_B significantly contributes to the intensity distribution. Such background makes the detection of electrons with very low kinetic energies particularly difficult. Fig. 2.2(b) is intended to show all the important angular parameters in a modern photoemission experiment with spin resolution, as well as an overview of a spin-resolved experimental apparatus. Among the angular parameters which determine the sample geometry, the most important are θ and ϕ_e , the polar and azimuthal angles of electron emission relative to the sample normal and the crystal axes respectively. Other angles are Ψ and ϕ_P , the polar and azimuthal angles of photon incidence. \mathbf{A} denotes the vector potential of the photons, which is related to the degree of polarization of the incident radiation with energy $h\nu$. The degree of linear polarization is generally expressed as the ratio of the electric field vector \mathbf{E} perpendicular (s-polarization) and parallel (p-polarization) to the plane of incidence ($\mathbf{E} = -\partial\mathbf{A}/\partial t$). Elliptical or circular polarization, on the other hand, corresponds to a phase angle δ between the s and p components. This type of experiment offers the possibility of determining the electron spin σ , which is *up*(\uparrow) or *down*(\downarrow) depending on an appropriately chosen spin quantization direction and the orientation of the sample magnetization \mathbf{M} . Therefore, the experiment is complete in the sense that it can provide all quantum numbers of the emitted photoelectron by simply measuring its kinetic energy as a function of the emission angles and the electron spin orientation, i.e., $E_{kin}(\theta, \phi_e, \sigma)$.

Experimentally, the electron energy spectra are measured with electrostatic analyzers [37]. These instruments can take many different forms, although, as shown in

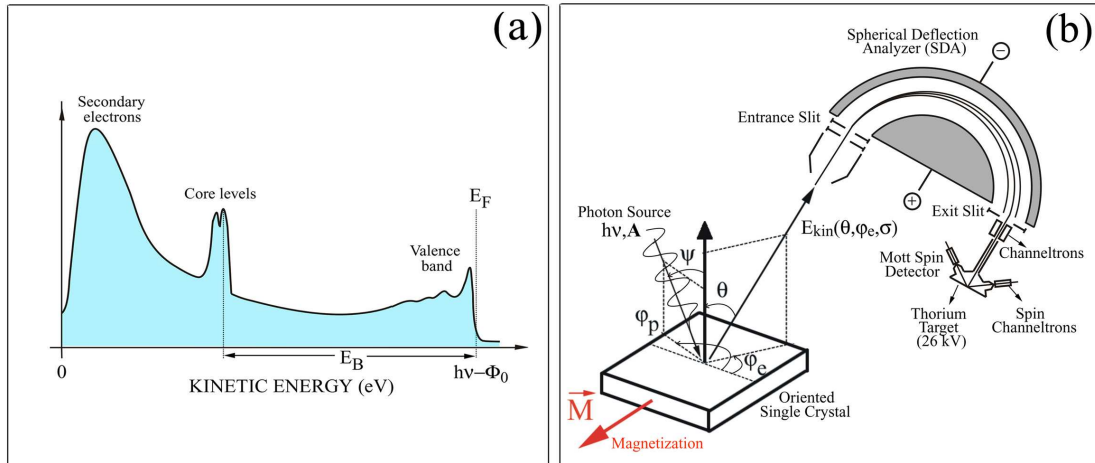


Figure 2.2: Schematics of (a) a photoelectron spectrum and (b) a spin- and angle-resolved photoemission experiment.

Fig. 2.2(b), the hemispherical deflection analyzer (HDA) is the most commonly used instrument at the present time. The kinetic energy of the electron is measured by retarding electrostatic fields applied between the two hemispheres of the instrument and the momentum of the electron is selected by defining a small angle of collection with an entrance slit providing the angular resolution. Once the emitted electrons pass through the entrance slit, they propagate further between the two charged metallic hemispheres where they are refracted due to the existing electric field, thus only electrons with a particular kinetic energy pass through. The pass energy can be tuned by changing the voltage between the hemispheres, which together with the exit slits located at the end of the analyzer defines the energy resolution. A spectrum is measured by applying a ramp voltage to the so-called Herzog plate, which decelerates the electrons to a constant pass energy (more details in section 3.2.1). The electrons are then counted by secondary electron amplifiers, also known as channeltron detectors [43].

2.1.2 Spin polarization

The other observable in a SARPES experiment is the electron spin polarization P which can be measured by coupling a Mott spin polarimeter to the hemispherical analyzer by an electrostatic transfer lens of high transmission. Among the different methods of measuring the spin polarization, the use of spin-dependent scattering via the spin-orbit interaction with heavy atoms is traditionally used. Therefore, scattering targets made of high- Z elements such as gold, tungsten or thorium are usually the choice for the fabrication of modern spin polarimeters. This type of scattering, known as *Mott scattering* [44], was discovered by Sir Nevill Francis Mott in 1929 [45], who realized that the spin dependent terms of the Coulomb scattering in heavy atoms arise from relativistic L - S coupling and lead to a left-right intensity asymmetry A . In other words, spin-orbit coupling of the electron in the potential of the target atoms leads to an asymmetry in the scattering which depends on the electron spin. Much of the

pioneering work in spin-polarized photoemission was carried out with spin polarimeters of these type, so-called medium and high-energy Mott-scattering spin detectors [46], where the electrons to be analyzed are scattered off at energies typically of the order of 20-120 keV. This type of spin detector, which has been used in the experiments presented in this thesis (see section 3.2 for details), is sketched in Fig. 2.2(b) and works with a thorium film as a target and accelerates the incident beam of electrons into the target at an energy of 26 keV. Electrons of opposite spin are elastically scattered at an angle of 120° and counted by two perpendicular pairs of symmetrically opposite spin channeltrons. Specially interesting is also the use of low-energy spin polarimeters which work in combination with the exchange interaction [47], low-energy diffuse scattering (i.e., employed in secondary electron microscopy with polarization analysis (SEMPA)) [48] or spin-polarized low-energy electron diffraction (SPLEED) [49]. In these cases the targets of such polarimeters are made of ferromagnetic single crystals (exchange-type detectors) or, as in the case of the high-energy spin detectors, of polycrystalline or single crystal thin films of high-Z elements (spin-orbit type detectors), respectively.

Measuring P requires to know a spin quantization direction, which depends on the magnetization direction in the case of ferromagnetic or ferrimagnetic materials and in a first instance is provided by the geometry of the experimental setup. If experiments with circularly polarized incident radiation in nonmagnetic systems are performed, it will also depend on the polarization vector of the incident light and thus on the photon helicity. Provided the spin quantization axis, P is defined as the expectation value of the Pauli spin operator σ and can be written as:

$$P = \langle \sigma \rangle = \text{tr}\{\rho\sigma\} = \frac{N^\uparrow - N^\downarrow}{N^\uparrow + N^\downarrow} \quad (2.3)$$

where ρ is the density matrix of pure spin states of the system and $N^{\uparrow,\downarrow}$ the number of spin-up and spin-down electrons. In a more practical way, since the number of electrons counted is directly related to the measured intensity, the spin polarization of a beam of electrons that has been preselected by the analyzer according to an energy E and wave vector \mathbf{k} is:

$$P(E, \mathbf{k}) = \frac{I^\uparrow(E, \mathbf{k}) - I^\downarrow(E, \mathbf{k})}{I^\uparrow(E, \mathbf{k}) + I^\downarrow(E, \mathbf{k})} \quad (2.4)$$

where $I^{\uparrow,\downarrow}$ are the spin-up and spin-down (or equivalently, *majority* and *minority* spin in ferromagnetic materials) SARPES spectra with magnetic moments parallel and antiparallel to the spin quantization axis, respectively. As noted before, the measured quantities are the spin-integrated spectrum $I(E, \mathbf{k}) = I^\uparrow(E, \mathbf{k}) + I^\downarrow(E, \mathbf{k})$ (as sketched in Fig. 2.2(a)) and the spin polarization $P(E, \mathbf{k})$, from which the spin-dependent spectra are obtained as:

$$I^{\uparrow,\downarrow}(E, \mathbf{k}) = I(E, \mathbf{k})(1 \pm P(E, \mathbf{k}))/2 \quad (2.5)$$

In real practice, two spin channeltrons placed symmetrically with respect to the electron beam axis measure the left (L)-right (R) asymmetry A of intensities backscattered from

the target:

$$A(E, \mathbf{k}) = \frac{I_L(E, \mathbf{k}) - I_R(E, \mathbf{k})}{I_L(E, \mathbf{k}) + I_R(E, \mathbf{k})} \quad (2.6)$$

This scattering asymmetry results from the spin-orbit interaction in the target region as previously mentioned but also depends on the polarization component perpendicular to the electron scattering plane. Since the asymmetry measured for a 100% polarized electron beam depends on the so-called Sherman function S [50] of the detector, the spin polarization can be calculated as:

$$P(E, \mathbf{k}) = \frac{A(E, \mathbf{k})}{S} \quad (2.7)$$

The Sherman function, which is related to the efficiency of the detector, depends on the electron kinetic energy, the target material and thickness, as well as on the electron scattering angle. The Sherman function can take values of almost up to 0.5 theoretically, and for ultimately thin target foils that avoid multiple elastic or inelastic scattering events. However, experimentally only a small fraction I/I_0 of the electrons in the beam are backscattered into the detectors and the Sherman function values are rather low. Another quantity which is useful for judging the efficiency of the spin detector is the figure of merit ($FOM = \eta = S^2 I/I_0$) [46], which in conventional spin polarimeters is in the range of 10^{-3} to 10^{-4} and gives the statistical error of a spin polarization measurement ($\Delta P \sim 1/\sqrt{I_0 \eta}$). Therefore, in order to minimize ΔP , the figure of merit η needs to be maximized. Sherman function values range from 0.02 to 0.27 in different devices [46, 49, 50]. Although low-energy detectors such as SPLEED detectors may have high FOM values, the low electron energies used in these systems make the Sherman function dependent on the condition of the target surface that may contaminate during one or several photoemission measurements and needs to be continuously reestablished. In medium and high-energy spin polarimeters such as Mott detectors, on the other hand, since the highly energetic electrons penetrate the target several hundreds of nanometers, it is possible to operate these devices over months in a reproducible way and without the need of calibrating the Sherman function before every set of measurements.

2.1.2.1 Spin polarization upon magnetization reversal

SARPES experiments on ferromagnetic samples demand for an exhaustive control of the sample magnetization. Firstly, the path between the analyzer and the sample should be free of magnetic stray fields which would lead to a precessional motion of the electron spin around the stray field direction. Secondly, the probing area of the experiment in the sample, which is around $0.1\text{-}0.5 \text{ mm}^2$ and typically much larger than the magnetic domain size, implies that the sample has to be remanently magnetized into a single domain state. Control of sample magnetization has the advantage of removing the instrumental asymmetry of the experiment by simply considering $\bar{A} = A(E, \mathbf{k})$ as the average of the measured asymmetries of two consecutive measurements with

reversed magnetization:

$$\bar{A} = \frac{\sqrt{I_L^+ I_R^-} - \sqrt{I_L^- I_R^+}}{\sqrt{I_L^+ I_R^-} + \sqrt{I_L^- I_R^+}} \quad (2.8)$$

where $I_{L,R}^{+,-}$ denote the intensities for opposite magnetization directions of the left and right spin channeltrons. The instrumental asymmetry is typically caused by different sensitivities of the detector spin channeltrons or by other factors such as defects or non-uniformities which may be present at the target surface.

2.1.3 The photoemission process

In the traditional approximation, the photoemission process is described within the so-called *three-step model* [51, 52] which is a sequence of three steps: (i) the photoexcitation of one electron into an unoccupied state of the sample band structure, (ii) transport of this electron to the surface and (iii) the escape of the photoelectron through the surface barrier and coupling to a free-electron state in vacuum.

Within the single particle picture, the total Hamiltonian of the system can be described as $H_{tot} = H_0 + H'$, where $H_0 = \frac{p^2}{2m} + V(\mathbf{r})$ and H' is the Hamiltonian of the interaction between the vector potential of the electromagnetic radiation field \mathbf{A} and the electron with momentum operator $\mathbf{p} = -i\hbar\nabla$.

(i) During the first photoemission step, the photoexcitation process can be interpreted as a quantum mechanical transition from an occupied initial eigenstate $|\psi_i\rangle$ to a final state $|\psi_f\rangle$. From Fermi's Golden Rule, the *transition rate* or transition probability per unit time of this process is:

$$P_{fi} = \frac{2\pi}{\hbar} |\langle \psi_f | H' | \psi_i \rangle|^2 \delta(E_f - E_i - \hbar\omega) \quad (2.9)$$

where the δ function provides the energy conservation of the process. Neglecting higher order contributions in \mathbf{A} , the interaction Hamiltonian H' is proportional to $\mathbf{p}\cdot\mathbf{A} + \mathbf{A}\cdot\mathbf{p} = 2\mathbf{A}\cdot\mathbf{p} - i\hbar\nabla\cdot\mathbf{A}$, where the $\nabla\cdot\mathbf{A}$ term is usually ignored by an appropriate choice of the Coulomb gauge ($\nabla\cdot\mathbf{A} = 0$). The remaining $\mathbf{A}\cdot\mathbf{p}$ term gives rise to \mathbf{k} -selective vertical optical transitions at low energies in the bulk or volume of the solid. However, at the surface the $\nabla\cdot\mathbf{A}$ term is non-zero and as a result, the matrix element $\langle \psi_f | \nabla\cdot\mathbf{A} | \psi_i \rangle$ contributes to the transition rate in Eq. (2.9) provided that both initial and final states have non-zero amplitudes. The dielectric discontinuity at the surface of the solid gives rise to a corresponding discontinuity in \mathbf{A}_\perp , yielding to a delta function after differentiation. Therefore, the surface photoemission term is non-selective in \mathbf{k}_\perp , and the resulting \mathbf{k}_\perp -dependent surface contribution in the photoemission spectra resembles a one-dimensional density of states for $\mathbf{k}_\parallel=0$.

The simplest case is given by the dipole approximation, in which the electron motion is confined into a small volume compared to the wavelength of the incident electromagnetic wave and \mathbf{A} can be considered constant and fixed in space. Given that $\nabla\cdot\mathbf{A} = 0$, this yields to:

$$P_{fi} = \frac{2\pi}{\hbar} |\langle \psi_f | \mathbf{p} | \psi_i \rangle \cdot \mathbf{A}|^2 \delta(E_f - E_i - \hbar\omega) \quad (2.10)$$

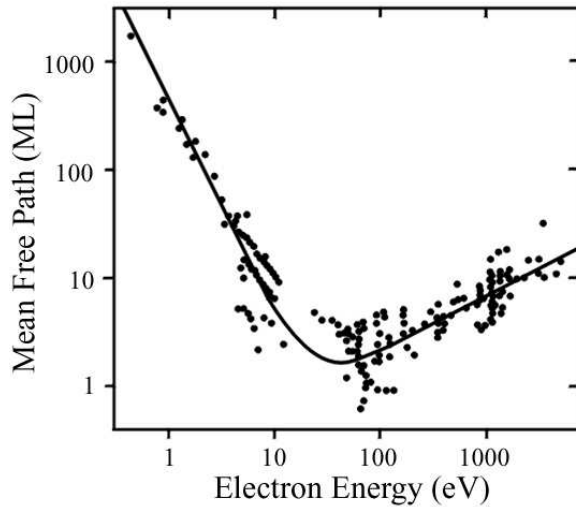


Figure 2.3: *Universal curve representing the kinetic energy dependence of the inelastic mean free path of the electrons in solid, reproduced from [53]. The dots are measurements for different materials and the solid curve is the semiempirical estimation.*

Considering now that $[\mathbf{p}, H_0] = -i\hbar\nabla \cdot V$ and $[\mathbf{r}, H_0] = i\hbar\mathbf{p}/m$, the matrix element can be written in the following form:

$$\langle\psi_f|\mathbf{p}|\psi_i\rangle = im\omega\langle\psi_f|\mathbf{r}|\psi_i\rangle = \frac{i}{\omega}\langle\psi_f|\nabla \cdot V|\psi_i\rangle \quad (2.11)$$

which depends on the gradient of V and indicates that the photoexcitation process cannot take place if the potential of the lattice or atoms is constant or zero, as it is the case of a free electron gas. Furthermore, besides the energy conservation, Eq. (2.11) establishes certain symmetry conditions and dipole selection rules for the initial states depending on the geometry of the experiment, as it will be discussed later. The most simple case in which photoemission occurs is a free electron system bound by a potential barrier located at the interface between the semi-infinite solid and vacuum. In this sense, the final state of a photoexcited electron with low kinetic energy is explicitly supplied by $V(\mathbf{r})$ and therefore defined by the unoccupied part of the bandstructure of the solid $E(\mathbf{k})$.

(ii) In the second photoemission step, the number N of photoelectrons that are transported to the surface and escape into vacuum depends on the film thickness d :

$$N = N_0 e^{-\frac{d}{\lambda}} \quad (2.12)$$

where N_0 is the initial number of electrons and λ is the inelastic mean free path of the electrons (IMFP). This relation indicates that the probing depth of photoemission is limited by effects of inelastic electron scattering and in turn, it can be a very surface sensitive technique if the values of λ are sufficiently small. For high energies, the IMFP is given by the semiempirical formula [53]:

$$\lambda[nm] = 0.41a[nm]^{3/2}\sqrt{E_{kin}[eV]} \quad (2.13)$$

with a the lattice constant of the film. The dependence of λ on the kinetic energy leads to the so-called *universal curve*, and as it can be seen in Fig. 2.3 for different materials, it exhibits a minimum of ~ 2 ML around 50 eV kinetic energy ($1\text{ML} \sim$

2Å). This behaviour is due to the dominance of different kinds of loss processes, i.e. electron-phonon, electron-electron and plasmon-plasmon collisions as the kinetic energy increases. These type of loss mechanisms are the same inelastic scattering processes which are responsible for the tailed background of secondary electrons explained above (Fig. 2.1(a)).

(iii) The third step, transmission of the photoexcited electron through the surface can be considered as the scattering of a Bloch electron wave from the surface-atom potential with translational symmetry parallel, but not normal to the surface. Due to the potential difference, the electron which traverses the surface barrier experiences the refraction process sketched in Fig. 2.4(a), which leads to a change in the direction of propagation of the emitted electron by an angle θ . In practical cases, this process can be treated by matching the internal Bloch wave functions to free-electron wave functions outside the crystal on the vacuum side. The momentum vector of the electron \mathbf{k} inside the crystal is the quantity of interest and it is given by $\mathbf{k}^{int} = \mathbf{k}_{\parallel}^{int} + \mathbf{k}_{\perp}^{int}$, where $\mathbf{k}_{\parallel}^{int}$ and \mathbf{k}_{\perp}^{int} are components parallel and perpendicular to the surface, respectively. Due to the two-dimensional (2D) translational symmetry, the transmission of the electron through the surface into the vacuum requires the conservation of the parallel component of its momentum vector, which due to the mentioned symmetry can be translated by a reciprocal surface lattice vector, i.e., $\mathbf{k}_{\parallel}^{int} \pm \mathbf{G}_{\parallel} = \mathbf{k}_{\parallel}^{ext}$. As the electron is free outside of the solid, by simple trigonometry and considering that $E_{kin} = \frac{\hbar^2}{2m}(\mathbf{k}^{ext})^2$, we have:

$$|\mathbf{k}_{\parallel}^{int}| = |\mathbf{k}_{\parallel}^{ext}| = \sqrt{\frac{2m}{\hbar^2} E_{kin} \cdot \sin(\theta)} \quad (2.14)$$

$$|\mathbf{k}_{\perp}^{ext}| = \sqrt{\frac{2m}{\hbar^2} E_{kin} \cdot \cos(\theta)} \quad (2.15)$$

On the other hand, the component normal to the surface \mathbf{k}_{\perp}^{int} is not conserved due to the lack of periodicity, and for the internal electron in the crystal this component can be determined by the energy conservation requirement:

$$E_{kin} = \frac{\hbar^2}{2m} ((\mathbf{k}_{\parallel}^{int})^2 + (\mathbf{k}_{\perp}^{int})^2) - V_0 \quad (2.16)$$

where V_0 is the average ionic potential of the solid, so-called *inner potential*, which can be taken as a value provided by theoretical calculations or by band mapping experiments, being in both cases an adjustable parameter which depends on the bottom binding energy of the valence band $|E_0|$ and the work function Φ_0 , i.e., $V_0 = |E_0| + \Phi_0$. Introducing Eq. (2.14) into Eq. (2.16), it is straightforward to obtain:

$$|\mathbf{k}_{\perp}^{int}| = \sqrt{\frac{2m}{\hbar^2} (E_{kin} \cdot \cos^2(\theta) + V_0)} \quad (2.17)$$

By systematically collecting electrons photoemitted along certain direction and measuring their kinetic energy E_{kin} , Eqs. (2.14) and (2.17) allow to determine the electron momentum \mathbf{k} in the crystal. The bandstructure of the solid in reciprocal space $E(\mathbf{k})$ is then provided by measuring for different polar angles θ the corresponding electron

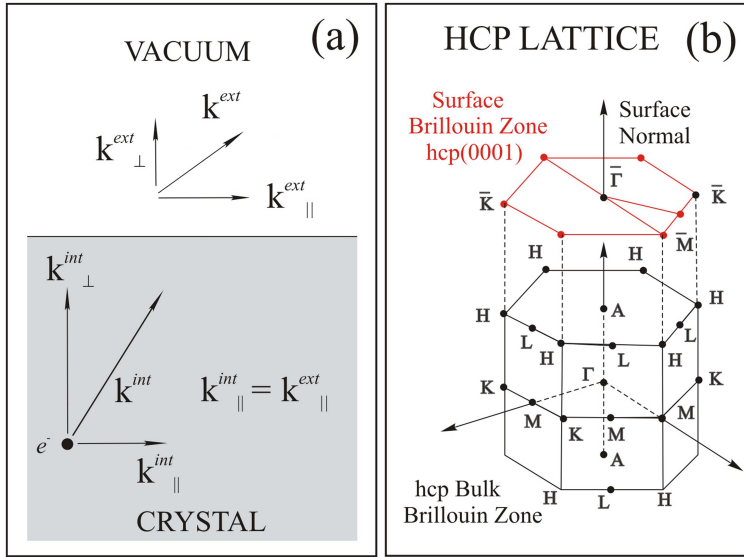


Figure 2.4: (a) Schematics of the refraction process experienced by the photoelectron which traverses the surface barrier; (b) relation between the (0001) surface Brillouin zone of a hcp lattice and the corresponding bulk Brillouin zone.

energy distributions. Figure 2.4(b) shows an illustrative example of the relation between the (0001) surface Brillouin zone (SBZ) and the corresponding bulk Brillouin zone (BBZ) of a hcp lattice, where high symmetry lines and points in reciprocal space are shown. For a given polarization and set of incidence angles Ψ and ϕ_P of the photon beam, it is possible to explore the bandstructure of the solid moving along these high symmetry lines in k -space by simply changing ϕ_e , θ and the photon energy $h\nu$.

If the *normal-emission* condition is chosen, i.e., $\mathbf{k}_{\parallel} = 0$, by changing the photon energy $h\nu$ of the incident beam (see Eq. (2.17)) the dispersion of the electronic states along the surface normal can be obtained (corresponding to the $\Gamma - A$ direction of the BBZ in Fig. 2.4(b)). By further increasing the photon energy, we would move from the first to the second and consecutive bulk Brillouin zones. Therefore, in normal emission and by moving through high symmetry points we can determine the energy dispersion of the initial states $E(\mathbf{k}_{\perp})$. This is the case if the dispersion of the final states is known, which for high enough energies ($h\nu \gtrsim 50eV$) can be approximated by a free electron parabola. At high energies, the crystal potential can be treated as a small perturbation, so the nearly-free electron approximation eventually works well for complicated materials, even at low energies if the Fermi surface of the system under investigation has a simple spherical free electron-like topology.

Concerning the investigation of low-dimensional systems and in particular surfaces, the uncertainty in \mathbf{k}_{\perp} does not play an important role. As mentioned above, the surface photoemission process is non-selective in \mathbf{k}_{\perp} and therefore, low-dimensional systems exhibit a negligible dispersion along the surface normal. In normal-emission, since $\mathbf{k}_{\parallel} = 0$, the only surface contribution in the photoemission spectra would arise from the $\bar{\Gamma}$ point (see SBZ of Fig. 2.4(b)) and changes in the intensity of the energy distributions as a function of the increasing photon energy would result from changes in the matrix element of Eq. (2.11). In off-normal emission, the initial state dispersion is therefore exclusively provided by \mathbf{k}_{\parallel} , from which $E(\mathbf{k}_{\parallel})$ is determined. However, when investigating three-dimensional systems both surface and bulk emission contribute to the SARPES

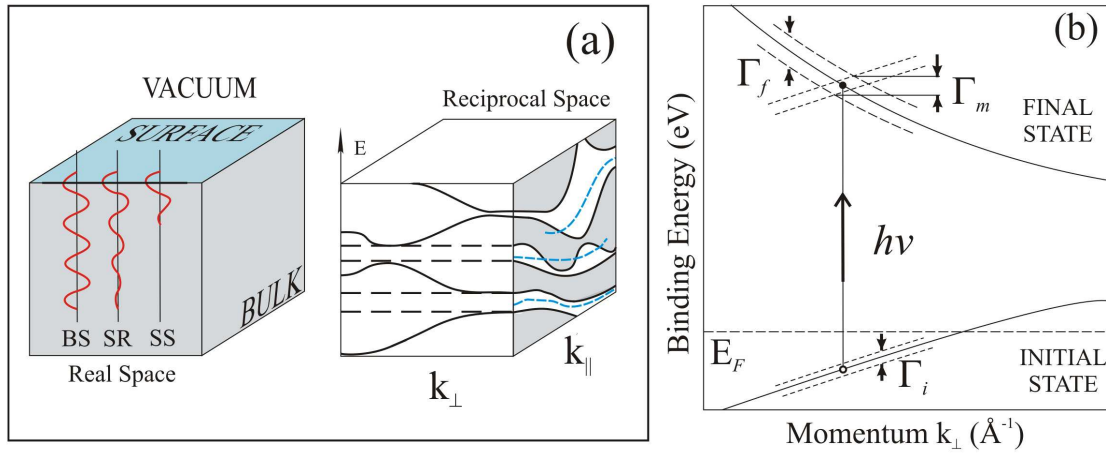


Figure 2.5: (a) *Left side: Sketch of the decay of the wave functions of bulk states (BS), surface resonances (SR) and surface states (SS) into the bulk. Right side: Hypothetical electronic structure of a crystal, where surface state bands (blue dashed lines) are plotted together with a projection of all bulk states (gray areas) in a certain $E(\mathbf{k}_{\parallel})$ plane where relative gaps (white areas) exist.* (b) *Schematic illustration of the contributions from initial and final state broadening to the total linewidth in normal-emission. Dashed lines indicate the inverse lifetime broadening, which is exaggerated for initial states.*

spectra. Therefore, it is not straightforward to distinguish whether a particular band arises from surface or bulk states. The first step in quantifying the contribution of the surface electronic structure in such an experiment is the classification of the possible electronic states that occur at the surface of a well-ordered crystal.

On the left hand side of Fig. 2.5(a), the crystal is sketched in real space, together with the decaying Bloch wave functions of a bulk state (BS), a surface state (SS) and a surface resonance (SR). Obviously, the wave functions of all electronic states extend into the surface region, where they are confined by the potential barrier. If the bulk states are high enough in energy, then the bulk wave functions in the solid can be matched to free electron final state wave functions and the electrons leave the solid. Bulk states exist with periodically varying amplitude through the crystal, while true surface states are localized strictly to the surface and are periodic in two dimensions. Surface resonances, on the other hand, result from the mixing of surface and bulk state wave functions and exhibit an exponentially decaying amplitude in the direction into the solid. They are equivalent to bulk wave functions with an enlarged amplitude in the surface region of the crystal.

On the right side of Fig. 2.5(a), the hypothetical electronic structure of the crystal is sketched, where surface state bands (dashed lines) are plotted together with a projection of all bulk states (gray areas) in a certain $E(\mathbf{k}_{\parallel})$ plane where relative energy gaps (white areas) exist. These relative gaps, which in some cases are due to hybridization effects, appear in the projected bulk band structure and may lead to specific surface states depending on the surface crystallographic orientation. True surface states (blue dashed lines inside the gaps), so-called Shockley [54] or Tamm [55] states, lie only inside

the relative gaps and are characterized by energy levels that are not degenerate with bulk bands. Although there is no physical distinction between them, Shockley states can be theoretically derived from the nearly-free electron model and are more localized, in contrast to Tamm surface states which are more delocalized and related to tightly bound electrons, thus calculated in the framework of the tight-binding model [56]. A mixing between surface and bulk bands occurs if one of these surface state penetrates into a part of the SBZ (blue dashed lines outside the gaps) where propagating bulk bands of the same symmetry exist, leading to surface resonances which as a result penetrate deep into the bulk.

While the three-step model has proven to be quite successful, a more accurate approach is the *one-step model* (1SM) [57–59], where the entire photoemission process is coherently described in one single step, with a final state wave function that includes not only the coupling of the photoelectron to the vacuum state in a so-called *time-reversed low-energy electron diffraction (LEED) state* [57], but also all the scattering events of the photoelectron into the surface, including the inelastic scattering processes which determine the IMFP.

2.1.4 Final state broadening

In three dimensional systems the linewidth contains contributions from both the photohole and photoelectron lifetimes, as introduced by Smith et al. [60]. Fig. 2.5(b) shows the schematic dispersion of an initial and final state band in normal-emission along with the inverse lifetime broadenings Γ_i and Γ_f respectively, both indicated by dashed lines. Other contributions to the linewidth are not included because they are typically known, as these are the energy resolution of the experimental system, scattering with defects or the phonon broadening, which at room temperature is about 25 meV. The photoelectron lifetime reflects final state scattering processes and thus the finite probing depth. If the IMFP (λ) is of the same order of magnitude or less than the interplanar spacing of the solid, the measured linewidth Γ_m will have a contribution of a \mathbf{k}_\perp broadening. Γ_m is determined by the common overlap between the individual broadenings of the initial and final states and the electron group velocities \mathbf{v}_i and \mathbf{v}_f , respectively. For a single nearly-free electron-like band in normal-emission ($\theta=0$), the linewidth of the energy distribution is given by:

$$\Gamma_m = \frac{\Gamma_i/v_{i\perp} + \Gamma_f/v_{f\parallel}}{\left| \frac{1}{v_{i\perp}} - \frac{1}{v_{f\perp}} \right|} \quad (2.18)$$

where $v_{i\perp}$ and $v_{f\perp}$ are the respective initial and final state group velocities $v_\perp = \hbar^{-1}\partial E/\partial k_\perp$ perpendicular to the sample surface. Note that for our purposes Eq. (2.18) shows a simplification of a more general relation between Γ_m and the angle of emission θ (see [60] for details). The limiting cases for the isolation of Γ_i which is the quantity of interest are the following:

(i) For initial states very close to E_F , $\Gamma_i \rightarrow 0$ and the linewidths are then determined by the final state broadening Γ_f .

(ii) When $|v_{i\perp}|$ is much smaller than the other group velocities, e.g., when the dispersion of the initial state band is very small, Eq. (2.18) can be approximated by

$$\Gamma_m \simeq \Gamma_i + \left| \frac{v_{i\perp}}{v_{f\perp}} \right| \Gamma_f \quad (2.19)$$

where in the extreme case in which $v_{i\perp} \rightarrow 0$ (a perfectly flat initial state band) gives $\Gamma_m = \Gamma_i$, which is a good approximation in high symmetry points of the BBZ.

(iii) In photoemission from surface states, since no dispersion normal to the surface exists $|v_{i\perp}| = 0$, and therefore $\Gamma_m = \Gamma_i$.

(iv) In the case in which Eq. (2.19) is a good approximation and for sufficiently high photon energies the final states can be approximated by a free electron parabola with energy $E = (\hbar^2 \mathbf{k}_\perp^2)/(2m)$, leading to:

$$\Gamma_m \simeq \Gamma_i + \frac{\hbar |v_{i\perp}|}{\lambda} \quad (2.20)$$

where λ is the IMFP of the electron. Eq. (2.20) is obtained by introducing into Eq. (2.19) the Heisenberg relation $\Gamma_f \tau_f = \Gamma_f \lambda / v_{f\perp} \simeq \hbar$, where τ_f is the photoelectron lifetime and $\hbar v_{f\perp} = |\partial E / \partial \mathbf{k}_\perp| = \hbar^2 |\mathbf{k}_\perp| / m$.

2.1.5 Symmetry of initial states and selection rules

The symmetry of initial state wave functions can be determined in SARPES experiments and depends on the matrix element $\langle \psi_f | \mathbf{A} \cdot \mathbf{p} | \psi_i \rangle$, also shown for the dipole approximation in Eq. (2.10). By considering special experimental geometries, selection rules for the observability of particular initial states $|\psi_i\rangle$ can be derived. Assuming that the crystal surface has a mirror plane and that both the detection direction of the photoelectron and the direction of incidence of the photon beam are within that mirror plane, the initial electronic states are even or odd respect to reflection in the mirror plane. The matrix element in Eq. (2.10) should be symmetric with respect to the mirror plane and thus the final state wave function must always be even, otherwise the detector located in the mirror plane would see a node of the emitted electron. Depending on the polarization of the incident light, the dipole operator $\mathbf{A} \cdot \mathbf{p}$ is even or odd respect to the mirror plane and therefore the symmetry of the initial states can be determined. If the polarization vector \mathbf{A} is perpendicular to the mirror plane (s-polarization), $\mathbf{A} \cdot \mathbf{p}$ is odd as the initial state. On the other hand, if the polarization vector is in the mirror plane (p-polarization), $\mathbf{A} \cdot \mathbf{p}$ is even and therefore the initial state wave function must also be even. Polarization dependent SARPES experiments are very useful to determine the different symmetries of the initial state wave functions with respect to the mirror plane. In the case of cubic crystals, the dipole allowed initial state symmetries and irreducible representations in normal emission can be found in [61], and for hcp crystals in [62].

2.1.6 Beyond the single particle picture

Our discussion of the SARPES experiment has been focusing on the one-electron states of a system of non-interacting electrons. In reality, this picture is hardly ever adequate because of the presence of electron-electron, electron-phonon or electron-magnon interactions where the latter two are typically much smaller than the former.

In a many-body system of N electrons, the interaction between the excited electron and the remaining $N - 1$ electron system leads to the so-called *correlation effects*. Because of the strong Coulomb repulsion, the motion of a given electron is substantially modified by the presence of all other electrons around. This situation also holds for the hole created in the photoemission process because the charge of the hole is screened by the remaining electrons. In response to the creation of the hole, the $N - 1$ electrons with initial energy of E_{N-1} rearrange in a new potential which leads to the relaxation of the system into a new many-body energy state, E'_{N-1} . The resulting energy difference, so-called *relaxation energy*, is transferred to the photoelectron, which in consequence acquires higher kinetic energy. This effect translates into a binding energy shift of the single particle photoemission peaks towards the Fermi level which at the same time receive a finite width, while at higher binding energies a much broader distribution of spectral weight occurs. This means that at low binding energies the missing electron or hole can be described as a coherent *quasiparticle* with effective mass m^* and well-defined energy E and momentum \mathbf{k}_i , which represents the lower energy state of the relaxed $N - 1$ electron system having a short lifetime or a finite peak width due to the strong interactions. The broader distribution at higher energies is due to the occurrence of a continuum of many-body states without well-defined energy and momentum, thus called *incoherent* part of the spectral weight.

To account for correlation effects, the description of the coupling of the photohole with the rest of the system is done by introducing an energy and momentum dependent complex self-energy function $\Sigma_i(\mathbf{k}, E) = \text{Re}\Sigma(\mathbf{k}, E) + i\text{Im}\Sigma(\mathbf{k}, E)$ in the framework of the *sudden approximation*, i.e., assuming that the photoelectron is suddenly created and decoupled from the remaining $N - 1$ electrons. Being $E = E_f - h\nu$, the δ -function in Eqs. (2.9) and (2.10) is then replaced by the spectral function of the hole state $A_i(\mathbf{k}, E)$:

$$A_i(\mathbf{k}, E) = \frac{1}{\pi} \frac{|\text{Im}\Sigma(\mathbf{k}, E)|}{|E - E_i(\mathbf{k}) - \text{Re}\Sigma(\mathbf{k}, E)|^2 + |\text{Im}\Sigma(\mathbf{k}, E)|^2} \quad (2.21)$$

This function presents a maximum for $E = E_i(\mathbf{k}) + \text{Re}\Sigma(\mathbf{k}, E)$, which means that real part of the self-energy describes the shift of the photoemission peaks with respect to the single particle energy. The imaginary part, on the other hand, describes the peak broadening or *scattering rate* (with a FWHM of $2\text{Im}\Sigma(\mathbf{k}, E)$), which in the single-particle approximation was simply described by a δ -function. Both $\text{Re}\Sigma$ and $\text{Im}\Sigma$ are related by the Kramers-Kronig transformation [37, 38]. If the energy E of the system has more than one solution, the spectral function in Eq. (2.21) is divided into quasiparticle peaks (main lines) and satellites or Hubbard bands, i.e., the coherent and incoherent part of the spectral function, respectively. This results in a mass enhancement $m^*/m_0 = (1 + \lambda)$, where m_0 is the single-particle mass and λ the so-called *mass enhancement factor* $\lambda = |\partial\text{Re}\Sigma/\partial E|_{E=E_F}$ [37, 38]. Since in a ferromagnetic material

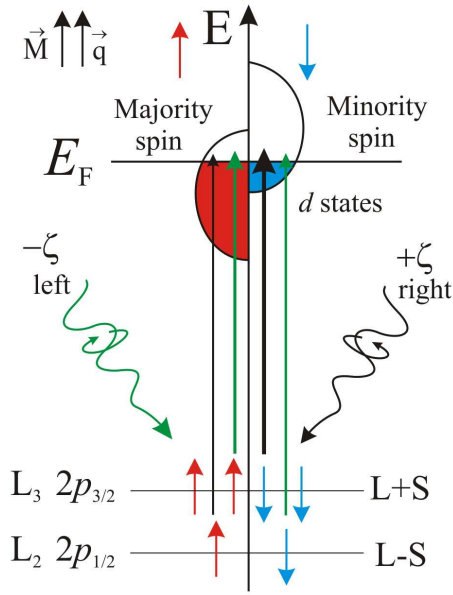


Figure 2.6: *Principle of x-ray magnetic circular dichroism in a weak ferromagnet, illustrated in the one-electron model. Transitions of different probabilities for different spin orientations occur from the spin-orbit split $2p$ core shell to empty conduction band states.*

these effects can be strongly spin dependent, further insight into the role of correlation effects in many-body electron systems will be given in Chapter 4, where state-of-the-art many-body calculations are compared to SARPES experiments in 3d ferromagnetic transition metals.

2.2 X-ray magnetic circular dichroism (XMCD)

The availability of synchrotron radiation sources which provide x-rays at high brilliance and extraordinary energy resolution together with a full control of the photon polarization lead to important improvements in the characterization methods to study magnetic systems with a wide range of excitation energies. Since its experimental discovery [21, 22], magnetic circular dichroism in x-ray absorption is a widely used technique suitable for the element-specific investigation of magnetic films and multilayers. X-ray magnetic circular dichroism (XMCD) is defined by the difference in the absorption intensities depending on whether the magnetization \mathbf{M} of the system under investigation is aligned parallel or antiparallel to the propagation direction \mathbf{q} of the incoming circularly polarized x-rays. In other words, changing the helicity ζ (or photon spin) of the incoming radiation at a fixed \mathbf{M} , is equivalent to fixing ζ and reversing the direction of \mathbf{M} . The effect is similar to the magneto-optical Faraday effect discovered by M. Faraday in 1846 [63], which clearly demonstrates that a magnetically ordered medium can indeed affect photons and change the polarization of the light. In a one electron model, the physical principle behind XMCD is sketched in Fig. 2.6 in the case of a weak ferromagnet, which follows two steps. Incident x-rays with positive ($+\hbar$) or negative ($-\hbar$) helicity are termed left and right circularly polarized respectively, where the angular momentum carried by the photons in the propagation direction is due to their intrinsic spin. The density of states is spin split due to the exchange interaction, which leads to a relatively large number of unoccupied states above the Fermi level

E_F . Restricting ourselves to the $L_{2,3}$ absorption edges, the excitation process involves the 2p core levels which are spin-orbit split into $2p_{1/2}$ (L_2) and $2p_{3/2}$ (L_3) states.

During the first step, right or left circularly polarized incident photons lead to a photoexcitation from the 2p core levels into the unoccupied density of states (DOS) below the vacuum level. Therefore, this process is more efficient in elements with high density of empty states, for example, those with only partially filled d- or f-shells. The excitation of 2p \rightarrow 3d transitions by circularly polarized radiation leads to excited electrons which are spin-polarized due to relativistic dipole selection rules [44]. Since spin flips are forbidden in electric dipole transitions, majority (minority) photoelectrons from the 2p core shell can only be excited into majority (minority) 3d hole states. In a simple picture, the angular momentum of the photons can be transferred in part to the spin of the excited photoelectron through the spin-orbit coupling and a distinct spin character can be selected in the transition. The spin polarization is aligned in the direction of the incident light \mathbf{q} and depending on the helicity, its direction will point either parallel or antiparallel to \mathbf{q} . Since the sign of the spin-orbit coupling is opposite for the L_2 ($L - S$) and L_3 edges ($L + S$), also the spin polarization changes sign for the excitation of the $2p_{1/2}$ and $2p_{3/2}$ states. Thus, right (left) circularly polarized x-rays excite more minority spin (majority spin) electrons from the $2p_{3/2}$ state, while the opposite is the case for the $2p_{1/2}$ state. The second step is the detection of these spin-polarized electrons by the imbalanced unoccupied majority and minority spin states of 3d character. Since there are more empty minority than majority states above E_F , the transition probability (described by the sum of all possible transitions given by Eq. (2.9)) will be higher for minority spin than for majority spin. The result is magnetic dichroism, i.e. the absorption intensities change as a function of ζ and \mathbf{M} , and the maximum XMCD signal ($I(+\zeta) - I(-\zeta)$), which is obtained when \mathbf{M} is parallel to \mathbf{q} , changes both in sign and magnitude when going from the L_3 to the L_2 edge. Finally, it is important to mention that the spin and orbital moments are related to the integrated areas of the XMCD signal by the integral *sum rules*, developed by Thole and Carra, and further insight into the method to calculate them can be found in [64, 65].

2.2.1 XMCD in photoelectron emission microscopy (PEEM)

In Chapter 6, XMCD is used in combination with photoelectron emission microscopy (PEEM) for time-resolved experiments. Since in the present PEEM experiment mainly secondary electrons are detected, the dichroic signal in the photoabsorption process is translated into a secondary electron yield signal, being the latter proportional to the former [66]. The kinetic energy distribution of the emitted photoelectrons is rather broad, containing not only primary photoelectrons of well-defined kinetic energy but also low-energy secondary electrons induced by the emission and capture of Auger electrons. The photon energy is tuned to excite electrons from a core level into the empty electronic states below the vacuum level, taking advantage of the characteristic absorption edges (Fig. 2.6). The core hole left behind is filled by a radiative (x-ray fluorescence) or non-radiative (Auger) process, being the probability of the latter much higher [67]. As a result, the core hole decay leads to the emission of highly energetic Auger electrons. These electrons suffer multiple scattering events

when passing through the solid, leading to a cascade of low-energy secondary electrons, the number of which is proportional to the XMCD absorption signal. These secondary electrons are detected in XMCD-PEEM in a two-step process. Firstly, the XMCD is converted into a dichroism in the Auger electron yield. Secondly, the Auger XMCD signal is translated into a helicity-dependent difference in the intensity of secondary electrons emitted from the sample surface which are conveniently picked up by the PEEM. This means that although initially the whole photoelectron spectrum is equally transmitted through the PEEM, the energy-dependent transmission of the microscope optics (see section 3.3.2) limits the photoelectron contribution only to lower energies (low pass). Thus, the information depth in XMCD-PEEM is mainly determined by the inelastic mean free path of secondary electrons (see section 2.1.3). Typically x-rays penetrate much deeper into the material but most of the signal is generated in the top 2-5 nm.

Chapter 3

Experimental aspects

In this chapter, details of the experimental systems used to perform the experiments will be presented. Starting with an overview of the general properties of synchrotron radiation and some characteristic parameters of the light source BESSY II, we will continue with a more detailed description of the spin and angle-resolved photoemission spectroscopy (SARPES) experimental system. Following that, the XMCD-PEEM experiment will be described together with its time-resolved version (time-resolved XMCD-PEEM). This includes the laser system and the scheme of synchronization between the picosecond x-ray and femtosecond laser pulses, focusing on the combination of synchrotron radiation and laser illumination as a tool to simultaneously gain access to the temporal resolution and the magnetization dynamics of the system.

3.1 Synchrotron radiation

The first dedicated synchrotron light sources, commonly known as of the second generation type, became available at the beginning of the 1970s. A second generation synchrotron light source is a particle accelerator in which electrons or positrons are accelerated to relativistic energies by a microwave cavity and then kept on a circular orbit by *bending* or *dipole magnets*. In most of the cases the electrons are first accelerated in a synchrotron and then injected into a *storage ring*, which is optimized for the stability, lifetime and beam size of the electrons and not for the initial acceleration. Synchrotron radiation is emitted by these charged particles when they travel through the magnets and undergo a transversal acceleration. If the velocity of the particles is very close to the speed of light ($v \approx c$), the angular distribution of the emitted radiation from one point in the magnet leads to a very narrow cone of emission. This cone is perpendicular to the radial acceleration and along the tangential electron velocity vector. The narrow angle θ of observation with respect to the direction of the electron motion is known as the *natural half emission angle* of synchrotron radiation. Considering that electron and observer are related to each other by a Lorentz transformation, it can be approximated by $\theta \approx 1/2\gamma$ [68], where $\gamma = 1/\sqrt{1 - \beta^2} = m/m_0$ is the Lorentz factor and $\beta = v/c$. Here m_0 and m are the rest and relativistic mass of the electron, respectively. Values of γ of the order of $10^3 - 10^4$ lead to θ values below 1 mrad ($\sim 0.06^\circ$). For the light

source BESSY II¹, where the experiments presented in this thesis have been performed, the value of the Lorentz factor γ is 3330, and thus one obtains $\theta \approx 0.15$ mrad (i.e., $\sim 0.009^\circ$). Due to such a small opening angle of the emission cone, the photon flux of the emitted radiation from a bending magnet is extremely high. However, horizontally, the radiation from a bending magnet is spread out in a much larger angle because the electron trajectory is curved and the electron motion direction is changing for each source point, so the total spread depends on the angle of total deviation within the magnet. In order to overcome this problem, magnets so-called *insertion devices* (IDs) are typically built in straight sections of the storage ring in between the bending magnets in modern synchrotrons, leading to third generation facilities such as BESSY II which began operating for the first time at the end of the 1990s.

3.1.1 Bending magnet radiation and insertion devices (IDs)

In a bending magnet, the photons are observed during the time in which the electrons pass a curved trajectory. In the reference frame of the observer, such a time interval is Lorentz contracted, so the resulting frequency distribution of the emitted synchrotron radiation is a continuum with the dominant contribution of a base circular frequency ω_0 and higher harmonics. The upper limit ω_c above which the frequency distribution decays rapidly is known as the *critical frequency*. Being R the radius of curvature of the bending magnet, the electrons are moving on a circular orbit due to the applied magnetic field B within the magnet. Thus, it is possible to calculate the *critical photon energy* $\hbar\omega_c$ [68, 69]:

$$E_c = \hbar\omega_c = \frac{3e\hbar\gamma^2 B}{2m_0} \Leftrightarrow E_c[\text{keV}] = 0.665 \cdot E_e^2[\text{GeV}] \cdot B[\text{T}] \quad (3.1)$$

where E_e is the electron energy and the right hand side of Eq. (3.1) is written in practical units, and $\gamma = E_e/m_0c^2$. In the storage ring BESSY II, with an electron energy of 1.7 GeV and typical bending magnet fields of about 1.3 T, from Eq. (3.1) the critical energy of the bending magnet radiation is 2.5 keV. This corresponds to a wavelength of 0.5 nm, which is in the soft x-ray regime. Furthermore, the emitted light exhibits well-defined polarization, being fully linearly polarized in the plane of the electron orbit. The light emitted off-plane, on the other hand, exhibits in general elliptical polarization. By accepting radiation above or below the orbital plane it is possible to switch the photon helicity. If the appropriate angle of emission is chosen, a degree of circular polarization higher than 90% can be achieved [70]. Nowadays modern synchrotrons and storage rings such as BESSY II are not circular but polygons with special sequences of IDs in the straight sections and bending magnets forming the circular path in the corners. Standard IDs are *wavelength shifters*, *wiggler magnets* and *undulators*, which have the capability of producing a much stronger magnetic field than that of a bending magnet without deviating the electrons out of the storage ring. Therefore, from Eq. (3.1), IDs offer the possibility of generating a larger spectral range of synchrotron radiation towards higher photon energies, which in some instances can

¹Berliner Elektronenspeicherring für Synchrotronstrahlung, Berlin, Germany.

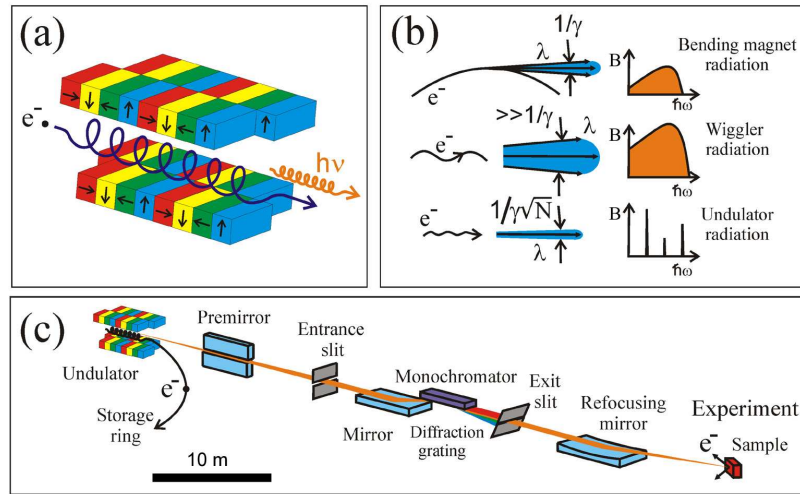


Figure 3.1: (a) Sketch of an elliptical undulator. By changing the longitudinal shift between the two split parts of the upper and lower magnets, electrons are forced to follow different trajectories. In this example, electrons are moving on a helical path giving rise to the emission of circularly polarized light. (b) Comparison between the emission angles and spectral distributions of a bending magnet, a wiggler and an undulator (adapted from [68]). (c) Schematics of a typical soft x-ray beamline at BESSY II.

be extended towards hard x-rays. In a wavelength shifter, depending on the strength of the applied magnetic field, the wavelength spectrum can be shifted towards smaller or higher wavelengths by a combination of three magnets. W wigglers and undulators, on the other hand, are periodical arrays of N magnet pairs with alternating fields, in which electrons undergo a sinusoidal movement so they oscillate and radiate. In Fig. 3.1(a) the typical layout of an ID system is sketched. A comparison of the IDs angular and spectral distributions to those of a bending magnet is sketched in Fig. 3.1(b). In general, undulators achieve a smaller angular distribution of emitted photons and much higher brilliance². The main difference between a wiggler and an undulator is that the oscillation amplitude in the former is bigger and the radiation contributions from each field period sum up independently, leading to a broad energy spectrum as the one of a bending magnet but of higher intensity and larger emission angle. In an undulator, in contrast, the oscillation amplitude of the electron motion is small and the emission angle decreases considerably depending on the number of magnet pairs. Therefore, the radiation displays interference patterns which lead to a spectral energy distribution which is concentrated and enhanced in several harmonics of very narrow width.

²The *brightness* ($B = P/\Delta A \cdot \Delta\theta$) describes the photon flux P from a source of unit area ΔA (cross section of the electron bunch $\sim 0.05 \text{ mm}^2$) emitted into a unit of solid angle $\Delta\theta$ ($\sim 1 \text{ mrad}^2$). The *spectral brightness* or *brilliance*, B_λ , is typically defined as the brightness for a spectral bandwidth (BW) $\Delta\lambda/\lambda$ of 0.1%. For BESSY II, in the soft x-ray regime, $B_\lambda \sim 4.6 \times 10^{18} (\text{photons/s})/(\text{mm}^2 \cdot \text{mrad}^2 \cdot 0.1\% \text{ BW})$.

3.1.2 Beamlines and monochromators

The emitted radiation is directed into beamline systems, which are a set of optical elements to guide the photons to the experiment (Fig. 3.1(c)). The first optical elements are used to focus the photon beam into a monochromator system, which tunes and filters out a particular wavelength of the incident light. In BESSY II working with soft x-rays, monochromators typically include normal-incidence gratings, plane, spherical and toroidal gratings. An optical grating is made up of a set of long and extremely narrow lines separated from each other by a distance of about $1 \mu\text{m}$. When light of certain wavelength is incident on the grating, Bragg diffraction occurs and each line acts as a point source. The photon energy is tuned by changing the incidence and exit angles of the photon beam in the grating. Depending on the dispersion given by the number of lines in the grating (typically 1000 lines/mm) and the size of the exit slit of the monochromator, the energy resolution of the beamline is given. After the exit slit, photons with well-defined energy are focused into a small spot on the sample by refocusing mirrors. In this thesis, experiments were performed in different beamlines at BESSY II which provide variable polarization: mainly the UE112-PGM1 beamline for SARPES experiments and the UE56/2-PGM1 and PGM2 beamlines for time-resolved XMCD-PEEM experiments. These beamlines are optimized for a photon energy range of about 20-600 eV and 60-1300 eV respectively, reaching spot sizes at the focus position in the sample which are below $100 \mu\text{m}^2$.

3.1.3 Time structure of synchrotron radiation

The emission of synchrotron radiation dissipates kinetic energy from the electrons and this loss should be compensated to keep the electrons circulating in the storage ring. This is performed by accelerating the electrons after each turn around the ring in a microwave cavity. Since this process depends on the microwave frequency, electrons are not evenly filled all around the orbit but are instead injected in electron packets or bunches because it leads to a much more effective initial acceleration. From the existence of electron bunches it follows directly that synchrotron radiation must have an intrinsic time structure, as light is only generated if an electron bunch passes through IDs or bending magnets. The time structure of synchrotron radiation strongly depends on the bunch pattern and the degree of filling, i.e., on the operation mode of the storage ring. Table 3.1 compiles some properties of the photon pulses generated in various operation modes of BESSY II. In general single-bunch (SB), multi-bunch (MB), low- α and hybrid modes are distinguished. In the less frequently available SB mode only one single electron bunch circulates the ring with a repetition rate of 1.25 MHz. In this case the pulse width is typically larger than in the other modes due to the higher filling of the individual bunch, ranging between 50 and 100 ps with decreasing electron beam current between two injections. In the MB mode the storage ring is filled with several hundred bunches which generate photon pulses of about 30 ps width with a repetition rate of 500 MHz, while in the low- α mode less intense photon pulses but as short as 3 ps are provided. The hybrid mode is a combination of both single- and multi-bunch modes, and contains a multi-bunch train of 700 ns followed by a 100 ns gap with an intense individual bunch every 800 ns in the middle of the gap. Most recently, multi-

bunch-hybrid and low- α -hybrid modes have been implemented as standard operation modes in BESSY II.

	SB	MB	Low- α	Hybrid mode
Pulse width (ps)	50-100	30	$\lesssim 3$	50-100 (SB) and 30 (MB)
Period (ns)	805	2	2 or 805	805 (SB) and 2 (MB)

Table 3.1: Values of the photon pulse width and period for the different operation modes in the storage ring BESSY II.

3.2 SARPES experiment

Details of the experimental set-up, where the SARPES experiments have been performed, are shown in Fig. 3.2. In Fig. 3.2(a) a photograph of the equipment in working conditions with all the components installed is shown, while in Fig. 3.2(b) a simplified schematics of the setup is given. The experimental chamber was prepared and installed before every experiment as end-station in the UE112-PGM1 beamline described above. All the system is under ultrahigh vacuum with a base pressure during experiments of $\sim 1 \times 10^{-10}$ mb, enough to keep sample surfaces in clean conditions for several hours. The system contains three main chambers: two preparation chambers and one analysis chamber. The sample was mounted in a high precision rotatable manipulator with a heating device allowing to reach high sample temperatures, so it is suitable for the preparation of all types of crystals, including tungsten. In this manipulator, both the polar and azimuthal angles can be changed with a precision of about 0.5° . The two preparation chambers were used for different purposes depending on the experiment and the number of flanges available. In one of these chambers, located just above the analysis chamber and along the vertical path of the manipulator, home-made exchange-

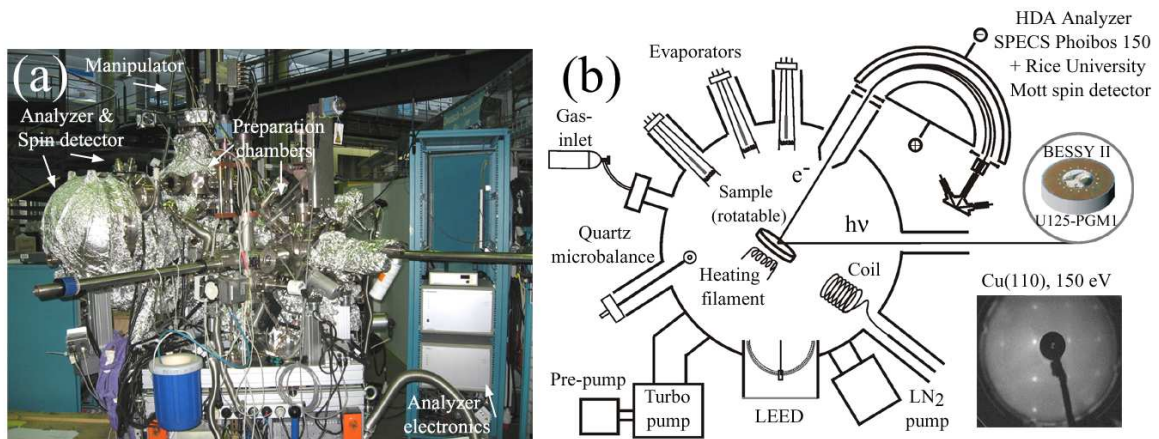


Figure 3.2: (a) SARPES experiment in working conditions. The HDA analyzer and the spin detector can be seen on the left side. (b) Simplified schematics of the experimental system. A LEED pattern of a clean Cu(110) crystal is also shown as an inset.

able evaporators of different materials were mounted, together with an adjustable gas-inlet valve for treatment of the sample with gases, a quartz microbalance for thickness calibration and a translation manipulator with a magnetic yoke at the end. For the application of magnetic fields, currents up to 40 A were applied to this yoke, reaching magnetic fields well above the coercivity of bulk ferromagnets at room temperature. An extra magnetic coil was also mounted in the main analysis chamber. In this case very short magnetic pulses of few milliseconds and high intensity were achieved by applying currents up to 150 A. Materials were either evaporated from a melted drop on a tungsten wire or from a rod heated by electron bombardment. Other evaporators, an extra quartz microbalance and another heating stage device were mounted in the other preparation chamber.

The analysis chamber is equipped with a low-energy electron diffraction (LEED) system, which was used to verify the surface order and its geometrical alignment. In LEED measurements, an electron gun irradiates the sample in normal incidence and backscattered electrons are filtered out by retarding grids suppressing the inelastic background. The backscattered elastic electrons are then accelerated towards a fluorescent screen and their angular distribution is recorded by a CCD camera. In Fig. 3.2(b) an example of a LEED pattern from a clean Cu(110) surface measured with this system is shown as an inset. Each spot corresponds to a $\bar{\Gamma}$ point of the surface Brillouin zone in reciprocal space. Particular attention is paid to the question if additional spots due to reconstructions in the surface appear in LEED, because this may contribute as additional bands or intensity changes in the measured $E(\mathbf{k})$ dispersions.

3.2.1 The hemispherical analyzer and the Mott spin detector

A hemispherical deflection analyzer (HDA) "SPECS PHOIBOS 150" coupled to a Rice University Mott-type spin polarimeter of the medium-energy type [46] were used for the detection of spin-integrated and spin-polarized signals (see Fig. 3.3(a)). The angular resolution of the equipment is better than 1° and the energy resolution about 100 meV at room temperature.

3.2.1.1 The SPECS hemispherical deflection analyzer (HDA) Phoibos 150

The PHOIBOS 150 deflection analyzer has 180° hemispheres and a mean radius R_0 of 150 mm. It uses non-magnetic materials inside a μ -metal shielding protecting the electrons from stray or external magnetic fields. It includes a transfer lens system which can be set electronically to adapt the analyzer to different tasks (Fig. 3.3(a)). The main issues of such a lens system are: (i) to define the sample area under analysis and the electrons acceptance solid angle, (ii) to accelerate or decelerate the electrons to the pass energy and (iii) to adjust the sample plane to the HDA entrance plane. Depending on the magnification of the lens system, sample areas of less than 0.1 mm^2 can be probed. Ten lens stages (T1–T10) are built together with an iris aperture right into the diffraction plane of the lens system, so the electrons passing through are focused into the entrance slit of the analyzer. Using the iris aperture, the angular resolution can be adjusted while keeping the acceptance area on the sample constant.

Inside the lens stage, the electrons pass through an intermediate image plane before they are refocused into the plane of the entrance slit by external voltages. Aberration effects can be always suppressed to well-known acceptable values by selecting the optimum combination between the magnification modes and acceptance angles. In angle-resolved experiments the lens acceptance angles are confined to minimum values allowing to easily set the magnification mode which leads to the higher transmission for a particular probing area. In the experiments presented in this work, with acceptance angles of less than 1° the optimum magnification settings at the sample focus position lead to probing areas of about 0.5 mm^2 .

Electrons of a specific initial kinetic energy emitted from the sample are retarded by an external voltage V_R which is applied simultaneously to the last lens element and to the Herzog plate, both located just before the entrance slit. Hence, the kinetic energy of the incoming electrons after passing through the entrance slit matches the nominal pass energy E_{pass} of the hemispherical analyzer. These electrons are focused in the central radial position at the exit slit plane. Other electrons with slightly different energies than E_{pass} also pass through the entrance slit due to the small energy spread of the analyzer. These electrons follow different trajectories and are not focused at the center of the exit slit. If their kinetic energy is higher (lower) than E_{pass} , they will be focused further outside (inside) the center of the exit slit plane.

In this work, the so-called *fixed analyzer transmission* (FAT) mode [71,72] has been

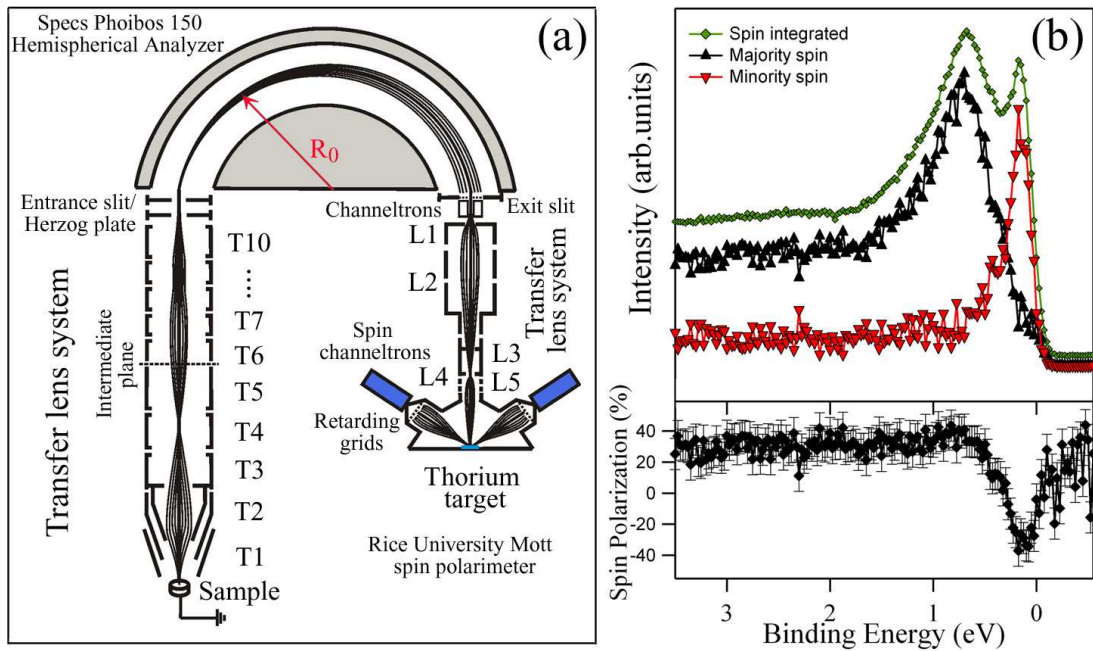


Figure 3.3: (a) Detailed sketch of the SPECS hemispherical deflection analyzer (HDA) PHOIBOS 150 coupled to a Rice University Mott-type spin polarimeter. Transfer lens systems and electron trajectories are indicated. (b) Measured spin-resolved spectrum and spin polarization in normal-emission for a 20 ML Fe(110) film near the Γ point of the bulk Brillouin zone ($h\nu=35 \text{ eV}$).

always used to record photoemission spectra, where E_{pass} is maintained constant and the spectrum is measured by ramping up V_R . Thus, the kinetic energy of the electrons emitted from the sample E_{kin} can be directly obtained since $eV_R = E_{kin} - E_{pass}$. The pass energy of the analyzer depends directly on the potential difference V_0 between the outer V_{OH} and inner V_{IH} hemisphere voltages, being $E_{pass} = -ekV_0 = -eC(V_{OH} - V_{IH})$, where C is a calibration constant³ and $V_{OH} > V_{IH}$. In the FAT mode, since E_{pass} is constant, the same energy resolution applies across the entire spectrum. Therefore, the HDA is acting solely as an energy dispersive device in which electrons in the central trajectory between hemispheres possess the nominal kinetic energy equal to E_{pass} . Note that E_{pass} can also be changed by selecting different values of the voltage in the hemispheres. However, scanning the voltages V_{OH} and V_{IH} is generally not practiced because of the need to have the same absolute resolution ΔE at all kinetic energies measured in a single photoemission spectrum. Considering that the relative energy resolution $\Delta E/E_{pass}$ is inversely proportional to the mean radius R_0 [71], this would generally require extremely large hemispheres.

The detection system consists of six standard non spin-resolving channeltrons (each one of them with an opening slit of 7×20 mm), where the off-center electrons are detected. A double gold grid in front makes the electrostatic field homogeneous. The channeltrons and corresponding slits are arranged in two blocks of three. The blocks are placed at the left and right sides of the central radial position of the exit slit of the analyzer, where the electron beam with a nominal energy E_{pass} goes through. The separation between each channeltron slit is about 1 mm, while the two blocks of slits are separated by about 25 mm. Since each channeltron detects electrons with different kinetic energies which are approximately equal to E_{pass} , the distance between channeltron slits is selected to meet the requirement of a constant kinetic energy difference between neighboring channeltrons. Therefore, by simply adding the number of electrons belonging to the same kinetic energy from each one of the channeltrons, the total number of electrons for each kinetic energy is obtained. If V_R changes, the process repeats again and in the final spin-integrated spectrum all the counts belonging to the same kinetic energy for each one of the V_R values and different channeltrons are added iteratively. This also results in a very good calibration of the kinetic energy scale, which in fact also depends on the work function of the analyzer ($\Phi_{analyzer} \sim 5eV$).

3.2.1.2 The Rice University Mott spin polarimeter

After the exit slit plane, the remaining electrons in the central trajectory of the hemispheres with nominal energy E_{pass} enter a transfer-acceleration lens system of high transmission through a 7 mm diameter aperture, followed by the Mott spin polarimeter (Fig 3.3(a)). All the voltages applied here depend on E_{pass} and are referred to the retardation voltage V_R . The transfer lens system consists of five sections of cylindrical symmetry which accelerate and focus the electrons into the scattering target. In the first two sections L_1 and L_2 , several electrodes allow the deflection of the electron beam and its focusing. While L_1 is at the same potential as the double gold grid

³The constant C is in general a function of the mean radius R_0 of the analyzer [71], being in this case $C \sim 0.9375$.

in front of the channeltron slits, L_2 acts as a deflector/stigmator depending on the applied voltage. L_3 has two circular apertures of 6 mm diameter separated by 17 mm. The secondary electrons scattered in these apertures are stopped from reaching the scattering target in the Mott polarimeter by applying a more negative potential in L_4 . The final acceleration and focusing occurs in the gap between L_4 and the last lens element L_5 , the latter forming part of the inner support assembly which is maintained at the same voltage as the scattering target (20-26 kV).

After scattering from the target (a $\sim 90 \mu\text{m}$ thick thorium disk cleaned in air with acid solutions), the electrons are detected by two pairs of channel electron multipliers or *spin channeltrons*. The pairs are placed in a 90° configuration allowing to simultaneously detect the two transverse components of the incoming electron beam spin polarization, which in this case is parallel to the sample surface and along the quantization axis. This means that electrons measured along the dispersion angle of the analyzer will have a quantization axis orthogonal to it. Each one of the spin channeltrons forming one pair are positioned symmetrically at $\pm 120^\circ$ from the scattering target, so electrons scattered in opposite directions are detected. Before arriving to each spin channeltron, the electrons pass through a cone-shaped aperture and are decelerated by a retarding grid. Only those electrons that have suffered small inelastic energy losses after scattering, pass through. After the retarding grids, the electrons are accelerated again towards each one of the spin channeltrons by external amplification voltages and are detected. By changing the potential applied to the retarding grids it is possible to optimize the energy window in which electrons are affected by inelastic losses. The two components of the in-plane spin polarization are determined by the measured asymmetry resulting from the different count rates at each one of the two spin channeltrons in one pair.

It is important to remark that with this equipment, extremely small energy splittings below 10 meV between states of opposite spin can be resolved, while the energy resolution of the experiment is about 100 meV at room temperature. The spin splitting measurements are in general not limited by the energy resolution of the photoemission setup since the spin-polarized signals are simultaneously measured in independent channeltrons. Interesting examples which show such an extreme situation are inverse photoemission experiments from Passek et al. [73] where with energy resolutions of 0.4 eV at room temperature spin splittings of 18.3 meV were resolved, or from Starke et al. [74], where spin splittings as small as 13 meV were found.

The use of a target made from thorium increases the Sherman function of the spin polarimeter considerably as compared to gold. In a simplified picture the Sherman function is proportional to the atomic number Z , although in reality this dependence is more complicated as it has to take into account a variety of other parameters [75]. Nevertheless, this would mean an increase in the Sherman function of about 14 % when going from gold to thorium, resulting in a reduction of the sensitivity to instrumental asymmetries and larger figure of merit η (FOM). A good approximation for the Sherman function in the present experiment is 0.16–0.17 for an energy loss window of about 800 V and a scattering target potential of 25-26 kV. Assuming that $I/I_0 \sim 5 \times 10^{-3}$ [50], the FOM of the polarimeter is $\eta \sim 1.4 \times 10^{-4}$. Operating the system at 26 kV, we obtain a Sherman function of about 0.16. Fig. 3.3(b) shows a spin-resolved spectrum

in normal-emission for a 20 ML Fe(110) film near the Γ point of the bulk Brillouin zone, measured with a photon energy of 35 eV and horizontal polarization. The spin-integrated signal (green full circles) together with its majority (upwards black triangles) and minority (downwards red triangles) components are shown. For a value of the Sherman function of ~ 0.16 , a spin polarization of $\sim -40\%$ is obtained, in agreement with the reference values given by SPECS [76]. Given the spin-integrated signal, the majority and minority spin spectra were calculated from Eq. (2.5), while the spin polarization was obtained from Eqs. (2.7) and (2.8).

3.3 Time-resolved XMCD-PEEM experiments

The combination of photoemission electron microscopy (PEEM) and synchrotron radiation offers unique possibilities for magnetic domain imaging. Together with XMCD as a contrast mechanism (see section 2.2) it provides the lateral resolution and the element selectivity (XMCD-PEEM). Furthermore, by taking advantage of the time structure of synchrotron radiation (section 3.1.3), it provides the temporal evolution of the magnetic properties (time-resolved XMCD-PEEM). In this section, some technical aspects of the instrumentation used for such experiments are presented.

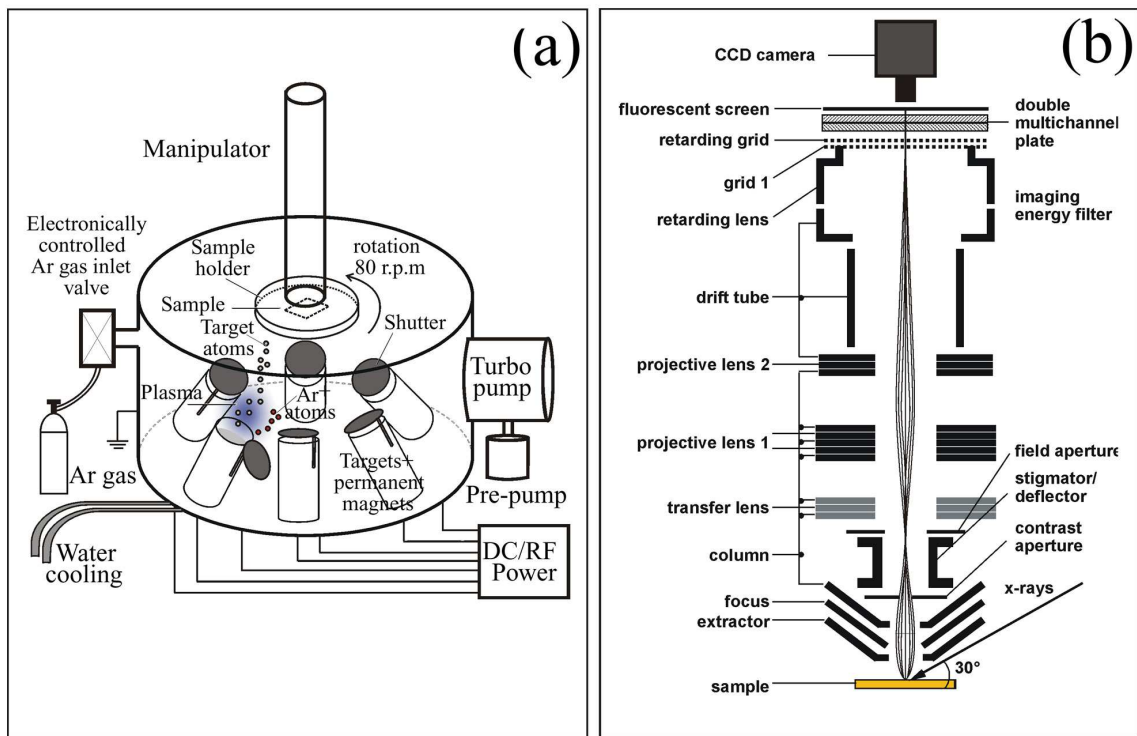


Figure 3.4: (a) Schematics of the Bestec magnetron sputtering system. (b) Layout of the Focus IS-PEEM microscope (adapted from [77]).

3.3.1 Magnetron sputtering system

For the fabrication of the samples used in the time-resolved XMCD-PEEM experiments we have used a magnetron sputtering system available in BESSY as a user facility. The samples were protected with 1 nm Cu layer to avoid oxidation during transport in air. Magnetron sputtering allows the deposition of thick films of good quality in an easy fashion. In Fig. 3.4(a), the schematics of the sputtering system is shown. It is a Bestec system [78] with six water cooled sputter targets (2 radio frequency (RF) and 4 diode current (DC) arranged in a confocal configuration. The substrate is placed in the focal point and rotated around its own axis at ~ 80 r.p.m, useful to improve the uniformity in the thickness of the deposited layers. The deposition rates are controlled by changing the target power between 20 to 300 W. The base pressure of the system is 2×10^{-8} mbar. Optionally, the sample holder can be heated up to 900°C and an external magnetic field of ~ 2 kOe can be applied in any direction. Through an electronically controlled inlet valve, argon gas is introduced continuously in the chamber. A pressure of $P_{Ar} = 1.5 \times 10^{-3}$ mbar is maintained stable during the complete deposition process. Magnetic fields around the targets are continuously created through permanent magnets placed below the target assembly. A high voltage is applied between the negatively charged sputtering target (cathode) and positively charged sample substrate (anode). Thus the argon gas becomes ionized and a plasma forms along the magnetic field near the target. Inside the plasma, free electrons trapped by the magnetic field hit continuously the outer shell electrons of neutral gas atoms in their path. In this way, the argon atoms become positively charged Ar^+ ions and secondary electrons are created. Part of these Ar^+ ions contribute to the regeneration of neutral argon atoms by interaction with secondary electrons, and the gain in energy during this process is released in the form of photons. The other part of Ar^+ ions are accelerated towards the target and through continuous bombardment, their kinetic energy is transferred to the surface atoms in the target. By this gain of kinetic energy, the atoms of the target are ejected at high speeds towards the sample substrate and deposited there.

3.3.2 The PEEM microscope

At the UE56/2-PGM1 and PGM2 beamlines at BESSY, a Focus IS-PEEM working at a lateral resolution of about 500 nm [77] was employed for all the time-resolved measurements presented in this work. Only in some cases an Elmitec PEEM installed in the U49-PGMa beamline was used at a lateral resolution of about 100 nm [79] for sample characterization before the beamtimes. Thus we will restrict ourselves to few technical details of the Focus IS-PEEM and only point out some of the differences with the Elmitec one. The scheme of the Focus IS-PEEM is presented in Fig. 3.4(b). X-rays illuminate the sample under an angle of 30° with respect to the surface normal. The sample is grounded and positioned at a distance of about 2 mm in front of the *objective lens*, an immersion lens system consisting of three electrodes: extractor, focus and column. Firstly, electrons with different kinetic energies leave the sample surface at large starting angles relative to the surface normal. These electrons are accelerated into the microscope by applying a strong electrostatic field (~ 10 kV/mm) between the

extractor and the sample, which significantly reduces their angular spread and relative kinetic energies. In order to ensure the cylindrical symmetry of the accelerating field and avoid image distortions, the surface normal should be aligned with the complete optical system of the microscope. Due to the acceleration, the electrons move in a curved trajectory into the immersion lens system. In the focus and column electrodes, they are immediately decelerated to the so-called column potential (~ 1 kV). As a result, the objective lens sees a virtual image of the sample at much lower starting angles and larger distance. Spherical and chromatic aberrations due to imperfections of the lens system cause the electron trajectories to go out of the image detector plane. In order to reduce these effects, electrons with a defined kinetic energy and direction are selected by a *contrast aperture*, positioned directly behind the objective lens in a suitable electron trajectory crossover. The contrast aperture should be carefully adjusted with respect to the electron optical axis. Using a motor piezo-driver, its size can be selected between 30 and 500 μm from a set of circular apertures. Although small sizes of the contrast aperture improve the lateral resolution, this also decreases the signal-to-noise ratio and thus longer acquisition times are needed for smaller aperture sizes. Note that, as briefly discussed in section 2.2.1 of the previous chapter, the energy-dependent transmission of the PEEM optics limits the photoelectron contribution to lower energies (low pass), thus secondary electrons are detected⁴. In fact the immersion lens system together with the contrast aperture considerably suppresses the high kinetic energy side of the photoelectron spectrum, and the smaller the diameter of the contrast aperture the narrower the width of the transmitted low energy interval.

In order to reduce the influence of non-spherical aberrations, the electrons pass through an octopole deflector/stigmator, located in the back-focal plane of the objective lens. With the octopole arrangement, astigmatism can be compensated in any rotational direction and the electron beam can be realigned again along the electron optical axis. The stigmator can be used as an x,y-deflector, allowing to change the field of view of the microscope up to 400 μm without actually moving the sample. The remaining part of the optical system consists of a two-stage projective lens system, where the image is magnified and projected onto a multichannel plate which intensifies it. The resulting image is then converted into visible light by means of scintillator crystal placed behind the multichannel plate and computer-recorded by a Peltier cooled slow scan CCD camera with 12-bit intensity resolution mounted outside the vacuum chamber. The sample holder forms an integral part of the electron optical column and thus the image quality is very little affected by vibrations. This allows its precise positioning with respect to the objective lens with a variable step size ranging between 40 and 400 nm in an area of 4×4 mm².

⁴Both Focus IS-PEEM and Elmitec PEEM have the option of filtering the electron energies for spectromicroscopic measurements. In this case a narrow window of the high-energy side of the photoelectron spectrum is selected and photo- or Auger electrons belonging to one particular electronic state or transition are imaged. This option was not used for the time-resolved XMCD-PEEM measurements presented in this work.

3.3.2.1 Lateral resolution and Elmitec PEEM

The Focus IS-PEEM microscope can be operated in two modes, the so-called *survey* and *high-resolution modes*. In the survey mode, low extraction fields are used and a field of view up to 700 μm can be used, but the lateral resolution is worst. In the high-resolution mode, high extraction voltages result in a field of view of about 20 μm . In this case, the lateral resolution is better than 30 nm in threshold photoemission [80] (i.e. with minimum energy spread⁵). The energy spread is an important aspect when determining the lateral resolution of the microscope, since the main contributions which determine it are the chromatic aberrations of the acceleration field and the immersion lens elements [67]. In the case of soft x-ray radiation from the synchrotron, the larger energy spread of the photon beam leads to energy-dependent trajectories of the electrons via chromatic aberration, which deteriorate the spatial resolution as compared to threshold photoemission. In general, increasing the extractor voltage and/or reducing the contrast aperture narrows the electron trajectory spread and improves the lateral resolution. However, when decreasing the aperture size diffraction effects become more pronounced. In ultimate conditions the so-called *diffraction limit*, which for soft x-ray excitation is about 50 nm [81], limits the lateral resolution. With an aperture of 70 μm and a field of view of 20-25 μm , in the best measurement conditions during single bunch mode at the UE56/2-PGM2 beamline and applying the maximum extractor voltage of 15 kV, the expected lateral resolution of the Focus IS-PEEM is ~ 300 nm. However, a larger value of about ~ 500 nm was achieved in real measurements due to imperfections and defects in the sample surface. These imperfections contribute to the formation of small electrostatic fields which are superimposed on the extractor voltage, causing a distortion of the electron trajectories and thus limiting the achieved spatial resolution, ultimately determined by the surface topography and homogeneity.

The working principle of the Elmitec PEEM is basically the same. In this case the sample is under -20 kV and the objective lens is grounded. It uses magnetic instead of electrostatic lenses slightly reducing the spherical and chromatic aberrations of the optical system. The high extractor voltage, together with an optimized intensity and a reduced spot size of about $5 \times 5 \mu\text{m}^2$ of the incident photon beam in the UE49-PGMa beamline, leads to an important improvement of the resolution of the system. This allows to reduce the contrast aperture and the field of view in normal operation as compared to the Focus IS-PEEM. In multibunch mode, with a contrast aperture of 50 μm and a field of view of $\sim 8 \mu\text{m}$, a lateral resolution of about 100 nm could be achieved for the same samples used in the time-resolved XMCD-PEEM experiments.

3.3.3 Contrast mechanisms in PEEM

There are several contrast mechanisms which do not depend on the magnetic state of the sample such as topological [82], work function [83] and elemental contrasts [84]. As pointed out before, the topological contrast is due to an electric field distortion due to defects in the sample surface. The work function contrast, on the other hand, is due

⁵A minimum energy spread can be realized in the laboratory, for example, by using a high pressure Hg discharge lamp, where the excitation energy is slightly higher than the work function of the sample and almost monoenergetic electrons from a narrow interval around the Fermi level are excited.

to variations in the photoemission intensity in regions of the sample with different work functions. This contrast mechanism is dominant in threshold photoemission and it may be suppressed at high photon energies due to the larger energy spread of the emitted secondary electrons. Furthermore, the chemical or elemental contrast can be obtained by simply tuning the photon energies of the incident x-rays through the absorption edges of the elements. Thus, different areas of the sample containing one particular element will appear brighter in the image.

The magnetic contrast has been the principal contrast mechanism used in this work and it will be explained in detail in the following. The information depth in XMCD-PEEM is mainly determined by the inelastic mean free path of secondary electrons λ_s and by the penetration depth of the incident light $\lambda_{h\nu}$. The latter depends on the photon energy and angle of incidence of the x-rays, as-well as on the absorption coefficient of the material under investigation. Since secondary electrons are produced as the result of an inelastic cascade of low energy electrons with large λ_s , absorption events below the surface region can also be detected. This means that magnetic imaging can also be performed through different layers, and this capability has potential applications for studying coupling phenomena in multilayer systems. At the photon energies of the $L_{2,3}$ absorption edges of ferromagnetic metals, x-rays penetrate much deeper into the material than the inelastic mean free path of the electrons and most of the signal is generated in the top 2-5 nanometers. However, in certain situations, if $\lambda_{h\nu}$ is comparable to λ_s , important saturation effects could appear in the measured XMCD signals [66]. Saturation effects could occur, for example, due to strong absorption or by using x-rays under grazing incidence angles.

XMCD images from 22 nm thick $\text{Fe}_{19}\text{Ni}_{81}$ permalloy microstructures measured in the Focus-IS PEEM are shown in Fig. 3.5(a) and in the Elmitec PEEM in Figs. 3.5(b) and 3.5(c). The images were recorded at the Fe L_3 (707 eV) edge. In Fig. 3.5(a) arrays of $10 \times 10 \mu\text{m}^2$ squares are shown in a field of view of $40 \mu\text{m}^2$. In Figs. 3.5(b) and 3.5(c), two isolated $5 \times 5 \mu\text{m}^2$ squares rotated 45° respect to each other are shown

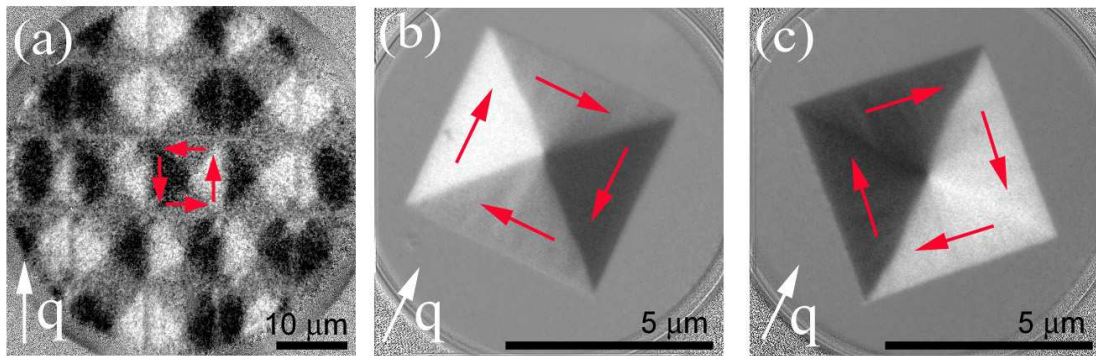


Figure 3.5: Landau patterns in XMCD images of permalloy microstructures recorded at the Fe L_3 (707 eV) edge. (a) Arrays of $10 \times 10 \mu\text{m}^2$ squares in a field of view of $40 \mu\text{m}^2$. (b) and (c): two isolated $5 \times 5 \mu\text{m}^2$ squares rotated 45° respect to each other in a field of view of $8 \mu\text{m}$. The propagation direction of the photon beam \mathbf{q} (white arrows) and the magnetization vector \mathbf{M} inside each domain (red arrows) are indicated.

in a field of view of $8 \mu\text{m}$. The propagation direction \mathbf{q} of the incoming x-rays (white arrows) and the orientation of the magnetization vector \mathbf{M} (red arrows) inside each domain are indicated. The microstructures were defined by electron beam lithography on a Au/GaAs substrate. The permalloy layer was grown in the magnetron sputtering system described in section 3.3.1, and then covered by a 1 nm Cu film to avoid oxidation during transportation into the PEEM chambers through air. These types of structures could be grown in a reproducible way and show stable flux-closure magnetic domains, known as Landau patterns, with a vortex in their center. They are a stable magnetic configuration suitable for time-resolved XMCD-PEEM experiments. The magnetic contrast was obtained from the calculated asymmetry A_{XMCD} given by the difference of two images measured with left ($-\zeta$) and right ($+\zeta$) circularly polarized light divided by the sum ($I(+\zeta) - I(-\zeta)/I(+\zeta) + I(-\zeta)$). This procedure allows to describe the magnetic contrast in a more quantitative way, ranging between -100% and 100%. Note that the non-magnetic contribution to the contrast ($\sim I(+\zeta) + I(-\zeta)$) containing the chemical and topographical information is properly eliminated by this procedure since it remains unaffected upon reversal of the photon helicity. The angular dependence of the magnetic contrast depends on the relative orientation of the magnetization \mathbf{M} and the propagation direction \mathbf{q} of the incoming circularly polarized x-rays, scaling as $A_{XMCD} \sim \mathbf{M} \cdot \mathbf{q}$. Thus, a maximum signal is obtained when \mathbf{q} and \mathbf{M} are aligned parallel (white domains) or antiparallel (black domains), while the signal is minimum if they are perpendicular to each other (gray domains). This angular dependence can be distinguished in the images in Figs. 3.5(b) and 3.5(c), where two different structures with the same Landau configuration exhibit different contrast inside each magnetic domain due to a rotation by 45° .

3.3.4 Time resolution in XMCD-PEEM

For time-resolved experiments we have used a pump-probe imaging technique by using a fs-laser system (pump) synchronized to the x-ray pulses from BESSY II (probe) in single bunch mode. Among the different possibilities to perform this type of experiments, our technique relies on the use of laser illumination for the generation of ps magnetic field pulses which are accurately synchronized at the sample position. After the magnetic excitation pulse, the dynamical response of the magnetization in the system is imaged by XMCD-PEEM. This response happens very fast, ranging from several ns down to the ps regime, depending on the duration of the magnetic excitation. Since the time needed to acquire an image is of the order of several seconds, this procedure must be repeated over millions of times until an image of sufficient quality is measured at a particular delay time after the arrival of the magnetic pulse. In consequence, the magnetic state of the sample must return to the same initial configuration over millions of times. This means that the excitation process must be absolutely reproducible and reversible to acquire an image with meaningful information.

The scheme of the experimental set-up is shown in Fig. 3.6(a). The magnetic field pulses are generated by focusing fs laser pulses onto a finger-shaped photoconductive switch of the Auston type [85, 86], the ends of which are under a tunable voltage difference. The switch is produced on top of a GaAs substrate grown by MBE at low

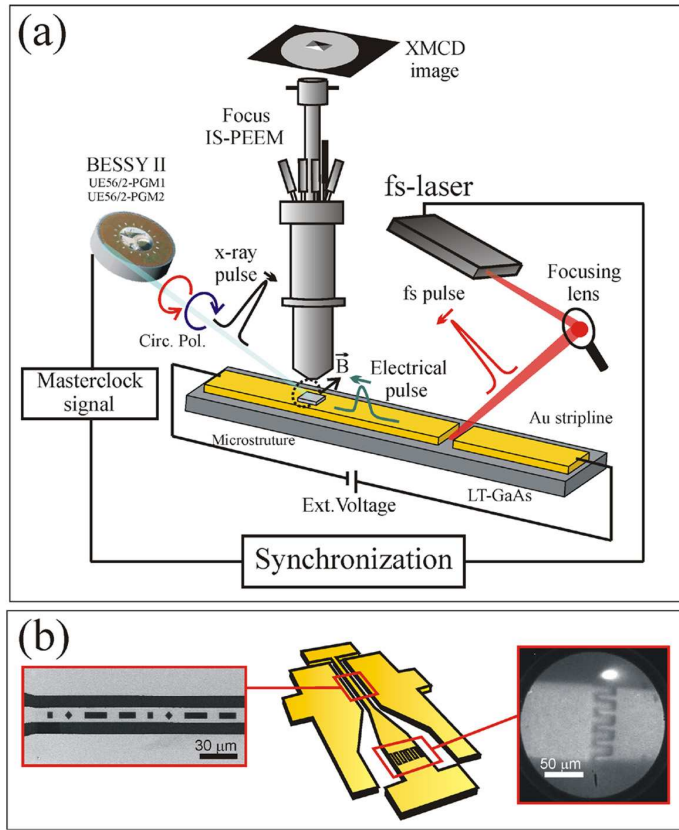


Figure 3.6: (a) Scheme of the experimental set-up used for time-resolved XMCD experiments. A short laser pulse, synchronized to the x-ray pulse frequency, triggers a current pulse through a lithographic stripline in an Auston photoconductive switch. The magnetic field pulse created is used to excite the sample, the magnetic properties of which are imaged with lateral and elemental resolution by the Focus-IS PEEM microscope. (b) In the center, a sketch of the sample used for the experiments with different regions indicated. On the right, a PEEM image of the photoconductive switch together with the laser spot. On the left side, a SEM image of the magnetic microstructures grown on top of the stripline.

temperature (LT-GaAs). Combined with magnetron sputtering, two electron beam lithography and lift-off cycles are performed to produce the Auston switch together with a 100 μm thick Au coplanar transmission line, so-called *stripline*, onto which several permalloy microstructures of different sizes and shapes are also created. In Fig. 3.6(b) a sketch of the sample geometry is shown. Different regions of the sample are indicated: on the left hand side, a scanning electron microscope (SEM) image of the Au stripline (10 μm wide) with the microstructures on top and on the right hand side, a PEEM image recorded with a Hg discharge lamp in which the laser spot and the Auston switch (100 μm wide) appear together. The switching area consists of 10 fingers of 5 μm , an arrangement which resulted in a much more effective effect of the laser beam on the switch and therefore on higher currents passing through the stripline. Here the laser spot (moved out of the photoconductive switch for better visibility) appears as a bright spot due to multiphoton photoemission induced by the laser pulse. After laser illumination, due to the excitation of electron-hole pairs in the LT-GaAs substrate an electrical pulse propagates along the stripline and produces, in turn, a magnetic field pulse. The magnetic field, which is oriented perpendicular to the stripline, excites the magnetic domain configuration of the microstructures on a time scale which is mainly determined by the lifetime of the electron-hole pairs created in the LT-GaAs substrate. This limiting factor leads to magnetic pulses of several tenths of ps duration in our experiments. The stripline is surrounded by two waveguides, connected on ground potential to improve the homogeneity of the electric field created

during laser illumination.

XMCD images of a selected permalloy microstructure with well-defined magnetic domain pattern are obtained with the Focus-IS PEEM microscope described in section 3.3.2 and x-ray single-bunch pulses of opposite helicity as a probe. Using the 500 MHz masterclock signal from BESSY II for synchronization and by electronically tuning the delay between laser and x-ray pulses, XMCD images at different delay times are measured, allowing to follow the magnetization dynamics of the system. It is important to remark that to hide the electrical connections in the Auston switch from the high extractor lens voltage in the microscope, an Omicron compatible sample holder was especially developed for time-resolved measurements. Since the technical development of the sample holder was a crucial step for obtaining the results presented in this work, further details on its performance will be given in Chapter 6.

3.3.5 The laser system and the synchronization scheme

We have used a COHERENT laser system composed by an infrared MIRA 900 Ti:Sapphire ($\text{Ti:Al}_2\text{O}_3$) fs-oscillator ($\lambda=800$ nm) pumped by a Verdi green laser ($\lambda=532$ nm) working at ~ 10 W power. Since the system produces pulses with an energy of ~ 1.5 eV, it is suitable for the excitation of electron-hole pairs across the bandgap of the LT-GaAs substrate of the Auston switch ($\Delta E_{\text{GaAs}} \sim 1.4$ eV at RT). The Verdi laser is a diode-pumped solid state (DPSS) laser in which 19 diode emitters are arranged in a confocal configuration by means of an optical fiber. The infrared light emitted from the optical fiber ($\lambda=808$ nm) pumps a water-cooled Nd:YVO₄ crystal which produces light lasing deeper in the infrared at 1064 nm wavelength through stimulated emission. The crystal is coated with a dielectric mirror which reflects at 808 nm and transmits at 1064 nm. The transmitted light is frequency doubled in a LiB₃O₅ (LBO) crystal, producing a continuous wave (CW) of green light at 532 nm wavelength as an output.

The intense green light enters the resonator cavity of the MIRA oscillator and is focused into a water-cooled Ti:Sapphire crystal by means of a pump focus lens. Two plane mirrors placed on the opposite ends of the cavity reflect the light back into the Ti:Sapphire crystal many hundreds of times. As a result, the infrared light which in a first instance is produced by spontaneous emission in the Ti:Sapphire crystal is considerably amplified by stimulated emission processes. One of these mirrors, the *output-coupler*, is a partial reflector which transmits a fraction of the infrared light producing the laser output. The lasing condition of the oscillator is achieved by an accurate alignment of the complete laser optics: the two beams propagating back and forth inside the resonator cavity should be perfectly coaligned, resulting in an infrared beam in the form of a CW with increased power.

Infrared laser pulses of ~ 100 fs duration and 800 nm wavelength are generated based on the *Kerr-Lens Modelocking* (KLM) technique [87, 88]. The firstly generated CW exhibits minor power fluctuations and a Gaussian beam profile which contains one or two longitudinal modes propagating inside the cavity. An intracavity mechanism is used to start the KLM. This mechanism is an oscillating mirror which produces rapid changes in the cavity length, resulting in an increase of the number of propagating modes and fast power fluctuations. Once the power fluctuations start, pulses of more

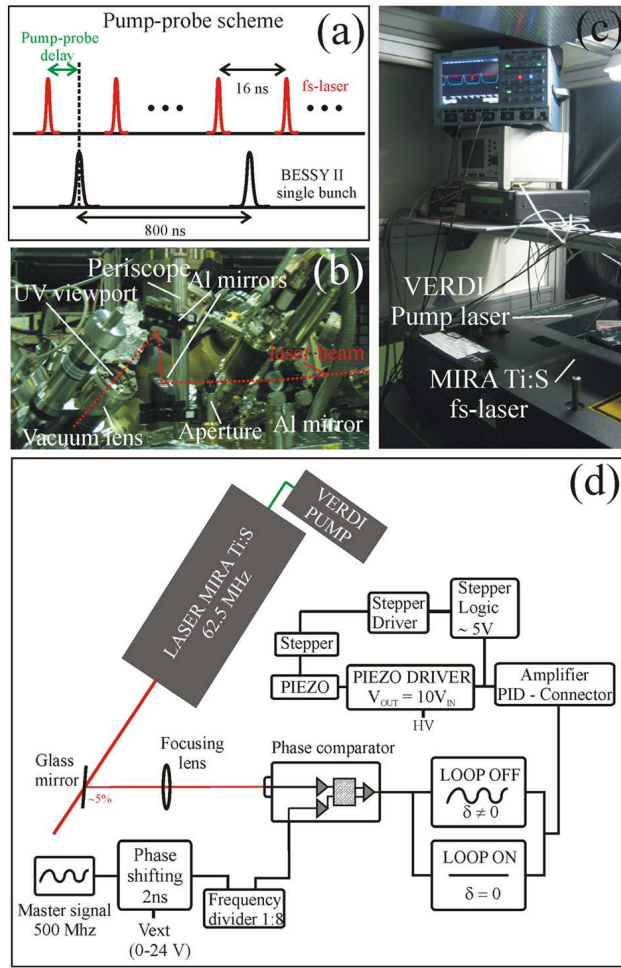


Figure 3.7: (a) Schematics of the relative delay between laser pump-synchrotron probe pulses in single-bunch mode. (b) Optical elements directing the laser beam into the PEEM chamber. (c) Laser system operating in a synchronized mode during the experiments. (d) The synchronization scheme.

or less intensity are formed and travel through the Ti:Sapphire crystal, which acts as a Kerr-Lens. This means that changes in the refractive index of the crystal are produced due to the electric field of the incoming light. These changes, which are large at the beam center and decrease with increasing distance from it, result in a self-focusing and narrowing of the laser beam. Thus, a randomly created pulse of high enough intensity is narrowed after passing through the Ti:Sapphire crystal while other pulses with lower intensity remain as an unnarrowed low-power background. A saturable absorber aperture aligned in the focal point of the cavity allows to interrupt the low-power contribution, so only the focused high-intensity pulses with well-defined time structure pass through unattenuated. The fraction of these pulses which is transmitted through the output-coupler is directed to the experiment using several aluminum mirrors, part of them mounted in periscopes of variable height. The group velocity dispersion of the other fraction of pulses reflected into the cavity is compensated by a sequence of two prisms. The linear polarization and the power of the laser output beam is changed by using a polarizer combined with a $\lambda/4$ plate and an intensity attenuator, respectively.

The relative delay between laser and synchrotron pulses during single-bunch operation is sketched in Fig. 3.7(a). Part of the optical elements used to drive the laser pulses to the experiment are shown Fig. 3.7(b), while Fig. 3.7(c) is a photograph of the laser

system in a synchronized mode. Synchronization is done by simply matching the laser frequency to a multiple number of the 500 MHz masterclock signal (2 ns period) which is generated in the microwave cavity of the synchrotron during multi-bunch operation. The masterclock signal is always electronically available at BESSY II just for synchronization purposes, independently of the operation mode of the synchrotron. Depending on the electronics used for synchronization, this signal can always be used since the repetition rate of 1.25 MHz (800 ns period) of the synchrotron pulses in single-bunch is directly proportional to it. The cavity length of the MIRA oscillator was therefore extended so the repetition rate of the femtosecond pulses was 62.5 MHz (16 ns period), which corresponds to 1/8 of the masterclock frequency (Fig. 3.7(a)). This means that every two photon pulses in single-bunch operation 50 synchronized laser pulses are produced. Thus, during time-resolved measurements only two of these laser pulses are in reality used and the extra pulses just define the maximum time window in which the experiment can be performed⁶. The signal from an avalanche photodiode placed in the UE56/2-PGM2 beamline at about ~ 3 m distance from the sample was used as reference to monitor the single-bunch pulses. Note that in order to exactly know when the laser and x-rays pulses arrive at the sample position it is necessary to determine the *time zero* of the experiment. This is the time in which the magnetic excitation pulse arrives at the position of the microstructure under investigation. The current pulse induces a transient image distortion in the PEEM image of the stripline due to the electric and magnetic fields. The maximum distortion which determines the time zero can be found by following the temporal change of contrast between the stripline and the surrounding grounded waveguides (see Chapter 6 for further details).

The synchronization scheme is shown in Fig. 3.7(d). The delay between pump-laser and probe-synchrotron pulses can be changed with an accuracy better than 10 ps by means of a voltage-controlled phase shifter circuit integrated together with the electronics for synchronization into a single device⁷. Approximately 5% of the laser output is reflected by a glass mirror placed outside the laser cavity and focused by an additional lens into a phase comparator where, after a frequency divider, 1/8 of the 500 MHz signal is introduced as an input. As an output signal, the phase difference Δ between the laser and 1/8 of the masterclock signal is obtained. The output signal is then amplified and used to control the voltage of a piezo driver. This modifies the laser cavity length and its frequency through the movement of a piezo crystal on top of which one of the end intracavity mirrors is placed. The synchronization is achieved when the phase difference Δ is zero. An additional circuit (stepper logic) translates the output from the phase comparator into a voltage difference, allowing to automatically maintain the synchronization by means of a feedback loop. This means that when the loop is closed, the voltage difference in the stepper logic is automatically readjusted in order to always keep the phase difference Δ at zero value. This is done through a stepper driver which corrects the position of the piezo crystal in small steps as a function of the voltage needed for readjustment. This correction responds to the fast jumps and drifts of the synchronization with a jitter of about 5 ps.

⁶A pulse-picking technique to suppress the extra laser pulses was not used in our experiments.

⁷The synchronization unit used in the experiments shown in this work was fabricated and developed by the technical department of the Max-Born Institute Berlin.

Chapter 4

Strength of correlation effects in the electronic structure of 3d ferromagnets

This chapter is devoted to a systematic experimental and theoretical study of the strength of correlation effects in the spin-dependent electronic structure of bulk ferromagnetic bcc Fe(110) and hcp Co(0001). The band structure of these systems is investigated by means of spin- and angle-resolved photoemission spectroscopy. The results are compared in detail to theoretical calculations within the three-body scattering approximation and within the dynamical mean-field theory, together with one-step model calculations of the photoemission process. This comparison indicates that the present state-of-the-art many-body calculations, although improving the description of correlation effects in 3d ferromagnetic transition metals, give too small mass renormalizations and scattering rates thus demanding more refined many-body theories including non-local fluctuations.

4.1 Introduction

Over the last decades, the electronic structure and the dynamics of electronic states in solids have attracted a lot of attention. A better understanding of the binding energies and quasiparticle lifetimes in correlated systems like 3d ferromagnets [89], transition metal oxides [90], 4f rare-earths [91] or high- T_c superconductors [92] has been achieved, together with important experimental progress in photoelectron and related spectroscopies [38]. On the theoretical side, the application of density functional theory (DFT) in the local density approximation (LDA) [93] has contributed with numerous calculations of single-particle $E(\mathbf{k})$ band dispersions of solids, surfaces, and ultrathin films. First attempts of comparing such calculations to the band dispersions obtained from angle-resolved photoemission experiments revealed a quantitative agreement in some cases, as for example, Cu metal [94]. In this case good agreement between the theoretical predictions of the ground state properties and the experimental band dispersions was obtained. In the case of magnetic transition metals, on the other hand, an extensive work in this respect has been carried out over the last thirty

years [28,37,95–97]. The partial filling of the 3d subshell causes nonvanishing magnetic moments which show ferromagnetic order in Fe, Co and Ni, whereas antiferromagnetic order occurs in Cr and Mn. These systems have been at the focus of a large number of photoemission and inverse photoemission studies which have been carried out since the beginning of the 80s [98–101]. However, their interpretation from a complete comparison of the full bunch of data acquired over all of this time to the existing theories is still an outstanding open discussion. For Fe and Co, which are the metals under study within the scope of this thesis, but also for Ni, no general consensus has been reached due to several aspects. The most important reasons for the disagreement between theory and experiments in these metals have been (i) the narrowing of the 3d bands due to correlation effects and (ii) the existence of new features in the photoemission data such as photoemission satellites in the core-level and valence band spectra which are not well described by single-particle approaches such as the generalized gradient approximation (GGA) [102] or the local spin-density approximation (LSDA)¹ in DFT. This was the case of Ni for example, in which the band structure calculations could not describe the photoemission satellite at 6 eV binding energy. Furthermore, the experimentally measured width of the occupied d-band was found to be about 30% narrower than the calculated one and the experimental spin splitting was by almost a factor of two smaller than the one obtained from LSDA calculations [30,103]. From this comparison it became clear that Ni is a strongly correlated system and that the narrowing of the 3d bands is substantial, with ratios of theoretical over experimental energy positions in between 1.3 and 1.5. Although one would expect a better agreement if the atomic number decreases within the 3d series, the case of Fe and Co is still an intriguing question. First attempts to compare experiment and theory indicated that for Fe and Co many-body effects can be considered small [99,104]. The deviations between measured critical point energies with those calculated by local-density methods indicated small corrections in the case of Fe, i.e., the energy positions with respect to the Fermi energy were about 10% smaller in the experiment [105]. Moreover, the Fe photoemission peaks showed a large linear broadening ($\sim 60\%$ of the binding energy) [105], much later on predicted to be accompanied by a strong loss in spectral weight [106]. For Co, the results indicated larger deviations than for Fe [99,107,108], but the amount of data was still insufficient for definite statements and more sophisticated theories beyond DFT-based calculations were needed to properly describe the underlying physical mechanisms behind the narrowing of the bands.

Since more than a half a century it is clear that the bandstructure together with exchange and correlation effects plays an important role for the appearance of ferromagnetism in 3d transition metals and their alloys [89]. Due to electronic correlation effects, low-energy electrons (or holes) become dressed by a cloud of excitations resulting in quasiparticles of a finite lifetime and an effective mass. Thus, calculations beyond DFT-based theories have to be developed to take into account many-body interactions, i.e., correlation effects, which normally are described by the energy and momentum dependent complex self-energy function $\Sigma(\mathbf{k}, E)$. Here, its real part $Re\Sigma$ is related to the mass enhancement while its imaginary part $Im\Sigma$ describes the scattering

¹Note that to avoid ambiguity, LSDA and LDA acronyms are generally used for magnetic and non-magnetic systems, respectively.

rate or the inverse quasiparticle lifetime (see sections 2.1.6 and 4.2 for details). One of the successful schemes for correlated electron systems is the dynamical mean-field theory (DMFT). It replaces the problem of describing correlation effects in a periodic lattice by a correlated impurity coupled to a self-consistent bath [109]. An alternative approach is the three-body scattering (3BS) approximation, which takes into account the scattering of a hole into an Auger-like excitation in the valence band, formed by one hole plus one electron-hole excitation [110]. Recently, such many-body calculations allowed a detailed but qualitative description of the "quenching" (i.e., reduction in intensity) of majority-channel quasiparticle excitations in Co [111] or the narrowing of the Ni 3d band [112,113]. While these theories give an improved interpretation of the electronic structure, our central question in this chapter is, whether they also lead to a *quantitative* agreement with experiments.

ARPES is a powerful method to determine the spectral function and by comparison to the single-particle bandstructure (usually approximated by DFT bandstructure calculations) to obtain the self-energy $\Sigma(E, k)$ [37]. Moreover, the spin-resolved version of this method (SARPES) is better suited to disentangle the complex electronic structure of ferromagnets, in particular for systems with strong overlap between majority and minority spin bands. In this chapter, SARPES spectra of ferromagnetic bcc Fe(110) and hcp Co(0001) will be presented. The experimental results will be compared to state-of-the-art many-body calculations (DMFT and 3BS) as mentioned above, including a full calculation of the one-step model (ISM) [114] of photoemission. Further insight in the results will be achieved by performing a detailed *quantitative* analysis of the experimental energy positions and linewidths of the photoemission peaks, by comparison to the theoretical spin-dependent spectral functions and imaginary part of the self-energy function, respectively. This comparison, which represents an important test for the agreement with the most recent theoretical predictions, gives us more quantitative information about the spin-dependent photohole lifetimes and "shrinking" of the bands due to correlation effects observed in the experimental spectra. We aim to establish if there occurs a quenching of the majority spin quasiparticle excitations in this type of systems due to short lifetimes, and also to determine up to which extent there is a spin dependent quasiparticle renormalization due to many-body effects. Our main conclusion is that *quantitative agreement*, in particular concerning the linewidths, *is not reached*. This clearly demonstrates the demand for further non-local many-body theories as it will be explained more in detail in the following sections.

4.2 Theoretical background

In this section, we give a brief introduction to the theoretical framework used for the electronic structure calculations presented in this chapter². In the following, we will only concentrate on the most important qualitative aspects of the different theoretical schemes used for the calculations without going into the details of their analytical

²The theoretical results were obtained by collaborators from the theory groups of Prof. F. Manghi (University of Modena, Italy), Prof. H. Ebert (Ludwig-Maximilians Universität München), Prof. M. I. Katsnelson (University of Nijmegen), Prof. O. Eriksson (Uppsala University) and Prof. A. I. Lichtenstein (Universität Hamburg).

and computational derivation. For a general overview on the details we address the reader to purely theoretical theses which were developed in parallel to the present one [115, 116].

The main task of such electronic structure calculations is to solve the Schrödinger equation for the many-body Hamiltonian in a solid³

$$\hat{H}\Psi = \left[\sum_i \left(-\frac{\hbar^2}{2m} \nabla_i^2 + \sum_I \frac{Z_I e^2}{|\mathbf{r}_i - \mathbf{R}_I|} \right) + \frac{1}{2} \sum_{i \neq j} \frac{e^2}{|\mathbf{r}_i - \mathbf{r}_j|} \right] \Psi = E\Psi \quad (4.1)$$

where the electrons, with mass m , and the atomic nuclei are denoted by the subscripts i and I , respectively. The first term of the Hamiltonian \hat{H} denotes the kinetic energy of the electrons, while the second and third terms denote the additional potentials due to the electron-nucleus and electron-electron interactions, respectively. It is the last term, i.e., the mutual Coulomb repulsion between the electrons, what makes a very difficult task to find an exact solution to Eq. (4.1) because it correlates the motion of all the electrons. Furthermore, due to the appearance of the many-body wavefunction $\Psi = \Psi(\mathbf{r}_1, \mathbf{r}_2, \dots, \mathbf{r}_N)$, which contains a tremendous amount of information and is almost impossible to handle with increasing number of particles N , an exact solution can only be calculated for at most a few tens of particles. One of the first attempts to solve Eq. (4.1) is the Hartree-Fock method (HF) [56], where the many-body wavefunctions are simplified by linear combinations of $N \times N$ Slater determinants [117] containing independent-particle wavefunctions of the form $\Psi_\nu(\mathbf{r}_\mu)$, where $1 \leq \nu, \mu \leq N$. Although with the HF method an exact solution can be calculated for small values of N , it often leads to discrepancies with the experimental ground-state binding energies. Given the impossibility of an exact general solution, several theoretical methods have been proposed over many years by the electronic structure community as it follows below.

4.2.1 Density functional theory in the local density approximation (DFT-LDA)

While many researchers were working on an improved version of the HF method, Hohenberg and Kohn [118] developed a conceptually different approach, the density functional theory (DFT). In this case, the many-body problem is solved within a single-particle scheme where every electron moves in a time-averaged potential determined by the nuclei and the other electrons. The main advantage of DFT is that the ground-state properties of the system can be calculated without requiring the complete knowledge of the many-body wavefunction, thus allowing the treatment of a larger number of particles as compared to the HF method. In a system with N particles (e.g. electrons) moving in an external potential $V_{ext}(\mathbf{r})$ (caused by e.g. the nuclei), this is achieved by working directly with the particle density distribution $n(\mathbf{r}) = \int d\mathbf{r}_2 \dots \int d\mathbf{r}_N \Psi^*(\mathbf{r}, \mathbf{r}_2, \dots, \mathbf{r}_N) \Psi(\mathbf{r}, \mathbf{r}_2, \dots, \mathbf{r}_N)$ and by minimization of the so-called

³For simplicity, spin-orbit terms arising from relativistic effects are neglected.

Kohn-Sham energy functional [119], which reads:

$$E_{KS}[n] = T_0[n] + E_H[n] + E_{xc}[n] + \int d\mathbf{r} V_{ext}(\mathbf{r})n(\mathbf{r}) \quad (4.2)$$

where T_0 is the kinetic energy of the non-interacting system, E_H the Hartree energy, E_{xc} the exchange-correlation energy and the last term arises from the interaction between the particle density and the external potential. The Hartree term E_H is due to the averaged particle-particle interaction, which is the same for any particle at a given site and still contains the interaction of each particle with itself. The unknown exchange-correlation energy contains all the deviations between the single-particle and the many-body system, including the self-interaction corrections. It can be understood in terms of the potential energy arising from the combined effect of the exchange and Coulomb interactions between a particle and the rest of the system. It is known as the energy of the so-called *exchange-correlation hole* $n_{xc}(\mathbf{r})$, since electrons interact correlating their motion so that they tend to avoid each other, and as a result every electron is surrounded by a hole in the electron density of equal spin and opposite charge. Within the local density approximation (DFT-LDA) [118–120], the solid is treated as a homogeneous electron gas of uniform density, leading to an energy E_{xc} which only depends on the spherical average of n_{xc} , thus simplifying the minimization of Eq. (4.2).

The Kohn-Sham energy functional is the consequence of the key idea of DFT, which is to replace the many-body problem by an non-interacting electron gas of independent particles whose density distribution $n(\mathbf{r})$ is the same as the one of the interacting system. This is related to the main assumptions behind DFT-LDA [118], which are that (i) Ψ and $V_{ext}(\mathbf{r})$ are uniquely determined by the electron density distribution $n(\mathbf{r})$ and (ii) for a given $V_{ext}(\mathbf{r})$, the energy functional of Eq. (4.2) can be defined such that its minimum is the ground-state energy of the system. This means that in the DFT-LDA method, the energy of the states is exactly calculated in the limit in which $n(\mathbf{r})$ corresponds to the ground-state density.

While the assumptions of the DFT-LDA scheme can appear rather drastic, they give an excellent description of various solids, in particular sp bonded ones. In this case the electrons are delocalized in the whole crystal, thus fitting with the picture of one effective potential. In other words, DFT-LDA represents a substantial simplification of the Coulomb interaction, in which an electron at a given site sees a time-averaged local density due to the other electrons and an averaged local potential V_{LDA} . However, it was soon realized that, although DFT methods could successfully describe *s*, *p* and some *d* electrons in various transition metals and their compounds, a more atomic-like description was needed for strongly localized electrons [121]. Here the electrons occupy less extended orbitals, thus acquiring a highly localized character, which usually leads to narrow *d* and *f* bands. In this case, due to the strong Coulomb repulsion between the electrons, the behaviour of the real system becomes very different from the single-particle picture of DFT-LDA, and one should refer to it as a strongly correlated system. The same argumentation holds for spin-polarized systems within the local spin-density approximation (DFT-LSDA) [120], where Kohn-Sham energy functionals for each component of the spin-density distribution $n_{\uparrow,\downarrow}(\mathbf{r})$ are minimized until convergence is reached.

4.2.2 Dynamical mean-field theory (DMFT) and three-body scattering approximation (3BS)

To describe d- and f-electron narrow band systems correctly, a more atomic-like theory in which genuine many-body effects are taken into account explicitly is desirable. Following this approach, Anisimov et al. [122, 123] developed the LDA+U method, where DFT-LDA standard band theory is merged with an atomic description of localized states. This method includes the effect of the on-site Coulomb interaction via the so-called Hubbard parameter U [124], which can be understood as the energy cost for accommodating two electrons with different spins on the same site. Depending on the value of U , additional shifts occur in the energy positions of the different bands arising from localized electrons.

However, the LDA+U method is not strongly sensitive to the degree of localization, which depends on the bandwidth W , a more accessible parameter in experiments, or more in particular on the ratio U/W . When U/W is small, the electrons retain much of their wave-like character and the system behaves as a weakly correlated metal, properly described on the basis of DFT-LDA. On the other hand, when $U/W > 1$, due to the strong Coulomb repulsion, the electrons do not find energetically favorable to move from site to site, and the system turns into a Mott insulator [125]. The LDA+U method is suitable in this regime and in most cases provides good results. However, it almost automatically predicts electron localization even if correlation effects are not strong. Missing in both LDA and LDA+U is e.g., the strongly correlated metallic phase found in transition metal oxides [126] and heavy fermion systems [127] at intermediate values of U . In this case the Mott insulator is doped and becomes metallic, resulting in a low-energy electronic behaviour which is dominated by quasiparticle⁴ physics.

More sophisticated methods, are the three-body scattering approximation (3BS) [110] and dynamical mean field theory (DMFT) [128]. Combined with DFT-LSDA to describe realistic materials with local Coulomb correlations, the resulting LSDA+3BS [110–112] and LSDA+DMFT [128, 129] schemes are the most universal state-of-the-art techniques which properly describe the entire regime of U/W values. Both LSDA+3BS and LSDA+DMFT treat short range intra-site interactions of narrow band systems starting from a generalized multiband Hubbard-like Hamiltonian [111, 124, 128], which in the second quantization is

$$\hat{H} = \sum_{i\alpha\sigma} \epsilon_{i\alpha\sigma} \hat{n}_{i\alpha\sigma} + \sum_{i\alpha j\beta\sigma} t_{i\alpha j\beta} c_{i\alpha\sigma}^\dagger c_{j\beta\sigma} + U \sum_{i\alpha\beta\sigma} \hat{n}_{i\alpha\sigma} \hat{n}_{i\beta-\sigma} + (U - J) \sum_{i\alpha\beta\sigma} \hat{n}_{i\alpha\sigma} \hat{n}_{i\beta\sigma} \quad (4.3)$$

where electron-electron interaction is explicitly included via the on-site screened Coulomb Hubbard parameter (U) and exchange integrals (J). Here α, β run over the d orbitals, i, j over the lattice sites and σ over the spin quantum number. The quantity $\hat{n}_{i\alpha\sigma} = c_{i\alpha\sigma}^\dagger c_{i\alpha\sigma}$ is the occupation number of a given state, where $c_{i\alpha\sigma}^\dagger$ and $c_{i\alpha\sigma}$ are the creation and annihilation operators, respectively. The first two terms of the Hamiltonian describe a system of non-interacting, delocalized electrons. The tight-binding

⁴We can think of quasiparticles as dressed electrons which move independently of each other, although with a larger effective mass m^* because the quasiparticle consists of the initial electron plus the electron–electron interaction with its environment.

hopping parameter $t_{i\alpha j\beta}$ is the energy gained by an electron jumping from site to site. It characterizes the overlap between the electron wavefunctions at different sites and quantifies the tendency towards delocalization. The two last terms in Eq. (4.3), on the other hand, describe the electron-electron interaction. The first of these terms, proportional to U , describes the interaction between two electrons with opposite spins sitting on the same lattice site, while the second, proportional to $U - J$, the interaction between two electrons with parallel spins, but in different orbitals.

According to the LSDA+3BS approach, the solution to the Schrödinger equation involving the Hubbard Hamiltonian of Eq. (4.3) is achieved perturbatively by expanding the interacting many-body wavefunctions into several configurations obtained by adding single electron-hole pairs to the ground state of the single-particle Hamiltonian. More details on this procedure can be found in [110, 116]. The response of the interacting system to the creation of one hole is then explicitly described in terms of interactions between configurations with one hole plus one electron-hole pair, giving rise to multiple hole-hole and electron-hole scattering. A simplified schematic representation of these type of interactions within the d band of a strong ferromagnet is shown in Fig. 4.1(a). They correspond to multiple scattering events in the initial and final states of the photoemission process from the majority and minority spin bands. A hole produced due to photoemission in the majority spin channel is accompanied by the phase space of electron-hole pair excitations of opposite spin, involving scattering of strength proportional to U . The analysis is the same for the removal of one minority spin electron, but a less intense scattering strength proportional to $U - J$ accounts for the interactions among parallel spin particles.

On the other hand, in the LSDA+DMFT scheme, the solution to the Schrödinger equation is obtained non-perturbatively by mapping it into a Single-Impurity Anderson Model [130]. This means that the lattice problem is replaced by a single site embedded in a dynamical effective field caused by a bath of non-interacting electrons, as sketched in Fig. 4.1(b). While the single site is treated as a correlated impurity which includes the effect of the Coulomb repulsion, the environment surrounding a given atom is replaced by an effective fermionic bath of a wavevector dependent ground-state energy $\epsilon_{\mathbf{k}\sigma}$ which is coupled to the atom through the exchange of electrons at a given potential energy $V_{\mathbf{k}}$. More details on the exact analytical derivation can be found in [115, 128].

While the LSDA+3BS and LSDA+DMFT schemes use different methods to solve the many-body problem, both use a Green function formalism to obtain the quantities of interest, i.e. the self-energies Σ_{DMFT} and Σ_{3BS} which determine the spectral function of the hole state $A(\mathbf{k}, E)$ (see section 2.1.6 for details).

The LSDA+DMFT and LSDA+3BS calculations of the SARPES spectra presented in this chapter have been performed within the framework of the spin-polarized fully relativistic Korringa-Kohn-Rostoker multiple scattering theory (SPRKKR) [131] and the Faddeev theory [132], respectively. Both spin-orbit coupling and exchange splitting were treated on equal footing in a fully relativistic approach. To account for electronic correlations beyond the LSDA approximation, the site-diagonal, local and complex energy-dependent self-energies Σ_{DMFT} and Σ_{3BS} were introduced self-consistently [133]. This allowed to determine the corresponding spectral functions $A(\mathbf{k}, E)$ for a semi-infinite lattice structure. Moreover, for a quantitative comparison

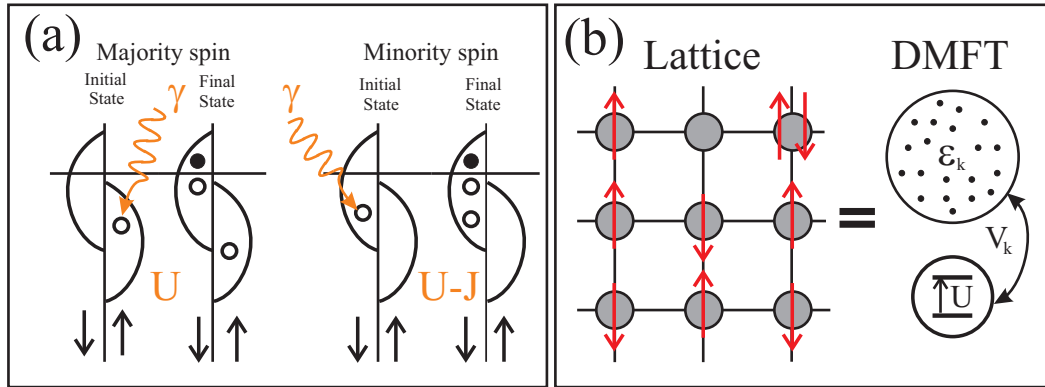


Figure 4.1: (a) Schematic representation within the *LSDA+3BS* scheme of the interactions involved in spin-dependent processes within the majority (left) and minority (right) spin bands of a strong ferromagnet in the initial and final states after removal of one electron. (b) Left: the lattice problem of a simplified single-orbital Hubbard model, where t is the hopping energy between nearest neighbors and U the energy cost for double occupation due to the Coulomb repulsion (upper atoms). At half-filling, if $U \gg t$ the electrons do not move anymore and the system turns into a Mott insulator (bottom atoms). Right: In the *LSDA+DMFT* scheme, the lattice problem is replaced by a single site embedded in a dynamical effective field caused by a bath of non-interacting electrons, which is coupled to the atom through the exchange of electrons at a given potential energy $V_{\mathbf{k}}$ (adapted from [115]).

with the measured SARPES spectra, it was inevitable to take into account the wave-vector and energy-dependent transition matrix elements calculated within the one-step model of photoemission (1SM) [113, 114]. This describes the excitation process, the transport of the photoelectron to the surface, as well as its escape into the vacuum. For a quantitative description of surface states and resonances, a realistic approach for the surface barrier was considered. It should be emphasized that in all the calculations, the broadening of the peaks due to final state effects is included (see section 2.1.4).

4.3 Experimental details

Experiments were performed with a SPECS Phoibos 150 hemispherical electron energy analyzer and a Rice-type Mott spin detector using linearly polarized undulator radiation at the UE112-PGM1 beamline (see section 3.2 for details). The angular resolution of the equipment was better than 1° and the average energy resolution about 100 meV. The Fe(110) and Co(0001) surfaces were prepared on W(110) by electron bombardment from high purity Fe and Co wires mounted in several home-made e^- -beam evaporators. In order to obtain a good structural quality it was necessary to anneal the films during 5 min. at $\sim 400^\circ\text{C}$ after evaporation. The tungsten sample was previously cleaned by several cycles of annealing in oxygen (1×10^{-7} mbar) at 1200°C followed by flashing at 2200°C . The base pressure during the experiments was $1-2 \times 10^{-10}$ mbar. The cleanliness of the tungsten substrate was checked by the absence

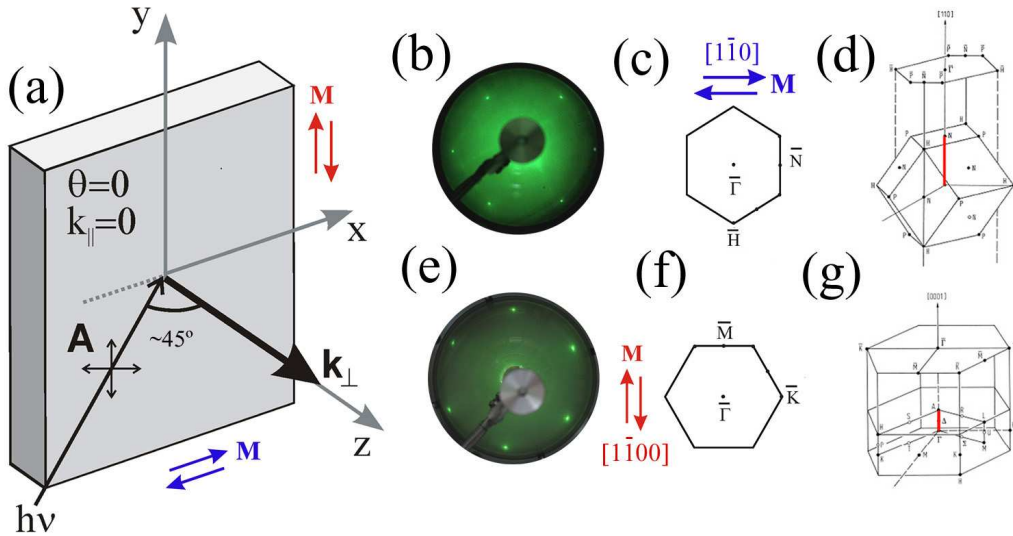


Figure 4.2: (a) Sketch of the geometry of the experiment. From left to right, bcc Fe(110) ((b), (c) and (d)) and hcp Co(0001) ((e), (f) and (g)) experimental geometries are shown; (b),(e): LEED patterns acquired at an energy of $\sim 150\text{eV}$; (c),(f): overview of the SBZ and magnetization orientations; (d),(g): Projected high symmetry directions (red lines) of the BBZ probed in the experiments (adapted from [37]).

of reconstructions in LEED as well as by the presence of a surface induced component in the W-4f core level spectrum. The normal emission condition was determined by measuring angle-resolved valence band dispersions of the clean W(110). A thickness of ~ 20 ML was enough to achieve the corresponding bulk-like Fe and Co bandstructure.

4.3.1 The geometry of the experiment and low-energy electron diffraction (LEED)

Figure 4.2 shows an overview of the geometry of the experiment (Fig. 4.2(a)), LEED patterns, surface orientations, magnetization directions, and the corresponding bulk (BBZ) and surface (SBZ) Brillouin zones of bcc Fe(110) (Figs. 4.2(b)-4.2(d)) and hcp Co(0001) (Figs. 4.2(e)-4.2(g)). The linear polarization of the incident photon beam was horizontal or vertical, and its angle of incidence with respect to the surface normal $\sim 45^\circ$. Hence, in the reference frame of the sample, the light had more p- or full s-character, respectively. The LEED patterns were acquired with an incident electron beam of ~ 150 eV (Figs. 4.2(b) and 4.2(e)). Note that each diffraction spot corresponds to a $\bar{\Gamma}$ point of the SBZ. Therefore, constructing the Wigner-Seitz cell in reciprocal space leads to a SBZ shape which is rotated by 90° (Figs. 4.2(c) and 4.2(f)) with respect to the measured LEED pattern. The magnetization directions are also indicated⁵. The measured LEED patterns confirm that the annealing procedure which follows the epitaxial growth leads to well-ordered surfaces of very high quality. The

⁵The notation follows simple Miller indices [hkl] for bcc Fe, while for Co the hexagonal close-packed (hcp) notation [hkj], where $j=-h-k$ is the redundant index.

six-fold symmetry appearing in the case of Co (Fig. 4.2(e)) gives evidence of its hcp structure. The high symmetry directions along which the spin-resolved measurements presented in this work were performed are highlighted with red lines in Figs. 4.2(d) and 4.2(g). These directions correspond to k_{\perp} points in the reciprocal space going from Γ to N (Σ line) and Γ to A (Δ line) for bcc Fe(110) and hcp Co(0001), respectively. Since the emitted electrons were detected in normal-emission, these high symmetry lines were probed by varying the photon energy of the incident beam. In this geometry, the surface contribution in the photoemission signal is limited to states located at the $\bar{\Gamma}$ point of the SBZ.

4.3.2 Easy axis of magnetization

For Fe on W(110), it has been shown by SARPES experiments that an in-plane to in-plane spin reorientation transition occurs at ~ 42 ML critical thickness [134, 135]. Its origin is typically explained in terms of a balance between the volume and surface magnetocrystalline anisotropy energies of the system. At values below the critical thickness, the easy axis of magnetization is along the Fe[$1\bar{1}0$] (or W[$1\bar{1}0$]) direction. For hcp Co(0001), the magnetization orientation has been found to be out-of-plane in bulk single crystals [136, 137] and in-plane due to surface anisotropy effects in ultrathin epitaxial films grown on W(110) [138, 139]. As we will discuss later on, this is an important difference that should be considered when comparing photoemission data from hcp Co single crystals and ultrathin films. In the in-plane configuration [140–142], the easy axis of magnetization is along the Co[$1\bar{1}00$] (or W[$1\bar{1}0$]) direction. Note that this direction is parallel to the $\bar{\Gamma}$ - \bar{M} symmetry line of the SBZ.

4.3.3 Growth mechanisms revisited

It is important to emphasize that the preparation methods used in this work are based in well-established procedures which are known to give surfaces of very good and comparable quality. We would not like to revisit or extend our study to those well-known growth methods within the scope of this thesis. However, we would like to address to the reader to interesting experiments which show in detail the typical growth modes of Fe and Co on W(110). It has been shown that Fe films on W(110) follow the Stranski-Krastanov growth mode (i.e., layer plus islands) and that continuous thick films can be successfully fabricated by deposition at room temperature followed by moderate annealing, or by rising the temperature of the substrate during deposition [143]. Despite the lattice mismatch of 9.6% between Fe and W, after annealing the resulting strain is accommodated in the first three atomic layers beyond which the lattice constant of bcc iron is relaxed [144]. For Co(0001), the first layer grows pseudomorphically, being strained and stable up to a temperature of 1300 K [145]. Further growth of the second and subsequent layers is characterized by a hcp structure which grows in the Frank van der Merwe mode or layer-by-layer growth. This type of growth was observed at temperatures below 100 K as well. Annealing at very high temperatures typically forms three dimensional islands on top of the first grown overlayers, breaking the films into compact clusters.

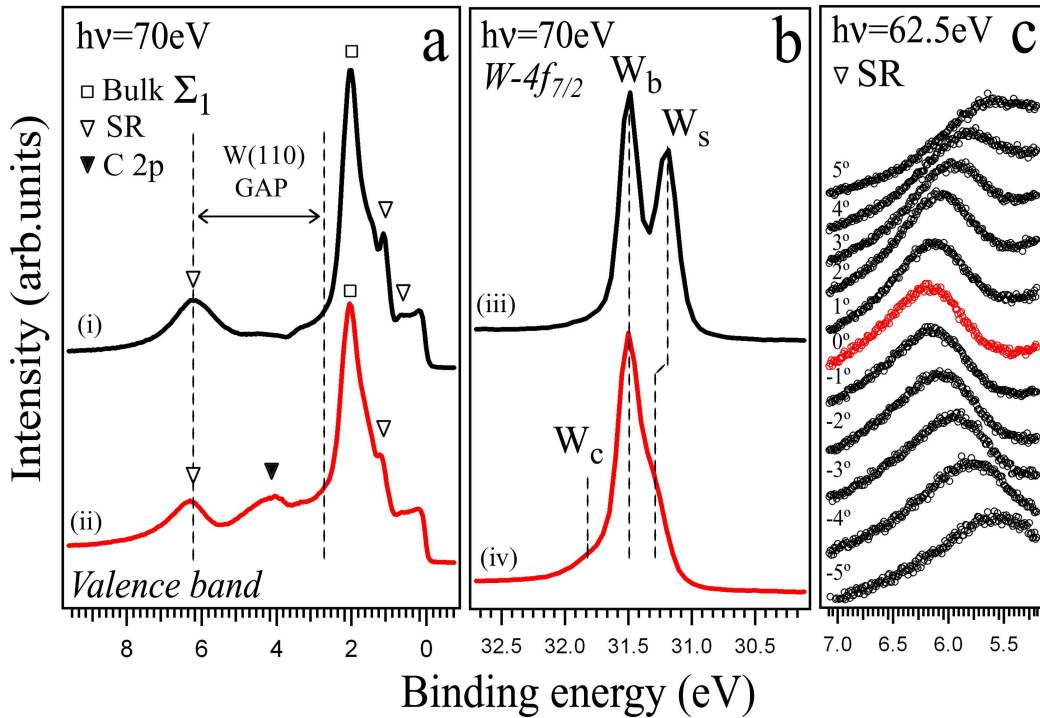


Figure 4.3: (a) Valence band photoemission spectra from $W(110)$, and (b) Core levels before (ii, iv) and after (i, iii) the cleaning procedure was completed, and (c) observed parabolic dispersion of the surface resonance located in the higher binding energy side of the $W(110)$ gap.

4.3.4 The clean $W(110)$ substrate in normal photoemission

The presence of surface related components in the valence band and core-level spectra of the $W(110)$ substrate [146] is an important issue to achieve homogeneous growth of the magnetic layers. Figure 4.3 shows spin-integrated and angle-resolved photoemission spectra from the $W(110)$ crystal recorded at 70 eV and 62.5 eV photon energies before and after finishing the cleaning procedure. In Fig. 4.3(a), valence band spectra in normal-emission are shown. Fig. 4.3(b) shows the corresponding core-level spectra. Measurements in Fig. 4.3(c) show a typical parabolic dispersion of the tungsten valence band surface resonance (SR) found at a binding energy (BE) of $E_B \sim 6.2$ eV, as marked together with other two surface resonances with open triangles in Fig. 4.3(a). In Figs. 4.3(a) and 4.3(b) two pairs of spectra (red and black) are shown, labeled from (i) to (iv). The black spectra ((i) and (iii)), which correspond to a clean $W(110)$ surface, were recorded after several cycles of annealing in oxygen followed by flashing at high temperature. The red spectra ((ii) and (iv)), on the other hand, correspond to a carbon contaminated $W(110)$ surface, basically the result of a cleaning procedure in which the sample was not properly annealed in oxygen and flashed.

The main difference between spectra (i) and (ii) is found within the surface-projected band gap of $W(110)$ (denoted by dashed lines) ranging from ~ 3 to ~ 6 eV. In the case of spectrum (ii), surface-derived carbon features dominate the spectra in that energy

range (C2p states denoted by full black triangles). The fact that they appear within the tungsten gap allows us to uniquely identify them as surface-localized states. The intensity of those carbon states within the gap completely disappears for the clean spectrum (i). In this case, the valence band emission shows prominent surface resonances (SR) which appear at ~ 0.6 , ~ 1.2 and ~ 6.2 eV. Particularly, we see that the intense peak of the surface resonance at $E_B \sim 1.2$ eV in the clean spectrum, is slightly suppressed and mostly substituted by a broader feature due to emission from W bulk d states of Σ_1 symmetry appearing at $E_B \sim 1.9$ eV. In a second-step and before deposition of magnetic materials, photoemission spectra of distinct $W4f_{7/2}$ core-levels were checked as shown in Fig. 4.3(b). Core-level binding energies are very sensitive to the chemical environment. In the core-level spectrum of a clean tungsten surface in which carbon and oxygen are absent, the bulk (W_b) and surface-induced (W_s) components are shifted respect to each other due to the narrower density of states of the atoms at the surface. The reduction of the number of neighboring atoms at the metallic surface leads to a Fermi level pinning causing a shift between valence states and core levels [147–149]. This is the situation in the spectrum (iii) of Fig. 4.3(b) for clean W(110), where one can clearly identify a bulk emission W_b placed at a BE of ~ 31.41 eV and a surface-induced component W_s shifted by about 0.32 eV towards lower BE. However, a reduction in the energy shifts between W_b and W_s may appear as a result of charge transfer by formation of chemical bonding with other elements such as oxygen or carbon. This happens in the carbon contaminated spectrum (iv), where the smaller BE shift between W_s and W_b is an indication of an additional chemical bonding and interaction with the carbon atoms in the surface. Besides, another feature labeled as W_c appears as a shoulder in the higher BE side of the main peak. This feature is due to specific carbon-induced chemical states which could be organized in defects or in junctions between domains of the carbon structure present at the tungsten surface. Apparently, the core level spectra are much more sensitive to the cleanliness of the W(110) surface than the direct measurement of the surface resonances in the valence band spectrum at 70 eV photon energy. In general, the intensity ratio between W_s and W_b determines the cleanliness of the system. For our purpose, an intensity ratio of about 50% was found enough to reach a homogenous growth of the magnetic films.

Measurements like those in Fig. 4.3(c) were usually performed at the beginning of each experiment in order to find in an accurate way the normal-emission condition of the system. A change of manipulator or sample holder may induce deviations of the nominal angle in which this position is reached. This method is straightforward and practically independent of the cleanliness of the sample. In general, it is enough to find a feature in the spectra which shows a pronounced dispersion. In Fig. 4.3(c), we follow the dispersion of the resonance feature which appears at the higher BE side of the W(110) gap in spectrum (ii) of Fig. 4.3(a). At 62.5 eV photon energy and with changing angle, we see that the surface resonance disperses parabolically, reaching a certain minimum at a BE of ~ 6.2 eV. The angle in which that minimum is reached is identified as 0° (red spectrum in Fig. 4.3(c)), leading to a very accurate determination of the normal-emission condition. In some situations, a He-Ne laser can be used in combination to this method to double-check the validity of the result. The laser is mounted in such a way that the beam passes through the iris aperture of the analyzer

and hits the sample. When the incident and reflected beams overlap, the normal-emission condition is determined, and therefore the resulting absolute angle.

4.4 Spin-dependent electronic correlations: a comparison theory-experiment

In this section, we investigate the effects of electron correlations near the Fermi level in the spin-dependent electronic structure of ferromagnetic bcc Fe(110) and hcp Co(0001). Spin-integrated and spin-resolved photoemission spectra are compared in detail to theoretical calculations within the LSDA+3BS and LSDA+DMFT schemes in combination with 1SM calculations. This comparison, which has not been carried out before, represents a strongly demanding test of the existing state-of-the-art many-body theories which lie at the heart of our understanding of electron correlations in condensed matter physics. It should be emphasized that the theoretical results presented here aim at the proper description of the correlation effects for a given set of orbitals, in this case the 3d states, but no correction is added for the other electrons. Therefore, the theory includes only correlation effects coming from a local many-body approach and without any additional semi-empirical contribution to the self-energy that would result in a fit of the experimental results. This procedure allows us to make a pure comparison theory-experiment in a quantitative way.

4.4.1 bcc Fe(110)

4.4.1.1 Spin and angle-resolved photoemission

For ferromagnetic Fe, several experimental photoemission and inverse photoemission studies exist [105, 150–154]. Despite this effort in experimental research, no general consensus has been reached about the strength of electron correlations in the spin-dependent electronic structure of this system. This means that the relative importance of the averaged on-site Coulomb interaction U between d electrons has not been established. Other issues, such as the existence of photoemission satellites [155], are still the object of scientific discussions as well. In all of the Fe calculations presented here for the comparison with the experimental results, unless specified, a value $U=1.5$ eV has been adopted, which is within the so-called experimental value $U\sim 1$ eV [107] and a value $U\sim 2$ eV derived from theoretical studies [156–158]. For the averaged on-site exchange interaction J , the generally accepted atomic value $J\sim 0.9$ eV [159] has been used.

As mentioned in the previous section, the linear polarization of the photon beam was switched from horizontal to vertical, which for Fe means that a more p- or full s-character of the incident light is achieved when $\mathbf{A}||[1\bar{1}0]$ or $\mathbf{A}||[001]$, respectively. As a result, the intensity of some particular peaks is suppressed with one polarization and not with the other due to matrix-element effects. Figures 4.4(a) and 4.4(b) display a comparison between spin-integrated ARPES data and theoretical LSDA+DMFT+1SM calculations broadened by the experimental energy resolution of bcc Fe(110) along the

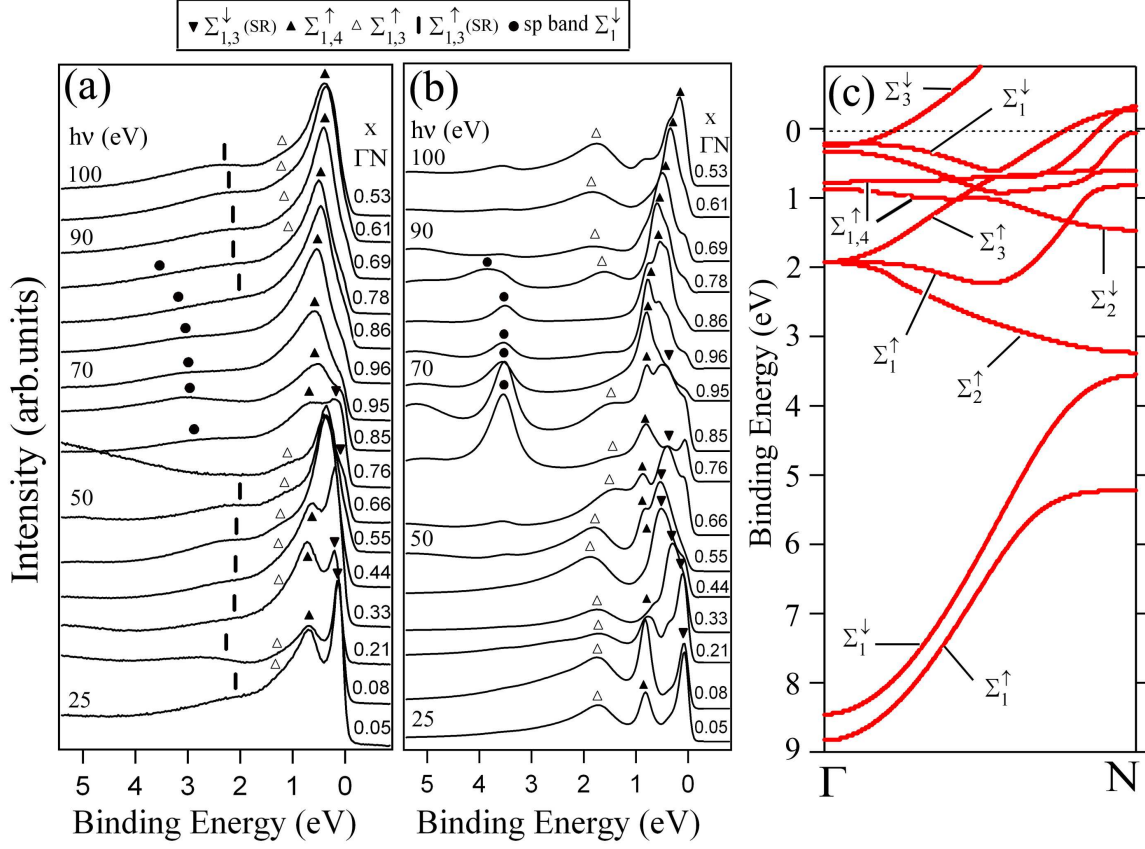


Figure 4.4: (a) *Experimental spin-integrated photoemission spectra of the Fe(110) surface measured with p-polarization in normal-emission along the ΓN direction of the bulk Brillouin zone at different excitation energies (steps of 5 eV). To the left, photon energies are given. To the right, the curves are labeled by the wavevectors in units of $\Gamma N=1.55\text{\AA}^{-1}$, the Γ point being at $x=0$ and the N point at $x=1$. Symbols used for peak assignment are given as well.* (b) *Corresponding calculation obtained by the LSDA+DMFT+1SM method including electronic correlations, matrix elements and surface effects.* (c) *Fully relativistic valence-band states of Fe(110) obtained self-consistently in the SPRKKR formalism by suppressing the imaginary part of the self-energy $\text{Im}\Sigma_{DMFT}$.*

ΓN direction of the bulk Brillouin zone (BBZ) with p polarization. The $k=k_\perp$ values were calculated from the used photon energies ranging from 25 to 100 eV and using an inner potential $V_0=14.5$ eV in Eq.(2.17). In order to identify the nature of the observed excitations, Fig. 4.4(c) shows fully relativistic calculations of the spectral function $A(\mathbf{k},E)$ obtained by introducing self-consistently the LSDA+DMFT self-energy into the SPRKKR formalism [133]. In these calculations, $\text{Im}\Sigma_{DMFT}$ was set to zero in order to make all the initial states visible. For the sake of simplicity, the assignment of the observed symmetries of the initial states contributing to the photoemission spectra follows the non-relativistic notation described by Hermanson for bcc crystals [61]. Although this notation is not totally correct since spin-orbit interaction is not negligible in 3d metals, in the case of bcc Fe it is simpler and more useful if one

wants to compare with other experimental and theoretical studies of this system. Note that forbidden transitions involving initial states of Σ_2 symmetry are not observed in the experiments or in the LSDA+DMFT+1SM calculations. Furthermore, although due to symmetry arguments the transitions observed with s-polarization are mainly Σ_3 -like and with p-polarization Σ_4 and Σ_1 -like, in most of the cases we have adopted double subscripts to indicate almost degenerated states or to avoid redundancy in the symbols used for the assignment of the peaks. Figure 4.5 displays analogous SARPES data (Figs. 4.5(a) and 4.5(b)) together with LSDA+DMFT+1SM calculations (Figs. 4.5(c) and 4.5(d)) for p and s-polarized photons. Similar calculations in the framework of LSDA+3BS+1SM were performed (not shown) and the results were good in agreement with all the LSDA+DMFT+1SM calculations presented here.

It is important to remark that our study is focused on the energy range $0.2 \leq E_B \leq 2$ eV where renormalization effects are predominantly caused by electron-hole excitations with and without spin flips. This energy range is quite different from that discussed in recent ARPES studies on Fe [154]. There, the very low-energy range $E_B \leq 200$ meV has been treated, in which a renormalization of the charge carrier dynamics by a coupling to magnetic excitations is important.

In Figs. 4.4 and 4.5, the observed peaks correspond to majority (\uparrow) and minority (\downarrow) spin states of different symmetries. They are due to direct interband transitions from t_{2g} and e_g bulk states which change their initial energy as the photon energy varies, as well as surface emission peaks and resonant structures. When increasing the photon energy and moving from Γ towards the N point, all the different peaks observed show a characteristic dispersion which is accompanied by relative changes in their intensity distributions. Let us now proceed to identify the origin of the observed transitions in terms of quasiparticle peaks following their order of appearance from the lower to higher BE side of the spectra.

Near the Γ point ($x \sim 0.06 \Gamma N$), the intense peak close to the Fermi level corresponds to a $\Sigma_{1,3}^\downarrow$ minority surface resonance. Experimentally, its Σ_3^\downarrow bulk component crosses the Fermi level at $x \sim 0.33 \Gamma N$, leading to a reversal of the measured spin polarization and to a strong reduction of the intensity at $x = 0.68 \Gamma N$ in the minority channel, in agreement with the theoretical results (see Figs. 4.5(b) and 4.5(d)). The peak at ~ 0.7 eV BE, visible mainly for p polarization in a large range of wave vectors between Γ and N, can be assigned to almost degenerate $\Sigma_{1,4}^\uparrow$ bulk-like majority states (see Figs. 4.4, 4.5(a) and 4.5(c)). For s polarization (Figs. 4.5(b) and 4.5(d)), a prominent Σ_3^\uparrow feature at ~ 1.1 eV BE dominates the spectrum at the Γ point. For p polarization, its degenerate Σ_1^\uparrow states form a shoulder around the same BE. The broad feature around 2.2 eV, visible at various k points, but not at the N point, is related to a majority $\Sigma_{1,3}^\uparrow$ surface resonance (we will come back to this issue below). Around the N-point ($0.76 \leq x \leq 1.0$) and at $BE \geq 3$ eV (Figs. 4.4(a) and 4.5(a)), a Σ_1^\downarrow band having strong sp character can be observed. The pronounced difference between its theoretical and experimental intensity distributions can be attributed to the fact that in the present calculations, as mentioned above, only local Coulomb repulsion between d electrons is considered, without additional lifetime effects for the sp bands. When correct values of $\text{Im}\Sigma$ for the sp-bands would be introduced, the sp features would also be strongly broadened in the calculated spectra. Note that this is a totally different scenario

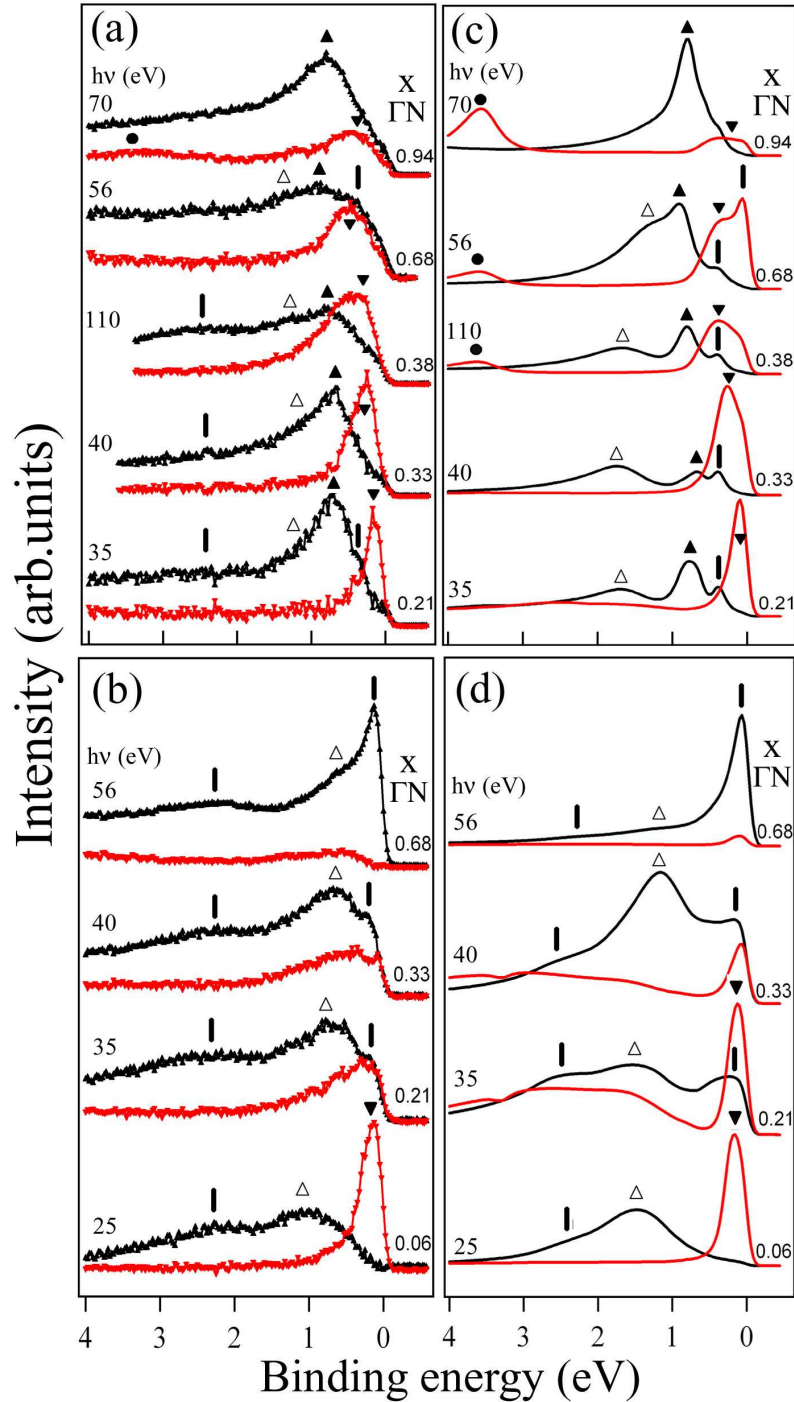


Figure 4.5: Analogous data as in Figs. 4.5(a) and 4.5(b) but now spin-resolved. (a), (b) Experiment (upwards small (black) triangles: majority spin spectra, downwards small (red) triangles: minority spin spectra). (c), (d): LSDA+DMFT+1SM theory (black and red lines for majority and minority spin spectra, respectively). (a),(c) for p - and (b), (d) for s -polarization. The symbols used for peak assignment are the same as in Fig. 4.5.

with respect to [160], where a semi-empirical contribution has been added to all the electrons to fit the experimental results. Moreover the spectra shown in [160] have been convoluted with a Gaussian with 0.5 eV full width half-maximum (FWHM) in order to reproduce the experimental broadening. This value should be compared to the average Gaussian broadening of 100 meV used in the present study. Finally, we notice that the background intensity of the experimental spectrum at $x=0.66 \Gamma N$, corresponding to a photon energy of 55 eV, is strongly increasing due to the appearance of the Fe 3p-3d resonance, i.e., the $M_3(3p_{3/2})$ final-state resonant structure. Since resonant-photoemission processes above the resonance threshold such as Auger electron emission are not considered in the present calculations, this prominent increase in intensity is not present in the theoretical spectra shown here. In this context, the existence of a photoemission satellite for bcc Fe below the resonance threshold and at a BE of ~ 5 eV is still the object of experimental discussions [155], as mentioned before. In this work this issue has not been investigated in detail, since we focus on a lower BE range. Nevertheless, it should be mentioned that although previous DFT-LDA or LDA+DMFT calculations did not reproduce this feature, the LSDA+DMFT and LSDA+3BS implementations used here indicate the existence of a non-coherent satellite at a BE of ~ 7 eV. Due to the low intensity of this feature, it could only be observed in calculations of the density of states (not shown) [115], but not in the calculated spectral functions or the LSDA+DMFT+1SM spectra.

4.4.1.2 Many-body aspects of the band structure

Comparing the experimental results from spin-integrated and spin-resolved ARPES measurements with LSDA+DMFT+1SM results, good agreement is obtained at low BE for many of the peak positions. This is also demonstrated in Fig. 4.6, where the BE positions of the most prominent features observed in the experimental SARPES data of Figs. 4.5(a) and 4.5(b) are compared to the calculated bulk-like spin-dependent spectral functions $A(\mathbf{k}, E)$ obtained in the framework of the LSDA+DMFT (Figs. 4.6(a) and 4.6(b)), LSDA+3BS (Figs. 4.6(c) and 4.6(d)) and LSDA (Figs. 4.6(e) and 4.6(f)) schemes. Majority spin states are shown in Figs. 4.6(a), 4.6(c) and 4.6(e) whereas minority spin states are shown in Figs. 4.6(b), 4.6(d) and 4.6(f). To account for the experimental energy resolution, a smearing parameter of 100 meV was considered in all these calculations. In a first approximation, Fig. 4.6 shows a comparison between the spin-dependent experimental $\text{Re}\Sigma$ and theoretical $\text{Re}\Sigma_{DMFT}$ or $\text{Re}\Sigma_{3BS}$. However, we should remember that this description in terms of a bulk spectral function, which only contains information about initial states, is still incomplete. Moreover, in these calculations matrix-element, surface effects and the actual steps of the photoemission process (i.e., propagation of the photoelectron to the crystal surface and its escape into the vacuum) are not considered. The experimental peak positions shown in Fig. 4.6 were extracted from a fitting procedure, and the results of the fits will be shown more in detail below. Note that there are no experimental data points from s-polarized measurements of Fig. 4.5(b) corresponding to the minority spin Σ_3^\downarrow bulklike peaks at $k=0.33 \Gamma N$ and $0.68 \Gamma N$ since these peaks are above the Fermi level. Furthermore, almost pure surface state features such as the Σ_3^\uparrow majority spin peaks appearing as a shoulder at the Fermi level for $x=0.21 \Gamma N$ and $0.33 \Gamma N$ have been excluded. Before

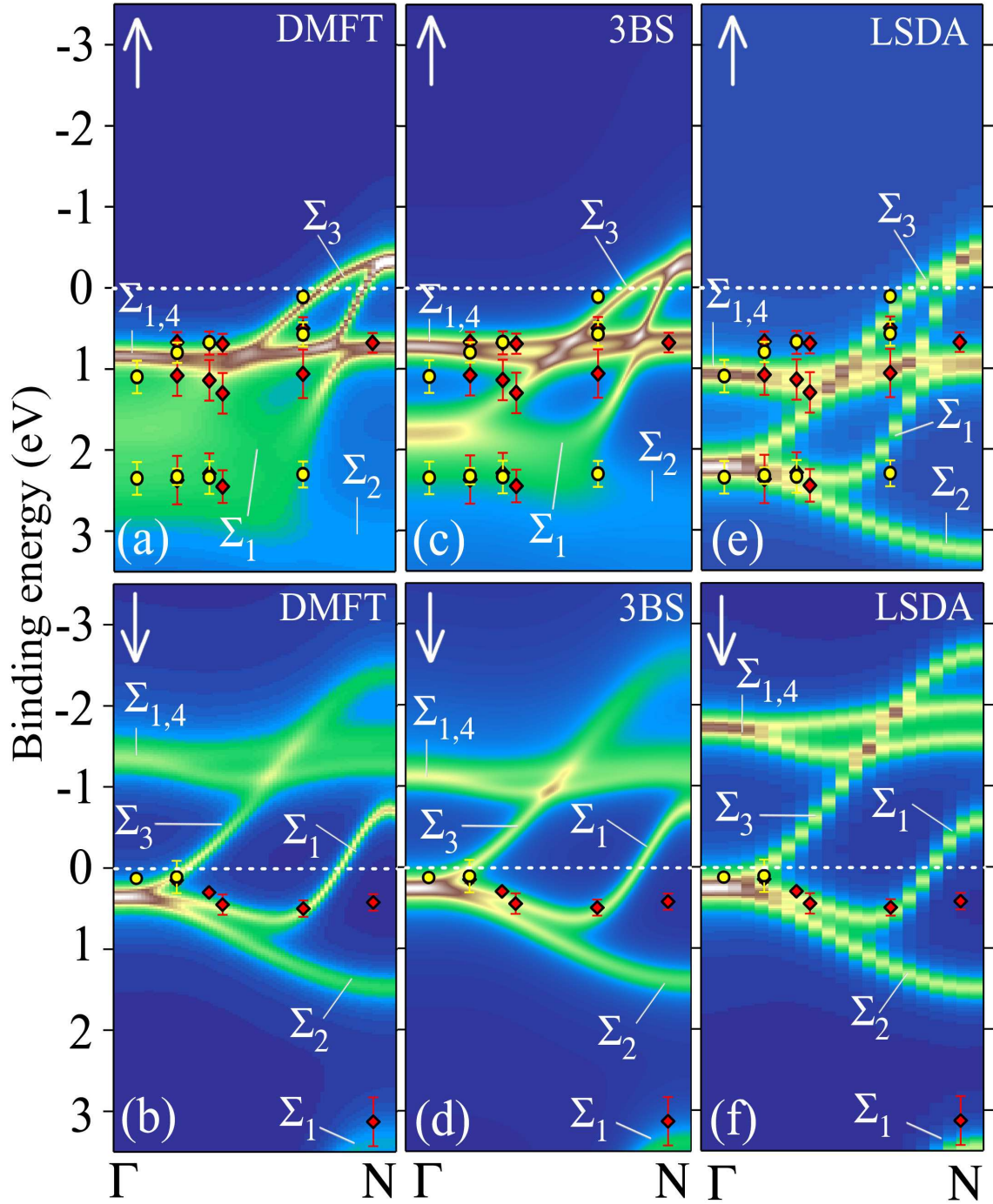


Figure 4.6: *Quasiparticle spectral functions of Fe(110) and the photoemission peak positions obtained from the spin-resolved measurements for different polarizations (\diamond for p- and \circ for s- polarization). Results obtained by the LSDA+3BS ((a),(b)), LSDA+DMFT ((c),(d)) and LSDA ((e),(f)) methods for majority and minority spin electronic states, respectively.*

proceeding, it should be noted that from Fig. 4.6, it is clear that the theoretical results derived from both LSDA+DMFT and LSDA+3BS methods are well in agreement with each other for the same values of U and J .

Let us focus first on the lowest BE majority spin states. Most importantly, the maxima of the spectral functions at a BE of ~ 0.65 eV in Figs. 4.6(a) and 4.6(c) corresponding to the almost non-dispersive $\Sigma_{1,4}^\uparrow$ bulk-like states better reproduce the experimentally obtained peak positions along the different k-points of the band structure for both polarizations than LSDA. When comparing to standard LSDA calculations of Fig. 4.6(e), it can be observed that all the LSDA peaks which correspond to the $\Sigma_{1,4}^\uparrow$ bands are shifted to a higher BE by about 1.2 eV, leading to an accidental agreement with the BE positions of the $\Sigma_{1,3}^\uparrow$ states appearing as a shoulder in Fig. 4.5(a) and as a peak near the Γ point in Fig. 4.5(b) (see below). This means that the LSDA peak at a BE of about 1.2 eV, which corresponds to the $\Sigma_{1,4}^\uparrow$ majority spin peak, should be shifted in the experiment to a BE of about 0.65 eV due to correlation effects. Therefore, one can conclude that to achieve best agreement between theory and experiment in the BE positions of the $\Sigma_{1,4}^\uparrow$ states, a shrinking of the 3d majority spin bands due to electronic correlations becomes necessary to properly describe the photoemission process involving these states.

On the other hand, *quantitative* agreement cannot be achieved for higher BE. In particular, the calculated LSDA+DMFT and LSDA+3BS majority spin spectral weight in Figs. 4.6(a) and 4.6(c) near Γ for the $\Sigma_{1,3}^\uparrow$ bands is in between the experimental features at BE's of 1.2 and 2.2 eV. Assuming negligible correlation effects would move the calculated feature to the LSDA value at 2.2 eV BE, and thus better agreement would be obtained in this case as it can be seen in Fig. 4.6(e). Thus, the experimental peak at 2.2 eV BE could be assigned to the bulk $\Sigma_{1,3}^\uparrow$ bands. However, a complete neglect of correlation effects in Fe would make the overall comparison between theory and experiment much worse: on the one hand, the energetic positions of the majority spin peaks at low BE would not be reproduced as mentioned before, and on the other hand, the narrow width of the peaks would not change with increasing BE as in LSDA, opposite to what is observed in the experiment. This situation also holds for calculations in the LSDA+1SM scheme. Thus, the experimental peak at 2.2 eV BE, instead of bulk $\Sigma_{1,3}^\uparrow$ state, it should be interpreted as a surface resonance, in agreement with previous experimental and theoretical studies [161]. The theoretical results presented here confirm this view, since changes in the surface barrier potential induced additional shifts in its BE position (not shown). On the other hand, a change in the surface barrier potential did not induce shifts in the energy position of pure bulk states. It should be mentioned here that in a relatively recent experiment by Hufner et al. [162], a non-coherent satellite in Fe was found at a BE of ~ 3.2 eV for a photon energy slightly below the 2p resonance energy (~ 706.8 eV). However, we do not observe any peak at 3.2 eV BE for the photon energies used in our experiments ($h\nu \leq 100$ eV), which are far below (by more than 600 eV) the Fe 2p absorption energy. Furthermore, the LSDA+DMFT and LSDA+3BS calculations do not reproduce a photoemission satellite at that BE.

Regarding the minority spin spectral functions shown in Figs. 4.6(b), 4.6(d) and 4.6(f), one can find good agreement between most of the experimental peak positions and all the three different theories. The only exception is the $\Sigma_{1,3}^\downarrow$ state appearing

close to the Fermi level and near the N point. Since the BE of this state is properly reproduced in the LSDA+DMFT+1SM calculations after including surface effects (see Fig. 4.5(a)), it can be assigned to a surface resonance. For the other peaks, note the small size of the differences observed for minority spin electrons between experiment and the LSDA+DMFT, LSDA+3BS and LSDA calculations. This small size of the deviations is something expected a priori, since from the theory we know that correlation effects should be more pronounced for majority spin electrons than for minority spin ones, which is a common feature for 3d transition metals. This can be easily explained by considering the creation of electron-hole pairs in the minority spin channel: since there are less minority spin electrons and thus more empty states of this kind, for any processes involving electron-hole pair creation, the pair is more likely to appear in the minority spin bands. This means that any scattering process involving majority spin electrons mostly leads to the creation of minority spin electron-hole pairs, with an effective interaction in the complete process proportional to U . On the other hand, scattering processes involving minority spin electrons also lead to the creation of minority spin electron-hole pairs, but the effective interaction for parallel-spin pairs is proportional to $U-J < U$. Therefore, correlation effects are expected to be stronger for majority spin electrons and in consequence, no big differences are observed between the minority spin spectral functions presented in Figs. 4.6(b), 4.6(d) and 4.6(f).

From the data shown in Fig. 4.6 and the overall agreement between experiment and theory we have just discussed, we conclude that correlation effects in the present calculations using $U=1.5$ eV are underestimated and that a stronger d-band narrowing is needed to achieve better results. Figure 4.7 demonstrates this for data close to the Γ point ($x \sim 0.05$ Γ N). Figure 4.7(a) compares the experimental spin-integrated ARPES spectra with the LSDA calculation broadened with the experimental energy resolution, the LSDA+DMFT calculation, and the LSDA+DMFT+1SM calculation. At low BE, perfect agreement between theory and experiment is achieved for the minority $\Sigma_{1,3}^\downarrow$ surface resonance in the LSDA+DMFT+1SM calculations. On the other hand, for the bulk $\Sigma_{1,4}^\uparrow$ peak at a BE of 0.65 eV, the agreement is good but not completely satisfactory. This also holds for the $\Sigma_{1,3}^\uparrow$ peak which appears in LSDA calculations at 2.2 eV. Because of correlation effects it is shifted in the experiment to ~ 1.2 eV BE causing in Fig. 4.7(a) at that energy a shoulder and in Fig. 4.5(b) for $x = 0.06$ Γ N a peak. This difference between the ARPES data and LSDA calculations can be explained with a linear $\text{Re}\Sigma = 0.7E$ corresponding to a mass enhancement $m^*/m_0 = 1.7$, where m_0 is the single-particle mass (see section 2.1.6). This experimental mass renormalization in the energy range $\text{BE} \leq 1.8$ eV should be contrasted to the theoretical $m^*/m_0 \approx 1.25$ derived from DMFT calculations for $U=1.5$ eV in the present work. One may speculate that the difference between the ARPES and the LSDA+DMFT+1SM peak positions could be reduced by choosing a higher U value (e.g., $U \approx 3$ eV). This value, however, is outside the previously mentioned range, and in addition, we still are left with the problem that the calculated width is far too small compared with the experimental value. This is further demonstrated in Fig. 4.7(b), where U -dependent LSDA+DMFT+1SM calculations for U ranging from 1.5 to 3 eV are shown. It is important to remark that the width of the peaks does not increase with increasing U . This can be explained in terms of an energy-dependent $\text{Im}\Sigma$ together with the fact

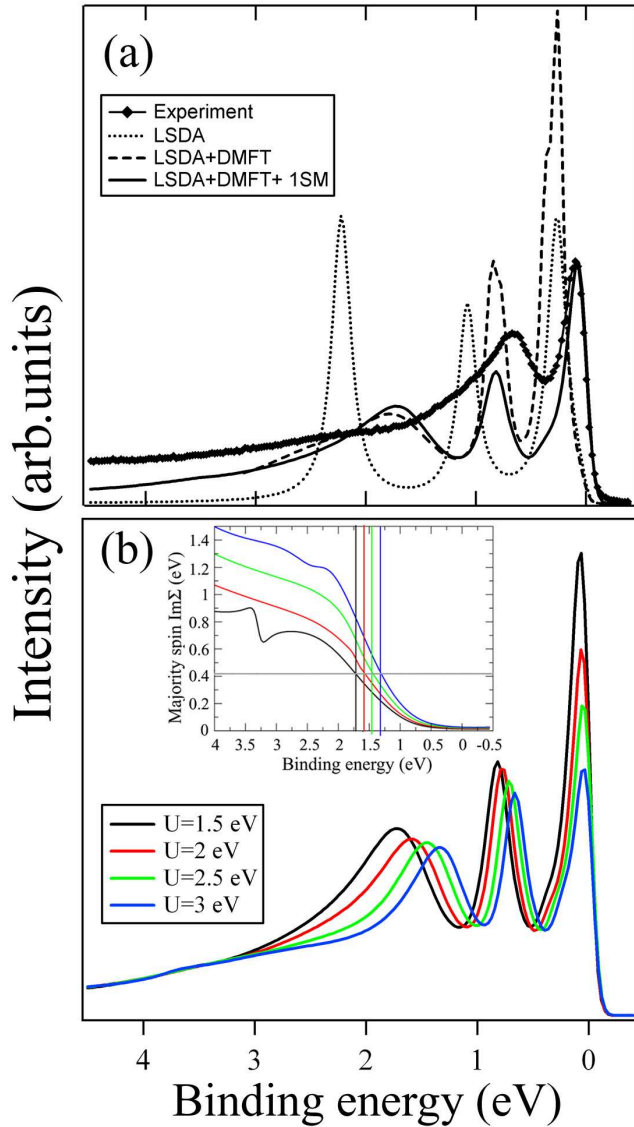


Figure 4.7: (a) Comparison between the spin-integrated experimental spectra at the Γ point for p -polarization with the single-particle LSDA-based calculation, the LSDA+DMFT spectra, and the LSDA+DMFT+1SM spectra. (b) U -dependent LSDA+DMFT+1SM calculations for $U=1.5$ to 3 eV. Inset: corresponding majority spin $\text{Im}\Sigma_{DMFT}$, together with vertical lines indicating the BE energy shift of the $\Sigma_{1,3}^{\uparrow}$ bands. The horizontal line shows how the peak widths do not increase with increasing U .

that with increasing U , the peak positions move to lower BE leading to an almost constant $\text{Im}\Sigma$. The energy dependence of $\text{Im}\Sigma$ also leads to slightly asymmetric peaks in the spectral function, an effect that manifests itself in the LSDA+DMFT+1SM calculations as well. This effect is more pronounced for higher binding energies than for lower ones and in particular for the $\Sigma_{1,3}^{\uparrow}$ majority spin bands discussed above, which in the case of Fig. 4.7(b) appear at a BE of about 1.7 eV for $U=1.5$ eV and shift to a BE of ~ 1.3 eV with increasing U up to 3 eV. For more quantitative details, in the inset of Fig. 4.7(b) the majority spin $\text{Im}\Sigma_{DMFT}$ is shown for different U values, where vertical lines indicate the BE energy shift of the $\Sigma_{1,3}^{\uparrow}$ majority spin bands. While $\text{Im}\Sigma_{DMFT}$ increases since correlation effects are stronger for larger U values, the horizontal line demonstrates how the width of these peaks does not increase with increasing U . In this case, with U -dependent peak positions of 1.72 eV ($U=1.5$ eV), 1.60 eV ($U=2$ eV), 1.45 eV ($U=2.5$ eV) and 1.32 eV ($U=3$ eV) a majority spin $\text{Im}\Sigma_{DMFT} = 0.42$ eV is obtained, which means that the lifetime around the peak maxima of the $\Sigma_{1,3}^{\uparrow}$ bands is

nearly identical for all U-values. Additionally, due to the strong energy dependence of $\text{Im}\Sigma_{DMFT}$ which increases almost linearly with increasing BE, the peaks appear with a more asymmetric profile for U=1.5 eV. This type of argumentation can be applied to all peaks that appear in the spectra.

It should be pointed out that the additional broadening observed in the experiment cannot be caused by final state effects, since those are fully taken into account in the 1SM calculations. Furthermore, since the 3d bands show a rather flat dispersion, in particular, close to the high symmetry points of the BBZ, the final state broadening (see section 2.1.4) can almost be neglected when compared with the experimental energy resolution. Moreover, the final state effects would cause a broadening which for a small initial state dispersion would be constant as a function of the BE. In this context, the broadening due to scattering with defects can be excluded since it is energy independent as well. In general, the additional experimental broadening can be observed when comparing all the theoretical and experimental photoemission spectra presented here, i.e. not only at the Γ point but also at all the other measured k-values.

4.4.1.3 Spin-dependent quasiparticle lifetimes

In the following we would like to obtain more quantitative information on the discrepancy between experiment and theory we have observed concerning the linewidths. As mentioned before, a fitting procedure was used to extract the experimental peak positions from SARPES experiments shown in Fig. 4.6. This evaluation is also useful for determining by how much the theoretical linewidths are underestimated compared to the experimental results. The need of spin-resolution is remarkably important in this case because from the spin-dependent behaviour of the self-energy in the theoretical calculations one would expect the contribution to experimental linewidths of the initial states to be spin-dependent as well.

The spin-resolved spectra were fitted at various k values by a sum of Lorentzians plus a background. In Fig. 4.8, the results of the fits of the SARPES data obtained by this procedure are presented. We should keep in mind that such an evaluation is problematic due to the strong energy-dependence of $\text{Im}\Sigma$ which leads to the formation of asymmetric Lorentzians, as discussed above. The appearance of such an asymmetry can be associated with the damping of quasiparticle excitations and the corresponding increase of the incoherent part of the spectral function with increasing BE. However, at energies close enough to the Fermi level, we would expect this asymmetry to be strongly reduced since most of the peaks are due to coherent excitations which correspond to quasiparticles with well-defined energy and momentum. More in particular, in the spectra from Fig. 4.7(b) it can be observed that the peaks are less asymmetric for energies smaller than 1 eV, so most of the deviations are expected to increase for binding energies larger than 1 eV. In each fit in Fig. 4.8, the number of peaks used and their initial state symmetries correspond to the peak assignments shown in Figs. 4.4 and 4.5. For the fitting procedure an experimental approach has been adopted: this means that if due to energy resolution or extra broadening two bands which are energetically very close to each other in the theoretical calculations cannot be resolved in the experiment, only one experimental peak has been considered for the fit. However, exceptions to this rule can only be confirmed experimentally through the polarization dependence of the

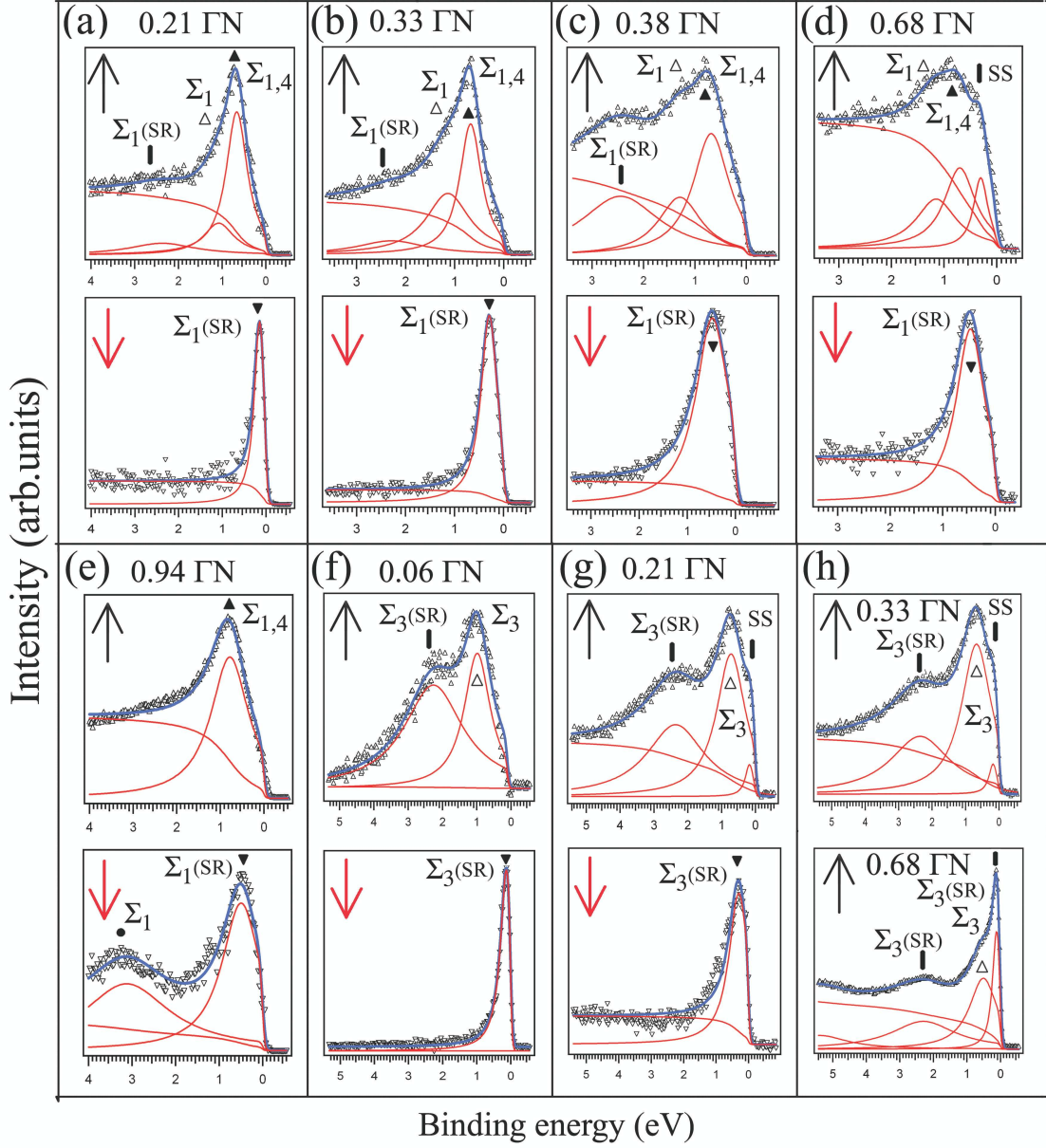


Figure 4.8: Fits to spin-resolved valence band spectra at various k -points of the bcc Fe Brillouin zone obtained by using Eq. (4.4). (a)-(e): p -polarization, (f)-(h): s -polarization. Up arrows (down arrows) for majority (minority) spin spectra. Note that in (h) only fits to majority spin data are shown since for $x=0.33 \Gamma N$ and $0.68 \Gamma N$ the corresponding minority spin bands have crossed the Fermi level.

SARPES spectra. For example: close to the Γ point, where most of the transitions are degenerated, we observe that the $\Sigma_{1,3}^\uparrow$ peak which for s -polarization data in Fig. 4.5(b) appears at a BE of about 1.2 eV causes for p -polarization data in Fig. 4.5(a) a shoulder at that energy. The observed difference in the relative intensities can be attributed to matrix-element effects since for s - and p -polarization we are more sensitive to the Σ_3^\uparrow and Σ_1^\uparrow components of this degenerated peak, respectively. Therefore, in the fits of the

majority spin SARPES spectra shown in Figs. 4.8(a)-4.8(c) for p-polarization, where the main contribution comes from the $\Sigma_{1,4}^\uparrow$ peak closer to the Fermi level which is almost perfectly resolved experimentally, an additional peak has been introduced to fit the shoulder at the higher BE side of this peak. When moving away from the Γ point, this shoulder can also be distinguished in the spin-integrated spectra of Fig. 4.4(a) for p-polarization. Finally, it should be noted that the spin-integrated spectra were measured with slightly better energy resolution than the SARPES measurements since due to the higher intensity reaching the channeltron detectors it was possible to slightly close the exit slit of the monochromator. This also increased the intensity of the peak at 2.2 eV BE in Fig. 4.4(a), while in the SARPES measurements with p-polarized photons it is slightly reduced due to the larger noise to intensity ratio detected in the signal.

The fitting procedure works as follows. For a particular \mathbf{k} -point, a SARPES spectrum containing N peaks is fitted by a function involving a convolution of the form:

$$I_k^{\uparrow,\downarrow}(E) = \left(f(E, T) \cdot \sum_{i=1}^N M_i^2 \cdot A_{ki}(E_i, \omega_i) + B_k(E) \right) \otimes G(h\nu) \quad (4.4)$$

where E_i , ω_i and the matrix-elements M_i are fitting parameters corresponding to the BE, width and intensity of the quasiparticle peaks for different polarizations. The Fermi function $f(E, T)$ is evaluated at room temperature, the spectral function $A_{ki}(E_i, \omega_i)$ approximated by Lorentzian functions and $B_k(E)$ assumed to be a Shirley-like background [163]. Here the subindex k denotes the \mathbf{k}_\perp points. The FWHM of the Gaussian slit function $G(h\nu)$ corresponds to the total energy resolution ΔE_{tot} of the experiment, which is photon energy-dependent, i.e.:

$$\Delta E_{tot} = \sqrt{(\Delta E_a)^2 + (\Delta E_{h\nu})^2} \quad (4.5)$$

where ΔE_a and $\Delta E_{h\nu}$ are the energy resolution of the electron energy analyzer and beamline monochromator, respectively. The Shirley-like background $B_k(E)$, which accounts for the effect of the inelastic scattering of electrons, is calculated as:

$$B_k(E) = C \cdot \left(\int_{E_0}^{\infty} dE \cdot \sum_{i=1}^N M_i^2 \cdot A_{ki}(E_i, \omega_i) \right) \quad (4.6)$$

where C is a fitting constant and the integration is done over all the spectrum with E as a running parameter over the kinetic energy (KE) axis. The reason to use Eq.(4.6) for the background correction is that in a first approximation, photoelectrons generated at a KE close to a peak maximum and deep enough in the material to escape without losing kinetic energy contribute with more intensity in the higher BE side of the peak than in the lower one. In other words, if each electron acts as a source for scattered electrons, the background at any KE in the spectrum is proportional to the total number of electrons with more than that KE. This means that at a given energy E_0 , the background is proportional to the sum of the areas under each quasiparticle peak obtained after integration over all kinetic energies equal or higher than E_0 .

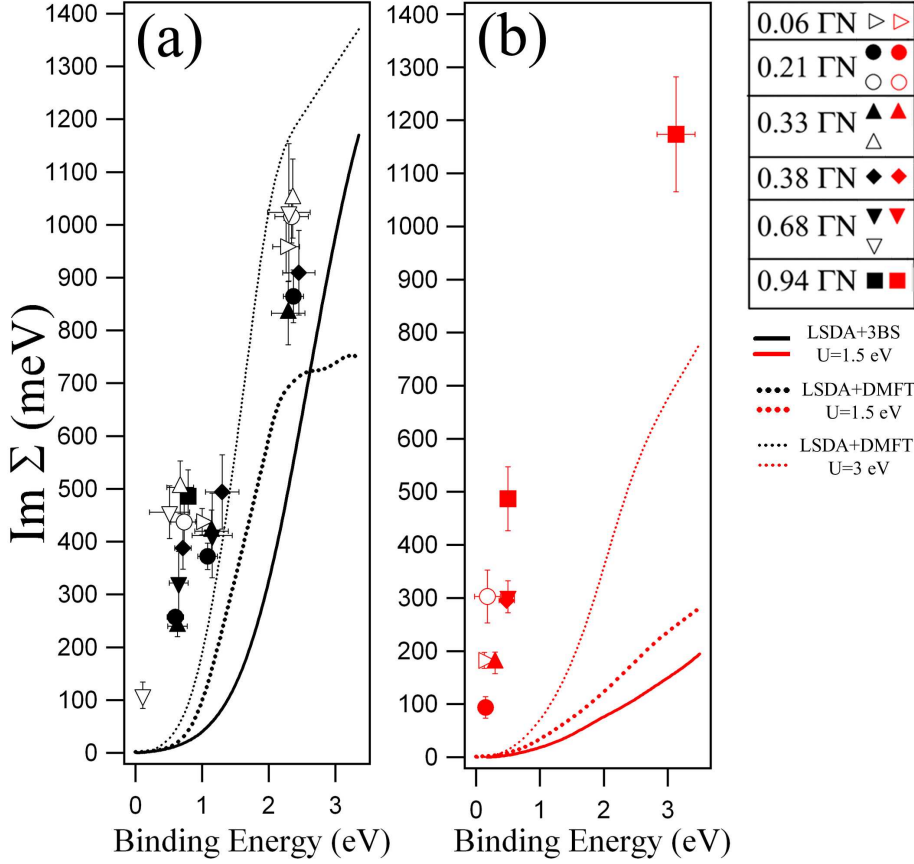


Figure 4.9: Comparison between the experimental and theoretical imaginary part of the self-energy of bcc Fe(110) for (a) majority (black color) and (b) minority (red color) spin electrons. The experimental data points were obtained from the half-width at half-maximum of the photoemission peaks after a correction for non-electronic contributions (see text). Labels to identify the different k -points are also given. The theoretical calculations correspond to $\text{Im}\Sigma_{DMFT}$ for $U=1.5$ eV (thick dotted lines) and $U=3$ eV (thin dotted lines) and to $\text{Im}\Sigma_{3BS}$ for $U=1.5$ eV (solid lines).

From this evaluation we have tried to extract the spin-dependent experimental $\text{Im}\Sigma_{exp}$ as a function of BE and $k=|\mathbf{k}_\perp|$. The results are shown in Fig. 4.9 for majority (Fig. 4.9(a)) and minority (Fig. 4.9(b)) spin electrons, together with the theoretical calculations of $\text{Im}\Sigma_{DMFT}$ ($U=1.5$ and 3 eV) and $\text{Im}\Sigma_{3BS}$ ($U=1.5$) for comparison. Once again, it is clear that concerning the linewidths, no quantitative agreement between the theoretical calculations and the experimental data is observed. In the experimental results, we obtain in a first approximation a k -independent $\text{Im}\Sigma_{Exp}$ which exhibits an almost linear energy-dependent behaviour ($\text{Im}\Sigma_{Exp} \sim 0.4E$) for both spin channels, similar to previous inverse photoemission studies [105]. The error bars have been extracted from the deviation between several fitting cycles in each spectrum and a simultaneous χ^2 minimization. Each one of the experimental data points shown in Fig. 4.9 has been obtained by subtracting most of the contributions to the broadening from the fitted linewidth values which do not have electronic origin. The only

extra contribution which is still present in the experimental data is due to electron-impurity scattering ($\text{Im}\Sigma_{imp} = \Gamma_{imp}/2$) since it can only be determined once all the other contributions have been corrected.

The theoretical calculations, on the other hand, only contain the electronic contribution. Since the broadening due to energy resolution is already included in the fitting procedure, the other experimental corrections are due to electron-phonon broadening (Γ_{e-ph}) and final-state broadening (Γ_f), where $\Gamma=2\text{Im}\Sigma$ is the scattering rate. In general, all these contributions add linearly and give the total scattering rate Γ_t such that

$$\Gamma_t = \Gamma_{e-e} + \Gamma_{e-ph} + \Gamma_{imp} + \Gamma_f \quad (4.7)$$

where Γ_{e-e} indicates the contribution to the linewidth due to electron-electron scattering. In the Debye model and for the high temperature limit [56, 164], the electron-phonon broadening depends linearly on the temperature T as:

$$\Gamma_{e-ph} = 2\text{Im}\Sigma_{e-ph} = 2\pi\lambda k_B T \quad (4.8)$$

where k_B and λ are the Boltzmann and electron-phonon coupling constants. Eq. (4.8) holds for temperatures $T \geq T_{Debye}/3$ (here $T=300$ K and $T_{Debye}(\text{Fe})=460$ K). From resistivity measurements we know that for Fe $\lambda \approx 0.34$ [165] and as a result $\text{Im}\Sigma_{e-ph} \approx 27$ meV.

The final state broadening contribution was also calculated in detail by using Eqs. (2.19) and (2.20) (section 2.1.4) [60]. Firstly, the initial state velocities were calculated from the derivative of the $E(\mathbf{k}_\perp)$ dispersions of the different majority and minority spin bands. Secondly, the IMFP values for the photon energies used were taken from the semiempirical estimation given by Penn [166] and available reference data [167]. In general, due to the relatively flat dispersions of the d bands, a maximum ratio $|v_{i\perp}/v_{f\perp}| \approx 0.04$ was obtained, equivalent to a maximum contribution to $\text{Im}\Sigma_{exp}$ of about 60 meV. This indicates that final-state effects are not the main broadening mechanism, as mentioned before.

Finally the electron-impurity scattering, an energy and temperature-independent quantity, can be directly estimated from Fig. 4.9 as an average for both spin channels. It corresponds to the value of $\text{Im}\Sigma_{Exp}$ exactly at the Fermi level position, and by extrapolation it amounts to $\text{Im}\Sigma_{imp} \sim 70$ meV. Note that the experimental results in Fig. 4.9 can be directly identified with the spin-dependent photohole inverse lifetimes if this constant value is subtracted from the data.

Coming back to the linewidths observed in Fig. 4.9, it is clear that the experimental results do not support the existence of a spin-dependent effect in the quasiparticle lifetimes, opposite to what is observed in the calculations. Furthermore, due to the large experimental broadening, the experimental $\text{Im}\Sigma$ is in average about a factor of three bigger than the calculated one for $U=1.5$ eV, and about a factor of two bigger for $U= 3$ eV. The discrepancy is more pronounced in the minority spin channel. This may indicate that in a weak ferromagnet like Fe, scattering processes involving minority spin electrons which lead to the creation of majority spin electron-hole pairs could play a role. Although further work is still needed to determine the origin of these strong differences, another possible explanation could be that in Fe there is a strong con-

tribution from non-local correlation effects. Such non-locality is caused by long-range electron-electron interactions, which are excluded from the Hubbard model. Thus, non-local effects would contribute with an additional correction to the self-energy functions Σ_{DMFT} or Σ_{3BS} . This would result in second-order variations in the calculated $\text{Re}\Sigma$ and $\text{Im}\Sigma$, which may lead to a better agreement between theory and experiment. The possibility that non-local correlation effects can have a certain influence on the intermediate energy states is closely related to the results presented in [153]. The authors of this work made an experimental evaluation of the effective mass of Fe in different points of the Brillouin zone, and found a strong k-dependence (up to 4 times difference between different points of the BBZ). From the results shown here, we conclude that these effects could also be important for higher binding energies. However, they are beyond the local many-body theories used in this work.

4.4.2 hcp Co(0001)

4.4.2.1 Spin and angle-resolved photoemission

A similar study as the one presented for bcc Fe(110) in previous section has been carried out for the hcp Co(0001) system, mainly because a clear conclusion about the role of correlation effects in this system has not yet been reached. Although in the case of Co several photoemission studies exist in the literature since the beginning of the 80s [99, 107, 139, 141, 168–171], only a few are devoted to a detailed comparison between many-body calculations and experiments [107, 111, 170].

Most recently, by comparing experimental photoemission spectra of fcc Co with the calculated LSDA+3BS spectral functions, it has been found that because of many-body effects no sharp quasiparticle peaks exist for binding energies larger than 2 eV in this system [111]. Interestingly, this effect has been theoretically explained by the existence of strong correlation effects which could particularly affect majority spin electrons [111], leading to a more pronounced renormalization of the majority spin quasiparticle spectral weight when compared to its minority counterpart. However, these conclusions were not supported by experiments involving spin resolution. On the contrary, it has been shown in a very recent photoemission experiment on a hcp Co bulk single crystal with out-of-plane magnetization [137] that for sufficiently high photon energies (488–654 eV), the spectral peak widths become narrower than previously observed in low-energy experiments and in consequence, quasiparticle bands of weak intensity can be observed even at binding energies larger than 3 eV. This effect has been attributed to the significant reduction of the final-state broadening contribution in the measured linewidths at this photon energy range. In addition, a detailed analysis of the linewidths of the photoemission peaks revealed excellent agreement between the experimental imaginary part of the self-energy and the one provided by LSDA+DMFT calculations [157]. Although this conclusion was supported for both majority and minority spin electrons, once again, no spin resolution was provided in these experiments to decompose overlapping contributions.

In this section, in contrast to earlier studies, we would like to exploit the use of spin resolution in order to give a experimental and theoretical corroboration to previous findings. Our system under study, as described in previous sections, is an ul-

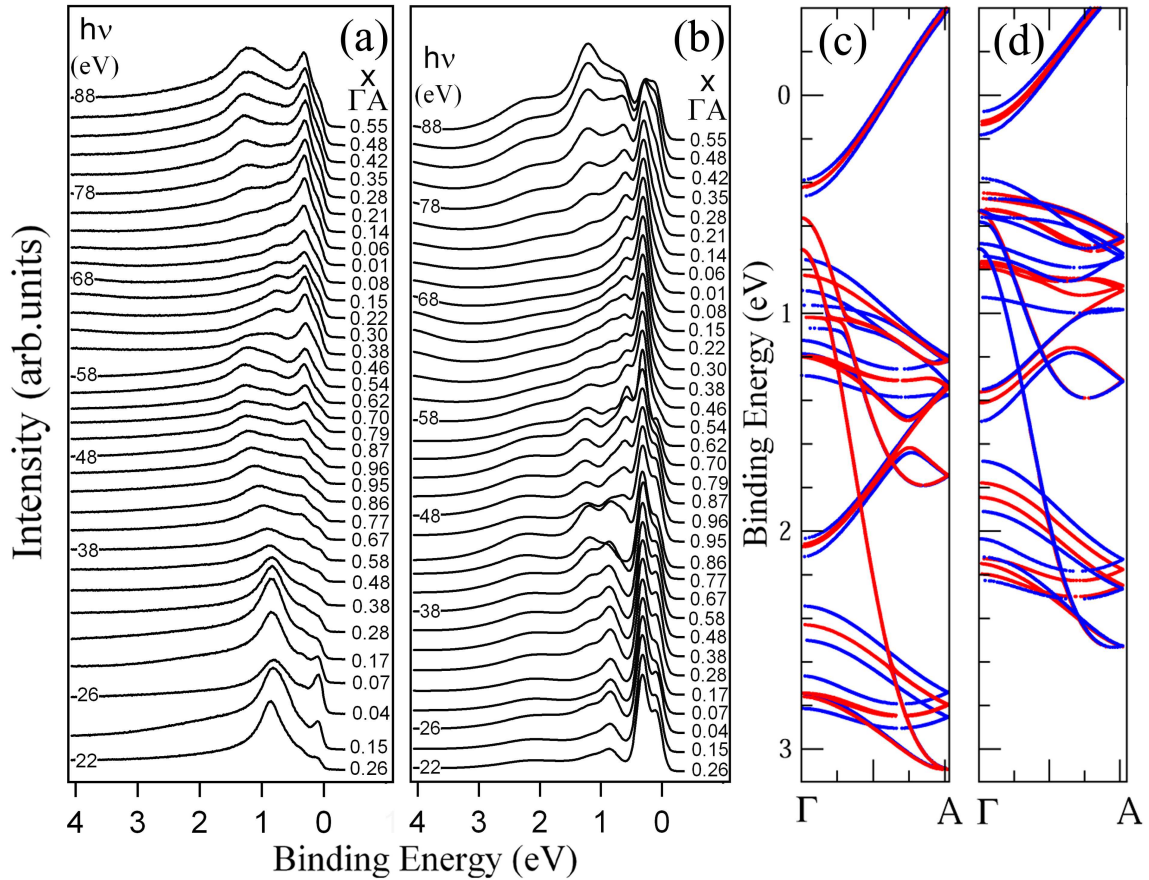


Figure 4.10: (a) *Experimental spin-integrated photoemission spectra of hcp Co(0001) measured with p polarization in normal-emission along the ΓA direction of the bulk Brillouin zone at different excitation energies (steps of 2 eV). On the left, selected photon energies are given. On the right, the curves are labeled by wavevectors in units of $\Gamma A=0.77\text{\AA}^{-1}$ (Γ point at $x=0$ and A point at $x=1$).* (b) *Corresponding calculation obtained by the LSDA+DMFT+1SM method for hcp Co with an in-plane magnetization along the $[1\bar{1}00]$ direction.* (c) and (d): *Spin-integrated band structure calculations for two configurations of the magnetization, out-of-plane (along $[0001]$ direction, blue lines) and in-plane (along $[1\bar{1}00]$ direction, red lines). In (c), LSDA calculations are shown, and in (d) fully relativistic valence band states obtained self-consistently in the SPRKKR formalism by suppressing the imaginary part of the self-energy $\text{Im}\Sigma_{\text{DMFT}}$.*

trathin hexagonal close packed Co film of about 20 ML thickness with an in-plane magnetization [138, 139]. This gives only a slightly different scenario as the one studied in [111, 137]. Figs. 4.10(a) and 4.10(b) show a comparison between the spin-integrated experimental spectra of hcp Co(0001) and the corresponding theoretical LSDA+DMFT+1SM calculations for p-polarization along the ΓA direction of the bulk Brillouin zone. The best correspondence between the BE positions of the experimental and theoretical peaks was found for values of the averaged on-site Coulomb and exchange interactions of $U=2.5$ eV and $J=0.9$ eV, in agreement with previous theoretical and experimental studies [111, 157]. Therefore, unless specified, these have been the

parameters of choice in all the calculations presented here. Figures 4.10(c) and 4.10(d) show LSDA and fully-relativistic LSDA+DMFT calculations of the spin-integrated spectral functions $A(\mathbf{k}, E)$ for different directions of the sample magnetization (along the out-of-plane $[0001]$ and in-plane $[1\bar{1}00]$ directions (blue and red lines, respectively). It can be observed how the different bands shift between Figs. 4.10(c) and 4.10(d) towards lower binding energies due to electron correlation effects for both magnetization orientations. With the exception of the data shown in Figs. 4.10(c) and 4.10(d) for out-of-plane magnetization, all the calculations in the present chapter have been performed for a system with an in-plane magnetization, in agreement with the experimental configuration. The out-of-plane calculations are shown in order to emphasize how due to spin-orbit coupling effects, changes in the orientation of the magnetization correspond to changes in the electronic structure of hcp Co. This purely relativistic effect [172–174] may gain importance if e.g., experimental and theoretical spectra of hcp Co bulk single crystals [137, 168] and overlayers [111, 139] need to be compared. A much weaker effect of this kind was also theoretically obtained in the case of bcc Fe(110) (thus not shown in the preceding section), in agreement with previous calculations [172]. This is because in hcp Co, due to the hexagonal structure, the magnetocrystalline anisotropy energy (E_{MAE}) is larger than in bcc Fe(110). To a first approximation, E_{MAE} is given by the average energy difference between the BE positions of the bands in Figs. 4.10(c) and 4.10(d) with in-plane and out-of-plane magnetization directions, respectively. The overall effect of the magnetic anisotropy on the band structure results in slight changes in the dispersion behaviour of some bands, additional BE shifts and most importantly, a considerable reduction of the spin-orbit splitting with an in-plane magnetization configuration. In this case, near the Fermi level and below 2 eV, most of the bands are degenerated while in the out-of-plane configuration, the spin-orbit splitting is ~ 0.1 eV in average, a value of the order of the experimental resolution. In principle this means that relatively narrower peaks would be expected in photoemission experiments with an in-plane configuration of the magnetization, as it is the case of Co overlayers rather than hcp Co bulk single crystals.

In Fig. 4.11, similar data to the ones presented in Figs. 4.10(a) and 4.10(b) are shown, but now at a few selected photon energies and spin resolved. Figures 4.11(a) and 4.11(b) show experimental spin-resolved spectra for p- and s-polarized photons, respectively, while Figs. 4.11(c) and 4.11(d) show the corresponding LSDA+DMFT+1SM calculations. The k -values were calculated from the measured photon energies, ranging from 22 to 80 eV and using an inner potential $V_0=14.8$ eV.

In contrast to previous studies in hcp Co [168] where the non-relativistic notation for fcc crystals was used to label the symmetry of the observed states, from now on we will follow the relativistic notation given by Benbow [62] for hcp crystals. Although this notation has not often been used in the literature, it is much simpler since due to the lower symmetry it only involves initial and final states of Δ_7 , Δ_8 and Δ_9 symmetries. This means that in the geometry used in the experiment (Figs. 4.2(a), 4.2(e)-4.2(g)) and due to selection rules, only transitions of Δ_7 and Δ_8 symmetries are suppressed for s-polarization when moving from Γ to A and from A to Γ in the next Brillouin zone, respectively. Hence, only transitions of Δ_9 symmetry can be observed with s-polarized photons. This effect of matrix-elements is also influenced by the symmetry of the

hcp crystal structure, which leads to a Brillouin zone-selection rule similar to the one reported in [175]. The symmetry is closely related to the close-packed arrangement of the atoms in the hexagonal structure, which follows an *ABABAB* arrangement of subsequent layers [56]. Therefore, to follow the nearest-neighbors of a given atom along the stacking direction or vertical *c*-axis, one needs an extra lattice vector which in a stack of many layers will follow a zig-zag configuration. This reduction in the translational symmetry due to zig-zag arrangement, which is characteristic of the hcp structure, suppresses the intensities of certain bands in a particular Brillouin zone but increases them in the next-higher one and so on. If this interference effect is combined with the optical selection rules mentioned above, the overall effect results in a bandstructure which is equivalent to the one of the fcc crystal if all the bands are unfolded back around the A point [168]. This also implies that states of Δ_7 and Δ_8 symmetry should be interchanged when crossing the A point while states of Δ_9 symmetry remain unaffected.

Let us now discuss the quality of the agreement between the theoretical and experimental spectra shown in Figs. 4.10 and 4.11. The first observation is that we find rather good agreement for most of the BE positions of the peaks appearing in the spectra. Note that this is a surprisingly different situation as compared to Fe, in which it was not possible to give a definite statement about the strength of electron correlation effects due to the larger deviations in the energetic positions of the different peaks [176]. The second observation, concerning the linewidths, is that the larger broadening of the experimental peaks indicates that the theory underestimates the scattering rates, similar to what was found in the Fe case [176]. From these two observations we may already conclude that in Co non-local correlations are also needed to properly describe the experimental photoemission spectra in the low BE range studied here. In this respect, it should be emphasized that our results, for both Fe and Co systems, do not imply a violation of the Kramers-Kronig consistency [37, 38] which holds between the real and imaginary parts of the self-energy, neither in the experiment nor in the theoretical calculations. This is because the Kramers-Kronig consistency results from a global transformation over an extremely large BE range, which runs up to infinity. This means that in the narrow BE energy interval studied here, the deviations between the experimental and theoretical self-energies may become substantial without any appreciable effect on the global behavior of the Kramers-Kronig transformation. To check this more in detail experimentally, time-consuming measurements over an extremely wide BE range would be necessary.

The third observation, in contrast to recent experimental conclusions [137], is that no quasiparticle bands derived from 3d states appear at binding energies higher than ~ 2 eV. At around 2 eV, this effect is even more pronounced in the experiment than in the theory due to the increased linewidth broadening mentioned above. This finding is in agreement with previous experimental and theoretical analysis in the framework of the 3BS theory [111], in which the quenching or intensity reduction of the majority spin channel quasiparticle excitations was identified as the main mechanism for this intriguing effect. Our results corroborate this conclusion in view of the spin-resolved experimental and theoretical spectra presented in Fig. 4.11. Only peaks with strong sp character are observed at higher BE energies than 2 eV, such as the minority spin sp-

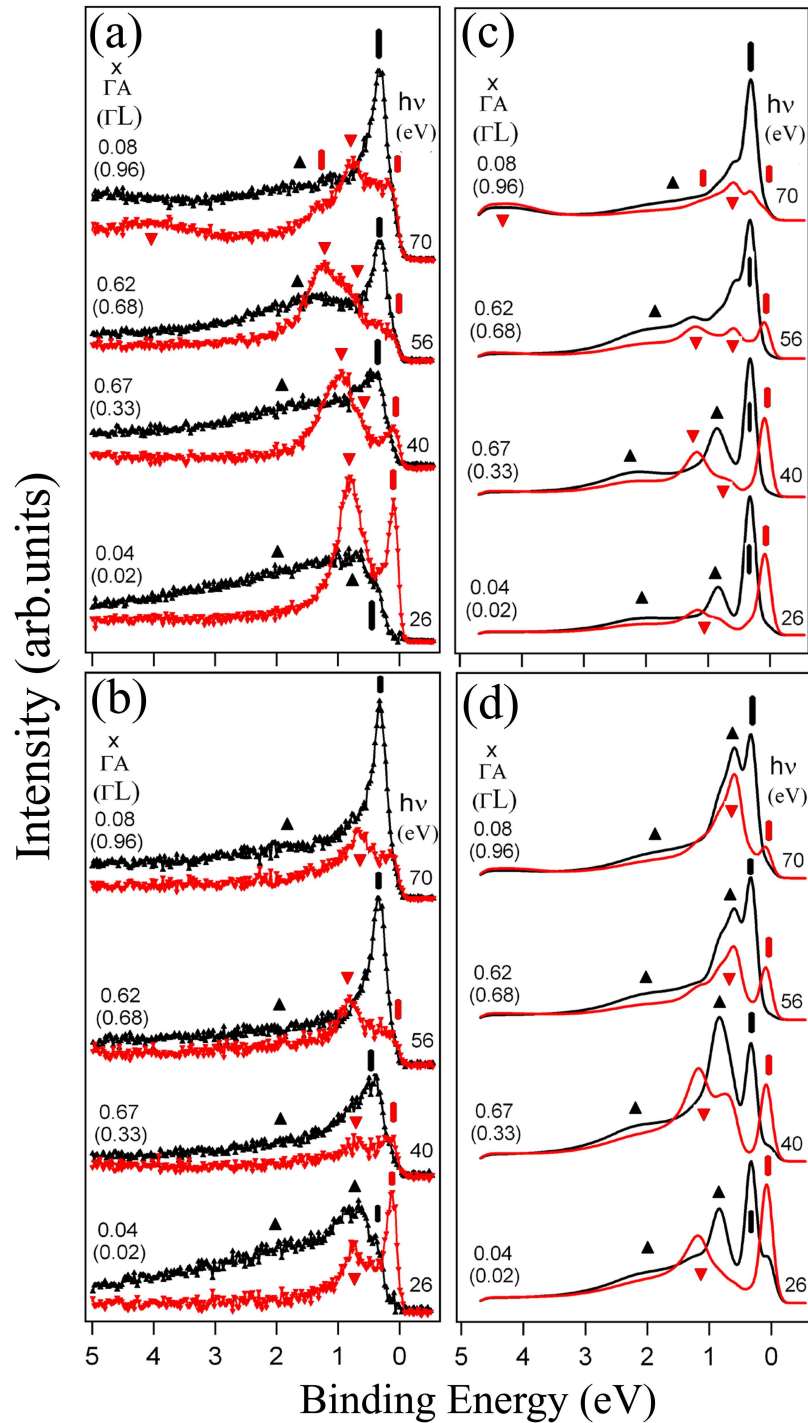


Figure 4.11: Spin-resolved spectra of hcp Co for different light polarizations. (a), (b) Experiment (black small upwards triangles: majority spin states, red small downwards triangles: minority spin spectra). (c), (d): LSDA+DMFT+1SM theory (black and red lines for majority and minority spin electrons, respectively). (a),(c) for p- and (b), (d) for s- polarization. Additional black large upwards (red large downwards) triangles above the spectra indicate majority (minority) bulk states, while vertical black (red) bars majority (minority) spin surface-related features. The curves are labeled by the photon energies (right) and the wavevectors (left) for both the hcp ($\Gamma A=0.77\text{\AA}^{-1}$) and fcc ($\Gamma L=1.54\text{\AA}^{-1}$) lattices for comparison.

band of Δ_8^\downarrow symmetry appearing at $k \sim 0.08 \Gamma A$ ($h\nu = 70 \text{ eV}$) in Fig. 4.11(a) and at a BE of about 4.3 eV for p-polarization. Note that in the corresponding calculated spectrum of Fig. 4.11(c), the sp-band appears somehow broadened as compared to what was found in Fe calculations, although no correction due to electronic correlations has been applied to the sp-states in the LSDA+DMFT+1SM spectra. Thus, we attribute this to intrinsic differences in initial and final-state dispersions of these bands between the two materials.

Now we will focus on the origin of the different transitions appearing in the theoretical and experimental spectra of Figs. 4.10 and 4.11, from lower to higher binding energies. All the peaks appearing near the Fermi level in the full photon energy range and for a BE lower than $E_B \sim 0.5 \text{ eV}$, can be attributed to the two majority and minority spin components of a Tamm-like surface feature, in agreement with previous experimental observations [171]. Closest to the Fermi level, the minority spin component of this state appears at $E_B \sim 0.05 \text{ eV}$, and it can be identified as a pure surface state of Δ_9^\downarrow symmetry, since it lies within the gap appearing near the Fermi level and its intensity is nearly the same for both p- and s-polarized photons (see Fig. 4.11). Only near the first Γ point and at $x \sim 0.04 \Gamma A$ ($h\nu = 26 \text{ eV}$), this peak is slightly influenced by the minority spin bulk-like band of $\Delta_{9,7}^\downarrow$ symmetry⁶ crossing the Fermi level. Thus, only at this photon energy it acquires a slightly bulk-like character and it can be identified as a surface resonance feature. A similar argumentation can be used for the majority spin component of the abovementioned surface-like Tamm state, which can be identified as a surface resonance feature of $\Delta_{9,7}^\uparrow$ symmetry (or equivalently, $\Delta_{9,8}^\uparrow$ symmetry in the next Brillouin zone), since it is located at the border of the gap and almost degenerated with the majority bulk bands appearing around the same BE. This state, which appears at $E_B \sim 0.4 \text{ eV}$, can be observed as a non-dispersing feature in the full photon energy range (Figs. 4.10(a) and 4.10(b)). However, when moving in the experiment from Γ to A in a photon energy range between 26 and 38 eV ($0.04 \leq x \leq 0.58$) (Fig. 5.10(a)), its intensity is much weaker as compared to the theoretical calculations (Figs. 4.10(b)). This can also be noticed in the results of Fig. 4.11 near the Γ point ($x \sim 0.08 \Gamma A$, $h\nu = 26 \text{ eV}$) for both p and s polarizations. In this case it can be observed as a majority spin shoulder close to the Fermi level, but in the theoretical spectra as a sharp peak. Since in the calculations its intensity does not seem to be strongly influenced by matrix-element effects and in addition it exhibits a significantly narrower linewidth, we attribute these strong differences to a theoretical underestimation of the multiple scattering events occurring between the surface and the bulk electron wavefunctions. Moreover, the intensity of this peak is strongly enhanced at higher energies in the experiment (Fig. 4.10(a)), particularly when moving from around the A point ($x \sim 0.98 \Gamma A$, $h\nu = 48 \text{ eV}$) to the second Γ point ($x \sim 0.01 \Gamma A$, $h\nu = 72 \text{ eV}$) and beyond. This increase in intensity can be attributed, on the one hand, to a slightly reduced surface sensitivity at higher photon energies, and on the other hand, to the contribution of the nearly-flat majority spin bulk-like band of $\Delta_{9,8}^\uparrow$ symmetry

⁶Note that the subscript notation of almost degenerated states always follows their order of appearance from lower to higher binding energies. To avoid redundancy, from now on and unless specified, double subscripts will be adopted for most of the bands independently of the light polarization. In this context, it should be kept in mind that only states of Δ_9 symmetry can be observed with s-polarization.

appearing around the same BE for photon energies $h\nu > 48$ eV. Note once again that due to the symmetry arguments mentioned above, for $h\nu \leq 48$ eV this bulk band has $\Delta_{9,7}^\uparrow$ symmetry⁷ and is located at a BE of about 0.7 eV near the first Γ point ($h\nu=26$ eV) (Fig. 4.11).

All the other bands that are left to describe are bulk-like and appear at a BE higher than ~ 0.5 eV for all the measured k-points. Firstly, we observe a minority spin band of $\Delta_{9,7}^\downarrow$ symmetry located in the experiment at $E_B \sim 0.8$ eV in the first Γ point (Figs. 4.10(a), 4.11(a) and 4.11(b)). Through the polarization dependence of the experimental spin-resolved data (Figs. 4.11(a) and 4.11(b)), it is possible to see that this band comprises several components which are all degenerated at the first Γ point. These components slightly disperse when the photon energy is increased, giving rise to shoulders which can be detected through polarization-dependent analysis. Most prominently, at $x=0.67\Gamma A$ ($h\nu=40$ eV) a minority spin shoulder at a BE of about 0.75 eV can be clearly distinguished in the lower BE energy side of the peak appearing at $E_B \sim 0.95$ eV for p-polarization data (Fig. 4.11(a)). Detailed analysis reveals that the BE position of this shoulder exactly coincides with the minority spin peak of Δ_9^\downarrow symmetry appearing in the corresponding spectrum for s-polarization (Fig. 4.11(b)). Further information on the symmetry of these states can be obtained from a comparison to the spin-resolved theoretical spectra of Figs. 4.11(c) and 4.11(d). In particular, it can be demonstrated that the peak appearing at 0.95 eV must be assigned to a state of Δ_7^\downarrow symmetry, and the shoulder to a state of $\Delta_{7,9}^\downarrow$ symmetry. A similar effect occurs at higher photon energies in the next Brillouin zone e.g. at $x=0.62\Gamma A$ ($h\nu=56$ eV), where the peak at $E_B \sim 1.2$ eV and the shoulder at $E_B \sim 0.8$ eV can be assigned to bands of Δ_8^\downarrow and $\Delta_{8,9}^\downarrow$ symmetries, respectively. In the next Γ point and at $x=0.08\Gamma A$ ($h\nu=70$ eV), the peaks show the same behaviour, with the difference that a weak shoulder appears at $E_B \sim 1.5$ eV, exactly in the higher BE side of the bulk-like $\Delta_{8,9}^\downarrow$ state located at $E_B \sim 0.8$ eV. Only by means of a detailed comparison to the theoretical spectra of Fig. 4.11(b), we can attribute this feature to a $\Delta_{8,9}^\downarrow$ surface resonance. The fact that it was not visible at lower photon energies is possibly related to the dispersion of the bulk-like minority spin peaks we have just discussed. Besides, this may also be related to the very short lifetime of surface resonance features at higher BE caused by the strong increase of $\text{Im}\Sigma_{DMFT}$ and the resulting very large broadening which makes it impossible to properly distinguish them in the experiment.

At last, we are only left with the majority spin bulk-like states at higher BE. These peaks are strongly broadened and more difficult to distinguish in the experiment, more in particular in the spectra of Fig. 4.10(a) due to the scaling of the intensities. Nevertheless, with the use of spin resolution they become clearly visible in a BE range from about 1.7 to 1.9 eV mostly for p-polarization data in Fig. 4.11(a) at $x=0.67\Gamma A$ ($h\nu=40$ eV) and $x=0.62\Gamma A$ ($h\nu=56$ eV), and for s-polarization data in Fig. 4.11(b) near the first Γ point at $x=0.04\Gamma A$ ($h\nu=26$ eV). In the calculations (Figs. 4.11(c) and 4.11(d)), on the other hand, the BE of these states seems to be well reproduced

⁷This argumentation holds for all the bands discussed here, meaning that in the full photon energy range the same band adopts two symmetry labels e.g., in between the Γ and A points ($h\nu \leq 48$ eV) the Δ_7 representation should be used, while in between the A and Γ points ($h\nu > 48$ eV) the Δ_8 representation should be interchanged by the Δ_8 representation.

but they are more pronounced in intensity due to the reduced linewidth broadening mentioned above. The analysis of the polarization dependence reveals that they are mostly suppressed with s-polarization, although a weak intensity is still present in all the spectra of Fig. 4.11(c) at binding energies around 2 eV. Due to the polarization dependence and by comparison to the theoretical calculations, the assignment of the symmetries can be derived from selection rules in a straightforward manner. Near the first Γ point ($h\nu=26$ eV), where all the states of this kind are degenerated, we can observe them with both polarizations, and thus the dominant symmetry should be Δ_9^\uparrow . At $x=0.67\Gamma A$ ($h\nu=40$ eV), however, since the peaks are mostly suppressed with s-polarization, the dominant symmetry should be Δ_7^\uparrow . Moving into the next Brillouin zone, the same argument applies and therefore, the dominant symmetries are Δ_8^\uparrow and $\Delta_{8,9}^\uparrow$ for $x=0.62\Gamma A$ ($h\nu=56$ eV) and $0.08\Gamma A$ ($h\nu=70$ eV), respectively.

4.4.2.2 Many-body aspects of the band structure

In order to obtain a more detailed comparison theory-experiment, we have done a similar quantitative analysis as the one shown in the previous section for Fe. Therefore, in the present section we will follow the same line of presentation for the Co results. In Fig. 4.12, the BE positions of the different experimental peaks we have just described are compared to the calculated bulk-like spin-dependent spectral functions $A(\mathbf{k},E)$ obtained in the framework of the LDSA+DMFT (Figs. 4.12(a) and 4.12(b)), LSDA+3BS (Figs. 4.12(c) and 4.12(d)) and LSDA (Figs. 4.12(e) and 4.12(f)) schemes. Majority spin states are shown in Figs. 4.12(a), 4.12(c) and 4.12(e) and minority spin states in Figs. 4.12(b), 4.12(d) and 4.12(f). The symmetry labels of the states are also given. In these calculations, the experimental energy resolution is considered by a smearing parameter of ~ 100 meV. The experimental peak positions were extracted from the experimental SARPES data of Figs. 4.11(a) and 4.11(b) by means of the same fitting procedure described in extensive detail for the analysis of Fe. It should be noted that the spectral functions contain more bands than the ones observed in the experiment, since Brillouin zone selection effects and matrix-element effects are not considered in these calculations. The results of the fits will be shown more in detail below. As it was the case for Fe, it is clear that the theoretical results derived from both LDSA+DMFT and LSDA+3BS methods are well in agreement with each other for identical values of U and J .

Let us focus first on majority spin states. From a first examination across the complete Brillouin zone, one can conclude that the LDSA+DMFT and LSDA+3BS spectral functions reproduce the experimental data better than standard LSDA calculations. This is most apparent at lower BE and for states near the A point, where the LSDA bands are shifted to higher BE as compared to the experimental points arising from the majority spin $\Delta_{9,8}^\uparrow$ symmetry surface resonance. The intensity of this surface resonance feature contains an important contribution of a degenerate bulk-like $\Delta_{9,8}^\uparrow$ majority spin band. Thus, in order to find best agreement with the experiment, we would need to shift by about 0.5 eV the corresponding majority spin LSDA bands towards lower BE. The second point to consider here is the remarkable intensity of the LSDA majority spin bands appearing in a BE range from 2.5 to 3 eV in the whole Brillouin

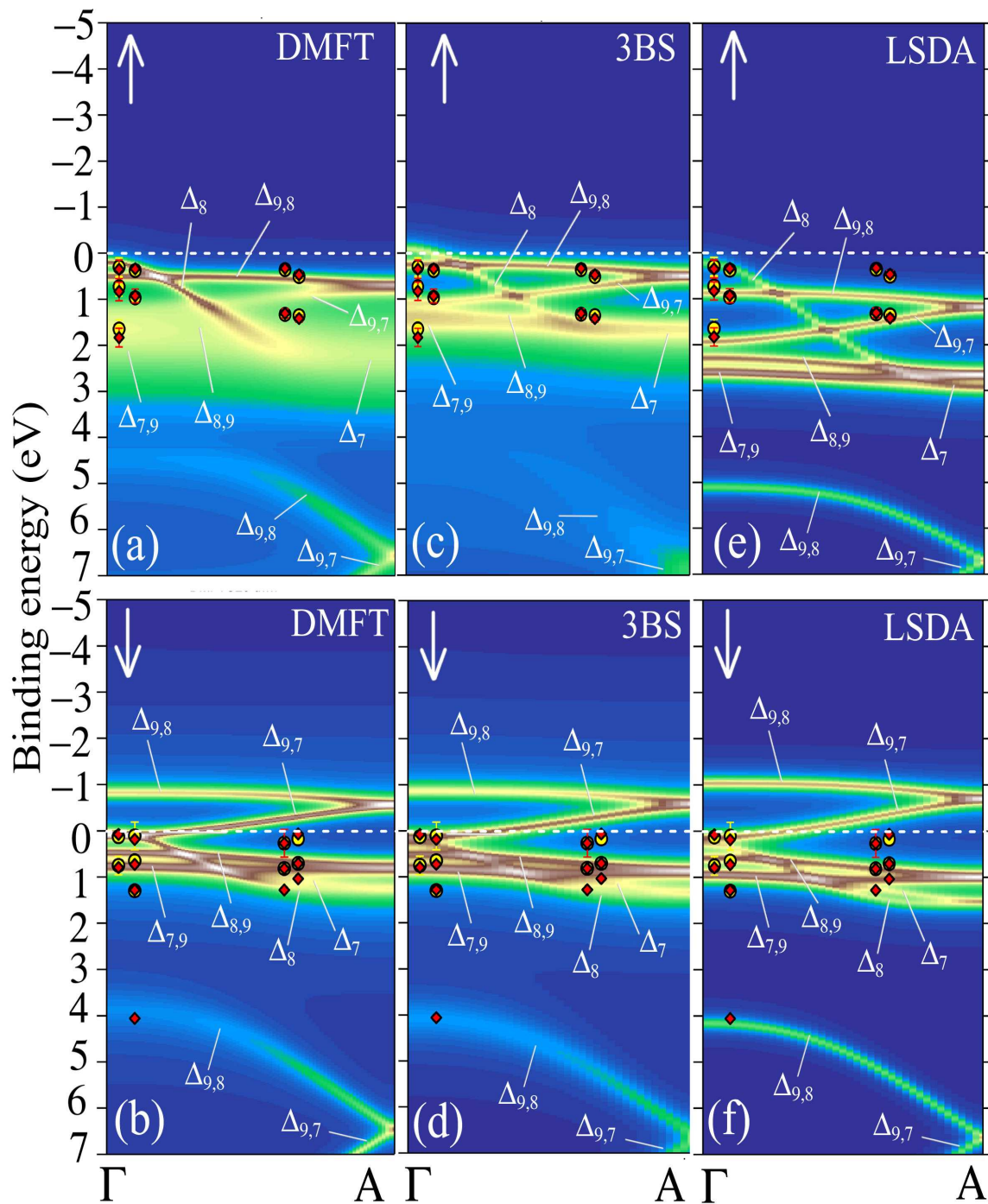


Figure 4.12: Quasiparticle spectral functions of Co(0001) and the photoemission peak positions obtained from the spin-resolved measurements of Fig. 5.11 for different polarizations (\diamond for p - and \circ for s - polarization). Results obtained by the LSDA+3BS ((a),(b)) and by the LSDA+DMFT ((c),(d)) methods for majority and minority spin states, respectively. The symmetries of the different states are indicated.

zone. As discussed before, these bands are strongly broadened in the experiment and appear at BE energies of around 1.7-1.9 eV. From the polarization-dependent analysis carried out before, we also know that for the different k-points of the bandstructure, the symmetries of these states [$\Delta_9(\Delta_{8,9})$ and $\Delta_7(\Delta_8)$] coincide with the symmetries of the LSDA bands appearing at $E_B > 2$ eV, which are not forbidden by selection rules. This means that in Fig. 4.12(e), the agreement between the peak positions from the experimental peaks around 1.9 eV with the LSDA bands of $\Delta_{9,7}^\uparrow$ appearing at binding energies below 2 eV is just accidental, since this agreement does not hold based on simple symmetry arguments. Therefore, also in this case a shift of these states by about 0.7-1 eV becomes necessary to properly explain the bandwidth reduction observed in the experiment. These two facts are already an indication that a shrinking of the 3d bands due to correlation effects becomes necessary to properly describe the experimental data. This is clearly demonstrated in Figs. 4.12(a) and 4.12(c) where a relatively good agreement is obtained for the BE positions of the experimental majority spin peaks for both p and s polarizations. In this case, a reduction of the bandwidth of majority spin states by $\sim 37\%$ was necessary, in agreement with the results presented in Fig. 4.10(c). Regarding the minority spin states, we have already emphasized in the previous section that correlation effects are weaker than for majority spin, but not negligible. In fact, the different minority spin bands in the LSDA+DMFT (Fig. 4.12(b)) and LSDA+3BS (Fig. 4.12(d)) calculations are shifted by about 0.2 eV with respect to the LSDA ones (Fig. 4.12(e)). This means that the BE positions of the different bands in the three different theoretical approaches show relatively good agreement with the experimental data. Note that close to the A point, the Δ_9^\downarrow minority spin component of the surface-like Tamm state discussed above is also visible. This state is not reproduced in the spectral function calculations because, like for Fe, surface effects are not included in these calculations. The next point that we should briefly discuss is the agreement between the experimental and theoretical LSDA+DMFT+1SM spectra as a function of the on-site Coulomb interaction U , as it was done in the preceding section for the Fe system. As already mentioned, the best agreement between theory and experiment for Co was found for $U=2.5$ eV and $J=0.9$ eV. The value of J adopted here can be considered a good general assumption for all 3d elements, since J is only a weakly screened parameter. This means that no differences are observed in the LSDA+DMFT+1SM spectra for different J values. Therefore, since the only parameter directly linked to the effect of electronic correlations which might lead to changes in the calculated spectra is U , we will proceed with discussing how much the theory is sensitive to this parameter in view of the experimental results.

In Fig. 4.13, we compare the spin-integrated experimental spectra measured for p-polarization at the Γ point ($x=0.01\Gamma A$, $h\nu=72$ eV) [Fig. 4.13(a)] and near the A point ($x=0.96\Gamma A$, $h\nu=48$ eV) [Fig. 4.13 (c)] to the LSDA+DMFT+1SM and LSDA calculations broadened by the experimental energy resolution. In this case, the LSDA calculations also include surface effects for a better comparison. Among the two spectra available in the data near the Γ point, the spectrum at $h\nu=72$ eV has been selected as a suitable choice because of the better agreement at higher photon energies between the experimental and theoretical intensities of the majority spin $\Delta_{8,9}^\uparrow$ surface resonance located near the Fermi level. The spin character and symmetry of the dif-

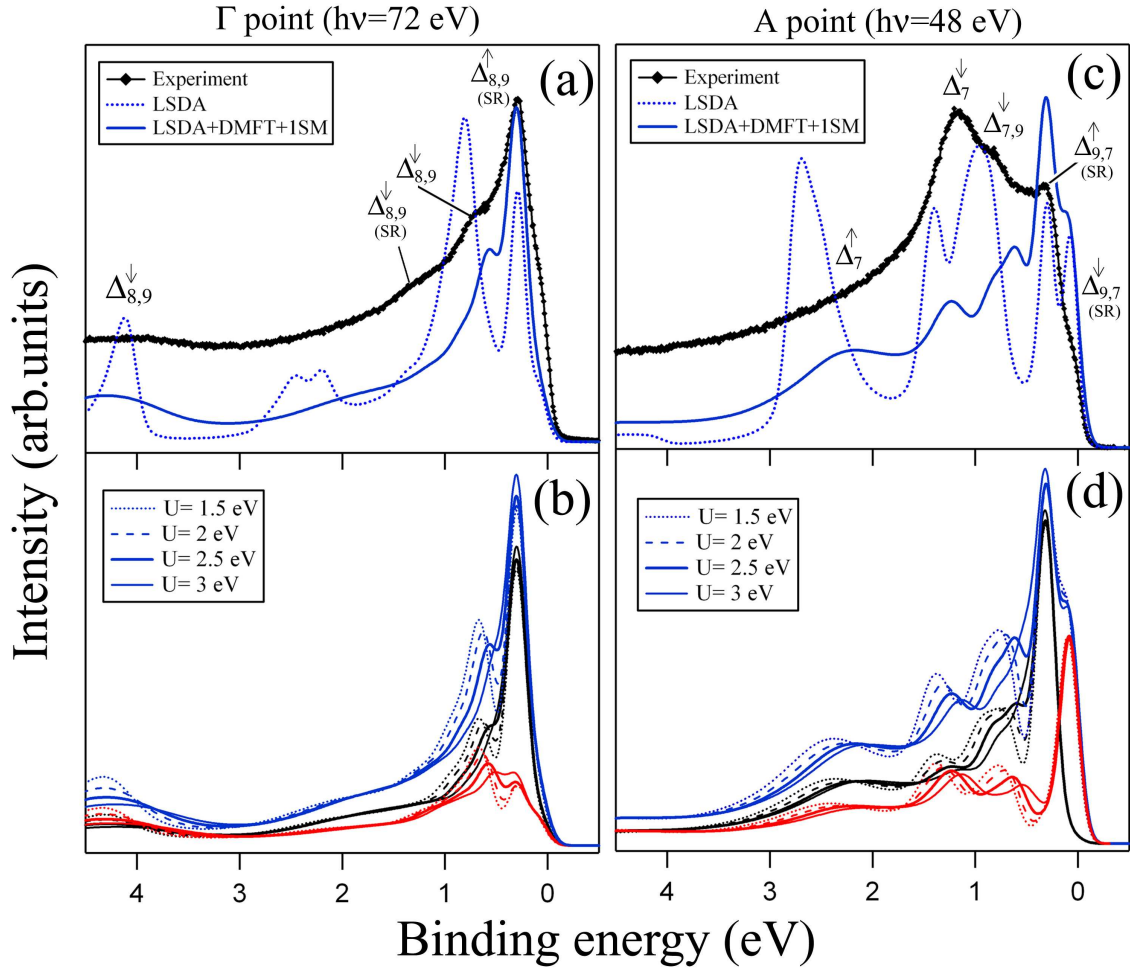


Figure 4.13: Comparison between experimental and theoretical spectra of hcp Co(0001) at the Γ [(a) and (b), ($h\nu=72$ eV)] and A points [(c) and (d), ($h\nu=48$ eV)] of the bulk Brillouin zone for p-polarization. (a) Spin-integrated experimental spectra [thick black dots], single-particle LSDA-based calculation including surface effects [dotted blue line] and LSDA+DMFT+1SM spectra [solid blue line]. (b) Spin-dependent LSDA+DMFT+1SM calculations for different U values. Black (red) colors denote majority (minority) spin and blue color the corresponding spin-integrated spectrum. In (c) and (d), analogous data as in (a) and (b). Symmetry labels in the two consecutive Brillouin zones of the hcp lattice are also indicated.

ferent experimental states are also given. In Figs. 4.13(b) and 4.13(d), spin-dependent LSDA+DMFT+1SM calculations for U ranging from 1.5 to 3 eV are also shown.

In general, for Co the LSDA+DMFT+1SM calculations lead to an important improvement as compared to the LSDA calculations. In both Figs. 4.13(a) and 4.13(c), the BE positions of the theoretical peaks agree reasonably well with the experimental ones if correlation effects are included. In Fig. 4.13(a), a good agreement is achieved for the BE position of the majority $\Delta_{8,9}^{\uparrow}$ surface resonance near the Fermi level for both the LSDA+DMFT+1SM and LSDA calculations. However, the bulk component

of this peak, which appears at $E_B \sim 0.78$ eV in the LSDA calculations, is shifted due to correlation effects in the LSDA+DMFT+1SM calculation to $E_B \sim 0.47$ eV (see Fig. 4.13(b), $U=2.5$ eV). In the experiment this peak cannot be distinguished at that BE due to the experimental energy resolution. The $\Delta_{8,9}^\downarrow$ minority spin bulk-like state, which in the LSDA calculation is located at a $E_B \sim 0.8$ eV, is shifted to $E_B \sim 0.66$ eV in the experiment (Fig. 4.13(a)) and to $E_B \sim 0.57$ eV in the LSDA+DMFT+1SM calculation (Fig. 4.13(b)) due to correlation effects.

A similar situation can be found in Fig. 4.13(c). Despite the lack of agreement between the experimental and theoretical intensities mentioned above, good agreement is found in the BE position of the $\Delta_{9,7}^\uparrow$ majority spin component of the Tamm-like surface state. Let us focus again on the most prominent bulk-like peaks appearing in the theoretical and experimental spectra. The $\Delta_{7,9}^\downarrow$ minority spin bulk-like state is shifted to $E_B \sim 0.79$ eV in the experiment (Fig. 4.13(c)) and to $E_B \sim 0.63$ eV in the LSDA+DMFT+1SM calculation (Fig. 4.13(d)) with respect to the LSDA value $E_B \sim 0.96$ eV. The Δ_7^\downarrow peak, on the other hand, is shifted to $E_B \sim 1.20$ eV in the experiment (Fig. 4.13(c)) and to $E_B \sim 1.22$ eV in the LSDA+DMFT+1SM calculation (Fig. 4.13(d)) compared to $E_B \sim 1.38$ eV in the LSDA calculation. This picture is consistent with an experimental mass enhancement $m^*/m_0 \approx 1.26$, which should be compared to the theoretical value of $m^*/m_0 \approx 1.29$ for $U=2.5$ eV. Such an agreement indicates that a value of $U=2.5$ eV is a good choice for the present LSDA+DMFT+1SM calculations. A similar analysis of the mass enhancement factors can be done for the LSDA+DMFT+1SM spectra shown in Figs 4.13(b) and 4.13(d) for U values around 2.5 eV. In particular, we obtain $m^*/m_0 \approx 1.22$ for $U=2$ eV, and $m^*/m_0 \approx 1.55$ for $U=3$ eV. Although the deviations between the mass enhancement factors for different U values are not large, it seems from this evaluation that $U=2.5$ eV is closest to the experiment. A much more precise determination of U requires a full analysis in the whole Brillouin zone. This was done in order to decide on the best choice of U in the present calculations, but with a slightly different approach: the complete set of experimental and LSDA+DMFT+1SM spectra were directly compared in terms of BE position, intensity and width of the peaks over the whole Brillouin zone for different values of U , and overall better agreement was found for $U=2.5$ eV. Another criterion which could also be combined with the one just mentioned is related to the spin character of the different bands. An example showing this can be noticed in e.g. Figs. 4.13(a) and 4.13(b), where the LSDA+DMFT+1SM spin-resolved spectra for $U=2$ eV exhibit a majority spin peak at $E_B \sim 0.6$ eV which in turn, is at the same BE as the experimental minority spin peak of $\Delta_{8,9}^\downarrow$ symmetry.

Furthermore, it can be seen in Figs. 4.13(b) and 4.13(d) that increasing the value of U does not shift the peaks significantly towards the Fermi level. This can be attributed to (i) most of the intensity in the spectra for $BE \leq 0.5$ eV being due to surface-related features, which are not strongly sensitive to changes in the U parameter, (ii) the shift of pure bulk-like states being limited to a narrow energy interval from 0.5 to 1.8 eV, otherwise their sensitivity to U is reduced through coupling to surface-related states near the border of the gap, (iii) there are no strong changes in Σ_{DMFT} in a region very close to the Fermi level. Because of these reasons, compared to Fe, in Co the peaks shift less with increasing U because they are closer to the Fermi level, and most of

the bulk bands are located in a narrow energy interval. Besides, the coupling between surface and bulk states is different in Co and Fe, since in Co there is a gap around the Γ point, while in Fe the gap is located in a different region of the Brillouin zone and exhibits a different shape. This is also related to the fact that in Co, the bands are more flat due to the hexagonal structure. Hence, this leads to real surface states in Co, whereas in Fe most of them are surface resonances and thus much more sensitive to changes in U . In this sense, Fe exhibits a strong bulk-surface coupling, while Co does not.

4.4.2.3 Spin-dependent quasiparticle lifetimes

The last issue to be discussed in this chapter is the quality of the agreement between the experimental and theoretical linewidths of the Co photoemission peaks. As it was pointed out at the beginning of this section, it is clear that the Co calculations presented here underestimate the scattering rates, similar to what we have found in the case of Fe. In Fig. 4.13, it can also be noticed that the width of the peaks does not increase with U . In the narrow BE range we are focusing on, increasing U shifts the peaks to lower BE and also leads to nearly-constant values of the energy-dependent $\text{Im}\Sigma_{DMFT}$. Besides, since the effect of U on the peak positions is even smaller as compared to Fe, a change in the linewidth can hardly be appreciated. This holds for both bulk-like and surface-related features. In relation to the additional broadening caused by final state effects [60], (i) its contribution to the linewidth of surface states can be neglected since no dispersion normal to the surface exists in this case ($|v_{i,\perp}| = 0$), (ii) it can be neglected when compared to the experimental resolution near the critical points (e.g. at the Γ and A points in Fig. 4.13), (iii) it is completely considered in the 1SM calculations, (iv) it is expected to be smaller for Co(0001) than for Fe(110) since due to the hexagonal structure the bands do not show strong initial state dispersion. Because of all of these reasons, we exclude final state effects as possible mechanism for the extra broadening observed in the experiment.

In order to check this more in detail, we have carried out a detailed quantitative analysis of the linewidths of the different majority and minority spin peaks appearing in the spin-resolved spectra of Figs. 4.11(a) and 4.11(b). This analysis is exactly the same as the one described for Fe on pages 65-67, and therefore it will not be repeated here. Figure 4.14 shows the results of the fits at all measured k-points and for both p (Figs. 4.14(a)-4.14(d)) and s (Figs. 4.14(e)-4.14(h)) polarized photons. We have adopted the experimental approach mentioned earlier, in which almost degenerated bands which cannot be resolved due to the experimental energy resolution are fitted with a single peak. One of the exceptions to this occurs when e.g. some bands can be suppressed due to matrix elements effects. In this context, polarization-dependent measurements are suited to analyze the linewidths of certain bands that are nearly-degenerated and cannot be resolved independently in certain light polarization conditions. This is the case of e.g. the minority spin states of Δ_9^\downarrow symmetry located at a $E_B \sim 0.7$ eV (Fig. 4.14(f)) and $E_B \sim 0.8$ eV (Fig. 4.14(g)) for s-polarization data, which form a shoulder in the corresponding p-polarization spectra at the same binding energies (Figs. 4.14(b) and 4.14(c)). This situation allows us to fix the width and BE positions obtained from s-polarization data to fit the shoulder observed with p-polarization.

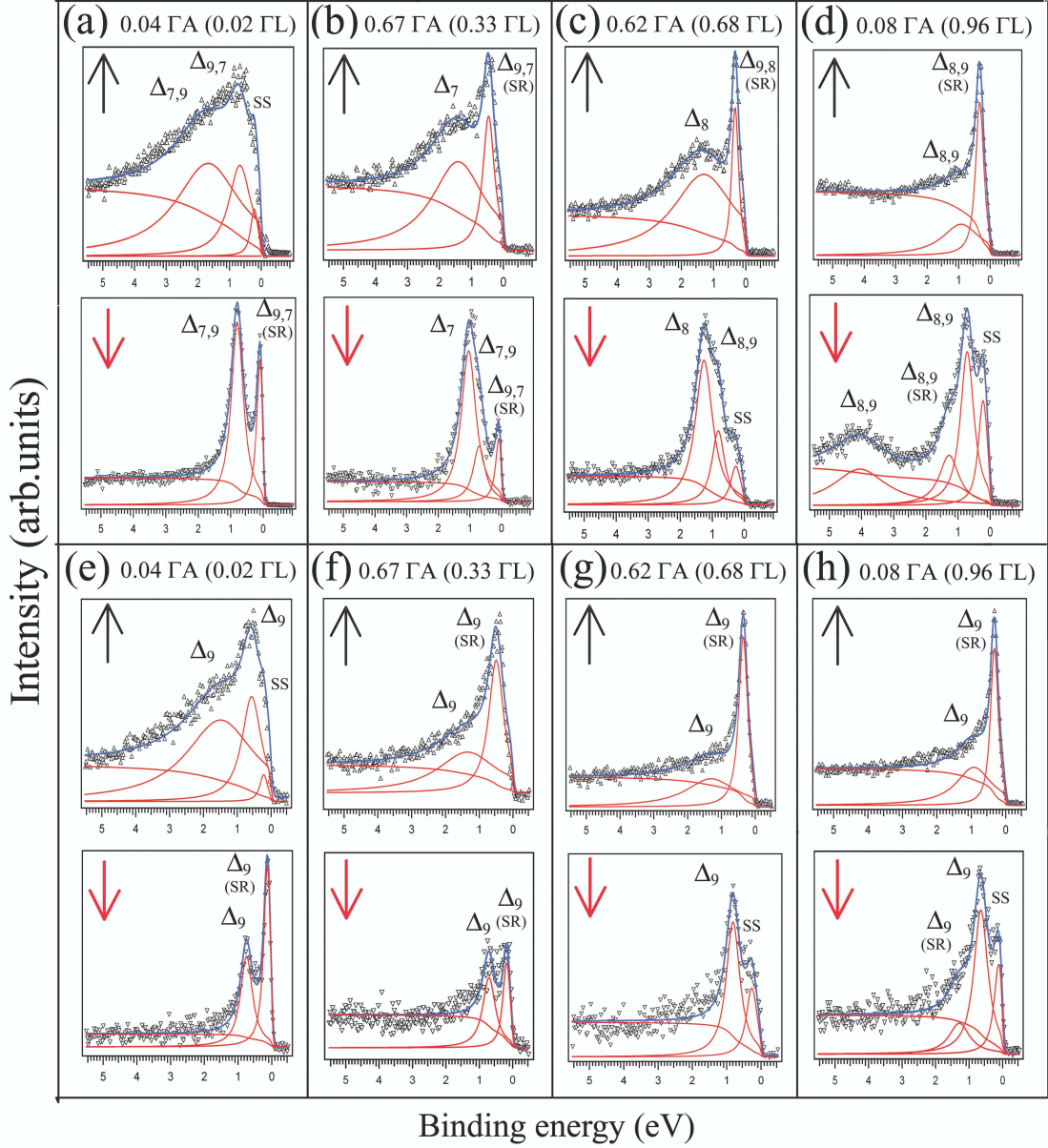


Figure 4.14: Fits to spin-resolved valence band spectra at various k -points of the hcp Co(0001) Brillouin zone. (a)-(d): p -polarization, (e)-(h): s -polarization. Up arrows (down arrows) for majority (minority) spin spectra. The k -points are denoted in terms of the size of the hcp and fcc Brillouin zones for comparison. Symmetry labels in the hcp relativistic representation, surface resonances (SR) and surface states (SS) are indicated.

The result of this analysis is presented in Fig. 4.15, where we have extracted the spin-dependent experimental $\text{Im}\Sigma_{exp}$ of Co as a function of BE and $k=|\mathbf{k}_\perp|$ and compared it to the theoretical one. The results for majority (minority) spin electrons are shown in Fig. 4.15(a) (Fig 4.15(b)), together with the corresponding LSDA+DMFT ($U=2.5$ and 3 eV) and LSDA+3BS calculations ($U=2.5$ eV). As usual, the experi-

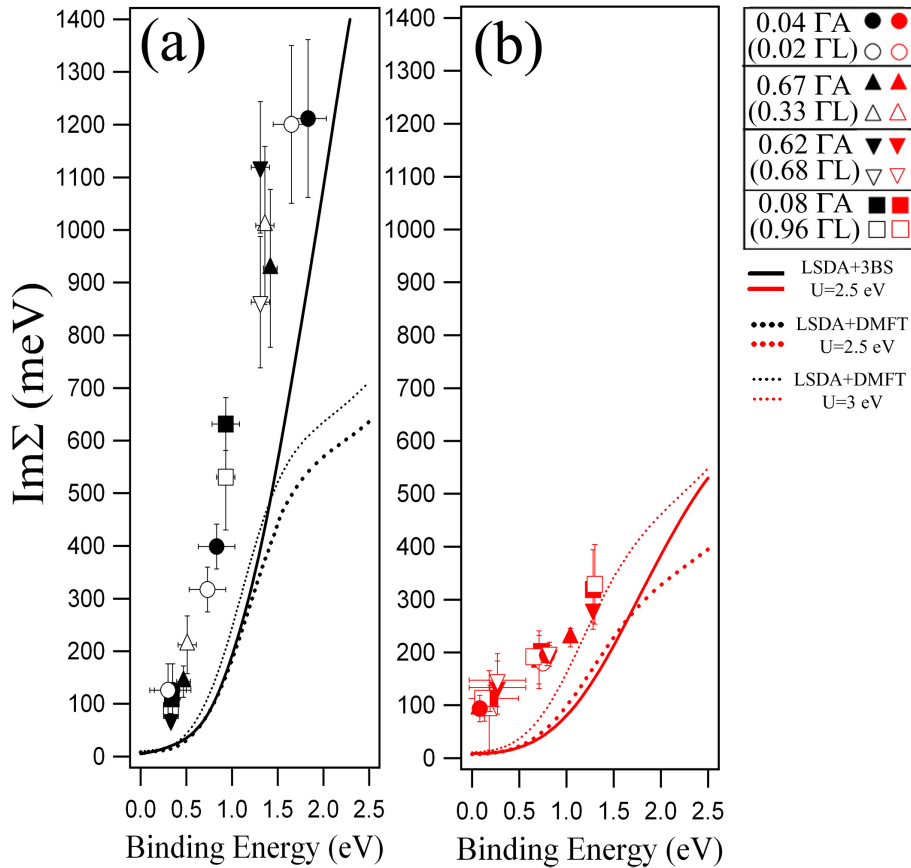


Figure 4.15: Comparison between the experimental and theoretical imaginary part of the self-energy of hcp Co(0001) for (a) majority (black color) and (b) minority (red color) spin electrons. The experimental data points only contain the electronic and impurity scattering contributions to the linewidth. Labels to identify the different k -points are also given for both hcp and fcc lattices. The theoretical curves correspond to $\text{Im}\Sigma_{\text{DMFT}}$ for $U=2.5$ eV (thick dotted lines) and $U=3$ eV (thin dotted lines) and to $\text{Im}\Sigma_{\text{3BS}}$ for $U=2.5$ eV (solid lines).

mental data points have been corrected by all the non electronic contributions to the broadening with the exception of impurity scattering, which by extrapolation can be estimated to be $\text{Im}\Sigma_{\text{imp}} \sim 50$ meV. The final state broadening was determined by unfolding the bands around the A point and calculating the experimental electron initial and final states velocities assuming a free electron parabola as a final state. Due to the flat dispersions of the d bands, a maximum ratio $|v_{i\perp}/v_{f\perp}| \approx 0.03$ was obtained, equivalent to a maximum contribution to $\text{Im}\Sigma_{\text{exp}}$ of about 40 meV and indicating that final-state effects are not the main broadening mechanism. For other non-electronic contributions, from Eq. (4.8) we obtain $\text{Im}\Sigma_{e-ph} \approx 25$ meV.

Although no quantitative agreement between the experimental and theoretical $\text{Im}\Sigma$ is obtained for Co, in contrast to Fe the results seem to be much better reproduced in both spin channels. Interestingly, the experimental data support the existence of a pronounced spin-dependent effect in the quasiparticle lifetimes in agreement with

previous observations [111]. However, this is the first time that the use of spin resolution has been exploited to demonstrate such a notorious effect. In the experimental results, we obtain in first approximation a k -independent $\text{Im}\Sigma_{Exp}$ which exhibits an almost linear energy-dependent behaviour approximated as $\text{Im}\Sigma_{Exp}^{\uparrow} \sim 0.84E$ and $\text{Im}\Sigma_{Exp}^{\downarrow} \sim 0.16E$ for majority and minority spin electrons, respectively. Furthermore, the relative overall agreement between the experiment and the theoretical predictions indicates that in the case of Co, the role of non-local correlations is not as important as in Fe but they are still necessary. This could be attributed to a reduction of the non-locality of correlation effects with increasing atomic number.

Regarding the theoretical calculations of $\text{Im}\Sigma_{DMFT}$ in Fig. 4.15, it can be seen that increasing U does not affect the global behaviour of the calculated curves as much as in the case of Fe in Fig. 4.9. Note that this is something expected following our previous discussion concerning the shifting of the peaks with increasing U , which was also not very pronounced for Co. The deviations from the experimental data in Fig. 4.15 seem to be equally pronounced for both majority and minority spin electrons, with the exception of the minority spin $\text{Im}\Sigma_{DMFT}$ for $U=3$ eV, which seems to agree better if the impurity scattering contribution is subtracted from the experimental curve. Nevertheless, the overall agreement shows that the experimental $\text{Im}\Sigma$ is roughly a factor of 2 too large in average when compared to the calculations. In the DMFT calculations, this discrepancy is more pronounced in the majority spin channel at higher binding energies than at lower ones. Note that both the $\text{Im}\Sigma_{DMFT}$ and $\text{Im}\Sigma_{3BS}$ agree well for the same U values with the exception of higher binding energies, where they start to deviate from each other. We attribute this difference to the fact that LSDA+3BS calculations are (i) based on different DFT codes and (ii) explicitly include electron-hole pair excitations (see section 4.2.2) which increase $\text{Im}\Sigma$. The extent of the present agreement contrasts a very recent non spin-resolved analysis by Moulazzi et al. [137], in which excellent agreement between experiment and previously reported results of $\text{Im}\Sigma_{DMFT}$ [157] is achieved for both spin channels due to an arbitrary linewidth assignment of nearly-overlapping spin contributions.

4.5 Summary of conclusions

In summary, in this chapter we have shown a detailed comparison between spin and angle-resolved photoemission experiments and state-of-the-art theoretical calculations of ferromagnetic bcc Fe(110) and hcp Co(0001) systems. We have analyzed in detail the agreement between the theoretical and experimental photoemission spectra. The theoretical methods lead to an important improvement compared to LSDA calculation by including, in a unified picture, many-body corrections with multiple-scattering, matrix-element and surface-related effects. However, we have demonstrated that these theories, at least in the present implementation, underestimate the mass renormalization and, in particular, the scattering rates. This result demands more refined many-body calculations, possibly with non-local schemes, which take into account non-local fluctuations in multiband systems. The long range part of the Coulomb interaction, excluded from the Hubbard model, may play a role in correcting hybridized s-p-d states. A method to overcome this limitation has been recently proposed in terms of a parameter-free

extended DMFT+GW scheme [177] in which both the on-site and off-site correlations are included. Moreover the *dual fermion* approach [178], where the problem is reformulated in terms of second order perturbation theory including non-local interactions, seems to be also promising. In this case, the momentum dependence of self-energy is calculated starting with single-site DMFT calculations or any local approximation, thus providing a quite satisfactory description of the non-local correlation effects in a broad range of U parameters. In the near future, it would be an important step to implement these approaches into realistic electronic structure calculations since it has not yet been done.

Chapter 5

Spin-dependent properties of graphene on 3d ferromagnets

In this Chapter we will show in detail monitoring by photoelectron spectroscopy how graphene can be grown by chemical vapour deposition on the transition-metal surfaces Ni(111) and Co(0001) and intercalated by a monoatomic layer of Au. For both systems, a linear $E(k)$ dispersion of massless Dirac fermions appears in the graphene π -band in the vicinity of the Fermi energy. In order to simultaneously study ferromagnetism and spin-orbit effects by spin- and angle-resolved photoelectron spectroscopy, the sample must be magnetized in remanence. To this end, a W(110) substrate is prepared, its cleanliness verified by photoemission from W(110) surface states and surface core levels, and epitaxial Ni(111) and Co(0001) thin films are grown on top. Spin-resolved photoemission from the π -band shows that the ferromagnetic polarization of graphene/Ni(111) and graphene/Co(0001) is negligible and that graphene on Ni(111) is after intercalation of Au spin-orbit split by the Rashba effect.

5.1 Introduction

In the past few years, graphene i.e., a single atomic layer of graphite, has been in the focus of a large number of experimental and theoretical studies not only due to its interesting electronic properties, which will be discussed further below, but also because it promises applications for future electronic devices. Shortly after its preparation for the first time by exfoliation [179], it was realized that graphene has similar advantages as carbon nanotubes [180], since both systems exhibit extremely high charge carrier mobilities of up to 1.5×10^4 cm²/Vs even at room temperature [181], indicating the presence of massless relativistic charge carriers with extremely long lifetime [182] and providing the basis for an extremely fast charge-based electronics. Thus, it is only very recently that carbon-related materials have been considered an important alternative to Si or Ge for electronic applications.

The main problems in building new electronic devices using graphite and diamond, the two bulk phases of carbon, have been the appearance of semimetallic properties in the former and the difficulty to obtain n-type doping in the latter. Therefore, it is not long ago that first diamond field-effect transistors have been built [183] and n-type

doping in diamond was achieved by different methods [184, 185]. As an alternative, further improvements in the preparation techniques have allowed the fabrication of nanoscopic systems which are stable at atmospheric pressure. Among them, both one-dimensional carbon nanotubes [186] and two-dimensional graphene [187, 188] have been used to build field-effect transistors of high efficiency [189, 190].

Besides the perspectives with respect to charge-based electronics, an acceleration of the electronic devices is further expected from spintronics, where the transport properties are not achieved via transmission of charge but spin. The spin-orbit coupling, which contributes to spin relaxation in solid systems, typically leaves an extremely stable spin degree of freedom in the case of carbon materials, since they exhibit rather small spin-orbit interaction ($\sim 10\text{--}100\mu\text{eV}$) [191]. Spin current manipulation has been demonstrated in carbon nanotubes [192] and the realization of a spin-valve device was reported based on graphene [193]. From spin-dependent transport measurements, a large spin relaxation length of $\sim 50\ \mu\text{m}$ in carbon nanotubes [194] and $1.5\text{--}2.0\ \mu\text{m}$ in graphene flakes attached to Permalloy or to Co with an alumina layer in between [195, 196] have been obtained. Although the spin relaxation length in graphene is still lower than in carbon nanotubes, the preparation processes for graphene are still in the stage of exploration. On the other hand, graphene has certain advantages over carbon nanotubes e.g., while only armchair-like carbon nanotubes¹ are conducting, freestanding graphene always shows conductivity and a particularly easy tunability of the electron density by an external gate voltage. For these reasons, a lot of attention has been devoted to the electronic properties of epitaxial graphene films grown on different substrates.

Spin- and angle-resolved photoemission investigations in epitaxial graphene represent a complementary tool to transport and magnetotransport measurements in this system. They allow not only to determine the complete occupied graphene bandstructure $E(\mathbf{k})$ and group velocities, but also lifetimes of quasiparticles, many-body effects and spin polarization of electronic states [52, 197]. Recent photoemission investigations of graphene grown on SiC(0001) [198, 199] have given access to the $E(\mathbf{k})$ dispersion of graphene massless Dirac fermions, and shown that the quasiparticle picture used to describe electron-correlation effects in graphite [200–202] is still valid in graphene. Regarding the applications in spintronics, most recently a Rashba effect in the photoemission spectra of an epitaxial graphene layer grown by chemical vapour deposition on top of Ni(111) has been reported [203]. It was shown how a \mathbf{k}_{\parallel} shift in the spin-integrated $E(\mathbf{k})$ dispersion of the graphene π -band appears upon reversal of the magnetization of the Ni substrate. This magnetic effect, interpreted in terms of a Rashba splitting, was attributed to the induced spin polarization of the graphene π states through their hybridization with the spin-polarized 3d states of Ni. Therefore, the use of spin resolution requires particular attention in such a scenario, because it may lead to important implications towards the fabrication of new-generation spintronic devices when Rashba effect and exchange interaction together control the electron spin.

In the following we will focus on how graphene can be grown by chemical vapour deposition on the transition-metal ferromagnetic surfaces Ni(111) and Co(0001) and

¹An armchair carbon nanotube can be imagined as a graphene sheet rolled at a chiral angle of 0° with respect to a plane perpendicular to the long axis of the nanotube.

subsequently intercalated by a single atomic layer of Au. After the intercalation process, changes in the electronic structure are observed by angle-resolved photoemission measurements from both systems. A linear $E(k)$ dispersion of massless Dirac fermions in the graphene π -band is observed in the vicinity of the Fermi energy (E_F), indicating the relativistic nature of the quasiparticle system. Spin-resolved photoemission measurements from the π -band show that the ferromagnetic spin-polarization of graphene/Ni(111) and graphene/Co(0001) is at the limit of detection, but graphene on Ni(111) leads after intercalation of Au to a pair of spin-orbit split states due the Rashba effect.

5.2 The Rashba effect

Combining independent spin and charge manipulation into a single spintronic device is a very promising issue that may lead to new functionalities and physical phenomena. An example is the spin transistor proposed by Datta and Das [31]. This manipulation could be achieved, for example, by the Rashba effect [31,204], which is one of the main issues discussed in this chapter. The Rashba effect is due to the spin-orbit interaction. It is generated by an electric field in a system with broken inversion symmetry at a two-dimensional (2D) interface. It basically leads to a rotation of the spin quantization axis of the electrons traversing the electric field, thus providing a possibility of manipulating single electron spins without external applied magnetic fields.

In the atomic representation, any relativistic electron that is moving with a velocity \mathbf{v} around the nucleus of an atom will experience an electric field \mathbf{E} due to the potential gradient $\nabla V(r)$ generated by the nuclear charge. Due to the Lorentz transformation, in the reference frame of the electron \mathbf{E} will act as an additional magnetic field $\mathbf{B} = \frac{1}{c}(\mathbf{v} \times \mathbf{E})$, which will couple to the electron spin $\boldsymbol{\sigma}$ via $-\boldsymbol{\sigma} \cdot \mathbf{B}$, causing a spin splitting of the energy levels. Assuming that the electric field is derived from a spherically symmetric potential $V(r)$, this leads to an extra spin-orbit coupling term in the Dirac Hamiltonian of the form:

$$H_{SO} = -\boldsymbol{\sigma} \cdot (\mathbf{p} \times \mathbf{E}(\mathbf{r})) = -\boldsymbol{\sigma} \cdot (\nabla V(r) \times \mathbf{p}) = \frac{1}{r} \frac{dV(r)}{dr} \boldsymbol{\sigma} \cdot (\mathbf{r} \times \mathbf{p}) = \xi \boldsymbol{\sigma} \cdot \mathbf{L} \quad (5.1)$$

where $\xi(r) = \frac{1}{r} \frac{dV(r)}{dr}$ is the material dependent spin-orbit coupling constant and \mathbf{L} the orbital momentum operator. The above equation describes the coupling between the spin and orbital moment of the electrons, i.e., between the spin and the magnetic field created due to the electrons orbital motion. Note that since for electrons close enough to the nucleus the potential will be more Coulomb-like ($V(r) = -\frac{Z}{r}$), $\xi(r)$ will be proportional to the atomic number Z and thus the spin-orbit coupling is expected to be larger for heavy atoms.

In an analogous way as in the case of an atom, the spin-orbit interaction manifests itself in systems without inversion symmetry and leads to the Rashba effect, as mentioned above. This inversion asymmetry can be easily realized by considering e.g., a 2D ultrathin film on a substrate with the vacuum potential on one side and the substrate potential on the other side, so that $V(\mathbf{r}) \neq V(-\mathbf{r})$. The potential gradient generated

in this way can be interpreted as an electric field $\mathbf{E} = (0, 0, E_z)$ perpendicular to the film plane. In the case of a non-magnetic system, time reversal symmetry holds, so the transformation $t \rightarrow -t$ changes the electron momentum from \mathbf{k} to $-\mathbf{k}$ and inverts the electron precessional motion and in consequence its spin. This leads to the so-called Kramers degeneracy, based on the energy relation:

$$E(\mathbf{k}, \uparrow) = E(-\mathbf{k}, \downarrow) \quad (5.2)$$

where \uparrow (\downarrow) denotes spin-up (spin-down) electrons. While in a crystal with inversion symmetry $E(\mathbf{k}) = E(-\mathbf{k})$ holds in addition, meaning that the bandstructure is symmetric about the center of the Brillouin zone ($\mathbf{k} = 0$) and all bands are spin-degenerated, in the absence of inversion symmetry we have:

$$E(\mathbf{k}, \uparrow) \neq E(\mathbf{k}, \downarrow) \quad (5.3)$$

which leads to a lifted degeneracy of the bands with different spins, in contrast to the symmetric case. Considering up to the first order term in the Taylor expansion of the potential on the electric field $V(\mathbf{r}) \sim V_0 + e\mathbf{E}(\mathbf{r}) + \dots$, in analogy to Eq. (5.1), we have the Rashba or Bychkov-Rashba Hamiltonian [32, 204]:

$$H_R = \alpha_R \boldsymbol{\sigma} \cdot (\mathbf{p} \times \mathbf{E}(\mathbf{r})) \quad (5.4)$$

where the Rashba-parameter $\alpha_R \propto \langle E_z \rangle$ depends linearly on the electric field and determines the strength of the Rashba spin-orbit coupling. Again, note that the Rashba Hamiltonian is strictly correct in the case of a 2D electron gas, basically for plane wave eigenstates as it is the case of e.g., 2D interfaces in between different materials or 2D electronic states at surfaces of crystals (Fig. 5.1(a)). Since in this case $\mathbf{k} = \mathbf{k}_{\parallel} = (k_x, k_y, 0)$ for electrons moving in the surface plane, the eigenenergies are:

$$E_{\pm} = \frac{\hbar^2 \mathbf{k}_{\parallel}^2}{2m^*} \pm \alpha_R |\mathbf{k}_{\parallel}| = \frac{\hbar^2}{2m^*} \left(\mathbf{k}_{\parallel} \pm \frac{\alpha_R m^*}{\hbar} \right)^2 - \frac{\alpha_R m^*}{2\hbar} \quad (5.5)$$

where \pm denotes spin-up and spin-down states and m^* the effective electron mass. The spin-orbit splitting is linear in $|\mathbf{k}_{\parallel}|$ and given by $\Delta_{SO} = E_+(\mathbf{k}_{\parallel}) - E_-(\mathbf{k}_{\parallel}) = 2\alpha_R |\mathbf{k}_{\parallel}|$. From the right-hand side of Eq. (5.5), a given parabolic energy dispersion of a 2D electron gas will be shifted in \mathbf{k}_{\parallel} by $|\mathbf{k}_{SO}| = \frac{\alpha_R m^*}{\hbar}$, but in opposite directions for spin-up and spin-down electrons as it is depicted in Fig. 5.1(b). Note that the spin orientation axis lies in the plane of the 2D electron gas and is always perpendicular to the propagation direction of the moving electron, leading to the Kramers degeneracy $E_{\uparrow}(\mathbf{k}_{\parallel}) = E_{\downarrow}(-\mathbf{k}_{\parallel})$ mentioned above.

Pioneering experiments identified a Rashba type spin-orbit splitting for the $\bar{\Gamma}$ surface state of $^{79}\text{Au}(111)$ [205]. Subsequently, spin-orbit split surface states were identified in other metals with high atomic number Z such as ^{74}W [206, 207], ^{83}Bi [208], and ^{64}Gd [209], while the low- Z metals ^{42}Mo [206] and ^{47}Ag [210] showed smaller or vanishing splitting. Furthermore, it was shown that adsorption of alkali and oxygen monoatomic layers increases Δ_{SO} , which is believed to be due to the extra potential

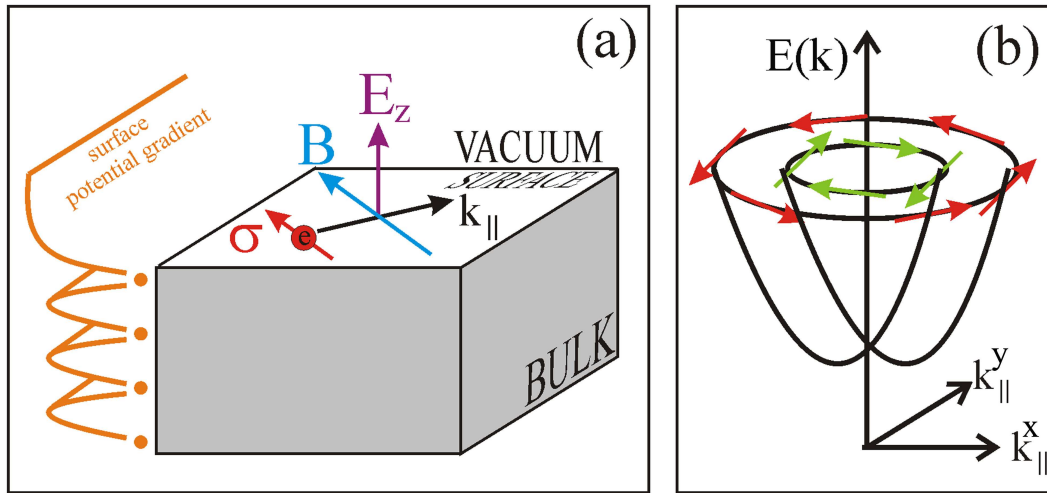


Figure 5.1: (a) Sketch of an electron moving in a potential gradient at a surface of an ultrathin non-magnetic film. The electric field \mathbf{E} generated is transformed into a magnetic field \mathbf{B} due to the relativistic motion of the electron, leading to the Rashba effect. The electron spin orientation σ lies in the plane of the surface, being perpendicular to \mathbf{E} and the electron wavevector \mathbf{k}_{\parallel} . (b) Effect of the Rashba-type spin-orbit interaction on the parabolic energy dispersions of a nearly-free electron system at the surface. The spin-degenerate bands are shifted by \mathbf{k}_{SO} and the energy splitting vanishes in the center of the surface Brillouin zone. The Fermi surface becomes two concentric circles with opposite spins.

gradient and electric field \mathbf{E} at the surface [206].

In a ferromagnetic system, on the other hand, the time-reversal symmetry is broken since there is an energetic shift between spin-up and spin-down electronic states due to the exchange interaction. Thus, Eq. (5.2) does not hold anymore, but instead:

$$E(\mathbf{k}, \uparrow) = E(\mathbf{k}, \downarrow) + \Delta_{ex} \quad (5.6)$$

where Δ_{ex} is the exchange splitting. If in addition the system has broken inversion symmetry, an additional Rashba-type spin-orbit splitting Δ_{SO} may contribute to the energy separation of the bands with opposite spin, leading to what we will call further on Rashba+exchange effect. In order to minimize the exchange energy, the electron spins in the crystal tend to be aligned in a parallel configuration, leading to a fixed direction of the magnetization \mathbf{M} in the system. Therefore, only electrons moving with a \mathbf{k}_{\parallel} which is perpendicular to the direction of magnetization would be sensitive to a Rashba-type spin-orbit interaction. We will come back to this point at the beginning of section 5.5.

5.3 Experimental details

Experiments have been performed at room temperature with the hemispherical SPECS Phoibos 150 electron energy analyzer and linearly polarized undulator radi-

ation at the UE112-PGM beamlines at BESSY. For spin analysis, a Rice University Mott-type spin polarimeter has been operated at 26 kV [50]. Both detectors were described in detail in section 3.2.1 and used for the experiments described in chapter 4. The Ni(111) and Co(0001) surfaces were prepared on W(110) by electron bombardment from high purity wires mounted in water-cooled e^- -beam evaporators. The measurement conditions, the preparation method of the ferromagnetic surfaces and the cleaning procedure of the W(110) substrate were described in detail in section 4.3. The cleanliness of the tungsten substrate was verified by the absence of reconstructions in low-energy electron diffraction (LEED) as well as by the presence of an intense surface induced component (W_s) in the W-4f core level spectrum (see section 4.3.4). The graphene layer was formed in a partial C_3H_6 pressure of 1×10^{-6} mbar with the sample held at 400°C during 5 min. A considerable advantage over other techniques of graphene preparation is that the graphitization of Ni is a self-terminating process which stops after a single layer of graphene has formed [211]. The geometry of the experiment is shown in Fig. 5.2(a).

The graphene/Ni(111) and graphene/Co(0001) films were remanently magnetized in the film plane along the $[1\bar{1}0]$ and $[1\bar{1}00]$ directions. Therefore, the \mathbf{k}_{\parallel} directions within the graphene surface Brillouin zone (SBZ) in which we expect a maximum Rashba+exchange effect in graphene/Ni and in graphene/Co are rotated with respect to each other by 90° [212] (see Figs. 5.2(b) and 5.2(c), respectively). The deposition of Au was done at room temperature from Au beads molten on thin W wires by Ohmic heating. The thickness of the Au overlayers was controlled by measuring the Au 5d photoemission signal. The annealing of the sample at $\sim 400^\circ\text{C}$ allowed for the intercalation of Au atoms underneath the graphene, restoring the complete graphene monolayer on top of the system [211].

As mentioned in section 4.3.4, the presence of the surface W_s component in the

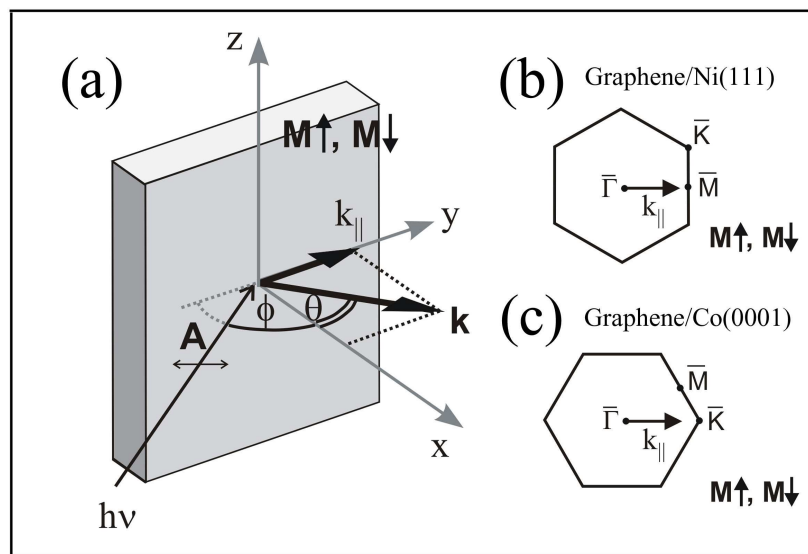


Figure 5.2: *The geometry of the experiment (a) and the directions of \mathbf{k}_{\parallel} within the graphene SBZ for (b) graphene/Ni(111) and (c) graphene/Co(0001).*

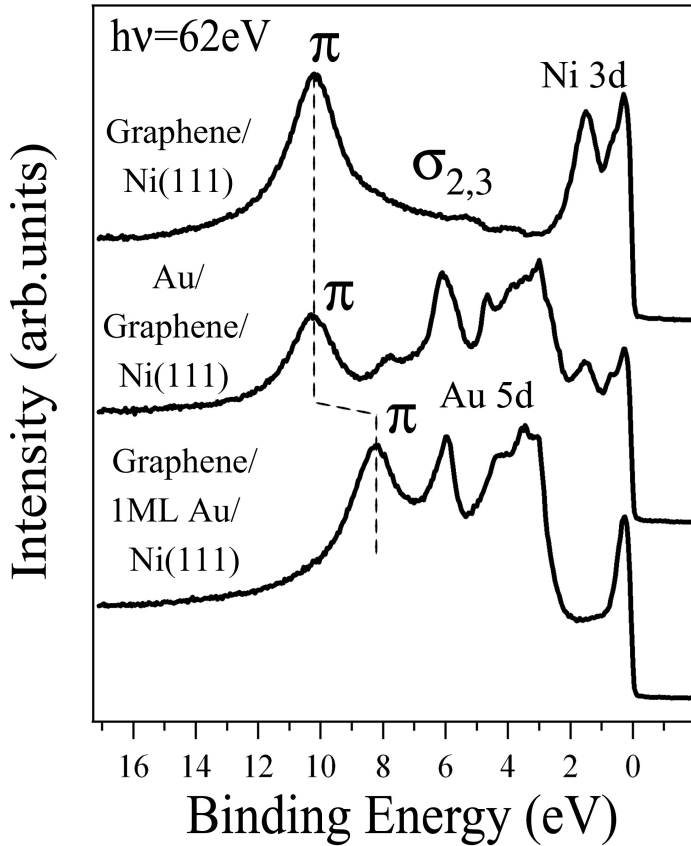


Figure 5.3: Steps followed during the fabrication process of the graphene/Au/Ni(111) system. From top to bottom, normal-emission valence band spectra from graphene/Ni(111), Au/graphene/Ni(111) after deposition of Au and graphene/Au/Ni(111) after the intercalation process driven by annealing.

core-level spectra is important to make sure that a homogenous growth of the first magnetic overlayers will take place during deposition, and it represents a very sensitive method to check the cleanliness of the W(110) crystal [146]. In general, the intensity ratio between W_b and W_s can be used to judge the cleanliness of the system. An intensity ratio of about 50% was found enough to obtain homogenous growth of the magnetic films and resulted in samples of high quality after the graphitization process, and therefore it was used as a reference during all the experiments.

5.4 Dirac-cone formation in quasi-freestanding graphene after intercalation of Au

Figure 5.3 shows the different steps followed during the fabrication process of the graphene/Au/Ni(111) system. From top to bottom, measurements in Fig. 5.3 correspond to normal-emission valence band spectra measured at 62 eV photon energy from graphene/Ni(111), Au/graphene/Ni(111) after deposition of Au and graphene/Au/Ni(111) after the intercalation process.

The spectrum of graphene/Ni(111) is characterized by the Ni 3d states located in a BE window of ~ 1.5 eV and by the graphene π and $\sigma_{2,3}$ states at a BE of about 10 and 5 eV, respectively. In graphene, the sp^2 hybridization between the C2s orbital and the two in-plane $C2p_x$ and $C2p_y$ orbitals leads to a trigonal planar structure with a

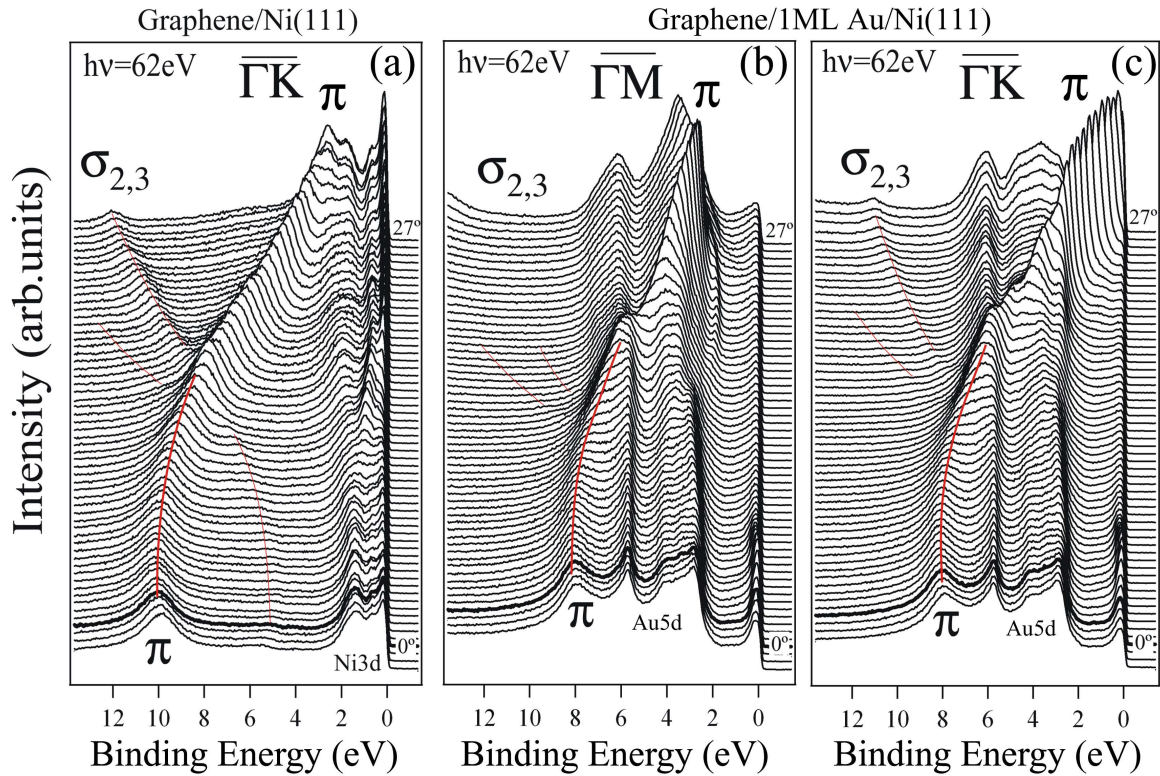


Figure 5.4: *Angle-resolved photoemission spectra of the $E(\mathbf{k}_{\parallel})$ band dispersions of graphene/Ni(111) (a) and graphene/Au/Ni(111) [(b),(c)] systems. Measurements were performed along the $\bar{\Gamma}\bar{K}$ [(a),(c)] and $\bar{\Gamma}\bar{M}$ (b) directions of the graphene surface Brillouin zone.*

formation of covalent σ bonds between carbon atoms. This results in three sp^2 hybrid orbitals which give rise to three different σ bands, typically labeled as $\sigma_{1,2,3}$. The π states, on the other hand, are derived from the out-of-plane $C2p_z$ orbitals which remain unaffected by hybridization and bind covalently forming π bonds between neighboring carbon atoms. In Fig. 5.3, after deposition of Au the intensities of the Ni 3d and graphene π states are significantly reduced without any apparent change in their BE positions. New intense peaks corresponding to Au 5d states in a BE range between 2 and 7 eV become dominant. In particular, the intensity of the graphene π states is about one-half of the intensity of the Au 5d states located at a BE of ~ 6.1 eV, meaning that the thickness of the Au overlayer is about 4 Å at the present photon energy of 62 eV [211]. The absence of Au surface states near E_F together with the presence of graphene and Ni states with lower intensity is an indication of the island-like character of the Au overlayer. After annealing the Au/graphene/Ni system at 400 °C, a high-quality graphene/Au/Ni sample is formed leading to significant changes in its photoemission spectrum as it will be discussed in the following. The photoemission spectrum of graphene/Au/Ni exhibits an increase in the intensity of the graphene π states which is accompanied by an energetic shift of about 2 eV towards lower BE. The intensity of the Ni 3d bands is suppressed and replaced by a surface-related Au peak near E_F and the Au 5d states are slightly shifted towards higher BE, as compared to the

Au/graphene/Ni spectrum. These changes are related to the penetration of Au atoms underneath the graphene and to the weaker interaction between the graphene and Ni layers due to surface intercalation, which leads to a nonrigid shift of the graphene bands towards lower BE. The intercalation of Au was found to be a self-terminating process which leads to a continuously distributed Au interlayer between graphene and Ni reaching as maximum one monolayer thickness [211].

Figure 5.4 displays angle-resolved photoemission data of the $E(\mathbf{k}_{\parallel})$ band dispersions along the $\overline{\Gamma K}$ (Figs. 5.4(a) and 5.4(c)) and $\overline{\Gamma M}$ (Fig. 5.4(b)) directions of the graphene surface Brillouin zone (SBZ) before intercalation (Fig. 5.4(a)) and after intercalation of a complete monolayer of Au (Figs. 5.4(b) and 5.4(c)). The spectra were measured in steps of 0.5° and at 62 eV photon energy. Similar data are also presented in Fig. 5.5. In this case, $E(\mathbf{k}_{\parallel})$ band dispersions of graphene/Ni(111) system measured at 50 eV photon energy are shown as intensity plots along $\overline{\Gamma K}$ direction of the SBZ before (Fig. 5.5(a)) and after Au intercalation (Fig. 5.5(b)). The derivative dI/dE of the photoemission intensity is shown in order to enhance the dispersing character of the different bands. Note that these measurements were done in a larger energy range allowing to monitor the dispersion of the σ states appearing at higher binding energies.

A pronounced dispersing character of the π bands can be observed in all cases. On the other hand, the intensity of the $\sigma_{1,2,3}$ states appears to be strongly reduced as compared to the one of the π states in the entire SBZ. This large difference in the intensities can be attributed to an interference effect of the photoelectron amplitudes from the two carbon atoms (which we will further on call A and B) placed in each graphene unit cell [175]. Note that this behaviour is expected to be the opposite in the case of the π^* and σ^* bands located in the unoccupied part of the band structure and basically to reverse each time we cross the zone boundaries of otherwise equivalent Brillouin zones. In Figs. 5.4(a) and 5.5(a), the rather flat Ni 3d bands only show small changes in their energetic positions when moving towards the \overline{K} point. After intercalation of Au, these bands are essentially invisible in Fig. 5.4(b), 5.4(c) and 5.5(b) and, as mentioned before, their intensity is replaced by emission of a surface-related Au peak near E_F and other Au 5d states at higher BE.

Concerning the results for the graphene/Ni(111) system presented in Figs. 5.4(a) and 5.5(a), our main observations are: (i) in all of the k-points the π and σ bands show a shift towards higher binding energies as compared to monocrystalline bulk graphite [213] and graphene/Au/Ni systems, (ii) the dispersion behaviour of the π band is not linear anywhere in the SBZ and (iii) the π band reaches a minimum BE of about 2.7 eV exactly at the \overline{K} point ($\mathbf{k}_{\parallel} \sim 1.7 \text{ \AA}^{-1}$, $\theta(h\nu = 62\text{eV}) \sim 26^\circ$ and $\theta(h\nu = 50\text{eV}) \sim 29^\circ$) which is by almost 1 eV lower than what would have been expected from a rigid downward shift of about 2 eV of the graphene/Au/Ni bands of Figs. 5.4(c) and 5.5(b).

These effects are due to the C2p-Ni3d interaction of the graphene sheet with the Ni layer underneath and the breaking of the predominantly three-fold symmetry between the two A and B atoms, as observed by scanning tunneling microscopy (STM) measurements [214]. In the valence band, the orbital mixing of the graphene π states with the Ni 3d states leads to a strong C(π)-Ni(d) hybridization and to an electronic redistribution between the bonding π and antibonding π^* states of graphene. On the

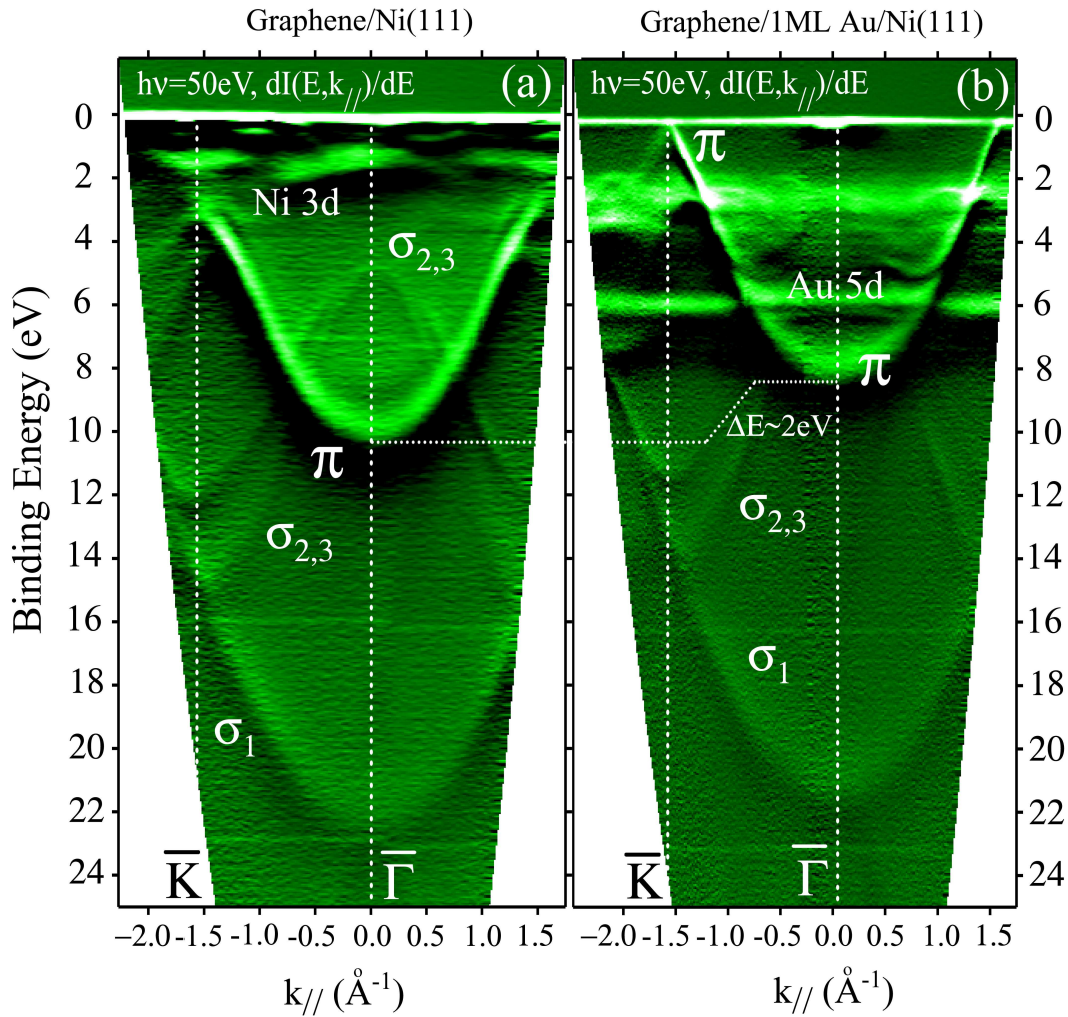


Figure 5.5: Angle-resolved photoemission of graphene/Ni(111) along $\overline{\Gamma K}$ before (a) and after (b) intercalation with one Au monolayer. The derivative dI/dE of the photoemission intensity is shown.

other hand, since the C(σ)-Ni(d) interaction is rather weak, the average BE of the σ states is less influenced than the one of the graphene π states. As a result, the graphene π band shifts nonrigidly towards higher BE by about 2 eV in average and loses its relativistic character, while the σ states shift only by 0.5-1 eV as compared to those of bulk graphite and graphene/Au/Ni systems. The intercalation of Au atoms underneath the graphene, however, leads to the opposite situation. In Figs. 5.4(b), 5.4(c) and 5.5(b), the graphene π and σ bands shift towards the characteristic energy positions of bulk graphite, indicating a remarkable weakening of the C2p-Ni(d) interaction due to intercalation. In particular, this process blocks the C(π)-Ni(d) hybridization, restoring the properties of the system closer to ideal freestanding graphene as it will be supported in the following.

The first evidence is a linear dispersion of the π band when moving towards the \overline{M}

and \bar{K} points, which represents a unique property of relativistic massless quasiparticles [187]. This effect is very pronounced near \bar{K} (see Figs. 5.4(c) and 5.5(b)) and its appearance distinguishes monolayer graphene [198] from bilayer graphene exhibiting a parabolic dispersion [215]. Near the \bar{K} point is where we obtain a maximum group velocity in the system of about $v_g \sim 1.15 \times 10^6$ m/s or $\sim c/260$, which is in the range of previous transport results yielding $\sim c/300$ [187, 216], where c is the speed of light in vacuum.

The second evidence is that at \bar{K} the π band touches the Fermi edge precisely at the Dirac crossing point E_D (note that at the \bar{M} point in Fig. 5.4(b) ($\mathbf{k}_{\parallel} \sim 1.4 \text{ \AA}^{-1}$, $\theta(h\nu = 62\text{eV}) \sim 22^\circ$) the π band does not cross E_F), meaning that the graphene system is gapless and exhibits charge neutrality (i.e., $E_F = E_D$). This is a remarkable result since it demonstrates that the intercalation of Au decouples to a larger extent the graphene layer from the Ni underneath as compared to the case of graphene grown on SiC where E_D is 0.45 eV below E_F [198]. These effects lead to the formation of a Dirac-cone with vertex at \bar{K} located exactly at the Fermi edge. Our experimental results are in agreement with the recently reported first-principles calculations [217, 218] in the framework of density functional theory (DFT). These calculations describe the doping of graphene in terms of the different graphene-metal substrate work functions and the graphene-substrate separation d , predicting that for graphene on Au a zero shift of the conical points with respect to the Fermi level appears for $d = 3.2 \text{ \AA}$. Further insight into the unique properties of the graphene/Au/Ni(111) system has been shown elsewhere [214]. In particular, we have shown that the Fermi surface consists of one sharp point exactly at \bar{K} ($E_F = E_D \pm 25$ meV) and that the constant-energy surfaces are conical, non circular and asymmetric in photoemission intensity. The latter indicates that after intercalation of Au the A-B symmetry of graphene sublattices is restored and not broken in terms of valence-band interference [175]. Other effects, such as the residual weaker interaction with the Au underneath have been revealed by the presence of a kink structure in the $E(k)$ dispersion of the π band at low temperature. From the results shown in this thesis we conclude that graphene prepared in this way is closer to ideal freestanding graphene than any other preparation on a solid substrate before, and therefore we will refer to it further on as quasi-freestanding graphene [214].

Such a quasi-freestanding graphene sheet can also be prepared by using Co(0001) instead of Ni(111) underneath, as it is demonstrated in Fig. 5.6. In general, the graphene/Au/Co system exhibits all of the aforementioned relativistic properties as well. Fig. 5.6(a) reveals a very similar electronic structure as compared to graphene grown on Ni. In order to investigate the existence of a Rashba+exchange effect, the use of Co(0001) as substrate for graphene requires particular attention due to the larger magnetic moment of this system as compared to Ni. This issue will be treated more in detail in section 5.5. Furthermore, it should be emphasized that this is the first time that graphene/Co(0001) and graphene/Au/Co(0001) have been produced as samples and investigated. At low BE, prominent Co 3d bands can be distinguished in a BE range of about 2 eV below E_F . As compared to freestanding graphene, despite the 1.2% and 2% lattice constant expansion of graphene grown on Ni and Co, respectively, critical point energies of the graphene bands are nearly the same, and the system reaches approximately the same level of doping by Au intercalation. In other words,

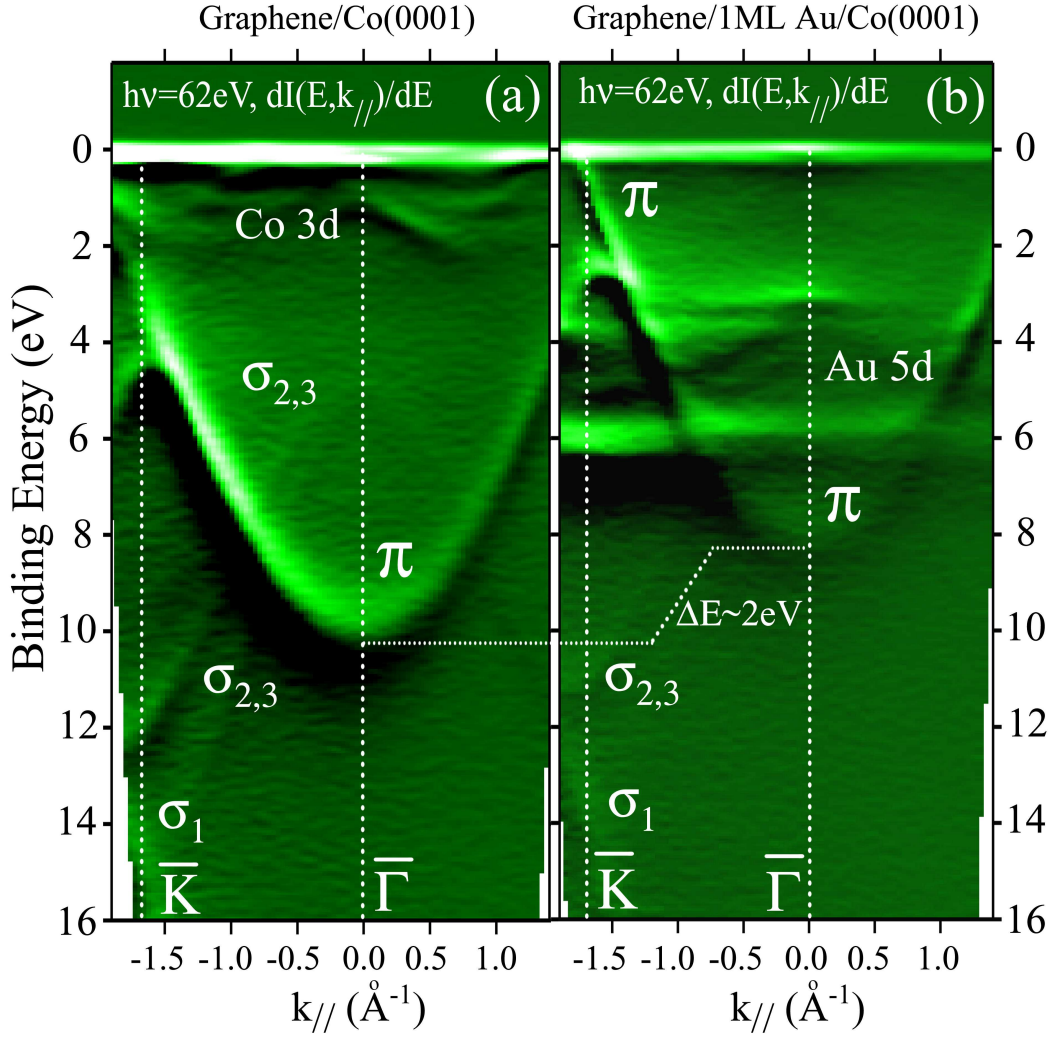


Figure 5.6: Angle-resolved photoemission of graphene/Co(0001) along $\overline{\Gamma K}$ before (a) and after (b) intercalation with one Au monolayer. The derivative dI/dE of the photoemission intensity is shown.

the bonding properties between graphene and its ferromagnetic substrate, the strength of the C(π)-Co(3d) and C(σ)-Co(3d) interaction, as well as the charge transfer and the overlayer-substrate hybridization are very similar for both graphene on Ni(111) and Co(0001) systems. In agreement with the LEED patterns of graphene on Co(0001) [219], we observe other contributions from different directions of the SBZ which are superimposed in the photoemission signal and lead to a pronounced enhancement of the π band intensity near \overline{K} (Fig. 5.6(a)) as compared to graphene on Ni (Figs. 5.4(a) and 5.5(a)). The reported LEED patterns exhibit a predominant $p(1 \times 1)$ structure which is in registry with the Co substrate together with weaker circle segments corresponding to domains of graphene slightly rotated with respect to the Co lattice. The STM measurements revealed a predominantly threefold symmetry similar to the case of graphene grown on Ni(111) [219]. The sample preparation and intercalation were

done in a similar way as discussed for graphene on Ni. In Fig. 5.6(b), no traces of unshifted bands are observed after intercalation of one monolayer of Au. The bands shift nonrigidly towards lower BE in a similar fashion as for the graphene/Au/Ni system. The π band exhibits a shift of about 2 eV leading to the closing of the gap and a linear dispersion at \bar{K} , meaning the realization of neutral graphene and the formation of a relativistic Dirac-cone with its vertex exactly at $E_F=E_D$. Moreover, the σ_1 (slightly visible near \bar{K} and at higher BE) and $\sigma_{2,3}$ bands shift by about 0.5-1 eV. Since these values are very similar to the ones of graphene/Au/Ni discussed above, we conclude that the intercalation of Au underneath the graphene leads in a similar way as for Ni to a blockade of the C(π)-Co(d) hybridization, resulting in a quasi-freestanding graphene layer which is almost completely decoupled from its ferromagnetic substrate.

5.5 Spin-dependent properties and Rashba splitting in graphene on Ni and Co

In this section, we would like to concentrate on the spin-dependent properties of graphene grown on Co and Ni before and after Au intercalation. We have used spin- and angle-resolved photoemission to analyze the spin polarization of the graphene π states along different directions of the SBZ. The use of spin resolution in this context allows us to verify spin-dependent hybridization between the graphene states and those of its ferromagnetic substrate. This issue was motivated by a recent study on graphene/Ni(111) [203], where it has been reported that the graphene $E(\mathbf{k}_{\parallel})$ band dispersion depends strongly on the direction of the magnetization of the Ni substrate. In particular, a \mathbf{k}_{\parallel} shift in the spin-integrated energy dispersions of the graphene π states along the $\bar{\Gamma M}$ direction of the SBZ is extracted from the photoemission spectra measured for two opposite directions of magnetization. The observed effect was, on the one hand, attributed to a manifestation of the Rashba effect [220] caused by the interaction of spin-polarized electrons in the π band of the graphene layer with a large electric field at the graphene/Ni(111) interface. On the other hand, the graphene π states are assumed to become spin polarized due to a strong hybridization with the Ni substrate. A similar interpretation was previously adopted for Gd(0001) and oxygen/Gd(0001) [209] as well as for other rare-earth metals [221]. We will discuss this problem in detail below but we want to mention already that in the case of Refs. [209] and [221], well-known 100% spin-polarized surface states were used to demonstrate the interplay between Rashba effect and exchange interaction without the need of spin resolution. However, in the case of graphene/Ni(111), this exchange-split pair is not yet established. It is not clear if the graphene π states become fully or partially spin polarized and/or exchange split leading to a Rashba-type spin-orbit interaction of the reported size ($\Delta_{SO} \sim 225$ meV) [203].

Let us now discuss the situation in which both the Rashba effect and the exchange interaction coexist in the same system. Considering a nearly-free-electron model, Fig. 5.7 shows the qualitative differences between the two opposite spin bands $E^{\uparrow}(\mathbf{k}_{\parallel})$ and $E^{\downarrow}(\mathbf{k}_{\parallel})$ of a solid in this case. Switching off both spin-orbit and exchange interactions leads to the degeneracy of the two spin subbands and therefore a single parabola is

observed (Fig. 5.7(a)). In nonmagnetic systems, the Rashba-type spin-orbit interaction splits the two spin-degenerate bands respect to the orientation of the \mathbf{k}_{\parallel} momentum and vanishes for $\mathbf{k}_{\parallel} = 0$, as illustrated in Fig. 5.7(b).

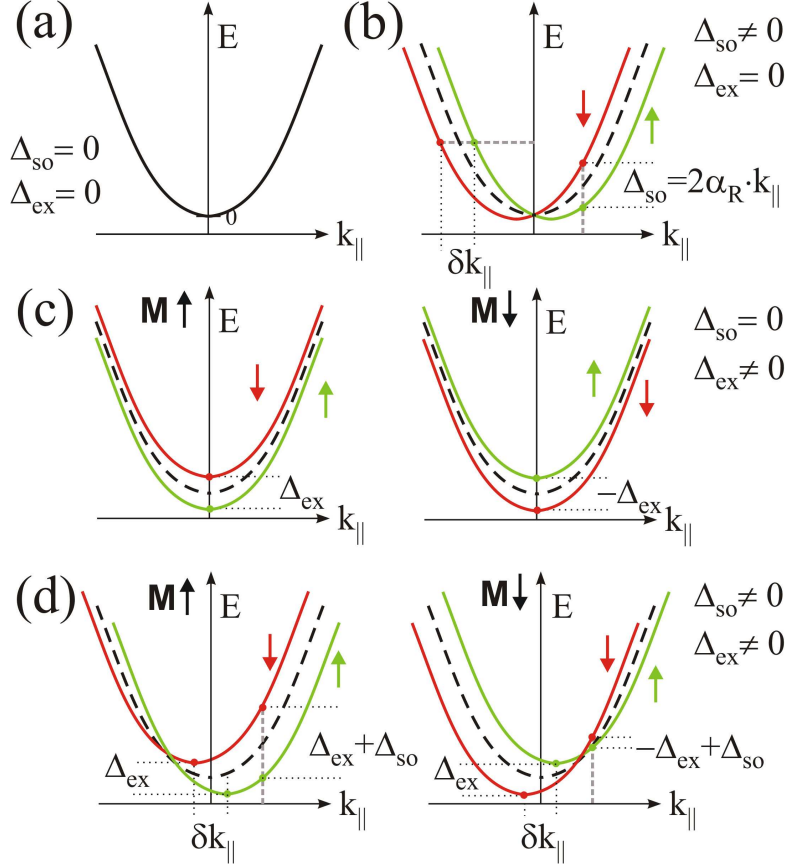


Figure 5.7: *Nearly-free-electron model showing the qualitative behaviour of the $E(\mathbf{k}_{\parallel})$ bands of a solid (a) without spin-orbit and exchange interactions, and with (b) Rashba effect, (c) ferromagnetic exchange and (d) both Rashba effect and exchange interaction coexisting.*

In the presence of band ferromagnetism, the electron spins are oriented along a quantization axis due to the exchange interaction, leading to a pair of exchange-split bands exhibiting positive or negative exchange splitting (Δ_{ex}) depending on the orientation of the magnetization (see Fig. 5.7(c)). An additional Rashba effect in such a situation introduces a different magnetization-dependent behaviour due to an extra $\delta \mathbf{k}_{\parallel}$ shift of the electron wave vector in the interface plane \mathbf{k}_{\parallel} (see Fig. 5.7(d)). As a result, the energy splitting consists of two terms, exchange Δ_{ex} and spin-orbit splitting Δ_{SO} , and its sign upon magnetization reversal will depend on the relative strength of the exchange and spin-orbit interactions.

The absence of structural inversion symmetry at a crystal surface or interface leads to the situation sketched in Fig. 5.6(b), where the spin-orbit splitting Δ_{SO} depends via the parameter $\alpha_R \propto \langle E_z \rangle$ linearly on the electric field \mathbf{E} at the interface (see section 5.2, Eqs. (5.4) and (5.5)). In this context, the use of spin resolution for verifying the Rashba

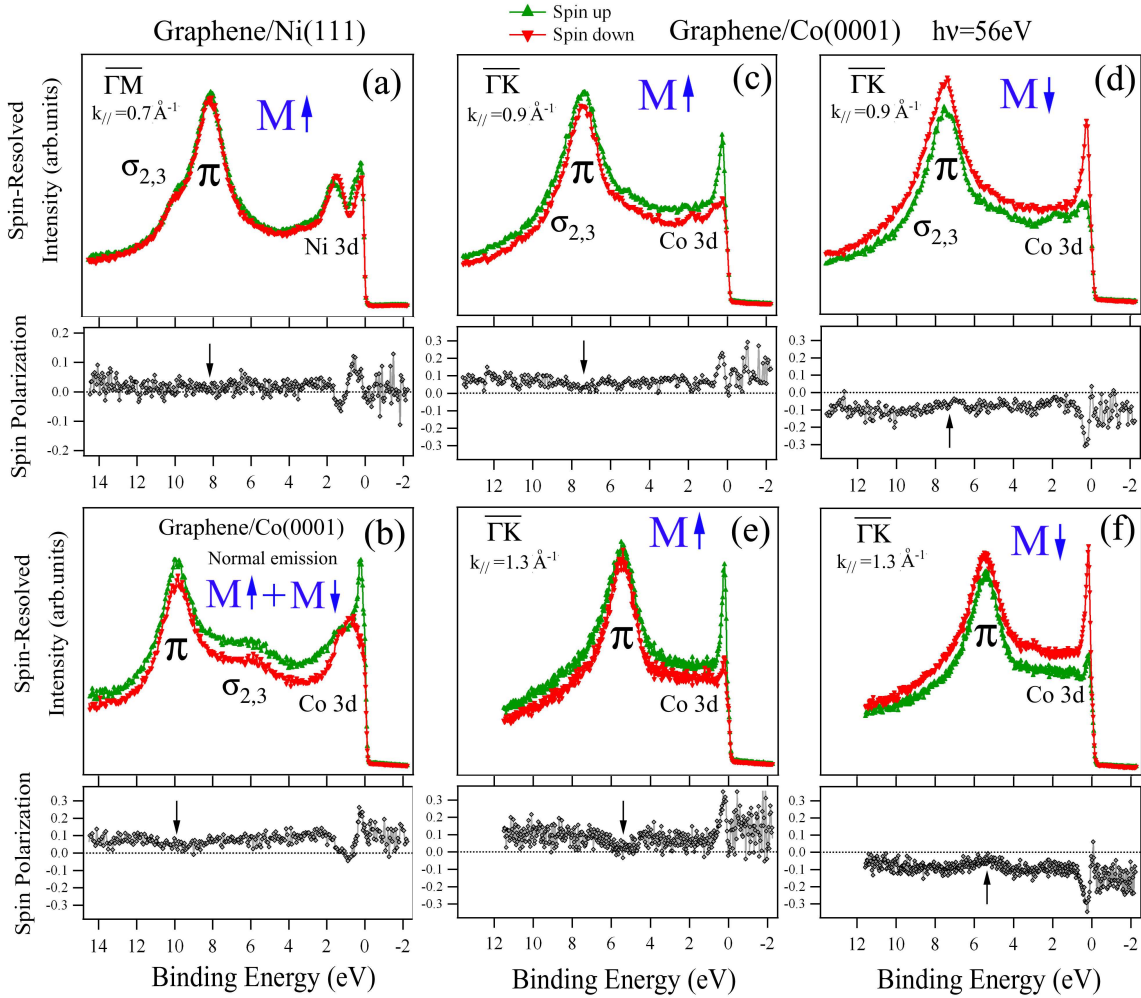


Figure 5.8: *Spin- and angle-resolved photoemission spectra of (a) graphene/Ni(111) along $\bar{\Gamma M}$ and (b)-(f) graphene/Co(0001) along $\bar{\Gamma K}$ directions of the SBZ, respectively. (b): Sum of the two opposite magnetizations, possible in normal-emission where the Rashba effect is absent. (a), (c) and (e): upwards $M\uparrow$ magnetization. (d), (f): downwards $M\downarrow$ magnetization. In addition, the in-plane spin polarization is given. Vertical black arrows indicate the BE position of the spin-integrated π -derived photoemission peak.*

effect has been demonstrated in several systems [207, 222–224]. On the other hand, in the presence of exchange interaction, the situation sketched in Fig. 5.6(d) would lead to an energy splitting of the form $\Delta_{SO} + \Delta_{ex} = \Delta_{ex} + 2\alpha_R k_{\parallel}$, which means that even if $\Delta_{SO} \gg \Delta_{ex}$ a Rashba+exchange effect of considerable size could be detected for large \mathbf{k}_{\parallel} vectors.

Figure 5.8 shows spin-resolved photoemission spectra for different magnetization directions of graphene/Ni(111) and graphene/Co(0001) measured at various k -points of the SBZ and at 56 eV photon energy. A maximum Rashba+exchange effect is expected when the three vectors \mathbf{E} , \mathbf{k} and \mathbf{M} are orthogonal to each other. Since Ni(111) and Co(0001) have the same growth orientation for graphene but their magnetization

directions perpendicular to each other (see Fig. 5.2(b) and 5.2(c)), measurements for graphene/Ni and graphene/Co are performed along the $\overline{\Gamma M}$ (Fig. 5.8(a)) and $\overline{\Gamma K}$ (Figs. 5.8(b)-5.8(f)) directions of the graphene SBZ, respectively. Figure 5.8(a) shows an off-normal spin-resolved photoemission spectrum of graphene/Ni(111) at $\mathbf{k}_{\parallel}=0.7 \text{ \AA}^{-1}$ measured for upwards magnetization ($\mathbf{M}\uparrow$). The Ni 3d states of Λ_3 and Λ_1 symmetries appearing in a BE range of about 0–2 eV from the Fermi level are spin polarized and exhibit an average exchange splitting of $\Delta_{ex} \sim 200 \text{ meV}$, in agreement with previous literature values [225]. This large difference between the two spin-up and spin-down channels, also visible in the spin-polarization ($p = (I^{\uparrow} - I^{\downarrow})/(I^{\uparrow} + I^{\downarrow})$) near E_F demonstrates that the Ni film underneath the graphene is remanently magnetized. In contrast, the graphene π states appearing at a BE of $\sim 8 \text{ eV}$ do not show such a difference, they are not spin-orbit and/or exchange split and the background-subtracted spin polarization is indistinguishable from zero ($p=(0\pm 2)\%$), which corresponds to a spin moment² of $(0\pm 0.02)\mu_B/\text{atom}$.

A similar result is demonstrated in Figs. 5.8(b)-5.8(f) for the graphene/Co(0001) system. Certainly, since the magnetic moment and exchange splitting of 3d states in Co is $\approx(3-4)\times$ larger than in Ni [103,168], we expect that the exchange splitting and/or the spin polarization of graphene π states should increase considerably. In this sense, an increase of the exchange splitting would lead to a larger energetic shift between graphene π states of opposite spin, while an increase in the spin polarization would lead to a change in their relative intensities even if the states are energetically degenerated. Note that the background spin polarization, which is smaller in graphene/Ni ($P\sim 2-3\%$) than in graphene/Co ($P\sim 6-10\%$), is to a first approximation proportional to the magnetic moment of the ferromagnetic substrate. Figure 5.8(b) shows spin-resolved spectra at $\mathbf{k}_{\parallel}=0$. Note that the spin-resolved spectra for opposite magnetization directions have been added with reversed spin channels. This was done to improve the statistics and is allowed here because the Rashba effect disappears in normal-emission (see Fig. 5.7(b)). In this case it is in principle possible to resolve Δ_{ex} of the graphene π band since the spin-orbit term Δ_{SO} is zero for $\mathbf{k}_{\parallel}=0$. We obtain $|\Delta_{ex}| \lesssim 0.045 \text{ eV}$. Figures 5.8(c)-5.8(f) show similar results at off-normal angles for upwards ($\mathbf{M}\uparrow$) and downwards ($\mathbf{M}\downarrow$) magnetization, where we would expect a larger effect due to the concomitant linear increase of Δ_{SO} with \mathbf{k}_{\parallel} . The results show how upon reversal of \mathbf{M} the roles of spin-up and spin-down electrons, as well as the sign of the spin polarization are reversed, confirming the ferromagnetic alignment of the system and its reversal. However, once again no spin splitting is resolved in this case, meaning that a Rashba-type spin-orbit effect is not present. Note that the measurements are done for sufficiently large \mathbf{k}_{\parallel} values in order to maximize the effect, corresponding to k-points of the SBZ which are placed approximately halfway between $\overline{\Gamma}$ and \overline{K} ($\mathbf{k}_{\parallel}=0.9\text{\AA}^{-1}$) and near \overline{K} ($\mathbf{k}_{\parallel}=1.3\text{\AA}^{-1}$). After averaging over all the measurements of Figs. 5.8(b)-5.8(f), the background-subtracted spin polarization of the π band amounts to $p=(-3\pm 4)\%$,

²In this case, background subtraction in spectra with opposite spins was performed in order to give an estimation of the relative changes in the spin polarization. Note that SARPES cannot be used to give an estimation of the absolute spin moment, in contrast to XMCD. The spin moment is obtained by assuming one electron per atom. This means that if the π band is 100% spin polarized, this electron will contribute with $1 \mu_B/\text{atom}$. The present crude estimate is appropriate in view of the simple band structure of the system.

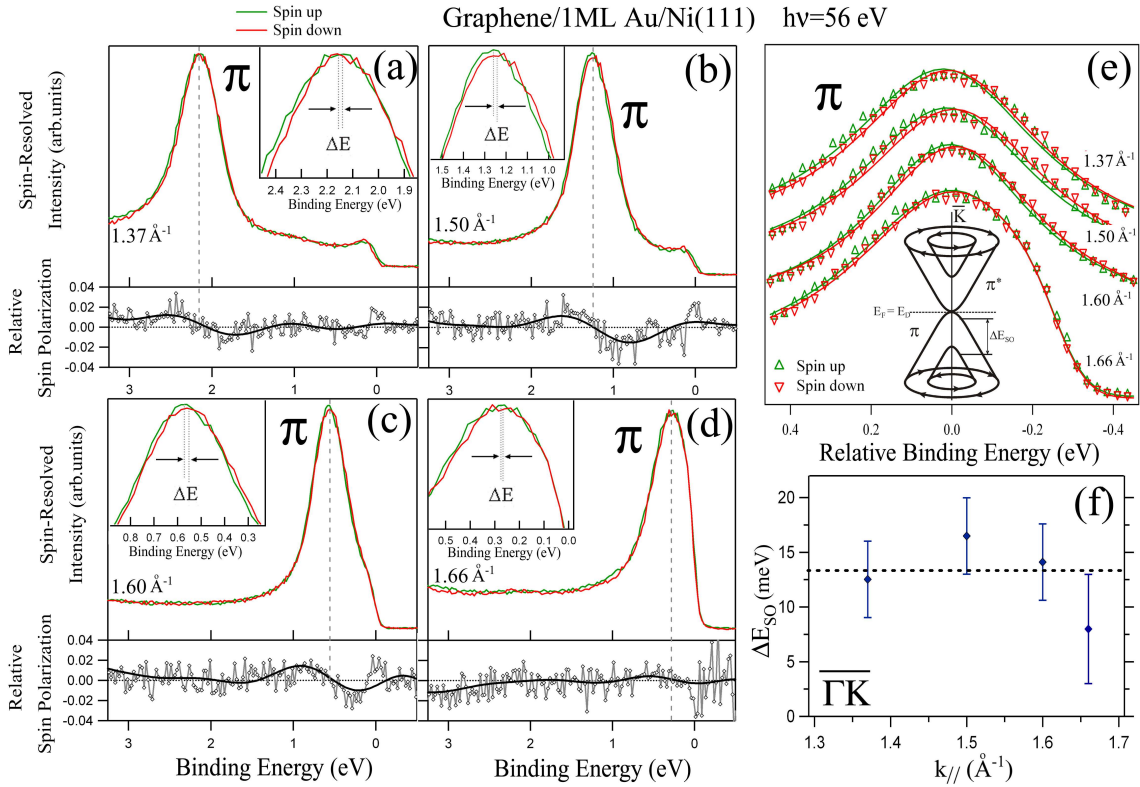


Figure 5.9: *Spin-resolved photoemission spectra of graphene/Au/Ni(111) along $\overline{\Gamma K}$ near the Fermi level. (a)-(d) Overview experimental spectra at various k -points. The in-plane spin polarization is shown, where the solid line gives an average, (e) π states at arbitrary energy offset together with a fit to the data and a model of the spin-polarized Fermi surface as an inset. (f) Spin-orbit splitting values at various \mathbf{k}_{\parallel} points of the graphene SBZ.*

which corresponds to a spin moment of $(-0.03 \pm 0.04)\mu_B/\text{atom}$ and is therefore negligible. This value is of comparable size to the one previously found in C/Fe multilayers, which amounts to only $\sim 0.05\mu_B$ per carbon atom at room temperature [226]. Note that the negative sign means antiferromagnetic coupling of the graphene to the Co. In view of these results, we conclude that the magnetic effect previously reported [203], which in principle would lead to a 100% spin polarization of the graphene π states, is not due to a Rashba-type spin-orbit interaction. Furthermore, the value $\Delta_{SO} \sim 225$ meV obtained in those experiments cannot be explained by the contribution of the ferromagnetic substrate, since Ni ($Z=28$) is probably not heavy enough for a Rashba splitting of that size. After completion of this work, the reasons for the different conclusions in Ref. [203] and the present work have been further investigated [219]. It was confirmed that such a magnetic effect does not exist neither for graphene on Ni(111) nor for graphene on Co(0001).

In Figure 5.9, further characterization by using spin resolution of the graphene/Ni system after intercalation of one monolayer of Au is presented. As we have shown above, graphene/Au/Ni and graphene/Au/Co systems exhibit very similar electronic

properties. Furthermore, we have shown that before intercalation of Au, the ferromagnetic substrate does not play an important role in the observed magnetic properties. The preparation method employed here allows us to fabricate graphene layers which are to a large extent decoupled from their ferromagnetic substrate. The strong weakening of the interaction between the graphene layer and the ferromagnet after surface intercalation leads to analogous magnetic properties when Ni(111) or Co(0001) are used as substrate. Therefore, in the following we will focus our study only on the graphene/Au/Ni system.

Figures 5.9(a)-5.9(d) show spin-resolved overview spectra at various k-points along the $\bar{\Gamma K}$ direction of the SBZ and in the vicinity of E_F where the π band exhibits a gapless and pronounced linear dispersion (see Fig. 5.4(c) and 5.5(b)). The vertical dashed lines correspond to the BE position of the spin-integrated π -derived photoemission peak. Zooms into the two spin components of the π band are given as insets to reveal a BE shift ΔE and thus the existence of a spin splitting of measurable size. The in-plane spin polarization is also shown, together with thick solid lines giving an average. In particular, we notice that the in-plane spin-polarization exhibits an inflexion point with its center of gravity located exactly at the BE of the spin-integrated π band peak, giving rise to the observed spin splitting. This effect will remain completely unnoticed in spin-averaging photoemission spectroscopy. In Figure 5.9(e), a zoom into the π band corresponding to the measurements of Figs. 5.9(a)-5.9(d) is given at an arbitrary BE offset, together with least-squares fits as solid lines from which the spin splitting is extracted and plotted as a function of \mathbf{k}_{\parallel} in Fig. 5.9(f). The fits were performed by Lorentzian functions plus a Shirley-like background both simultaneously convoluted by the energy resolution of the system in a single fitting function (see Eq. (4.4) of previous chapter). Therefore, the proximity of the π band to E_F for $\mathbf{k}_{\parallel}=1.66\text{\AA}^{-1}$, leads to a larger error bar and a smaller effect in its corresponding spin polarization. A spin splitting of (13 ± 3) meV in average is observed. It is useful to remark that the detection of spin splittings is not limited by intrinsic linewidths or the energy resolution of the photoemission setup (~ 100 meV) because the synchronous acquisition of the two partial spin spectra is done with different spin counters [50, 73, 74]. The reversal in sign of the spin splitting was verified upon reversal in sign of \mathbf{k}_{\parallel} and was found to be independent of the magnetization of the ferromagnetic substrate. Therefore, we identify it as Rashba-type spin-orbit splitting of the kind sketched in Fig. 5.7(b). Interestingly, it can be observed from Fig. 5.9(f) that the spin-orbit splitting is widely constant across the various k-points belonging to the linear part of the π band including E_F (see Figs. 5.4(c), 5.5(b) and 5.6(b)). This effect is a genuine consequence of the relativistic properties of quasi-freestanding graphene, from which a linear dispersion in the π states leads to constant Δ_{SO} values and a spin-polarized Fermi surface of the type shown in the inset of Fig. 5.9(e) [227, 228]. Since a value of $\Delta_{SO} \sim 13$ meV is by three orders of magnitude larger than the spin-orbit splitting of ~ 0.01 meV for freestanding graphene [229, 230], we conclude that extrinsic rather than intrinsic contributions play a dominant role on the enhancement of the spin-orbit splitting in quasi-free standing graphene. We conclude that the extrinsic spin-orbit coupling originates from the intercalated Au at the graphene interface and its high nuclear charge. This extrinsic origin was recently confirmed theoretically, and it was shown that it leads to a coupling of

spin and pseudospin in graphene [227, 228]. In a similar way, because of the equivalent sublattices A and B in graphene the band dispersions measured in this work can be assigned to a pseudospin, the spin of which is connected to the propagation direction \mathbf{k}_{\parallel} . Because the Rashba effect reverses with the sign of \mathbf{k}_{\parallel} the experimental observation of Fig. 5.9 ultimately demonstrates that the Rashba effect couples spin and pseudospin in graphene.

5.6 Summary of conclusions

In summary, by using angle-resolved photoemission spectroscopy, we have shown how it is possible to fabricate quasi-freestanding graphene overlayers of high quality by simply monitoring the changes in the electronic structure of the samples during the different steps followed in their preparation. We have focused on the electronic properties of graphene grown on Ni(111) and Co(0001) and shown how the intercalation of one monolayer of Au leads to the formation of a relativistic Dirac cone with a gapless linear π -band dispersion near \bar{K} and a Dirac crossing energy equal to the Fermi energy. Spin-resolved photoemission measurements from the graphene π -band show that the ferromagnetic polarization and the spin-orbit interaction of graphene/Ni(111) and graphene/Co(0001) are negligible while, after intercalation of one monolayer of Au between graphene and Ni(111), the system is spin-orbit split by the Rashba effect.

Chapter 6

Imaging of ps-resolved magnetization dynamics in magnetic microstructures

This chapter is devoted to study the time evolution of collective excitations in small magnetic structures. In the following, a picosecond time-resolved x-ray magnetic circular dichroic-photoelectron emission microscopy study of the evolution of the magnetization components of a microstructured permalloy ($\text{Fe}_{19}\text{Ni}_{81}$) platelet comprising three cross-tie domain walls is presented. A laser-excited photoswitch is used to apply a 80 Oe triangular magnetic pulse of 160 ps duration. The detailed comparison between the experimental results and micromagnetic calculations leads to good agreement, both in time and frequency, and illustrates the large angle precession in the magnetic domains with magnetization perpendicular to the applied pulse. Further insight into the magnetization dynamics of the system is achieved beyond the spatial resolution of the experiment by analyzing the complex local behavior of the magnetic vortices and antivortices which results from the simulations. This analysis indicates that during the global dynamical process of the magnetization in the system, the magnetic vortices switch their core magnetization while the antivortices remain unperturbed.

6.1 Introduction

Over about the last ten years, the important progress in the experimental techniques for time-resolved magnetic imaging and the increasing capabilities of numerical simulations have given the possibility to study the magnetization dynamics of ultra-small magnetic elements on the pico- and nanosecond time scales in combination with spatial resolution. One of the most important aspects of magnetization dynamics for spintronics applications is the understanding of magnetization reversal processes which occur in nano- or micron-sized magnetic elements in ultrashort time scales, as there is a strong demand to push the densities and speeds of future spintronics devices to the limit. On this pathway, the future evolution of spintronics towards quantum information processing strongly depends not only on the investigation of the fundamental questions of magnetism at the nanoscale, but also on the understanding of the dynam-

ical behaviour of magnetic and spin systems in order to overcome the limitations of magnetic switching processes. All these aspects of modern magnetism can be exploited in current and near-future magnetic recording media such as spin valves, magnetic tunnel junctions, giant magnetoresistive elements or magnetic random access memories (MRAMs) to name a few examples [2, 3, 231, 232].

Apart of the technical importance due to the potential applications in modern spintronic devices, ferromagnetic nano- or microstructures are very interesting for fundamental studies since the static and dynamical behaviour of the magnetization in small confined geometries is non-trivial. On the one hand, this includes finite-size effects contributing to the global behaviour of the magnetic anisotropy in the system, and on the other hand, it holds for the complex temporal evolution of the magnetization vector in ultrashort time scales. Particularly, the combination of photoelectron emission microscopy (PEEM) with pulsed photon sources such as synchrotron radiation or lasers has opened a highly promising way for various time-resolved experiments with high spatial and temporal resolution. Furthermore, nowadays extremely high temporal resolution is possible with pulsed laser sources. By using an all-optical pump-probe technique for time-resolved PEEM experiments, an ultimate temporal resolution of 30 attoseconds has been achieved, allowing to monitor the phase evolution of localized plasmon excitations [233]. Among several possibilities, this type of experiments offers the possibility of measuring hot-electron lifetimes, which could be exploited as contrast mechanisms in the femtosecond regime. This issue is also related to the femtosecond spin dynamics of ferromagnetic thin films and nanostructures probed by spin-polarized two-photon photoemission electron microscopy experiments [234]. Here we use a different approach than in all-optical experiments, which relies on the element selectivity provided by synchrotron radiation and on its variable polarization, giving access to contrast mechanisms such as x-ray magnetic circular dichroism (XMCD) (see section 2.2). As described in section 3.3, in this type of experiment the ultimate temporal resolution is limited by the width of the synchrotron pulse, which for x-rays and in the BESSY II single bunch operation mode is about 50-70 ps. Although the fundamental time scales for magnetization reversal processes range down to a few femtoseconds, at present the technologically interesting time scales are of the order of sub-nanoseconds.

On such short time scales, precession of the atomic spins or precessional switching [235–238], rather than domain creation or domain wall motion [239–241], dictate the response of quasi-two-dimensional magnetic structures. When finite-sized, soft magnetic microstructures are considered, the demagnetization energy forces the formation of flux-closure magnetic domain patterns that may contain domain walls (DWs) and circular or cross Bloch lines, also known as vortices or antivortices. These magnetic structures react at different times to fast magnetic pulses, resulting in a complex global behavior. In the simplest case, the response of a permalloy squared structure to a fast magnetic pulse comprises precession in the domains, oscillation of the domain walls and changes in the vortex positions. The two latter may generate spin waves that interact with those originated at the domains [242–244]. Furthermore, due to its potential application in magnetic storage media, vortex core switching, a process in which the out-of-plane component of the magnetization is reversed while retaining the overall in-plane pattern, has lately been at the focus of experimental [245, 246] and theoretical

investigations [247–251]. Here we present a study which includes all the aforementioned aspects by comparing temporally resolved microscopy results of a permalloy (Py) rectangular microstructure comprising three cross-tie DWs with micromagnetic calculations based on the Landau–Lifshitz–Gilbert equation. The magnetic response includes the magnetization precession in the domains with magnetization oriented perpendicular to the magnetic field pulse direction, as well as the oscillation in DWs, vortices, and antivortices. From the micromagnetic calculations we conclude that the vortices show much larger motions as compared to the ones of the antivortices, and that in certain cases the perpendicular component of the vortex magnetization can be switched at the applied pulse strength.

Taking into account that laser-pump synchrotron-probe time-resolved XMCD-PEEM experiments were not performed in BESSY II before completion of this work, the aim of the present chapter is (i) to demonstrate that technically the experiment is possible and (ii) to induce a faster magnetic response in the precessional motion of the magnetization of the system as compared to previous experiments in similar systems. Moreover, we go beyond the experiment by providing OOMMF calculations which allow us to conclude that the relatively fast precessional motion of the magnetization we observe is directly linked to the nature of the vortex/antivortex dynamics and its response to the external magnetic perturbation. In particular, the simulations indicate that the response of the vortex cores is the main source of spin waves, while the antivortices remain unaffected. This includes the time-dependent reversal of the vortex core polarization, a process which is beyond the limit of detection in modern experiments.

6.2 Fundamentals of magnetization dynamics

In this section, a brief introduction to the fundamentals of magnetization dynamics is given. After introducing the micromagnetic approximation, the different contributions to the total energy of a magnetic system are described. This is followed by a discussion of the Landau–Lifshitz–Gilbert equation for magnetization dynamics.

6.2.1 The micromagnetic approximation

Firstly, a few words should be devoted to the fact that magnetism at different length scales is generally described by different theoretical approximations. Since the length scale in magnetism can vary over many orders of magnitude from astronomic to atomic dimensions of a few Å, completely different theoretical descriptions going from classical to quantum mechanics are required. The most detailed study of the magnetic properties of solids in atomic dimensions, in particular of 3d ferromagnetic transition metals, is given by the theoretical description of the spin-dependent electronic structure of these systems. In chapter 4 of this thesis, it has been shown that local many-body approaches for correlated electron systems such as LSDA+DMFT or LSDA+3BS do a fair job in describing many of the spin-dependent properties of bcc Fe and hcp Co thin solid films. In these theories, the electron spin is one of the fundamental quantities that governs the effect of electronic correlations. In this case, the ideal crystal is defined by a unit cell which may contain several (up to ~ 100) atoms and is repeated

indefinitely according to translational symmetry, thus simplifying the calculations to a large extent. Periodic boundary conditions are used to describe the infinite crystal by simply knowing all the properties in one unit cell. The other point is of course the time scale, since spin-dependent quasiparticle excitations are as fast as a few femtoseconds.

However, it is obviously not possible to describe all relevant aspects in magnetism only with quantum electron theory if other important magnetic phenomena take place at larger length scales than one unit cell. This means, for example, that the pure electronic description of a complicated magnetic domain structure in a ferromagnetic particle of hundreds of unit cells in size, in which long range magnetostatic interactions dominate at length scales of several μm , is basically impossible with quantum electron theory and therefore a completely different theoretical approach is required. Compared to the ultrafast electronic excitations, this also applies for the slower time scale of the dynamical motion of different magnetic structures, such as DWs or spin waves, where displacement amplitudes larger than $1 \mu\text{m}$ typically occur.

In the next level of approximation we have the atomistic Heisenberg model [252, 253], which assumes each atom of a ferromagnetic solid to carry a magnetic moment which is interacting with the magnetic moments of the adjacent atoms at each lattice site. However, as mentioned above, since in many cases the length scales of magnetic interactions are much larger than the lattice constants of a solid, or other magnetic structures such as DWs may extend over several hundreds of nm in a bulk material, the Heisenberg model becomes impractical.

Since the main focus in this chapter is precisely the study of the dynamical evolution of the complex magnetic domain structure of a micron-sized Py rectangular platelet comprising several magnetic domains and DWs, we apply the so-called *micromagnetic approximation*. In this approximation, the transition from the atomistic to the microscopic representation is done by replacing the summation over the effective spins of different electronic states by a summation of microscopic magnetic moments which is then replaced by an averaged quantity, the magnetization \mathbf{M} . Two of the main tasks of micromagnetic problems consists in calculating the spatial distribution of the magnetization $\mathbf{M}(\mathbf{r})$ and its temporal evolution $d\mathbf{M}/dt$, assuming that it preserves its magnitude $|\mathbf{M}| = M_S$, where M_S is the saturation magnetization.

6.2.2 Contributions to the total micromagnetic energy

In order to understand the magnetic domain configuration of a micron-sized ferromagnet, it is useful to briefly revise the different contributions to the total micromagnetic energy. In a stable equilibrium state, the magnetization $\mathbf{M}(\mathbf{r})$ tends to minimize the total magnetic energy of the system E_M , reaching either a global or a local minimum. If several local minima can be reached, the magnetic history of the sample defines the most suited equilibrium configuration. In most of the micromagnetic calculations, E_M is minimized by a variational calculation or by means of converged solution of the Landau–Lifshitz–Gilbert (LLG) equation (discussed in the next section) in which the condition of convergence is reached when $\mathbf{M}(\mathbf{r})$ does not change further in time. In the presence of an external magnetic field \mathbf{H}_{ext} , a magnetic structure containing a single

layer of magnetic material exhibits a total magnetic energy of the form:

$$\begin{aligned} E_M &= E_{MCA} + E_{ex} + E_{demag} + E_{ext} = \int_V e_M dV \\ &= \int_V [K_{MCA} + A_{ex}(\nabla \cdot \mathbf{m})^2 - \frac{\mu_0}{2} \mathbf{H}_{demag} \cdot \mathbf{M} - \mu_0 \mathbf{H}_{ext} \cdot \mathbf{M}] dV \end{aligned} \quad (6.1)$$

where μ_0 is the vacuum permeability and e_M is the micromagnetic energy density, which is integrated over the volume V of the sample to account for all the magnetic moments. The micromagnetic energy terms are the magnetocrystalline anisotropy (E_{MCA}) and the exchange (E_{ex}), stray field (E_{demag}) and Zeeman (E_{ext}) energies. The equilibrium orientation of $\mathbf{M}(\mathbf{r})$ in the sample depends on the competition of these terms [254, 255]. The exact mathematical derivation of the energy terms and a discussion of their relative importance can be found in textbooks [256, 257] and shall not be repeated here. Note that other energy terms arising from the magnetoelastic or surface anisotropies are not considered here. The electronic origin of the first term, the magnetocrystalline anisotropy E_{MCA} , relies in the spin-orbit coupling and the crystal field generated by neighbouring atoms in the system. It strongly depends on the crystal structure of the material and thus on the magnetocrystalline anisotropy constant K_{MCA} (for more details also see [258]). In simple micromagnetics, this term can be understood as the energy needed to align the magnetization from one crystallographic direction to another. The second term, the exchange energy E_{ex} , represents the short-range exchange interaction between neighbouring magnetic moments and it depends on the exchange anisotropy constant A_{ex} and $\mathbf{m} = \mathbf{M}/M_S$. It can be obtained from a Taylor expansion of the Heisenberg Hamiltonian assuming small-angle deviations between neighbouring moments [257, 259]. It represents the tendency to keep neighbouring magnetic moments parallel to each other. The third term, the stray field energy E_{demag} , arises from the long-range magnetostatic interaction between magnetic moments in the sample. It depends on the stray magnetic field or demagnetizing field \mathbf{H}_{demag} , which contributes to a reorientation of $\mathbf{M}(\mathbf{r})$. The stray field is determined by the dipolar interaction between magnetic moments and by the shape of the sample, i.e. the shape anisotropy, which is also a pure magnetostatic effect. A quantitative description of the shape anisotropy requires the calculation of the demagnetization factors, and examples on different samples geometries can be found, e.g. within the Stoner-Wohlfarth model [260]. Finally, the Zeeman term E_{ext} represents the energy of the interaction between the magnetization and the external applied magnetic field \mathbf{H}_{ext} .

6.2.3 The Landau–Lifshitz–Gilbert equation

If a short perturbation like a magnetic field pulse is applied to a micron-sized magnetic element, the magnetization will respond to this perturbation following a more or less complex trajectory around the direction of the applied field, a process which typically occurs in the pico- and nanosecond time scales. This fast dynamical evolution of the magnetization can be described by the fundamental Landau–Lifshitz–Gilbert

(LLG) equation [261] for magnetization dynamics:

$$\frac{d\mathbf{M}(t)}{dt} = -\gamma[\mathbf{M}(t) \times \mathbf{H}_{eff}(t)] + \frac{\alpha}{M_S}[\mathbf{M}(t) \times (\mathbf{M}(t) \times \mathbf{H}_{eff}(t))] \quad (6.2)$$

where α is the phenomenological Gilbert damping constant and $\gamma = \frac{g|e|\mu_0}{2m_e}$ the gyro-magnetic ratio, g being the Landé factor, e the electron charge and m_e its mass. The so-called effective field \mathbf{H}_{eff} , can be written as:

$$\mathbf{H}_{eff}(t) = -\frac{1}{\mu_0} \frac{\partial e_M}{\partial \mathbf{M}(t)} \quad (6.3)$$

The effective field is defined as the variational derivative of the micromagnetic energy density e_M with respect to the magnetization. Its formal derivation can be found, e.g. in [262]. It contains all effects from micromagnetic energy contributions due to external and internal magnetic fields. This means that after a short external magnetic perturbation of the system, the effective field is only determined by the internal magnetic properties of the sample. Besides, note that only the component of \mathbf{H}_{eff} perpendicular to \mathbf{M} has a strong influence on the magnetization dynamics, since it exerts a torque on \mathbf{M} of the form $-\gamma(\mathbf{M} \times \mathbf{H}_{eff})$. Going back to Eq. (6.2), we see that it contains two terms. The first term is proportional to γ and related to the precession of the magnetization around the effective field, while the second term is proportional to α and related to the damping of the magnetization due to energy dissipation. This is illustrated in Figs. 6.1(a) and 6.1(b). In Fig. 6.1(a), the damping term is neglected ($\alpha = 0$) and thus the precession of the magnetization around the effective field once initiated would continue forever. This is a fictitious situation which contradicts the experimental observation in which the magnetization can be rapidly aligned along an external magnetic field. In Fig. 6.1(b), the damping term is considered and as a result \mathbf{M} follows a spiral trajectory around the effective field which ends when both are aligned with respect to each other.

The micromagnetic calculations shown in this chapter were performed with the free access Object Oriented MicroMagnetic Framework (OOMMF) software package, which solves the Landau-Lifshitz-Gilbert (LLG) equation and allows to use an adaptative mesh of variable size in the volume of the sample. A detailed description of the working principle of OOMMF can be found in [263]. An example of the previously mentioned converged solution of the LLG equation for a 5 nm thick Py rectangle with $3 \times 1 \mu\text{m}^2$ in size is shown in Fig. 6.1(c). A $5 \times 5 \times 5 \text{ nm}^3$ cell size and typical magnetic parameters for Py were used as input (saturation magnetization $M_s = 796 \text{ kA}\cdot\text{m}^{-1}$, exchange constant $A_{ex} = 1.3 \times 10^{-11} \text{ J}\cdot\text{m}^{-3}$, magnetic damping constant $\alpha = 0.01$, and uniaxial magnetocrystalline anisotropy $K_{MCA}=0$). The maximum cell size is determined by the so-called exchange lengths [264]. In soft magnetic materials, it is given by the magnetostatic exchange length of the stray field $l_s = \sqrt{2A_{ex}/\mu_0 M_s^2}$ ($\sim 5.7 \text{ nm}$ for Py), whereas in hard magnetic materials, by the magnetocrystalline exchange length $l_K = \sqrt{A_{ex}/K_{MCA}}$. Both l_s and l_K are directly related to the width of Néel [265] and Bloch [266] DWs: while in the former the rotation of the magnetization between two domains with antiparallel magnetization occurs in the film plane, in the latter it

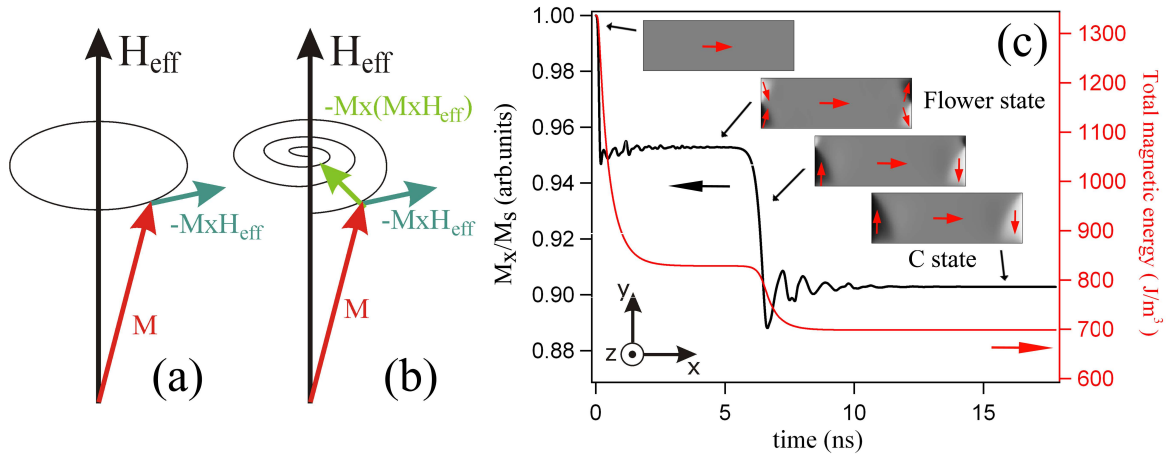


Figure 6.1: Sketch of the dynamics of the magnetization \mathbf{M} given by the two terms of the LLG equation ((a) and (b)). If the Gilbert damping is neglected ($\alpha = 0$) (a), \mathbf{M} will rotate forever in a trajectory of constant radius around \mathbf{H}_{eff} . When $\alpha \neq 0$ (b), \mathbf{M} will follow a spiral trajectory, reaching equilibrium when it is coaligned with $(H)_{\text{eff}}$. (c) An example of a converged solution of the LLG equation for a Py rectangle with $3 \times 1 \mu\text{m}^2$ in size, without external applied magnetic field. In the initial configuration, the Py rectangle is homogenously magnetized along the long edge. The magnetization oscillates around different equilibrium configurations until convergence. After a first local energy minimum, the so-called Flower state relaxes into a C-state.

occurs in the out-of-plane direction. In Fig. 6.1(c), the Py rectangle is homogenously magnetized along the long edge in the initial state. The magnetization oscillates around the effective field in different equilibrium configurations until convergence. In a first local minimum of the magnetic energy, the domain configuration reaches the so-called Flower state, and by further energy minimization, it relaxes into a C-state. The Flower and the C-states are well-known high-remanent states in thin-film elements [267]. Both are composed of very stable end domains which may represent well-defined nucleation sites for the switching of the magnetization in a reproducible fashion. For a soft material like Py, they mainly arise from the competition between the magnetostatic and exchange energies, since the averaged magnetocrystalline anisotropy is negligible. The best minimization strategy of the magnetostatic energy results from avoiding the sources of the stray field, i.e. the magnetostatic surface charges or magnetic poles, known as the Brown's pole avoidance principle [262]. In the case of the Flower or C-states, the partial alignment of \mathbf{M} with the short edges leads to a reduction of the surface charges, while a large homogenous magnetization configuration still maintained in the microstructure since the exchange energy is also minimized.

6.3 Experimental details

As discussed in section 3.3, laser-pump synchrotron-probe time-resolved XMCD-PEEM experiments are of particular importance for magnetic investigations since both the high spatial and temporal resolution, together with chemical and magnetic sensi-

tivity are fulfilled together. In these experiments, magnetic dichroic effects manifest in sample areas with different magnetization directions by different intensities (see sections 2.2 and 3.3.3). Furthermore, time-dependent effects can be investigated by applying magnetic field pulses of several picoseconds to the samples. These pulses can be generated by shining a femtosecond laser onto a photoconductive switch placed between the two ends of a stripline which are under a constant voltage difference (see section 3.3.4). By tuning the delay time between the laser and the x-ray pulses, the evolution of the magnetization can be temporally and laterally resolved [268]. Firstly, such an experiment requires special sample holders that can provide the voltage difference to the stripline ends and protect the stripline-sample unit from the high-voltage difference applied to the first lens of the microscope to maximize the extracted electron yield. Secondly, another important requirement is stabilization of a magnetic domain pattern in the samples such that they can be fabricated in a reproducible and easy way. This is also important for technological applications in magnetic recording media, where a non-destructive read-back of the bit pattern and a recovery of the input information are needed. This means that the restoration of the initial magnetic configuration in the sample during stroboscopic measurements is a very important issue. Since the detection systems work at speeds ranging from milliseconds to several seconds, in general much longer times are needed to obtain an integrated magnetic signal which is free of noise. This means that the initial magnetization of the system should return to its initial configuration over million of times in a single set of stroboscopic measurements.

We have fulfilled this requirement by optimizing the preparation of Py microstructures of about 22 nm thickness by magnetron sputtering at room temperature without post-annealing. For films with such large thicknesses, magnetron sputtering provides much lower roughness and smoother interfaces as compared to the ones made by evaporation employed in previous chapters. Without the need of ultrahigh vacuum, it leads to smooth interfaces and a well-ordered growth which is perfectly maintained even for areas as large as several cm^2 , thus allowing to grow several samples at once. After deposition, the samples were transported to the PEEM chamber in air by simply covering the films with a 1 nm thick Cu capping layer to avoid oxidation.

6.3.1 Sample holder for time-resolved investigations in the Focus IS-PEEM

In this section, a recently developed custom-made Omicron-compatible [269] sample holder suited for time-resolved XMCD-PEEM experiments is presented¹. It is compatible with the Focus-IS PEEM integral sample stage and incorporates chip carriers that host the sample. It includes a sample plate with four contacts to the chip carrier where the sample is mounted. Covering the sample holder, a 6 mm diameter mask protects electrostatically the sample from the extractor lens voltage while keeping the imaging quality unaffected. A sketch and a photograph of the mounting system are shown in Figs. 6.2(a) and 6.2(b). The sample was described in greater detail in section 3.3.4. The sample substrate consists of a GaAs film ($7 \text{ mm} \times 7 \text{ mm} \times 0.3 \text{ mm}$ in size) with

¹The final construction was carried out by the technicians and scientific collaborators at the department of Prof. W. Kuch at the Freie Universität Berlin.

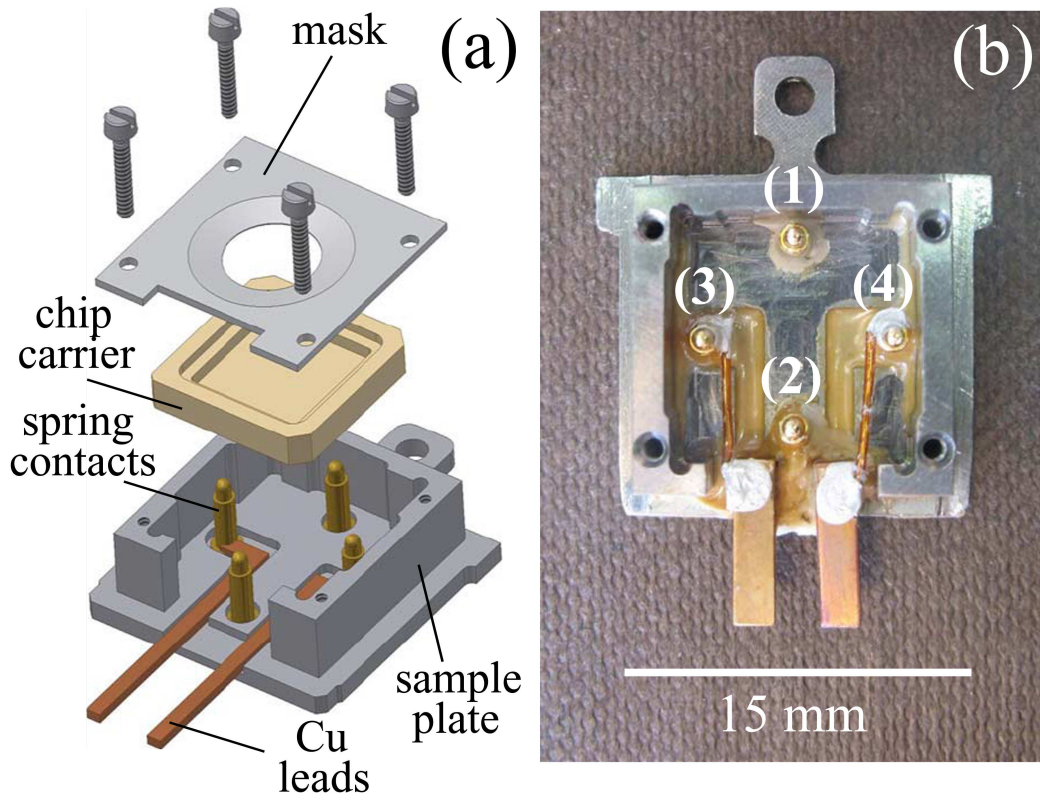


Figure 6.2: (a) Sketch of the sample holder comprising the sample plate with spring contacts, chip carrier, and mask. In (b), a photograph of the sample plate with mounted spring contacts (numbered from (1) to (4)). The spatial scale is also given.

an additional $1\ \mu\text{m}$ thick GaAs film grown on top by MBE at low temperature (LT-GaAs), used to improve the performance of the Auston switch [270]. The stripline is surrounded by a waveguide on ground potential used to improve the homogeneity of the field along the stripline.

As mentioned in section 3.3.4, during each laser pulse shining on the switch, the charge carriers created in the LT-GaAs substrate lead to a short current pulse which propagates along the Au stripline. The current pulse arrives at the microstructures with some delay and creates a short magnetic field pulse which is oriented perpendicular to the Au stripline. The duration of the magnetic excitation depends on the time scale of the laser pulse but the determining factor is the lifetime of the electron-hole pairs created in the LT-GaAs substrate, which typically leads to magnetic pulses of several tenths of picoseconds. Each finger of the photoconductive switch, which is a gap in the Au stripline reaching all the way down to the semiconducting substrate, is relatively covered by the mask, while the magnetic microstructures are placed below a circular opening in its center. The main improvements of this mounting system are longer sample lifetimes and the possibility to apply much higher currents in the stripline thus providing intensified magnetic field pulses at the microstructure position.

Among all the technical difficulties which were found during the time-resolved

XMCD-PEEM experiments, two major challenges were to apply a dc voltage to the ends of the stripline and to keep the sample surface as clean as possible during long periods of time. Previous sample holder mounting systems comprised the use of silver glue to electrically contact the two pads of the GaAs wafer to two Cu leads mounted onto the sample plate and isolated from it. Under the high-voltage potential of the extractor lens, the silver glue was accidentally degassing in bursts, and in most of the cases this caused the complete destruction of the stripline. Other problems raised in the region of the electrical contacts or near the Auston switch, when all the system was in measurement conditions. In most of the cases it was impossible to increase the dc voltage applied to the ends of the stripline above certain values before the breaking of the switch. This issues did not allow us to achieve currents in the stripline providing magnetic field pulses which were intense enough in order to observe a pronounced dynamical effect in the magnetization of the microstructures.

In order to solve all these technical challenges, a completely new mounting scheme was adopted, avoiding the use of silver glue on the sample surface and keeping the electrical connections away from the extractor lens. As shown in Fig. 6.2(a), this scheme is composed of a modified Omicron-compatible Ti sample plate where a leadless chip carrier [271] is placed on top. The chip carrier was wire bonded before every experiment to the four sections of the sample, two of them located in the stripline and two in the waveguide. The Au pads on the back side of the chip carrier touch the four spring contacts [272] when the chip carrier is pressed down by the sample holder mask which is screwed from above. Two of these contacts, numbered as (1) and (2) in Fig. 6.2(b), are equipotential with the sample holder and connected to the two sides of the waveguide. The other two spring contacts, (3) and (4), are isolated from the sample plate and connected to the Cu leads at the bottom side of the sample plate. These leads enter in physical contact with two corresponding spring hooks mounted on the PEEM manipulator when the sample holder is properly inserted into it. From there, two of the available wires of the feedthrough plugs are used to power the stripline voltage with a standard power supply. Since the samples were relatively close to the power supply, and the stripline voltage was applied continuously, impedance matching between the stripline and the cables was not considered important.

Once the sample was mounted and all the electrical connections between the chip carrier and the spring contacts checked, the mask was screwed to ensure the mechanical stability of the chip carrier. Under working conditions, the 6 mm diameter opening in the mask allowed the laser and x-ray beam to access the stripline. Note that since the switching region in the stripline was partially covered by the mask, the laser beam had to be extremely well aligned and very stable in a small area of the sample of about $100 \mu\text{m}^2$ and at almost grazing incidence ($\lesssim 20^\circ$). The opening in the mask acts as an extra lens of the electron microscope that reduces the electron yield captured by the microscope. However, its dimension and height with respect to the stripline (~ 0.8 mm) could be chosen so that the four wire bonding sets and the photoconductive switch were protected from the extractor voltage, and this resulted in a substantial increase of the lifetime of the samples allowing as a consequence the experiments to be performed. From the practical point of view, a quick in-vacuum sample transfer to the PEEM system and the exchange of the samples was also provided. All in all, the

most important advantages of the new sample mounting system were (i) a remarkable increase in the lifetime of the switch under normal operation conditions of laser power and extractor voltage, allowing in some cases to measure the same sample for several weeks, (ii) maintenance of the imaging properties of the microscope and the profile of the magnetic field pulses and (iii) higher currents through the stripline allowing to reach magnetic fields of almost one order of magnitude larger than in previous mounting schemes. Concerning the imaging properties, Fig. 6.3 shows characteristic XMCD-PEEM images of two 22-nm-thick Py microstructures on top of a 10 μm wide Au stripline, obtained with the old mounting (Fig. 6.3(a)) and the new sample holder (Fig. 6.3(b)). The images were acquired at a photon energy of 707 eV, corresponding to the Fe L_3 edge.

The procedure to obtain these images was described more in detail in section 3.3.3. Areas with different intensities inside the structures correspond to different magnetic domains in which the magnetization is oriented along different directions with respect to the propagation direction of the photon beam. This is indicated by arrows in some of the magnetic domains in both Figs. 6.3(a) and 6.3(b). While in Fig. 6.3(a) the magnetization is mainly pointing along an intermediate direction, most of the areas in the microstructures of Fig. 6.3(b) exhibit closed flux lines forming a magnetic domain patterns of the Landau type, as the ones described in section 3.3.3. It is clear that the spatial resolution in these images is not compromised by the mask of the new sample holder, although the exposure time was about four times longer for the image in Fig. 6.3(b). Regarding the properties of the magnetic field pulses produced by the stripline with the new mounting scheme, Fig. 6.4 shows a comparison between the different pulse shapes obtained with the old and the new sample holders measured

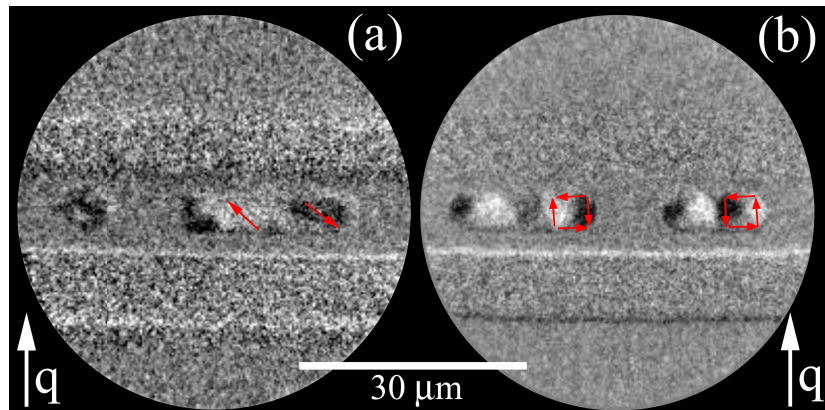


Figure 6.3: XMCD-PEEM images measured (a) with the previous mounting scheme and (b) with the new sample holder. Two magnetic structures on top of the stripline are imaged in each case, displaying brighter and darker areas in regions with opposite magnetization directions. The orientation of the magnetization inside some domains (red arrows) and the propagation direction of the photon beam are indicated. Most of the areas in the microstructures exhibit closed flux lines forming a magnetic domain patterns of the Landau type.

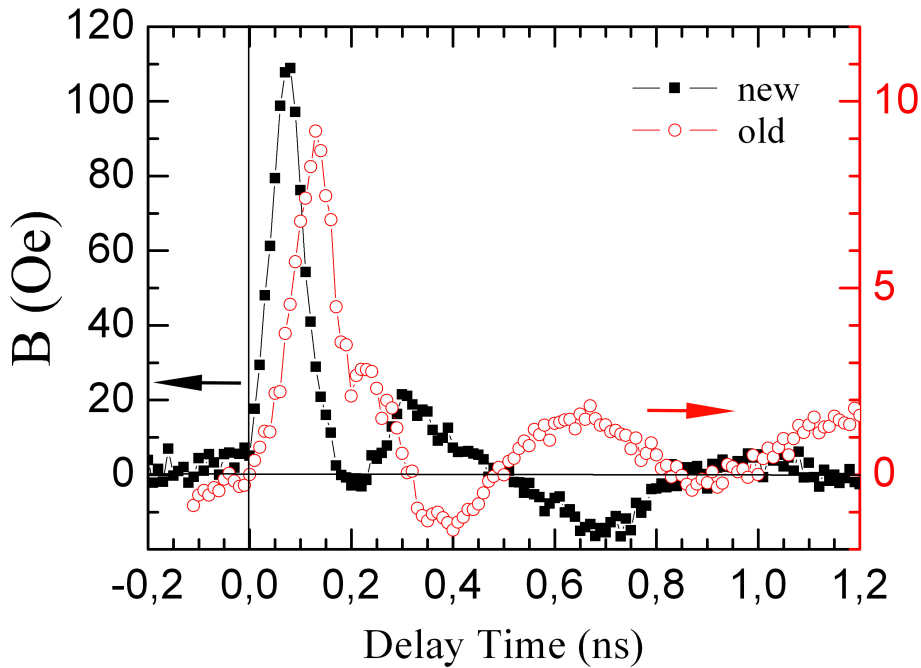


Figure 6.4: *Temporal evolution of the magnetic field pulses produced by the stripline with the new setup (full black squares) and with the previous one (red open circles).*

with the same parameters of laser power and applied voltage. The pulse shapes are derived from the image distortion in the border region between the stripline and the waveguide, normalized to the average current flowing through the stripline [268]. This procedure, which also allows for the accurate determination of the so-called *time zero* of the experiment (briefly introduced in section 3.3.5), will be explained a little bit more in detail in the next section.

From Fig. 6.4, we see that in both cases, the pulse shape comprises a first main peak followed by a number of oscillations, a typical ringing effect from current reflections in the different parts of the stripline circuit. The main difference is that with the new design, a narrower pulse of about 70 ps FWHM is obtained, together with an intensified magnetic field strength of approximately ten times larger maximum as compared with the previous sample holder setup.

6.3.2 Determination of the time zero and pulse shape of the experiment

In our stroboscopic laser-pump synchrotron-probe experiment, the time scale is always defined with respect to the pump (magnetic field) pulse. This is known as the time zero of the experiment, as mentioned earlier. This means that before every experiment, the position of the pump pulse on the time line needs to be accurately determined. This is also necessary every time a new sample is used for measurements, since the propagation of the pulse along the stripline may vary from sample to sample.

As mentioned in section 3.3.5, a reference signal produced by the synchrotron pulses in an avalanche photodiode placed in the beamline at about 3 m distance from the sample is used as a relative time scale in a first step. After time zero determination, all the delay values in the measurements are referenced to it, leading to the absolute time scale of the experiment.

The basic principle for time zero determination is based on the additional deflection which happens to the emitted electrons when the current pulse is traveling through the stripline. Since the two waveguides around are electrically grounded, a current pulse propagating along the stripline causes an additional electric field pulse between the stripline and the two waveguides. This field is superimposed on the extractor field of the immersion lens system of the PEEM. As a result, the imaging parameters change a little bit and produce a relatively small but detectable change in the magnification of the image. The measurement of this change also allows to record the shape of the magnetic pulse, as previously plotted in Fig. 6.4. The size of the change depends on the magnitude of the electric field pulse, and therefore on the current applied through the stripline. This effect, also known as chromatic aberration of the magnification [273], leads to the so-called *breathing effect* of the image as a function of the delay time between the magnetic field and synchrotron pulses.

In Fig. 6.5, an example of the procedure to determine the time zero and the pulse shape is presented. The analysis is done for the magnetic pulse which is actually used for the experimental results which will be shown in the next section. These measurements were acquired by applying 80 V to the stripline and at 400 mW laser power, resulting in an averaged current of $\bar{I} \sim 850 \mu\text{A}$, as measured by a conventional multimeter. This current was optimized by measuring several I-V curves of the Auston switch at different laser powers. To visualize this effect more clearly, narrow stripes from a series of images acquired with 10 ps time increment have been compiled in the time sequence, and the result is shown in Fig. 6.5(a), where the horizontal axis corresponds to the same narrow time interval as in Fig. 6.5(b). In the inset of Fig. 6.5(b), an image acquired at a delay time before the arrival of the current or electric field pulse into the field of view of the PEEM is shown, where the red narrow stripe in the image indicates the small area in which the analysis has been performed. In Fig. 6.5(a), the change in the magnification of the image is clearly seen near the edges of the stripline and in consequence, a shift in the image occurs when the electric pulse passes through the field of view (darker areas). The shift is caused by the Lorentz force originating from the magnetic field pulse, which in turn deflects the electrons from their path to the microscope lens. By plotting the total shift in the image as a function of time at one edge of the stripline, the pulse shape can be determined [236, 268], and the result is shown in Fig. 6.5(b). In this case, a magnetic pulse with raising and decay slopes of about 80 ps is obtained (after deconvoluting an x-ray pulse length of ~ 70 ps). The time zero at the microstructure position is determined as the onset of the pulse. Note that the values in the vertical axis are already given in units of magnetic field, as it was done for the measurements shown in Fig. 6.4 for different samples. The magnetic field is determined by using the law of Biot-Savart for a semi-infinite conductor ($B=I/2d$) [274], where d is the width of the stripline ($\sim 10 \mu\text{m}$). Since the current measured in the multimeter is averaged over a time of 16 ns corresponding

to the time delay between two consecutive laser pulses, the current I in this case should be normalized by a constant factor. This factor is determined by integrating the shift of the image over time, i.e. the pulse shape, and normalizing the result by the average current \bar{I} flowing through the stripline ($\sim 850 \mu\text{A}$). In this case, considering the maximum shift value in the image, a maximum field of about 80 Oe is obtained. We had selected this value as the best compromise concerning the sample lifetime during the complete experiment. Therefore, it is a little bit lower than the one shown in Fig. 6.4 of about 110 Oe measured from a different sample.

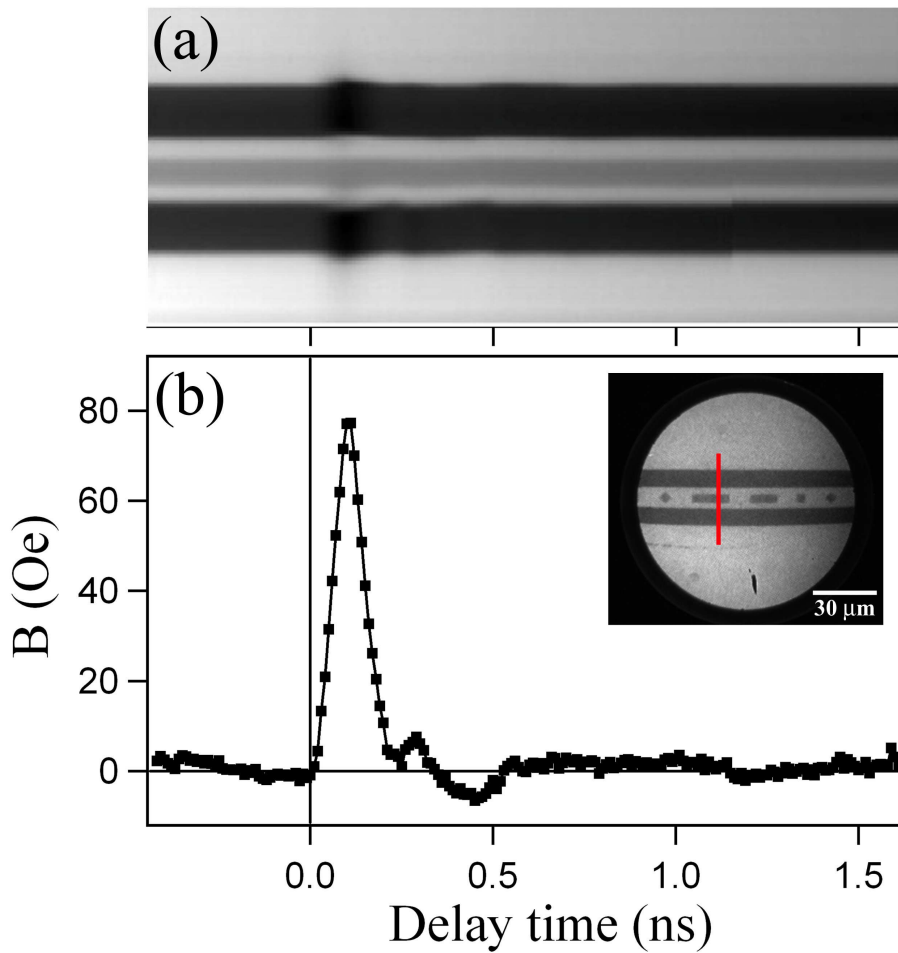


Figure 6.5: (a) Sequences of narrow stripes in the PEEM image compiled in the time domain. The maximum shift appears at the arrival of the electrical pulse and is most visible near the edges of the stripline. (b) Shape of the magnetic field pulse applied during the experiments presented in this work. It was obtained from the shift at one edge of the stripline, from which the time zero is determined as the onset of the pulse. In the inset, a PEEM image of the strip line and microstructures taken before the arrival of the electric field pulse into the field of view. The red narrow stripe indicates the area under analysis.

6.4 Results and discussion: dynamics of cross-tie domain walls

In this section the magnetization dynamics of cross-tie domain walls in a permalloy (Py) microstructure is discussed in detail. As discussed earlier, the magnetization state of the system is probed by the synchrotron x-ray pulses of BESSY II in the single-bunch mode (repetition rate of 1.25 MHz), so that the temporal resolution is ultimately limited by the ~ 70 ps maximum x-ray pulse length. The magnetic field pulse which excites the sample corresponds to the one shown in Fig. 6.5(b). The evolution of the laterally resolved magnetization in the microstructure is followed by setting a delay time Δt between the laser pulse and the x-ray probe in steps of 50 ps (for more details on synchronization issues see section 3.3.5). The XMCD-PEEM images with magnetic sensitivity are calculated as the asymmetry of the images for left- and right-circularly polarized light, as discussed in section 3.3.3. The 16 ns time interval between magnetic field pulses is more than sufficient for the microstructure magnetization to return to its initial configuration between pulses, as it will be shown below. This ensures full access to the magnetization dynamics of the system until it is completely relaxed and guarantees the reproducibility of the complete experiment. The Focus IS-PEEM instrument was used at a lateral resolution of ~ 500 nm [77] (see section 3.3.2.1), together with the custom-made sample holder [275] described above.

A $5 \times 15 \mu m^2$ Py microstructure of about 22 nm thickness was deposited by magnetron sputtering onto the Au stripline. Electron-beam lithography was employed to define both the stripline and the magnetic microstructure². All the time-resolved XMCD-PEEM images were corrected for shifts and size changes that result from the distortion of the emitted electron trajectories during the pulse. As mentioned before, the micromagnetic calculations were performed with the OOMMF software package [263]. The calculations presented in this section were done by relaxing three dimensional spins in a two-dimensional squared mesh of half of the structure size, keeping its aspect ratio constant. A $5 \times 5 \times 20$ nm³ cell size and the typical magnetic parameters for Py described in section 6.2.3 were used as input in the calculations. Note that although laterally the cell size is smaller than the Py exchange length of ~ 5.7 nm, it is much longer in the z-direction. This is a good assumption if the magnetic domain structure does not change significantly along the film thickness, as expected for a ~ 22 nm thick Py layer. The simulations were running until convergence of the LLG equation, reached when the total magnetic torque was smaller than 10^{-6} N·m.

Figure 6.6(a) shows the XMCD-PEEM image of the magnetic domain pattern in the as-grown state, sketched in the top right side. It is formed by two flux-closing domain configurations of the Landau type dressing two vortices with a cross-tie DW appearing in the central part. This diamond-shaped magnetic structure contains two 90° Néel DWs crossing each other, four 45° Néel DWs connecting their ends, and an antivortex in the crossing point. It basically reduces the total magnetic energy compared to, for example, a symmetric 180° Néel wall across two distant vortices [256]. The cross-tie

²The complete electron-beam lithography process and wire bonding of the samples was done by the scientific collaborators of the department of Prof. M. Aeschlimann at the Technical University of Kaiserslautern.

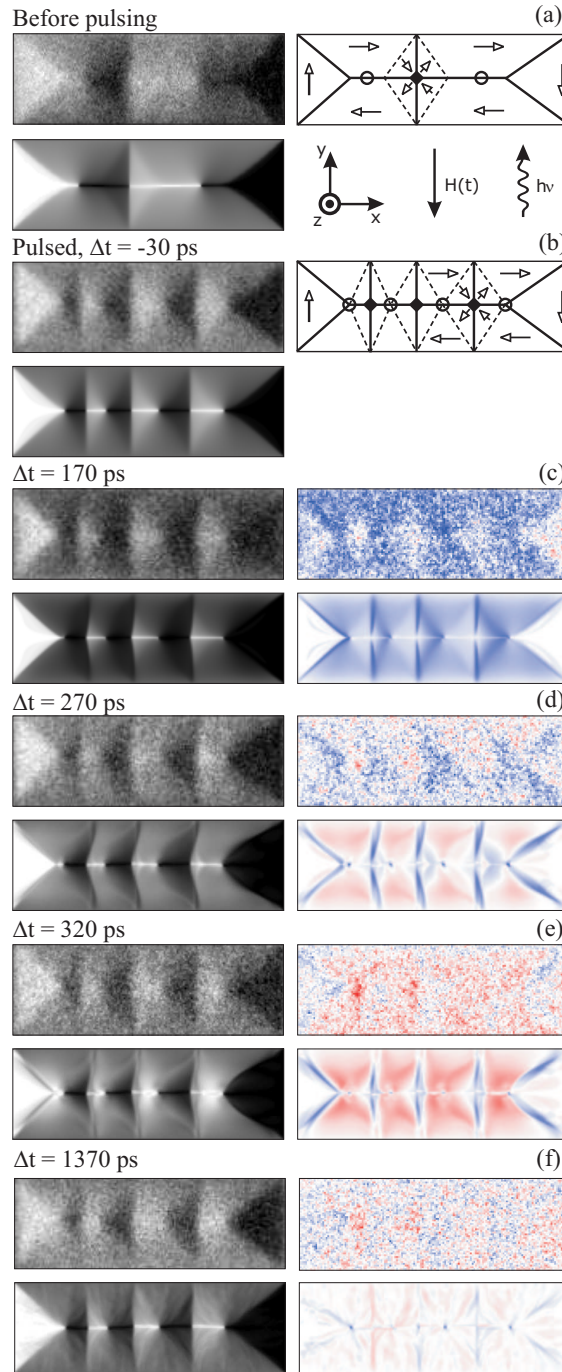


Figure 6.6: (a) Magnetic domain pattern of the as-grown state of the $5 \times 15 \mu\text{m}^2$ Py microstructure as seen by XMCD-PEEM (top) and simulated by micromagnetic calculations (bottom). From (b)-(e), on the left, experimental (top) and calculated (bottom) images of the magnetic state after pulsing, at selected delay times. Difference images for the experimental and calculated results, using the $\Delta t = -30$ ps image as reference are also shown. Red (blue) indicates positive (negative) changes in the XMCD contrast, with white as neutral color. Schematic sketches of the magnetic domain patterns are shown for the as-grown (a) and pulsed (b) states, comprising 90° DWs (full lines), 45° DWs (dashed lines), vortices (\circ) and antivortices (\blacklozenge). The relative directions of the magnetic field pulse and of the incoming x-rays are also shown.

domain wall was first reported by Huber et al. [276], and was subsequently interpreted by various authors at the end of the 50s and beginning of the 60s [277, 278]. In a simple view, it can be understood as a series of vortex and antivortex structures that are connected by 90° Néel walls. Since the magnetization in the center of the vortex and antivortex is perpendicular to the surface of the microstructure, a Bloch-like transition of the magnetization from one domain to the next occurs along a line perpendicular to the vertical 90° Néel DWs through the vortex and antivortex cores. In the regions outside the vortices and antivortices the magnetization remains in-plane, and thus all the DWs have Néel character.

Coming back to the experimental XMCD-PEEM image of Fig. 6.6(a), it can be observed that the position of the vertical wall is not symmetric with respect to the center of the microstructure. Such an asymmetry is most likely due to small defects that act as pinning centers, possibly at the microstructure boundaries. These defects were not included in the simulation, instead the positions of the DWs and Bloch lines were used to draw a simplified domain pattern similar to the one provided by the Van den Berg scheme [279, 280], whose $m_{x,y}$ magnetization distributions were set as the initial state in the calculations. These distributions varied during the relaxation process of the initial state configuration in all the simulations. This basically means that the positions of the DWs, vortices or antivortices changed around their initial value until the total magnetic energy of the system was further minimized. The result of relaxing this domain pattern in the calculation is shown on the bottom left side of Fig. 6.6(a), yielding to a good agreement with the experimental one.

More intriguing, after applying magnetic field pulses in the experiment the microstructure reached a magnetically lower energy state by irreversibly converting into a new domain pattern (top left in Fig. 6.6(b)), now displaying two additional cross-tie walls. Further pulsing had no influence on the cross-tie configuration for several days of measurements, proving that it is one of the stable states. Experimentally, this effect was previously found by Neudert et al. [281], who observed by time-resolved Kerr microscopy the creation of additional vortex-antivortex pairs in cross-tie domain walls after applying a series of short magnetic-field pulses in 50 nm thick Py microstructures of $80 \times 160 \mu\text{m}^2$ in size. In particular, they observed that the cross-tie spacing can decrease by a factor of 2–4 relative to the initial equilibrium state depending on the frequency and the rise times of the magnetic field pulses. Note that this effect is similar to the one observed with increasing film thickness in the case of extended magnetic films [256], where a continuous increase of the cross-tie density is also observed experimentally. This can be related to an anisotropy effect, since Bloch DWs are favored in thick films and Néel DWs in thin films. This means that increasing the film thickness reduces the minimum energy density needed for the creation of Bloch-like transitions. As a result, the cross-tie spacing gets smaller and smaller down to a certain limit depending on the total volume of the sample.

In the case of applied magnetic field pulses for a constant thickness, the decreased cross-tie spacing can be explained as a dynamical effect triggered by the short magnetic field pulse. As shown in the sketch of Fig. 6.6(a), the local magnetization around the antivortex position in the center of the cross-tie domain wall shows four segments delimited by two 90° and four 45° Néel DWs. After the magnetic pulse, the rotation of

magnetization leads to a change in the angle of the vertical DWs towards a 180° configuration, an effect which should be more pronounced in the two segments on the left side of the antivortex, where the magnetization is antiparallel to the pulsed magnetic field. If the change in angle is pronounced enough, a cross-tie wall is energetically favorable as compared to a horizontally symmetric 180° Néel wall, leading to the creation of new vortex-antivortex pairs mostly emerging in the antiparallel domain wall segments. This process should also depend on the intensity of the applied magnetic field. In order to simulate the transition from the as-grown state to the pulsed domain state in the micromagnetic calculations, an 80 Oe external magnetic field pulse of triangular shape and 80 ps rising and decaying slopes was applied to the initially calculated single cross-tie wall state. Single pulses were able to create either one or two additional cross-tie walls but not more. We can thus deduce that the effect of many more pulses used in the experiment saturates the magnetic structure with three cross-tie walls, the maximum number allowed by the lateral dimensions [282]. The slightly different positions of the two new vertical DWs as compared to the measured pattern can be assigned to local pinning centers. This deviation does not play an important role in the magnetization dynamics of the structure.

Figs. 6.6 (c)-(f) show the measured images for selected delay times (top left), the corresponding calculated images (bottom left). In order to make the changes in the magnetic contrast more visible, the respective difference images (right side) at the corresponding delay time relative to the image before the magnetic pulse at time $\Delta t = -30$ ps were calculated. By using this method only the changes during the dynamical process of the magnetization are visible. In these images, for the sake of clarity red (blue) contrast has been used, indicating positive (negative) changes in the XMCD contrast. The most pronounced effect in the magnetic contrast appears 170 ps after the onset of the magnetic field pulse (Fig. 6.6(c)). This is when the magnetization in the magnetic domains that are initially magnetized along the x direction (referred to as gray domains in the following) displays a maximum brightness reduction when compared to the reference image. This can be clearly distinguished in the corresponding difference image, where blue contrast dominates the regions of the gray domains within the microstructure. Such a behavior is expected, since the local magnetization \mathbf{m} in these domains is perpendicular to the applied magnetic pulse \mathbf{H} , thus maximizing the magnetic torque $\boldsymbol{\tau} = \mathbf{m} \times \mathbf{H}$ caused by the field pulse. Although the resulting torque points along the z direction, the demagnetization field allows only a small excursion into that direction. Detailed analysis of the XMCD contrast yields a maximum deviation angle of m_y from the static orientation of about 20° . At larger delay times, the XMCD contrast in the gray domains vanishes and reverses its sign, following a damped quasi-harmonic oscillation with a main frequency of about 3.7 GHz, as it will be demonstrated below.

The next important magnetic effect appears at the 90° DWs dressing the black and white domains of larger size at the left and right sides of the microstructure and at those of the cross-tie walls. In order to illustrate this, Fig. 6.6(d) shows the images for a time delay $\Delta t = 270$ ps. Compared to the magnetization precession in the gray domains, these DWs have a longer oscillation period. This can be deduced from the simultaneous appearance in the corresponding difference image of blue and red contrast at the DWs

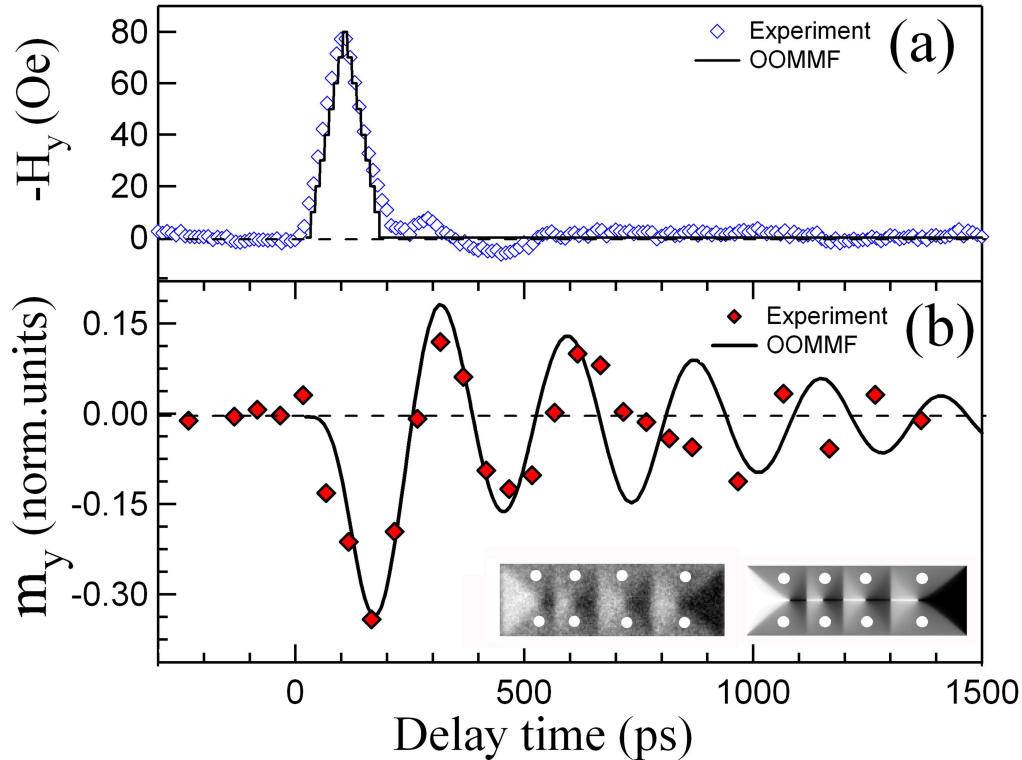


Figure 6.7: (a) Applied experimental (open blue symbols) and calculated (thin black line) magnetic field pulses before and after deconvoluting with the x-ray pulse length, respectively. (b) Time-dependent XMCD contrast of the gray domains from the experimental data (full red symbols) and the OOMMF calculation (thick black line). In the inset, the areas for integration (full white circles) used in the experiment (left) and calculation (right) are shown.

positions and within the gray domains, respectively. Although the magnetic torque in the black and white domains is zero, both are affected by the large oscillation of their DWs [244]. At $\Delta t = 320$ ps (Fig. 6.6(e)), the deviation of m_y in the gray domains has completely reversed with respect to the situation at $\Delta t = 170$ ps. The initial magnetic domain structure is almost completely recovered after 1370 ps (Fig. 6.6(f)).

The precessional switching of the magnetization can be clearly seen in Fig. 6.7, where the time dependence of the integrated XMCD contrast in the gray domains is shown. Fig. 6.7(a) shows the experimental and calculated magnetic field pulses. Since the simulations do not account for the temporal resolution, the FWHM of the magnetic pulses used in the calculations resulted from the deconvolution of the experimental pulse shape with a Gaussian function of about 70 ps FWHM, corresponding to the x-ray pulse length. Fig. 6.7(b) shows the calculated and experimental quasi-harmonic oscillations obtained from the small area analysis of the XMCD contrast in the gray domains. These areas are indicated as an inset on top of both the experimental and calculated XMCD patterns of the microstructures before the arrival of the pulse. In

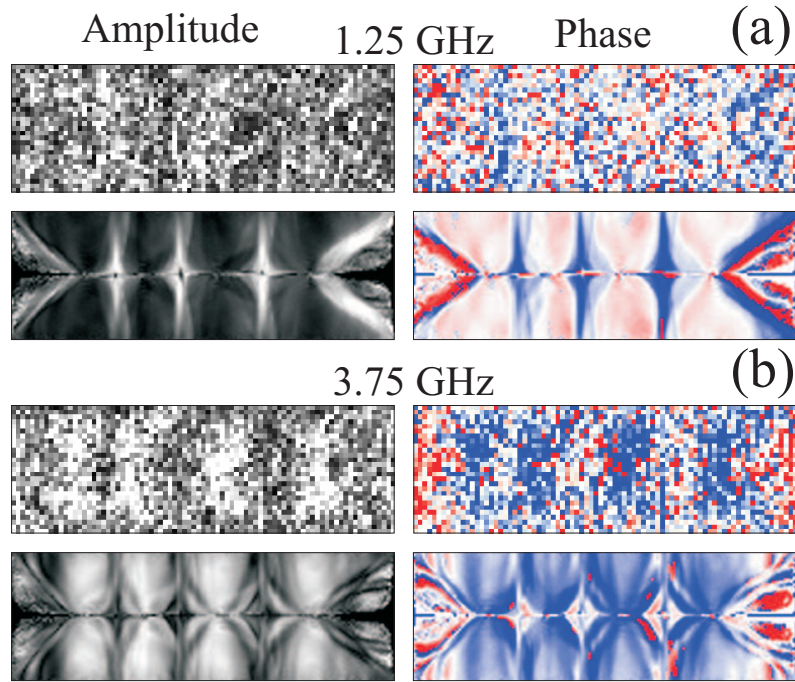


Figure 6.8: *Laterally resolved images of the amplitude (left) and phase (right) for (a) 1.25 GHz and (b) 3.75 GHz, obtained from the Fourier transform of the time-dependent experimental results (top) and calculations (bottom). On the right side, $+90^\circ$ (-90°) phase is indicated in red (blue).*

general, good agreement between the XMCD contrast of the central gray domains and the corresponding curve obtained from the calculated images can be observed. The main oscillation frequency is about 3.7 GHz. These changes in magnetic contrast can be assigned to an attenuated quasi-harmonic magnetization precession in the gray domains, at least during the first and second periods.

Deeper insight into the magnetization dynamics of the structure caused by the magnetic pulse can be obtained by computing the Fourier transformation (FT) of the measured and calculated images. This yields laterally resolved images of the dominating frequencies which are present in the microstructure. The resulting amplitudes and phases of the Fourier-transformed images are shown in Fig. 6.8. In order to improve the signal-to-noise level of these images, a 2×2 binning in the XMCD-PEEM images was used. This type of images are obtained by computing the FT of each one of the pixels present in the XMCD images. This is done by extracting the temporal evolution of the XMCD contrast pixel by pixel, and recompiling the results into laterally-resolved images, but now in the frequency domain. Merely two frequencies show high amplitudes, around 1.25 GHz (Fig. 6.8(a)) and 3.75 GHz (Fig. 6.8(b)) and 1.25 GHz (Fig. 6.8(b)), showing a reasonable agreement between experiment and simulation. In Fig. 6.8(b), a large amplitude can be distinguished (white contrast) in the areas of the gray domains, meaning that they are oscillating with a main frequency of 3.75 GHz, in agreement with the frequency found from Fig. 6.7. The phase of this oscillation

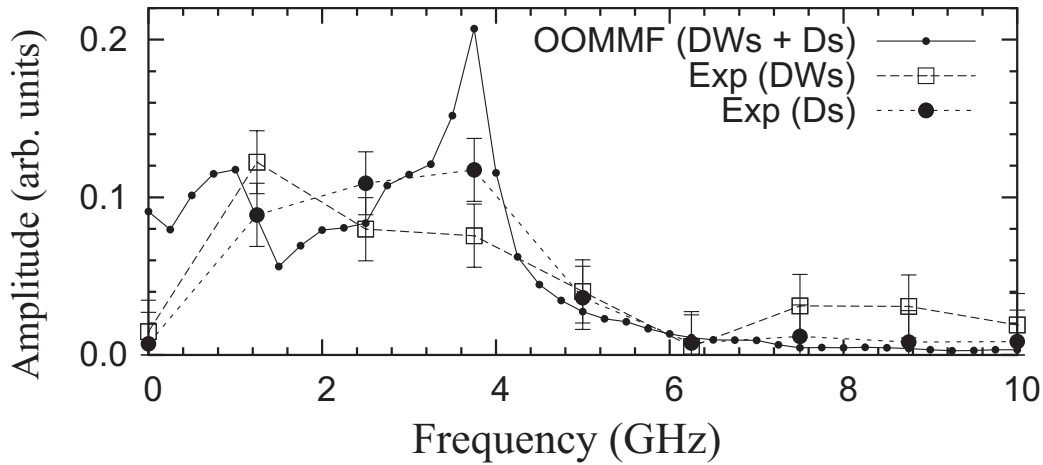


Figure 6.9: *Fourier analysis of the full simulated structure (full line), and of experimental areas on the gray domains (●) and domain walls (□).*

is -90° (blue contrast). At 1.25 GHz, on the other hand, the amplitude in the gray domains is strongly reduced in the experiment and basically zero in the calculations (black contrast). From this comparison, one can conclude that only the diagonal 45° and vertical 90° DWs are affected. In this case, although the effect is certainly more pronounced in the calculations, these amplitudes can also be slightly distinguished in the experimental results. Near the regions of the DWs, a phase of -90° can also be distinguished, indicating that both the gray domains and DWs are oscillating in phase.

Fig. 6.9 shows the Fourier spectra obtained from the transformation of the m_y values obtained in the full area of the simulated microstructure (indicated as OOMMF (DWs+Ds)), and from different areas located at the gray domains (Exp (Ds)) and at the DWs (Exp (DWs)) of the measured XMCD images. This analysis consists on doing the FT of the laterally-resolved oscillations obtained in a similar way as the results presented in Fig. 6.7, but in this case also for small areas only near the DWs. In general, the main frequencies at the domains and DWs coincide with the simulated ones, although contributions from other components are not negligible. These results agree qualitatively with previous studies in similar systems [283, 284]. Discrepancies in the observed frequencies can be due to the different pulse shapes used in those experiments.

Now, let us briefly discuss the role of the Bloch lines (vortexes and antivortexes) in the dynamics of the system. It has been observed that the signs of the m_z components of the vortex and antivortex cores also play an important role for the magnetization dynamics in a single cross-tie wall [285]. This typically results in different amplitudes of the core gyration depending on their relative orientations. Certainly, since a lateral resolution of ~ 500 nm in this experiment is well above the theoretically predicted ~ 10 nm size [286] of the vortex and antivortex cores, we will restrict our discussion only to the results obtained in the simulations, since no observable effect can be distinguished in the experimental results. It should be mentioned here that due to their small size,

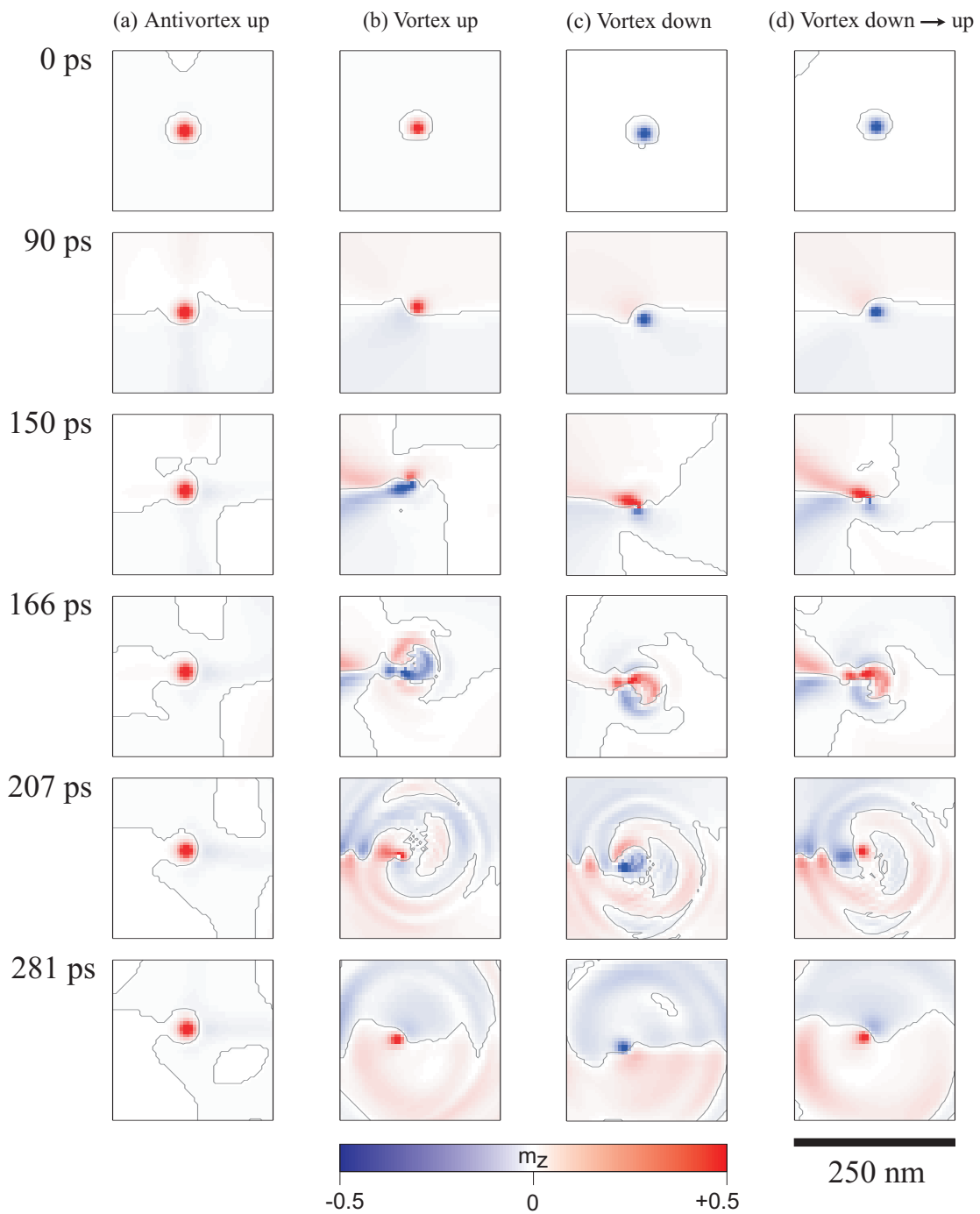


Figure 6.10: Zoomed-in plots of the calculated m_z components in the vicinity of one antivortex (a) and several vortices (b-d) at some selected delay times. For the sake of clarity, the color scale has been stretched so that values of m_z higher (lower) than $+0.5$ (-0.5) appear homogeneously red (blue). Contour lines for $m_z = 0$ are indicated as black lines.

vortex and antivortex cores could not be observed experimentally for about 40 years after their theoretical prediction [287]. Only by spin-polarized scanning tunneling microscopy has it recently become possible to very precisely measure the profile of a magnetic vortex [288]. Furthermore, the gyration of a vortex or antivortex core occurs with a characteristic frequency of a few 100 MHz³, which is below the frequencies studied here for precessional switching at faster time scales. Let us concentrate on the behaviour of the vortex and antivortex cores in shorter time scales, i.e. during the precession of the magnetization in the gray domains of the microstructure. In such short time scales, the magnetic core switching becomes a particularly interesting topic with potential applications in future ultrafast spintronic devices.

Fig. 6.10 shows the calculated out-of-plane m_z component of the magnetization (or core polarization) in areas near several vortex and antivortex cores at some selected delay times during the first half of the oscillation period of the gray domains, where red (blue) indicates positive (negative) magnetization. Completely different behaviors are apparent for an antivortex (Fig. 6.10(a)) and a vortex (Fig. 6.10(b)), both pointing up. While the antivortex core in Fig. 6.10(a) remains relatively unaffected by the magnetic pulse, the vortex core in Fig. 6.10(b), which corresponds to one in the external sides of the microstructure, is strongly perturbed. Firstly, a core with opposite m_z appears next to the pre-existing one as in a magnetic dipole configuration, approximately when the precession in the gray domains reaches its maximum ($\Delta t = 150$ ps). These two cores collapse onto each other in an annihilation process, creating a series of circular spin waves that travel away from the initial core position. At $\Delta t = 281$ ps a clear vortex core is visible, only slightly shifted from the original position and with the same core polarization as the initial vortex. At this time, the creation-annihilation process is finished, corresponding to the time when the magnetization precession of the gray domains crosses zero (see Fig. 6.7). For later times, the precession of m_y in the gray domains does not suffice to provoke the switching behavior, and the net magnetization along the vertical component of this vortex core remains invariant (not shown).

The different behavior of the antivortex cores, compared to the vortex ones, can be understood either by the individual trajectories of magnetic flux lines surrounding the two types of Bloch lines, or by the influence of the different DWs around them. As discussed above, the antivortex is located in the crossing point of four 90° DWs, whereas the vortices are surrounded by either two 90° and four 45° DWs, or by three 90° and two 45° DWs depending on whether they are placed in the center or in the external sides of the microstructure, as in Fig. 6.10(b). In order to clarify this, we show in Fig. 6.10(c) the corresponding images for one of the central vortex cores, in this case with a core polarization initially pointing down. It is evident that the core undergoes a very similar behavior of creation and annihilation of opposite m_z as for the previous vortex, again maintaining the original m_z core polarization, implying that the detailed surrounding of the vortex is not relevant for its behavior.

Further micromagnetic calculations were performed with three different initial combinations of m_z at the vortex/antivortex cores among the 2⁷ possible configurations. These combinations were homogeneous [uuuuuuu], alternate [udududu], and random

³Note that the exact value of this resonance frequency depends on the aspect ratio of the system under study [289].

[*uddudud*], where $u(d)$ denotes the core polarization pointing up (down). The simulation results indicate an statistical random behavior in the switching of the vortex core polarizations m_z . The random switching was independent of the vortex position in the microstructure. An example is shown in Fig. 6.10(d), where an initially d vortex core reverses its m_z component. Strikingly, there are no significant differences in the images of Figs. 6.10(c) and 6.10(d) for $\Delta t = 150$ and 166 ps. The main difference occurs at $\Delta t = 207$ ps, when a u vortex core appears and remains stable after the initial vortex core is washed away. In the case of antivortices, on the other hand, no core switching was ever observed in the present calculations, probably stabilized by the magnetic flux lines around them, which prevent the formation of opposite m_z circulating around. The described switching behavior of the vortex core agrees qualitatively with experimental [238] and calculated micromagnetic [247] studies of the vortex reversal. These studies consider magnetic structures with squared and circular shapes in which the vortex cores are in a different magnetic environment than the vortex cores studied in this work. Comparing to the results presented in Fig. 6.10, one may conclude that the effect of additional DWs surrounding the vortex core is to attenuate its overall dynamics. However, the ultrafast switching of the vortex core polarization in about 280 ps is still visible in Fig. 6.10(d), indicating that this micromagnetic process can be as fast as the precessional switching observed in Fig. 6.7. Although a better lateral resolution would be needed to clarify this, the random nature of the core switching for this range of exciting magnetic field strength is incompatible with the stroboscopic approach currently used. In this sense only single-shot experiments which are possible at e.g., free electron lasers, and with a lateral resolution below 20 nm would be able to follow it. Furthermore, it would be interesting to perform this type of experiments in different magnetic environments around the vortex cores, since from recent simulations [247] it has been shown that a switching time of about 50 ps can be achieved. This makes the vortex core polarization reversal the fastest magnetization switching process known up to date.

6.5 Summary of conclusions and outlook

In summary, several important aspects of the time-resolved XMCD-PEEM experiments performed in this thesis have been discussed. For the first time in BESSY II, technical feasibility of time-resolved XMCD-PEEM experiments has been demonstrated using a laser system as a magnetic pump, synchronized with the x-ray pulses produced in single bunch mode. This technique allows to generate magnetic excitation pulses of less than 150 ps duration, opening a window for studies of magnetization dynamics in the sub-ns regime with lateral resolution. In this chapter, firstly on the technical side, a new sample holder compatible with the Focus IS-PEEM has been described. It has been demonstrated that with this new mounting scheme, while the image properties remain unaffected, it is possible to perform time-consuming measurements at much higher currents flowing through the stripline, thus providing magnetic field pulses of almost one order of magnitude larger than with previous sample holders.

Secondly, it has been demonstrated how a triangular 80 Oe magnetic field pulse can strongly influence the temporal evolution of the magnetic components present in a rect-

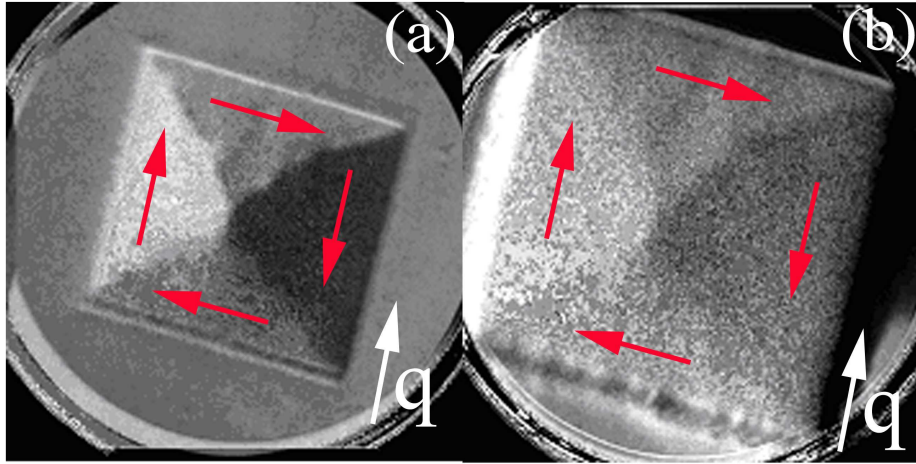


Figure 6.11: XMCD-PEEM images of a 15 nm Co / 2 nm Cu / 4 nm Py microstructure of $5 \times 5 \mu\text{m}^2$ in size, measured at the Fe L_3 edge (a) and at the Co L_3 edge (b). The two layers are ferromagnetically coupled through the 2 nm Cu. The field of view is $8 \mu\text{m}$ and $5 \mu\text{m}$ in (a) and (b), respectively.

angular Py microstructured platelet comprising three cross-tie domain walls. A large magnetization precession is observed in the domains with initial magnetization perpendicular to the applied field, yielding a deviation of m_y of up to 20° with a frequency of 3.75 GHz. At longer timescales, the domain walls oscillate with a typical frequency of 1.25 GHz. The experimental XMCD-PEEM results are compared to micromagnetic calculations, yielding good agreement in time and frequency. We conclude from the calculations that only the vortex cores are susceptible to reverse their out-of-plane magnetization components, in a process triggered by the magnetization precession of the much larger gray domains and with random switching probability. In contrast, the antivortices seem to be insensitive to the magnetic pulse.

In the near future it would be very interesting to implement this type of study in trilayered microstructures as well. This would allow to investigate the time evolution of magnetic coupling phenomena in the sub-ns time scale, a topic of potential application for the implementation of spin valve devices with faster performance. During the time of this thesis, first steps have been undertaken in the preparation of Py/Cu/Co microstructures for different Cu thicknesses by magnetron sputtering and the static characterization of their domain configuration in the Elmitec PEEM microscope. An example showing first results is presented in Fig. 6.11. It corresponds to a 15 nm Co/2 nm Cu/4 nm Py trilayered microsquares of $5 \times 5 \mu\text{m}^2$ in size. The measurement in Fig. 6.11(a) was taken at the Fe L_3 edge (~ 707 eV), while in Fig. 6.11(b) at the Co L_3 edge (~ 778 eV) with a $\sim \times 10$ larger acquisition time. The two layers show a stable Landau domain pattern and are clearly ferromagnetically coupled through the 2 nm Cu. Such a domain configuration was obtained by applying a 2 kOe external magnetic field along the in-plane direction during growth.

The other part of the work involved pilot time-resolved XMCD-PEEM experiments

in trilayered microstructures in the focus IS-PEEM microscope. Only preliminary results from experiments in these systems were obtained. Since the continuation of this project aims for a better lateral resolution, only possible in the Elmitec PEEM microscope, the complete installation is now permanently adapted in the UE49-PGMA beamline at BESSY II. This required a new laser system and sample holder mounting scheme similar to the ones described in this work.

Summary

This thesis is focused on the fundamental electronic, spin-dependent and dynamical properties of magnetic systems with reduced dimensions. Photoemission-related techniques in combination with synchrotron radiation were applied to study the spin-dependent properties of these systems in the energy and time domains. The first part of this work contains an overview of the most relevant aspects of modern research in magnetism, together with a description of the methodical background and the experimental techniques used in this thesis. This includes the basic principles of spin- and angle-resolved photoemission and time-resolved XMCD-PEEM techniques, but also detailed technical information on the instrumentation used during the experiments.

The scientific part of this work starts with a detailed quantitative investigation of the spin-dependent quasiparticle lifetimes and electron correlation effects in ferromagnetic bcc Fe(110) and hcp Co(0001) by means of spin- and angle-resolved photoemission spectroscopy. The experimental spectra were compared in detail to state-of-the-art theoretical calculations within the three-body scattering approximation and within the dynamical mean-field theory, together with one-step model calculations of the photoemission process. From this comparison, it was demonstrated that although strong local Coulomb interactions are of major importance for the qualitative description of spin-dependent correlation effects in these systems, more sophisticated many-body calculations including non-local interactions are still needed to improve the quantitative agreement between theory and experiments, in particular concerning the linewidths. From the experimental and theoretical data a better overall agreement in the case of Co as compared to Fe was obtained, a result that was attributed to a reduction of the non-locality of correlation effects with increasing atomic number.

In the next scientific part of this thesis, photoelectron spectroscopy was used to demonstrate how two-dimensional graphene layers can be grown by chemical vapour deposition on the transition-metal surfaces Ni(111) and Co(0001) and intercalated by a monoatomic layer of Au. Ferromagnetism and spin-orbit effects were studied simultaneously by means of spin- and angle-resolved photoemission. From a detailed analysis of spin-resolved photoemission data of graphene/Ni(111) and graphene/Co(0001), it was shown that the π -band shows a negligible ferromagnetic polarization, in contrast to recent studies. Furthermore, it was demonstrated that after intercalation of one monolayer of Au between graphene and Ni(111), the system becomes spin-orbit split due to the Rashba effect. The experimental data show a large spin-orbit splitting value which is by three orders of magnitude larger than the spin-orbit splitting for freestanding graphene. It was concluded that it originates from the intercalated Au at the graphene interface and its high nuclear charge.

The last part of this work was devoted to study the evolution of the magnetization components of a permalloy ($\text{Fe}_{19}\text{Ni}_{81}$) microstructure by means of time-resolved XMCD-PEEM experiments. Considering that experiments of this type were not successfully performed in BESSY II before completion of this work, it was firstly demonstrated that with the use of a custom-made sample holder the experiment is technically possible. Following that, it was shown how we can induce a fast magnetic response in the precessional motion of the magnetization in a permalloy platelet comprising three cross-tie domain walls. This was achieved by using a laser-excited photoswitch to generate magnetic excitation pulses of about 150 ps duration and 80 Oe applied magnetic field. A comparison between the experimental results and micromagnetic calculations revealed a good agreement in the time and frequency domains, illustrating the large precessional motion of the magnetization within the different magnetic domains. From the calculations it was concluded that the relatively high precessional frequency observed in the experiments is directly linked to the nature of the vortex/antivortex dynamics and its response to the magnetic perturbation. In particular, the simulations indicate that the response of the vortex cores is the main source of spin waves, while the antivortexes remain unaffected. This includes the time-dependent reversal of the vortex core polarization, a process which is beyond the limit of detection in modern experiments.

Zusammenfassung

Die Verfügbarkeit der Synchrotronstrahlung und die damit verbundene Entwicklung moderner experimenteller Techniken eröffnen neue Wege, die vielen interessanten Eigenschaften von Festkörpern auf der Nanoskala zu untersuchen. Die vorliegende Arbeit beschäftigt sich mit der Untersuchung grundlegender elektronischer, magnetischer und dynamischer Eigenschaften magnetischer Systeme mit reduzierten Dimensionen. Diese Eigenschaften werden auf der Zeit- und Energieskala mittels Photoemissionstechniken unter Verwendung von Synchrotronstrahlung erforscht.

Der erste Teil dieser Arbeit ist der experimentellen und theoretischen Untersuchung der elektronischen Struktur der ferromagnetischen Metalle bcc Fe(110) und hcp Co(0001) im Volumen mittels spin- und winkelaufgelöster Photoemissionsexperimente (SARPES) gewidmet. Der Vergleich zwischen Photoemissionsspektren und modernsten theoretischen Rechnungen zeigt auf, dass obwohl die gegenwärtige physikalische Beschreibung dieser Systeme auf der Basis elektronischer Wechselwirkungen qualitativ gültig ist, eine quantitative Übereinstimmung zwischen Theorie und Experiment nicht erreicht werden kann. Die Gründe für die beobachteten Abweichungen werden untersucht und im Detail diskutiert, unter besonderer Beachtung der Lebensdauern der elektronischen Zustände.

Im zweiten Teil der Arbeit wird Graphen, d. h., eine einzelne Lage von Kohlenstoffatomen auf den ferromagnetischen Oberflächen fcc Ni(111) und hcp Co(0001) hergestellt. Mittels der SARPES-Methode werden die Eigenschaften dieser Systeme im Detail untersucht. Insbesondere wird gezeigt, dass es möglich ist, das Graphen von seinem ferromagnetischen Substrat zu entkoppeln, indem eine Au-Lage durch einen Interkalationsprozess eingefügt wird. Die SARPES-Messungen zeigen, dass ohne diese Interkalation von Au die ferromagnetische Polarisation des Graphens unterhalb der Nachweisgrenze liegt. Jedoch wird gezeigt, dass nach der Interkalation das System relativistische Eigenschaften annimmt und durch den sogenannten Rashba-Effekt spinpolarisiert wird.

Im letzten Teil dieser Arbeit werden schnelle Magnetisierungsprozesse in mikrometergroßen $\text{Fe}_{19}\text{Ni}_{81}$ -Strukturen untersucht. Mit einem Lasersystem, das mit den Lichtpulsen des Speicherrings BESSY II synchronisiert wurde, wird gezeigt, wie magnetische Pulse von etwa 150 Pikosekunden Länge und hohen Intensitäten generiert werden können. Diese Pulse werden dazu genutzt, eine magnetische Störung zu erzeugen, die zu einer Präzession der Magnetisierung des Systems mit einer Frequenz von etwa 3.7 GHz führt. Mikromagnetische Rechnungen werden mit Mikroskopie-Messungen verglichen, die gute Übereinstimmung im Zeit- und Frequenzbereich zeigen. Mit den Rechnungen wird gezeigt, dass der diesem Prozess zugrundeliegende Mechanismus die

Erzeugung von Spinwellen aufgrund verschiedenartiger Wechselwirkungen im Innern der Mikrostruktur ist. Insbesondere geben die Simulationen Einsicht in die Dynamik der Vortizes und Antivortizes. Während Vortices ihre Polarisation umkehren und dabei Spinwellen erzeugen, bleiben Antivortizes unbeeinflusst vom anregenden Magnetfeldpuls. Diese Prozesse sind an der Detektionsgrenze moderner Experimente.

Acknowledgements

During this work I have enjoyed a lot the synchrotron world and all of its possibilities, in particular all what is related to magnetism science. The first time I entered BESSY, I became really fascinated just by looking all the sophisticated instrumentation and equipment around. After a few explanations about the experimental systems, I could not avoid to do my thesis. And now, if I look back in time and I think about all of these years, I know that at the beginning I had never imagined how much I was going to learn from it.

I would like to give my deepest acknowledgement to Dr. Oliver Rader for all his invaluable support and encouragement. I really do not have words to express how thankful I am for all the help I received from him. His advice has been always crucial to me, and I have learned not only about physics and science but also about what means to be a good scientist and a good and respectful person.

I want to thank deeply Prof. Jörg Fink not only for his support during the experiments, but also for all his help in the development of my scientific activity during the entire course of this work. Our collaboration has been invaluable for the results obtained in this thesis. I would also like to acknowledge Dr. Andrei Varykhalov for all his support during these years. His help has been also crucial to obtain a large part of the results presented in this thesis. I appreciate and enjoyed very much his continuous scientific and technical advice.

I am really indebted to all the scientific collaborators who have contributed to my work during the time I have been in BESSY. Firstly, I would like to acknowledge Dr. Jürgen Braun and Dr. Jan Minár for all their help and fruitful discussions about electron correlations. I have really enjoyed our collaboration a lot and hope that we will continue in the same line during the next years. I also appreciate very much the collaboration with Prof. Franca Manghi, Prof. Alexander Lichtenstein, Dr. Igor Di Marco and Dr. Valentina Boni. I am thankful to all of them for their contribution to the theoretical calculations and stimulating discussions.

I am also grateful to Prof. W. Kuch and Dr. Jorge Miguel. I appreciate all the advice and help I have received from them during the development of my work, in particular concerning the time-resolved experiments presented in this thesis. I would also like to express my gratitude to all the scientific collaborators from the Freie Universität Berlin : Julia Kurde, Dr. Matthias Bernien and Dr. Martin Piantek for their help during the experiments. Next, I want to thank Prof. Martin Aeschlimann for his indirect support and to Daniela Bayer from the University of Kaiserslautern, for all her work on the preparation of the Auston switches and her help during the time-resolved experiments. I am thankful to Dr. Florin Radu for all his help and scientific advice.

I am grateful for all the support from Dr. Sergio Valencia and all the stimulating discussions about physics and life we had together in and out of BESSY.

I appreciate the help from Prof. Wolfgang Eberhardt and Dr. Hermann Dürr, who gave me the possibility to start working in the synchrotron world. I would also like to thank Dr. Walter Braun, Dr. Christian Jung, Dr. Philippe Wernet, Dr. Rolf Follath, Mike Sperling, Dr. Elio Vescovo and Prof. A. Shikin for all their support and stimulating discussions. I am thankful to all the colleagues from BESSY for the nice working atmosphere and for all the technical support. I gratefully acknowledge the indirect support from Prof. Antonio Hernando, Prof. Guillermo Rivero and Dr. Pilar Marin from the Universidad Complutense of Madrid. I would also like to thank all my friends who have been supporting me since I came to Berlin, most in particular to Manuel Lucas for all the nice scientific and non-scientific discussions we always have together and to Dr. Ignacio Caretti for his indirect support from Spain.

Finally, I would like to acknowledge all my family, in particular my parents who always have been helping and motivating me to become a better scientist. I am also very thankful to Angela, my girlfriend, who has supported me from the beginning until the end of this thesis, not only in my work but also in all aspects of my life.

Bibliography

- [1] P. Grünberg, R. Schreiber, Y. Pang, M. B. Brodsky, and H. Sowers, *Phys. Rev. Lett.* **57**, 2442 (1986)
- [2] M. N. Baibich, J. M. Broto, A. Fert, F. N. Van Dau, F. Petroff, P. Etienne, G. Creuzet, A. Friederich, and J. Chazelas, *Phys. Rev. Lett.* **61**, 2472 (1988)
- [3] G. Binasch, P. Grünberg, F. Saurenbach, and W. Zinn, *Phys. Rev. B* **39**, 4828 (1989)
- [4] M. Jullière, *Phys. Lett.* **54A**, 225 (1975)
- [5] J. S. Moodera, L. R. Kinder, T. M. Wong, and R. Meservey, *Phys. Rev. Lett.* **74**, 3273 (1995)
- [6] M. I. Dyakonov and V. I. Perel, *Phys. Lett. A* **35**, 459 (1971)
- [7] M. König, S. Wiedmann, C. Brüne, A. Roth, H. Buhmann, L. W. Molenkamp, X.-L. Qi, and S.-C. Zhang, *Science* **318**, 766 (2007)
- [8] M. I. Katsnelson, V. Y. Irkhin, L. Chioncel, A. I. Lichtenstein, and R. A. de Groot, *Rev. Mod. Phys.* **80**, 315 (2008)
- [9] H. Ohno, *Science* **281**, 951 (1998)
- [10] N. A. Spaldin and M. Fiebig, *Science* **309**, 391 (2005)
- [11] R. Ramesh and N. A. Spaldin, *Nat. Mater.* **6**, 21 (2007)
- [12] H. J. Richter, *J. Phys. D* **40**, R149 (2007)
- [13] W. Wernsdorfer, D. Maily, and A. Benoit, *J. Appl. Phys.* **87**, 5094 (2000)
- [14] J. Bachmann, J. Escrig, K. Pitzschel, J. M. Montero, J. Jing, D. Görlitz, D. Altbir, and K. Nielsch, *J. Appl. Phys.* **105**, 07B521 (2009)
- [15] M. Bolte, R. Eiselt, G. Meier, D.-H. Kim, and P. Fischer, *J. Appl. Phys.* **99**, 08H301 (2006)
- [16] M. J. Benitez, O. Petravic, E. L. Salabas, F. Radu, H. Tüysüz, F. Schüth, and H. Zabel, *Phys. Rev. Lett.* **101**, 097206 (2008)
- [17] M. Shiraki, Y. Wakui, T. Tokushima, and N. Tsuya, *IEEE Trans. Magn.* **21**, 1465 (1985)
- [18] J. I. Martin, J. Nogues, K. Liu, J. L. Vicent, and I. K. Schuller, *J. Magn. Magn. Mater.* **256**, 449 (2003)
- [19] S. Morup, D. E. Madsen, C. Frandsen, C. R. H. Bahl, and M. F. Hansen, *J. Phys.: Condens. Matter.* **19**, 213202 (2007)
- [20] S. S. P. Parkin, M. Hayashi, and L. Thomas, *Science* **302**, 190 (2008)
- [21] B. T. Thole, G. van der Laan, and G. A. Sawatzky, *Phys. Rev. Lett.* **55**, 2086 (1985)
- [22] G. van der Laan, B. T. Thole, G. A. Sawatzky, J. B. Goedkoop, J. C. Fuggle, J.-M. Esteva, R. Karnatak, J. P. Remeika, and H. A. Dabkowska, *Phys. Rev. B* **34**, 6529 (1986)
- [23] J. Stöhr, Y. Wu, M. G. Samant, B. D. Hermsmeier, G. Harp, S. Koranda, D. Dunham, and B. P. Tonner, *Science* **259**, 658 (1993)

- [24] E. Gerdau, R. Ruffer, H. Winkler, W. Tolksdorf, C. P. Klages, and J. P. Hannon, *Phys. Rev. Lett.* **54**, 835 (1985)
- [25] L. Baumgarten, C. M. Schneider, H. Petersen, F. Schäfers, and J. Kirschner, *Phys. Rev. Lett.* **65**, 492 (1990)
- [26] S. Eisebitt, J. Lüning, W. F. Schlotter, M. Lörger, O. Hellwig, W. Eberhardt, and J. Stöhr, *Nature* **432**, 885 (2004)
- [27] C.-C. Kao, C. T. Chen, E. D. Johnson, J. B. Hastings, H. J. Lin, G. H. Ho, G. Meigs, J.-M. Brot, S. L. Hulbert, Y. U. Idzerda, and C. Vettier, *Phys. Rev. B* **50**, 9599 (1994)
- [28] P. D. Johnson and G. Güntherodt, *Spin-polarized Photoelectron Spectroscopy as a Probe of Magnetic Systems*, in: *Handbook of Magnetism and Advanced Magnetic Materials*, Ed. by H. Kronmüller and S. Parkin (John Wiley and Sons, 2007)
- [29] H. Hopster, R. Raue, G. Güntherodt, E. Kisker, R. Clauberg, and M. Campagna, *Phys. Rev. Lett.* **51**, 829 (1983)
- [30] W. Eberhardt and E. W. Plummer, *Phys. Rev. B* **21**, 3245 (1980)
- [31] S. Datta and B. Das, *Appl. Phys. Lett.* **56**, 665 (1990)
- [32] Y. A. Bychkov and E. I. Rashba, *Sov. Phys. JETP Lett.* **39**, 78 (1984)
- [33] M. R. Freeman, W. K. Hiebert, and A. Stankiewicz, *J. Appl. Phys.* **83**, 6217 (1998)
- [34] B. Koopmans, M. van Kampen, J. T. Kohlhepp, and W. J. M. de Jonge, *Phys. Rev. Lett.* **85**, 844 (2000)
- [35] A. Scholl, L. Baumgarten, R. Jacquemin, and W. Eberhardt, *Phys. Rev. Lett.* **79**, 5146 (1997)
- [36] J. Vogel, W. Kuch, M. Bonfim, J. Camarero, Y. Pennec, F. Offi, K. Fukumoto, J. Kirschner, A. Fontaine, and S. Pizzini, *Appl. Phys. Lett.* **82**, 2299 (2003)
- [37] S. Hüfner, *Photoelectron Spectroscopy: Principles and applications* (Springer, Berlin, 1995)
- [38] S. Hüfner, *Very High Resolution Photoelectron Spectroscopy* (Springer, Berlin, 2007)
- [39] H. Hertz, *Ann. Physik* **267**, 983 (1887)
- [40] A. Einstein, *Ann. Physik* **17**, 132 (1905)
- [41] A. Einstein, *Ann. Physik* **325**, 199 (1906)
- [42] K. Siegbahn, *ESCA applied to free molecules* (North-Holland Publishing, Amsterdam, 1969)
- [43] J. F. Watts and J. Wolstenholme, *An Introduction to Surface State Analysis by XPS and AES* (John Wiley and Sons, England, 2003)
- [44] J. Kessler, *Polarized Electrons* (Springer, Heidelberg, 1985)
- [45] N. F. Mott, *Proc. Roy. Soc. A* **124**, 425 (1929)
- [46] G. Ghiringhelli, K. Larsson, and N. B. Brookes, *Rev. Sci. Instrum.* **70**, 4225 (1999)
- [47] D. Tillman, R. Thiel, and E. Kisker, *Z. Phys. B* **77**, 1 (1989)
- [48] M. R. Scheinfein, J. Unguris, M. H. Kelley, D. T. Pierce, and R. J. Celotta, *Rev. Sci. Instrum.* **61**, 2501 (1990)
- [49] J. Kirschner and R. Feder, *Phys. Rev. Lett.* **42**, 1008 (1979)
- [50] G. Burnett, T. J. Monroe, and F. B. Dunning, *Rev. Sci. Instrum.* **65**, 1893 (1994)
- [51] C. N. Berglund and W. E. Spicer, *Phys. Rev.* **136**, A1030 (1964)
- [52] A. Damascelli, Z. Hussain, and Z. Shen, *Rev. Mod. Phys.* **75**, 473 (2003)
- [53] M. P. Seah and W. A. Dench, *Surf. Interface. Anal.* **1**, 2 (1979)

- [54] W. Shockley, *Phys. Rev.* **56**, 317 (1939)
- [55] I. Tamm, *Phys. Z. Soviet Union* **1**, 733 (1932)
- [56] N. W. Ashcroft and N. D. Mermin, *Solid State Physics* (Saunders College, Philadelphia, 1976)
- [57] G. D. Mahan, *Phys. Rev. B* **2**, 4334 (1970)
- [58] C. Caroli, D. Lederer-Rozenblatt, B. Roulet, and D. Saint-James, *Phys. Rev. B* **8**, 4552 (1973)
- [59] P. J. Feibelman and D. E. Eastman, *Phys. Rev. B* **10**, 4932 (1974)
- [60] N. V. Smith, P. Thiry, and Y. Petroff, *Phys. Rev. B* **47**, 15476 (1993)
- [61] J. Hermanson, *Solid State Commun.* **22**, 9 (1977)
- [62] R. L. Benbow, *Phys. Rev. B* **22**, 3775 (1980)
- [63] M. Faraday, *Phil. Trans. Roy. Soc.* **136**, 1 (1846)
- [64] B. T. Thole, P. Carra, F. Sette, and G. van der Laan, *Phys. Rev. Lett.* **68**, 1943 (1992)
- [65] P. Carra, B. T. Thole, M. Altarelli, and X. Wang, *Phys. Rev. Lett.* **70**, 694 (1993)
- [66] R. Nakajima, J. Stöhr, and Y. U. Idzerda, *Phys. Rev. B* **59**, 6421 (1999)
- [67] C. M. Schneider and G. Schönhense, *Rep. Prog. Phys.* **65**, 1785 (2002)
- [68] D. Attwood, *Soft X-rays and Extreme Ultraviolet Radiation* (Cambridge University Press, 1999)
- [69] D. Eastman and Y. Farge, *Handbook on Synchrotron Radiation* (Amsterdam, North-Holland, 1983)
- [70] F. Schäfers, W. Peatman, A. Eyers, C. Heckenkamp, G. Schönhense, and U. Heinzmann, *Rev. Sci. Instrum.* **57**, 1032 (1985)
- [71] D. Roy and D. Tremblay, *Rep. Prog. Phys.* **53**, 1621 (1990)
- [72] K. D. Sevier, *Low Energy Electron Spectrometry* (John Wiley and Sons, New York, 1972)
- [73] F. Passek and M. Donath, *Phys. Rev. Lett.* **69**, 1101 (1992)
- [74] K. Starke, K. Ertl, and V. Dose, *Phys. Rev. B* **45**, 6154 (1992)
- [75] T. J. Gray and F. B. Dunning, *Rev. Sci. Instrum.* **63**, 1635 (1992)
- [76] Y. Dedkov and C. Laubschat, *SPECS Application Note: Spin Resolved Photoemission* (2008)
- [77] W. Kuch, L. I. Chelaru, F. Offi, M. Kotsugi, and J. Kirschner, *J. Vac. Sci. Technol. B* **20**, 2543 (2002)
- [78] <http://www.bestec.de/index.php?page=12>
- [79] F. Kronast, R. Ovsyannikov, A. Kaiser, C. Wiemann, S.-H. Yang, D. E. Bürgler, R. Schreiber, F. Salmassi, P. Fischer, H. A. Dürr, C. M. Schneider, W. Eberhardt, and C. S. Fadley, *Appl. Phys. Lett.* **93**, 243116 (2008)
- [80] G. F. Rempfer, W. P. Skoczylas, and O. H. Griffith, *Ultramicroscopy* **36**, 196 (1991)
- [81] S. Anders, H. A. Padmore, R. M. Duarte, T. Renner, T. Stammel, A. Scholl, M. R. Scheinfein, J. Stöhr, L. Séve, and B. Sinkovic, *Rev. Sci. Instrum.* **70**, 3973 (1999)
- [82] J. Stöhr and S. Anders, *IBM J. Res. Develop.* **44**, 535 (2000)
- [83] O. Renault, R. Brochier, P.-H. Haumesser, N. Barrett, B. Kromker, and D. Funnemann, *J. Surf. Sci. Nanotech.* **4**, 431 (2006)
- [84] T. Schmidt, S. Heun, J. Slezak, J. Díaz, K. C. Prince, G. Lilienkamp, and E. Bauer, *Surf. Rev. Lett.* **5**, 1287 (1998)
- [85] D. H. Auston, *IEEE J. Quantum Electr.* **19**, 639 (1983)

- [86] U. D. Keil, H. J. Gerritsen, J. E. M. Haverkort, and H. J. Wolter, *Appl. Phys. Lett.* **66**, 1629 (1994)
- [87] D. R. Heatley, A. M. Dunlop, and W. J. Firth, *Opt. Lett.* **18**, 170 (1993)
- [88] D. E. Spence, P. N. Kean, and W. Sibbett, *Opt. Lett.* **16**, 42 (1991)
- [89] C. Herring, *Exchange interactions among itinerant electrons*, in: *Magnetism, Vol. IV*, Ed. by G. T. Rado and H. Suhl (Academic Press, New York, 1966)
- [90] H. Wadati, T. Yoshida, and A. Fujimori, *Lect. Notes Phys.* **715**, 327 (2007)
- [91] A. Sekiyama, S. Imada, A. Yamasaki, and S. Suga, *Lect. Notes Phys.* **715**, 351 (2007)
- [92] J. Fink, S. Borisenko, A. Kordyuk, A. Koitzsch, J. Geck, V. Zabolotnyy, M. Knupfer, B. Büchner, and H. Berger, *Lect. Notes Phys.* **715**, 295 (2007)
- [93] V. L. Moruzzi, A. R. Williams, and J. F. Janak, *Calculated Electronic Properties of Metals* (Pergamon Press, Oxford, 1975)
- [94] P. Thiry, D. Chandessris, J. Lecante, C. Guillot, R. Pinchaux, and Y. Petroff, *Phys. Rev. Lett.* **43**, 82 (1979)
- [95] S. D. Kevan, *Angle Resolved Photoemission, Theory and Current Applications* (Elsevier, Amsterdam, 1992)
- [96] R. Feder, *Polarized Electrons in Surface Physics* (World Scientific, Singapore, 1985)
- [97] E. Kisker, in: *Metallic Magnetism*, Ed. by H. Cappellmann (Springer, Berlin, 1987)
- [98] E. W. Plummer and W. Eberhardt, *Adv. Chem. Phys.* **49**, 533 (1982)
- [99] L. Davis, *J. Appl. Phys.* **59**, R 25 (1986)
- [100] F. Himpsel, *Adv. Phys.* **32**, 1 (1983)
- [101] M. Donath, *Surf. Sci. Rep.* **20**, 251 (1994)
- [102] J. P. Perdew and W. Yue, *Phys. Rev. B* **33**, 8800 (1986)
- [103] F. J. Himpsel, J. A. Knapp, and D. E. Eastman, *Phys. Rev. B* **19**, 2919 (1979)
- [104] O. Rader and W. Gudat, *Electronic structure of solids: Photoemission spectra and related data, Landolt-Börnstein, New Series, Group III Vol 23C2*, Ed. by A. Goldmann (Springer, Berlin, 1999)
- [105] A. Santoni and F. J. Himpsel, *Phys. Rev. B* **43**, 1305 (1991)
- [106] M. I. Katsnelson and A. I. Lichtenstein, *J. Phys.: Condens. Matter.* **11**, 1037 (1999)
- [107] M. M. Steiner, R. C. Albers, and L. J. Sham, *Phys. Rev. B* **45**, 13272 (1992)
- [108] U. Alkemper, C. Carbone, E. Vescovo, W. Eberhardt, O. Rader, and W. Gudat, *Phys. Rev. B* **50**, 17496 (1994)
- [109] A. Georges, G. Kotliar, W. Krauth, and M. J. Rozenberg, *Rev. Mod. Phys.* **68**, 13 (1996)
- [110] C. Calandra and F. Manghi, *Phys. Rev. B* **50**, 2061 (1994)
- [111] S. Monastra, F. Manghi, C. A. Rozzi, C. Arcangeli, E. Wetli, H.-J. Neff, T. Greber, and J. Osterwalder, *Phys. Rev. Lett.* **88**, 236402 (2002)
- [112] F. Manghi, V. Bellini, J. Osterwalder, T. J. Kreutz, P. Aebi, and C. Arcangeli, *Phys. Rev. B* **59**, R10409 (1999)
- [113] J. Braun, J. Minár, H. Ebert, M. I. Katsnelson, and A. I. Lichtenstein, *Phys. Rev. Lett.* **97**, 227601 (2006)
- [114] J. Braun, *Rep. Prog. Phys.* **59**, 1267 (1996)

- [115] I. Di Marco, *PhD Thesis, University of Nijmegen* (2009)
- [116] V. Boni, *PhD Thesis, University of Modena, Italy* (2010)
- [117] J. C. Slater, *Phys. Rev.* **81**, 385 (1951)
- [118] P. Hohenberg and W. Kohn, *Phys. Rev.* **136**, B864 (1964)
- [119] W. Kohn and L. J. Sham, *Phys. Rev.* **140**, A1133 (1965)
- [120] R. O. Jones and O. Gunnarsson, *Rev. Mod. Phys.* **61**, 689 (1989)
- [121] D. van der Marel and G. A. Sawatzky, *Phys. Rev. B* **37**, 10674 (1988)
- [122] V. I. Anisimov, J. Zaanen, and O. K. Andersen, *Phys. Rev. B* **44**, 943 (1991)
- [123] V. I. Anisimov, F. Aryasetiawan, and A. I. Lichtenstein, *J. Phys.: Condens. Matter* **9**, 767 (1997)
- [124] J. Hubbard, *Proc. Roy. Soc. A* **276**, 238 (1963)
- [125] N. F. Mott, *Proc. Roy. Soc. A* **62**, 416 (1949)
- [126] A. Liebsch and A. I. Lichtenstein, *Phys. Rev. Lett.* **84**, 1591 (2000)
- [127] G. Zwirnagl, *Adv. Phys.* **41**, 203 (1992)
- [128] K. Held, *Adv. Phys.* **56**, 829 (2007)
- [129] A. I. Lichtenstein and M. I. Katsnelson, *Phys. Rev. B* **57**, 6884 (1998)
- [130] P. W. Anderson, *Phys. Rev.* **124**, 41 (1961)
- [131] J. Minár, L. Chioncel, A. Perlov, H. Ebert, M. I. Katsnelson, and A. I. Lichtenstein, *Phys. Rev. B* **72**, 045125 (2005)
- [132] L. D. Faddeev, *Sov. Phys. JETP* **12**, 275 (1963)
- [133] J. Minár, H. Ebert, C. De Nadai, N. B. Brookes, F. Venturini, G. Ghiringhelli, L. Chioncel, M. I. Katsnelson, and A. I. Lichtenstein, *Phys. Rev. Lett.* **95**, 166401 (2005)
- [134] I.-G. Baek, H. G. Lee, H.-J. Kim, and E. Vescovo, *Phys. Rev. B* **67**, 075401 (2003)
- [135] H. Lee, I. Baek, and E. Vescovo, *Appl. Phys. Lett.* **89**, 112516 (2006)
- [136] S. Kaya, *Tohoku Imp. Univ.* **17**, 1157 (1928)
- [137] M. Mulazzi, J. Miyawaki, A. Chainani, Y. Takata, M. Taguchi, M. Oura, Y. Senba, H. Ohashi, and S. Shin, *Phys. Rev. B* **80**, 241106 (2009)
- [138] H. H. Fritzsche, J. Kohlhepp, and U. Gradmann, *J. Magn. Magn. Mater.* **148**, 154 (1995)
- [139] M. Getzlaff, J. Bansmann, J. Braun, and G. Schönhense, *J. Magn. Magn. Mater.* **161**, 70 (1996)
- [140] A. Rampe, D. Hartmann, and G. Güntherodt, *Linear magnetic dichroism in angle-resolved photoemission spectroscopy from Co(0001) and Fe(110) valence bands*, in: *Spin—Orbit-Influenced Spectroscopies of Magnetic Solids*, Ed. by W. Beiglböck, 49–63 (Springer, Berlin, 1996)
- [141] C. Math, J. Braun, and M. Donath, *Surf. Sci.* **482**, 556 (2001)
- [142] A. Bettac, J. Bansmann, V. Senz, and K. H. Meiwes-Broer, *Surf. Sci.* **454**, 936 (2000)
- [143] O. Fruchart, P. Jubert, M. Eleoui, F. Cheynis, B. Borca, P. David, V. Santonacci, A. Liénard, M. Hasegawa, and C. Meyer, *J. Phys.: Condens. Matter* **19**, 053001 (2007)
- [144] H. Bethge, D. Heuer, C. Jensen, K. Reshöft, and U. Köhler, *Surf. Sci.* **331**, 878 (1995)
- [145] B. Johnson, P. Berlowitza, D. Goodman, and C. Bartholome, *Surf. Sci.* **217**, 13 (1987)
- [146] A. Varykhalov, O. Rader, and W. Gudat, *Phys. Rev. B* **72**, 115440 (2005)

- [147] E. D. Tober, R. X. Ynzunza, F. J. Palomares, Z. Wang, Z. Hussain, M. A. Van Hove, and C. S. Fadley, *Phys. Rev. Lett.* **79**, 2085 (1997)
- [148] W.-H. Soe, K.-H. Rieder, A. M. Shikin, V. Mozhaiskii, A. Varykhalov, and O. Rader, *Phys. Rev. B* **70**, 115421 (2004)
- [149] H. Ishii, N. Hayashi, E. Ito, Y. Washizu, K. Sugi, Y. Kimura, M. Niwano, Y. Ouchi, and K. Seki, *Phys. Status Solidi A* **201**, 1075 (2005)
- [150] R. Feder, A. Rodriguez, U. Baier, and E. Kisker, *Solid State Commun.* **52**, 57 (1984)
- [151] A. M. Turner, A. W. Donoho, and J. L. Erskine, *Phys. Rev. B* **29**, 2986 (1984)
- [152] E. Kisker, K. Schröder, M. Campagna, and W. Gudat, *Phys. Rev. Lett.* **52**, 2285 (1984)
- [153] J. Schäfer, M. Hoinkis, E. Rotenberg, P. Blaha, and R. Claessen, *Phys. Rev. B* **72**, 155115 (2005)
- [154] J. Schäfer, D. Schrupp, E. Rotenberg, K. Rossnagel, H. Koh, P. Blaha, and R. Claessen, *Phys. Rev. Lett.* **92**, 097205 (2004)
- [155] A. Gutiérrez and M. F. López, *Phys. Rev. B* **56**, 1111 (1997)
- [156] A. I. Lichtenstein, M. I. Katsnelson, and G. Kotliar, *Phys. Rev. Lett.* **87**, 067205 (2001)
- [157] A. Grechnev, I. Di Marco, M. I. Katsnelson, A. I. Lichtenstein, J. Wills, and O. Eriksson, *Phys. Rev. B* **76**, 035107 (2007)
- [158] O. Miura and T. Fujiwara, *Phys. Rev. B* **77**, 195124 (2008)
- [159] V. I. Anisimov and O. Gunnarsson, *Phys. Rev. B* **43**, 7570 (1991)
- [160] M. Getzlaff, J. Bansmann, J. Braun, and G. Schönhense, *Z. Phys. B* **104**, 11 (1997)
- [161] H. J. Kim, E. Vescovo, S. Heinze, and S. Blügel, *Surf. Sci.* **478**, 193 (2001)
- [162] S. Hüfner, S.-H. Yang, B. S. Mun, C. S. Fadley, J. Schäfer, E. Rotenberg, and S. D. Kevan, *Phys. Rev. B* **61**, 12582 (2000)
- [163] D. Shirley, *Phys. Rev. B* **5**, 4709 (1972)
- [164] A. V. Fedorov, T. Valla, F. Liu, P. D. Johnson, M. Weinert, and P. B. Allen, *Phys. Rev. B* **65**, 212409 (2002)
- [165] P. B. Allen, *Phys. Rev. B* **36**, 2920 (1987)
- [166] D. R. Penn, *Phys. Rev. B* **35**, 482 (1987)
- [167] W. S. M. Werner, K. Glantschnig, and C. Ambrosch-Draxl, *J. Phys. Chem. Ref. Data* **38**, 1013 (2009)
- [168] F. J. Himpsel and D. E. Eastman, *Phys. Rev. B* **21**, 3207 (1980)
- [169] D. E. Eastman, F. J. Himpsel, and J. A. Knapp, *Phys. Rev. Lett.* **44**, 95 (1980)
- [170] J. Osterwalder, *J. Elec. Spec. Rel. Phen.* **117**, 71 (2001)
- [171] F. J. Himpsel and D. E. Eastman, *Phys. Rev. B* **20**, 3217 (1979)
- [172] B. Ackermann, R. Feder, and E. Tamura, *J. Phys. F.: Met. Phys.* **14**, L173 (1984)
- [173] J. Braun, *New developments in UPS and XPS from ferromagnetic materials*, in: *Band-Ferromagnetism: Ground-State and Finite-Temperature Phenomena*, Ed. by ed K. Baberschke, M. Donath and W. Nolting (Springer, Berlin, 2001)
- [174] J. Braun and M. Donath, *J. Phys.: Condens. Matter* **16**, S2539 (2004)
- [175] E. L. Shirley, L. J. Terminello, A. Santoni, and F. J. Himpsel, *Phys. Rev. B* **51**, 13614 (1995)

- [176] J. Sánchez-Barriga, J. Fink, V. Boni, I. Di Marco, J. Braun, J. Minár, A. Varykhalov, O. Rader, V. Bellini, F. Manghi, H. Ebert, M. I. Katsnelson, A. I. Lichtenstein, O. Eriksson, W. Eberhardt, and H. A. Dürr, *Phys. Rev. Lett.* **103**, 267203 (2009)
- [177] S. Biermann, F. Aryasetiawan, and A. Georges, *Phys. Rev. Lett.* **90**, 086402 (2003)
- [178] A. N. Rubtsov, M. I. Katsnelson, and A. I. Lichtenstein, *Phys. Rev. B* **77**, 033101 (2008)
- [179] K. S. Novoselov, A. K. Geim, S. V. Morozov, D. Jiang, Y. Zhang, S. V. Dubonos, I. V. Grigorieva, and A. A. Firsov, *Science* **306**, 666 (2004)
- [180] D. S. Bethune, C. Klang, M. S. de Vries, G. Gorman, R. Savoy, J. Vázquez, and R. Beyers, *Nature* **363**, 605 (1993)
- [181] A. K. Gleim and K. S. Novoselov, *Nature Mat.* **6**, 183 (2007)
- [182] C. Berger, Z. Song, X. Li, X. Wu, N. Brown, C. Naud, D. Mayou, T. Li, J. Hass, A. N. Marchenkov, E. H. Conrad, P. N. First, and W. A. de Heer, *Science* **312**, 1191 (2006)
- [183] K. Hirama, S. Miyamoto, H. Matsudaira, K. Yamada, H. Kawarada, T. Chikyo, H. Koinuma, K. Hasegawa, and H. Umezawa, *Appl. Phys. Lett.* **88**, 112117 (2006)
- [184] S. Bhattacharyya, O. Auciello, J. Birrell, J. A. Carlisle, L. A. Curtiss, A. N. Goyette, D. M. Gruen, A. R. Krauss, J. Schlueter, A. Sumant, and P. Zapol, *Appl. Phys. Lett.* **79**, 1441 (2001)
- [185] P. Strobel, M. Riedel, J. Ristein, and L. Ley, *Nature* **430**, 439 (2004)
- [186] K. Tsukagoshi, B. W. Aalphenaar, and H. Ago, *Nature* **401**, 572 (1999)
- [187] K. S. Novoselov, A. K. Geim, S. V. Morozov, D. Jiang, M. I. Katsnelson, I. V. Grigorieva, S. V. Dubonos, and A. A. Firsov, *Nature* **438**, 197 (2005)
- [188] M. I. Katsnelson, K. S. Novoselov, and K. Geim, *Nature Phys.* **2**, 620 (2006)
- [189] A. Javey, J. Guo, Q. Wang, M. Lundstrom, and H. Dai, *Nature* **424**, 654 (2003)
- [190] B. Özyilmad, P. Jarillo-Herrero, D. Efetov, and P. Kim, *Appl. Phys. Lett.* **91**, 192107 (2007)
- [191] N. B. Brandt, S. M. Chudinov, and Y. G. Ponomarav, *Semimetals 1. Graphite and its Compounds* ((North Holland, Amsterdam, 1988)
- [192] S. Sahoo, T. Kontos, J. Furer, C. Hoffmann, M. Graber, A. Cottet, and C. Schonenberger, *Nature Phys.* **1**, 99 (2005)
- [193] Y. G. Semenov, K. W. Kim, and J. M. Zavada, *Appl. Phys. Lett.* **91**, 153105 (2007)
- [194] L. E. Hueso, J. M. Pruneda, V. Ferrari, G. Burnell, J. P. Valdes-Herrera, B. D. Simons, P. B. Littlewood, E. Artacho, A. Fert, and N. D. Mathur, *Nature* **445**, 410 (2007)
- [195] E. W. Hill, A. K. Geim, K. Novoselov, F. Schedin, and P. Blake, *IEEE Trans. Magn.* **42**, 2694 (2006)
- [196] N. Tombros, C. Jozsa, M. Popinciuc, H. T. Jonkman, and B. J. van Wees, *Nature* **448**, 572 (2007)
- [197] P. D. Johnson, *Rep. Prog. Phys.* **60**, 1217 (1997)
- [198] A. Bostwick, T. Ohta, T. Seyller, K. Horn, and E. Rotenberg, *Nature Phys.* **3**, 26 (2007)
- [199] A. Bostwick, T. Ohta, J. McChesney, K. V. Emtsev, T. Seyller, K. Horn, and E. Rotenberg, *New J. Phys.* **9**, 385 (2007)
- [200] S. Y. Zhou, G. H. Gweon, and A. Lanzara, *Ann. Phys.* **321**, 1730 (2006)
- [201] C. D. Spataru, M. A. Cazalilla, A. Rubio, L. X. Benedict, P. M. Echenique, and S. G. Louie, *Phys. Rev. Lett.* **87**, 246405 (2001)
- [202] T. Kihlgren, T. Balasubramanian, L. Walldén, and R. Yakimova, *Phys. Rev. B* **66**, 235422 (2002)

- [203] Y. S. Dedkov, M. Fonin, U. Rüdiger, and C. Laubschat, *Phys. Rev. Lett.* **100**, 107602 (2008)
- [204] Y. A. Bychkov and E. I. Rashba, *J. Phys. C: Solid State Phys.* **17**, 6039 (1984)
- [205] S. LaShell, B. A. McDougall, and E. Jensen, *Phys. Rev. Lett.* **77**, 3419 (1996)
- [206] E. Rotenberg, J. W. Chung, and S. D. Kevan, *Phys. Rev. Lett.* **82**, 4066 (1999)
- [207] M. Hochstrasser, J. G. Tobin, E. Rotenberg, and S. D. Kevan, *Phys. Rev. Lett.* **89**, 216802 (2002)
- [208] J. I. Pascual, G. Bihlmayer, Y. M. Koroteev, H.-P. Rust, G. Ceballos, M. Hansmann, K. Horn, E. V. Chulkov, S. Blügel, P. M. Echenique, and P. Hofmann, *Phys. Rev. B* **76**, 153305 (2007)
- [209] O. Krupin, G. Bihlmayer, K. Starke, S. Gorovikov, J. E. Prieto, K. Döbrich, S. Blügel, and G. Kaindl, *Phys. Rev. B* **71**, 201403(R) (2005)
- [210] F. Reinert, G. Nicolay, S. Schmidt, D. Ehm, and S. Hüfner, *Phys. Rev. B* **63**, 115415 (2001)
- [211] A. M. Shikin, G. V. Prudnikova, V. K. Adamchuk, F. Moresco, and K.-H. Rieder, *Phys. Rev. B* **62**, 13202 (2000)
- [212] O. Rader, A. Varykhalov, J. Sánchez-Barriga, D. Marchenko, A. Rybkin, and A. M. Shikin, *Phys. Rev. Lett.* **102**, 057602 (2009)
- [213] A. M. Shikin, S. L. Molodtsov, A. G. Vyatkin, V. K. Adamchuk, N. Franco, M. Martin, and M. S. Asensio, *Surf. Sci.* **429**, 287 (1999)
- [214] A. Varykhalov, J. Sánchez-Barriga, A. M. Shikin, C. Biswas, E. Vescovo, A. Rybkin, D. Marchenko, and O. Rader, *Phys. Rev. Lett.* **101**, 157601 (2008)
- [215] T. Ohta, A. Bostwick, T. Seyller, K. Horn, and E. Rotenberg, *Science* **313**, 951 (2006)
- [216] Y. Zhang, Y.-W. Tan, H. L. Stormer, and P. Kim, *Nature* **438**, 201 (2005)
- [217] G. Giovannetti, P. A. Khomyakov, G. Brocks, V. M. Karpan, J. van den Brink, and P. J. Kelly, *Phys. Rev. Lett.* **101**, 026803 (2008)
- [218] P. A. Khomyakov, G. Giovannetti, P. C. Rusu, G. Brocks, J. van den Brink, and P. J. Kelly, *Phys. Rev. B* **79**, 195425 (2009)
- [219] A. Varykhalov and O. Rader, *Phys. Rev. B* **80**, 035437 (2009)
- [220] E. I. Rashba, *Sov. Phys. Solid State* **2**, 1109 (1960)
- [221] O. Krupin, G. Bihlmayer, K. Döbrich, J. E. Prieto, K. Starke, S. Gorovikov, S. Blügel, S. Kevan, and G. Kaindl, *New J. Phys.* **11**, 013035 (2009)
- [222] A. Varykhalov, J. Sánchez-Barriga, A. M. Shikin, W. Gudat, W. Eberhardt, and O. Rader, *Phys. Rev. Lett.* **101**, 256601 (2008)
- [223] T. Hirahara, K. Miyamoto, I. Matsuda, T. Kadono, A. Kimura, T. Nagao, G. Bihlmayer, E. V. Chulkov, S. Qiao, K. Shimada, H. Namatame, M. Taniguchi, and S. Hasegawa, *Phys. Rev. B* **76**, 153305 (2007)
- [224] M. Hoesch, M. Muntwiler, V. N. Petrov, M. Hengsberger, L. Patthey, M. Shi, M. Falub, T. Greber, and J. Osterwalder, *Phys. Rev. B* **69**, 241401(R) (2004)
- [225] K.-P. Kämper, W. Schmitt, and G. Güntherodt, *Phys. Rev. B* **42**, 10696 (1990)
- [226] H.-C. Mertins, S. Valencia, W. Gudat, P. M. Oppeneer, O. Zaharko, and H. Grimmer, *Europhys. Lett.* **66**, 743 (2004)
- [227] E. I. Rashba, *Phys. Rev. B* **79**, 161409(R) (2009)
- [228] F. Kuemmeth and E. I. Rashba, *Phys. Rev. B* **80**, 241409(R) (2009)
- [229] J. C. Boettger and S. B. Trickey, *Phys. Rev. B* **75**, 121402(R) (2007)

- [230] C. L. Kane and E. J. Mele, *Phys. Rev. Lett.* **95**, 226801 (2005)
- [231] G. Prinz, *Science* **282**, 1660 (1998)
- [232] S. Wolf, D. D. Awschalom, R. A. Buhrman, J. M. Daughton, S. von Molnár, M. L. Roukes, A. Y. Chtchelkanova, and D. M. Treger, *Science* **294**, 1488 (2001)
- [233] A. Kubo, K. Onda, H. Petek, Z. Sun, Y. S. Jung, and H. K. Kim, *Nano Lett.* **5**, 1123 (2005)
- [234] B. Heitkamp, F. Kronast, L. Heyne, H. A. Dürr, W. Eberhardt, S. Landis, and B. Rodmacq, *J. Phys. D: Appl. Phys.* **41**, 164002 (2008)
- [235] C. H. Back, D. Weller, J. Heidmann, D. Mauri, D. Guarisco, E. L. Garwin, and H. C. Siegmann, *Phys. Rev. Lett.* **81**, 3251 (1998)
- [236] S.-B. Choe, Y. Acremann, A. Scholl, A. Bauer, A. Doran, J. Stöhr, and H. Padmore, *Science* **304**, 420 (2004)
- [237] K. W. Chou, A. Puzic, H. Stoll, D. Dolgos, G. Schütz, B. Van Waeyenberge, A. Vansteenkiste, T. Tylizszczak, G. Woltersdorf, and C. H. Back, *Appl. Phys. Lett.* **90**, 202505 (2007)
- [238] B. Van Waeyenberge, A. Puzic, H. Stoll, K. W. Chou, T. Tylizszczak, R. Hertel, M. Fähnle, H. Brückl, K. Rott, G. Reiss, I. Neudecker, D. Weiss, C. H. Back, and G. Schütz, *Nature* **444**, 461 (2006)
- [239] F. Romanens, J. Vogel, W. Kuch, K. Fukumoto, J. Camarero, S. Pizzini, M. Bonfim, and F. Petroff, *Phys. Rev. B* **74**, 184419 (2006)
- [240] K. K. Fukumoto, W. Kuch, J. Vogel, F. Romanens, S. Pizzini, J. Camarero, M. Bonfim, and J. Kirschner, *Phys. Rev. Lett.* **96**, 097204 (2006)
- [241] W. Kuch, J. Vogel, J. Camarero, K. Fukumoto, Y. Pennec, S. Pizzini, M. Bonfim, and J. Kirschner, *Appl. Phys. Lett.* **85**, 440 (2004)
- [242] J. Raabe, C. Quitmann, C. H. Back, F. Nolting, S. Johnson, and C. Buehler, *Phys. Rev. Lett.* **94**, 217204 (2005)
- [243] K. S. Lee, S. Choi, and K. S. K., *Appl. Phys. Lett.* **87**, 192502 (2005)
- [244] M. Buess, J. Raabe, K. Perzlmaier, C. H. Back, and C. Quitmann, *Phys. Rev. B* **74**, 100404 (2006)
- [245] K. S. Lee, S. K. Kim, Y. S. Yu, Y. S. Choi, K. Y. Guslienko, H. Jung, and P. Fischer, *Phys. Rev. Lett.* **101**, 267206 (2008)
- [246] A. Vansteenkiste, *Nature Phys.* **5**, 332 (2009)
- [247] R. Hertel, S. Gliga, M. Fähnle, and C. M. Schneider, *Phys. Rev. Lett.* **98**, 117201 (2007)
- [248] O. A. Tretiakov and O. Tchernyshyov, *Phys. Rev. B* **75**, 012408 (2007)
- [249] S. Komineas, *Phys. Rev. Lett.* **99**, 117202 (2007)
- [250] S. Komineas, , and N. Papanicolaou, *New J. Phys.* **10**, 043021 (2008)
- [251] K. Y. Guslienko, K.-S. Lee, and S.-K. Kim, *Phys. Rev. Lett.* **100**, 027203 (2008)
- [252] W. Heisenberg, *Z. Phys.* **38**, 441 (1926)
- [253] W. Heisenberg, *Z. Phys.* **49**, 619 (1928)
- [254] J. Sánchez-Barriga, M. Lucas, G. Rivero, P. Marin, and A. Hernando, *J. Magn. Magn. Mater.* **312**, 99 (2007)
- [255] J. Sánchez-Barriga, M. Lucas, F. Radu, E. Martin, M. Multigner, P. Marin, A. Hernando, and G. Rivero, *Phys. Rev. B* **80**, 184424 (2009)
- [256] A. Hubert and R. Schäfer, *Magnetic Domains - The Analysis of Magnetic Microstructures* (Springer, Berlin, 1998)

- [257] A. Ahanaroni, *Introduction to the Theory of Ferromagnetism* (Oxford Science Publications, 1996)
- [258] P. Bruno, *Physical origins and theoretical models of magnetic anisotropy* (Forschungszentrum Jülich, 1993)
- [259] H. Kronmüller and M. Fähnle, *Micromagnetism and the Microstructure of Ferromagnetic Solids* (Cambridge University Press, Cambridge, New York, 2003)
- [260] E. C. Stoner and E. P. Wohlfarth, *Phil. Trans. Roy. Soc.* **240**, 599 (1948)
- [261] L. D. Landau and E. Lifshitz, *Phys. Z. Sowjetunion* **8**, 153 (1935)
- [262] W. F. Brown Jr., *Micromagnetics* (Interscience publishers, John Wiley and Sons, New York, London, 1963)
- [263] <http://math.nist.gov/oommf/>
- [264] H. Kronmüller, *Zeitschrift für Physik* **168**, 478 (1962)
- [265] C. Néel, *Acad. Sci. Paris* **237**, 1468 (1953)
- [266] B. Lilley, *Phil. Mag.* **41**, 792 (1950)
- [267] R. Hertel, *Z. Metallkd.* **93**, 957 (2002)
- [268] S. B. Choe, Y. Acreman, A. Bauer, A. Scholl, A. Doran, J. Stöhr, and H. A. Padmore, *Synchrotron Radiat. Instrum.* **705**, 1391 (2004)
- [269] *Omicron Nanotechnology GmbH*
- [270] J. Darmo, G. Strasser, T. Muller, R. Bratschitsch, and K. Unterrainer, *Appl. Phys. Lett.* **81**, 871 (2002)
- [271] *Part No. LCC02834, Spectrum Semiconductor Materials, Inc.*
- [272] *Part No. BP3, Interconnect Devices, Inc.*
- [273] P. W. Hawkes and E. Kasper, *Principles of Electron Optics, Vol. 2* (Academic Press, London., 1996)
- [274] J. D. Jackson, *Classical Electrodynamics (3rd ed.)* (Wiley, New York, 1999)
- [275] J. Miguel, M. Bernien, D. Bayer, J. Sánchez-Barriga, F. Kronast, M. Aeschlimann, H. A. Dürr, and W. Kuch, *Rev. Sci. Instrum.* **79**, 033702 (2008)
- [276] E. E. Huber Jr, D. O. Smith, and J. B. Goodenough, *J. Appl. Phys.* **29**, 294 (1958)
- [277] R. M. Moon, *J. Appl. Phys.* **30**, 82S (1959)
- [278] S. Middlehoek, *J. Appl. Phys.* **34**, 1054 (1963)
- [279] H. A. M. Van den Berg, *J. Appl. Phys.* **57**, 2168 (1985)
- [280] H. A. M. Van den Berg, *J. Appl. Phys.* **60**, 1104 (1986)
- [281] A. Neudert, J. McCord, R. Schäfer, R. Kaltofen, I. Mönch, H. Vinzelberg, and L. Schultz, *J. Appl. Phys.* **99**, 08F302 (2006)
- [282] N. Wiese, S. McVitie, J. N. Chapman, A. Capella-Kort, and F. Otto, *Europhys. Lett.* **80**, 57003 (2007)
- [283] J. P. Park, P. Eames, D. M. Engebretson, J. Berezovsky, and P. A. Crowell, *Phys. Rev. B* **67**, 020403 (2003)
- [284] K. Perzlmaier, M. Buess, C. H. Back, V. E. Demidov, B. Hillebrands, and S. O. Demokritov, *Phys. Rev. Lett.* **94**, 057202 (2005)

- [285] K. Kuepper, M. Buess, J. Raabe, C. Quitmann, and J. Fassbender, *Phys. Rev. Lett.* **99**, 167202 (2007)
- [286] E. Feldtkeller, *Z. Angew. Phy.* **19**, 530 (1965)
- [287] T. Shinjo, T. Okuno, R. Hassdorf, K. Shigeto, and T. Ono, *Science* **289**, 930 (2000)
- [288] A. Wachowiak, J. Wiebe, M. Bode, O. Pietzsch, M. Morgenstern, and R. Wiesendanger, *Science* **298**, 577 (2002)
- [289] K. Y. Guslienko, B. A. Ivanov, V. Novosad, I. Otani, H. Shima, and K. Fukamichi, *J. Appl. Phys.* **91**, 8037 (2002)

Publication List

1. J. Sánchez-Barriga, M. Lucas, G. Rivero, P. Marin and A. Hernando, *Magneto-electrolysis of Co nanowire arrays grown in a track-etched polycarbonate membrane*, Journal of Magnetism and Magnetic Materials **312**, 99 (2007).
2. J. Miguel, M. Bernien, D. Bayer, J. Sánchez-Barriga, F. Kronast, M. Aeschlimann, H. A. Dürr and W. Kuch, *A new sample holder for laser-excited pump-probe magnetic measurements on a Focus photoelectron emission microscope*, Review of Scientific Instruments **79**, 033702 (2008).
3. A. Varykhalov, J. Sánchez-Barriga, A. M. Shikin, C. Biswas, E. Vescovo, A. Rybkin, D. Marchenko and O. Rader, *Electronic and Magnetic Properties of Quasifreestanding Graphene on Ni*, Physical Review Letters **101**, 157601 (2008).
4. A. Varykhalov, J. Sánchez-Barriga, A. M. Shikin, W. Gudat, W. Eberhardt and O. Rader, *Quantum Cavity for Spin due to Spin-Orbit Interaction at a Metal Boundary*, Physical Review Letters **101**, 256601 (2008).
5. O. Rader, A. Varykhalov, J. Sánchez-Barriga, D. Marchenko, A. Rybkin and A. M. Shikin, *Is There a Rashba Effect in Graphene on 3d Ferromagnets?*, Physical Review Letters **102**, 057602 (2009)
6. J. Miguel, J. Sánchez-Barriga, D. Bayer, J. Kurde, B. Heitkamp, M. Piantek, F. Kronast, M. Aeschlimann, H. A. Dürr and W. Kuch, *Time-resolved magnetization dynamics of cross-tie domain walls in permalloy microstructures*, Journal of Physics: Condensed Matter **21**, 496001 (2009)
7. J. Sánchez-Barriga, M. Lucas, F. Radu, E. Martin, M. Multigner, P. Marin, A. Hernando, and G. Rivero, *Interplay between the magnetic anisotropy contributions of cobalt nanowires*, Physical Review B **80**, 184424 (2009).
8. J. Sánchez-Barriga, J. Fink, V. Boni, I. Di Marco, J. Braun, J. Minár, A. Varykhalov, O. Rader, V. Bellini, F. Manghi, H. Ebert, M. I. Katsnelson, A. I. Lichtenstein, O. Eriksson, W. Eberhardt, and H. A. Dürr, *Strength of Correlation Effects in the Electronic Structure of Iron*, Physical Review Letters **103**, 267203 (2009).
9. J. Sánchez-Barriga, A. Varykhalov, M. R. Scholz, O. Rader, D. Marchenko, A. Rybkin, A.M. Shikin and E. Vescovo, *Chemical vapour deposition of graphene on Ni(111) and Co(0001) and intercalation with Au to study Dirac-cone formation and Rashba splitting*, Diamond and Related Materials **19**, 734 (2010).
10. J. Sánchez-Barriga, J. Braun, J. Minár, A. Varykhalov, V. Boni, I. Di Marco, O. Rader, V. Bellini, F. Manghi, H. Ebert, M. I. Katsnelson, A. I. Lichtenstein, O. Eriksson, W. Eberhardt, H. A. Dürr and J. Fink, *Quantitative determination of spin-dependent quasiparticle lifetimes and electronic correlations in hcp Co*, Physical Review B **82**, 104414 (2010).
11. J. Kurde, J. Miguel, D. Bayer, J. Sánchez-Barriga, F. Kronast, M. Aeschlimann, H. A. Dürr and W. Kuch, *Magnetostatic Coupling of 90 degree domain walls in FeNi/Cu/Co trilayers*, submitted to New Journal of Physics (2010).

Curriculum Vitae

Personal Data

Jaime Sánchez-Barriga
c/o Helmholtz-Zentrum Berlin für Materialien und Energie, Albert-Einstein-
Str. 15, D-12489, Berlin
Tel.: 0049-30-(0)-1734221844
E-Mail: sbarriga@bessy.de
Mother: Maria Teresa González-Aller
Father: Antonio Sánchez-Barriga
Date of birth: 22 June 1977
Place of birth: Madrid (Spain)

Education

- Oct. 1995 - Feb. 2001 Physics Degree (Licenciado en Ciencias Físicas), Universidad Autónoma de Madrid, Spain.
- Oct. 2000 - Oct. 2001 Studies of Geophysics and Oceanography, Universidad de Vigo, Spain.
- Jan. 2002 - Sep. 2002 European Voluntary Service (E.V.S) at the General Hospital of Corinth, Greece.
- Sep. 2002 - Aug. 2005 Research Scholarship at the Instituto de Magnetismo Aplicado, Universidad Complutense de Madrid, Spain.
- Oct. 2002 - Dec. 2002 Scientific visit at the Instituto de Ciencia de Materiales de Madrid (CSIC, Surface Physics department), Spain.
- Oct. 2003 - Oct. 2004 Master on Physics Didactics (C.A.P Certificate), Universidad Complutense de Madrid, Spain.
- June. 2003 - Aug. 2005 Advanced Master Degree in Experimental Physics (Diploma de Estudios Avanzados (D.E.A)), Universidad Complutense de Madrid, Spain.
- Oct. 2005 - May. 2010 PhD Thesis in Helmholtz-Zentrum Berlin für Materialien und Energie, Elektronenspeicherring BESSY II.